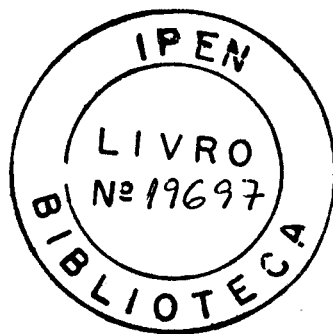


THE FATIGUE DAMAGE IN A FIBRE REINFORCED ALLOY

JESUALDO LUIZ ROSSI, M.Sc.

Orientador : R. Pilkington

A Thesis submitted to the
UNIVERSITY OF MANCHESTER
for the degree of
DOCTOR OF PHILOSOPHY
in the Faculty of Science



University of Manchester
Manchester Materials Science Centre
Grosvenor Street, Manchester M1 7HS

November 1991

To my family and to the memory of my dearest aunt Helena.

ABSTRACT

The fatigue damage behaviour of composite material produced by a liquid metal infiltration technique was examined by uniaxial tension-tension fatigue tests. The material consisted of a cast aluminium-silicon alloy reinforced with a continuous boron fibre coated with silicon carbide. The material was supplied in two different batches, one containing 28% fibre volume fraction and the other 48% fibre volume fraction. The as received material showed a cast microstructure consisting of aluminium dendrites, a eutectic interdendritic region and intermetallic particles. The presence of these particles was associated with contamination of the molten aluminium during composite manufacture. The composite material presented a weak matrix-fibre interface. During fatigue and tensile testing this type of interface led to fibre debonding, fibre pull out and to poor off-axis mechanical properties.

Tests were performed on the material with the fibres orientated parallel (0°) and with the fibres orientated at 10° to the tensile axis. The fatigue tests suggested that the composite life was only slightly sensitive to changes in stress range under repeated tensile loading for the 0° fibre orientation. In contrast, at 10° fibre orientation, the composite showed both a significant decrease in fatigue strength and a sensitivity to changes in stress range. The fatigue damage evaluation revealed a stiffness loss associated with the fatigue damage that was dependent on the fatigue stress range. When the composite material was tested below a stress range threshold no damage was observed, and thus it was considered to be fatigue proof under these conditions.

A comparison between a damage model developed for diffusion bonded material and some experimental results showed that the calculated average shake down stress ranges were higher than the allowed stress which did not cause stiffness loss in the type of composite used in this work. Conversely, the allowable matrix stresses could not be predicted from an examination of the matrix material in isolation.

It was shown that the mechanism by which the composite fatigue damage occurred

depended on the presence of surface defects, on defects internal to the matrix, brittle second phase particles and initial fibre breakage, all of which led to transverse matrix cracks. Many fibres remained intact for much of the specimen life, bridging matrix cracks perpendicular to the tensile stress direction. Dislocation density measurements, on either tensile or fatigue tested specimens, revealed no general change when compared to the as received material. However, the presence of prismatic loops and dislocation debris in the fatigued material was observed.

The fatigue damage results led to the proposition of a four stage mechanism for the effect of fatigue damage on the composite stiffness loss, for an aluminium-silicon matrix reinforced with silicon carbide coated boron fibres at 0° fibre orientation.

Declaration

No portion of work referred to in this thesis has been submitted in support of an application for another degree or qualification of this or any other university or other institute of learning.

JESUALDO LUIZ ROSSI

ACKNOWLEDGEMENTS

The author would like to thank Professors R. J. Young and F. R. Sale of the Manchester Materials Science Centre, for providing research facilities, to the "Conselho Nacional de Desenvolvimento Científico e Tecnológico" (CNPq) and the "Instituto de Pesquisas Energéticas e Nucleares" (IPEN-CNEN), Brazil, in the provision of a scholarship, and to the Ministry of Defence, U. K., for funding and material supply.

The author would also wishes to thank:

Dr. R. Pilkington, his supervisor, for helpful discussions and encouragement throughout this work.

Mr. R. L. Trumper, ARE., for his interest and useful suggestions.

Mr. P. B. Kenway, Mr. I. Brough, Mr. G. Cliff and Mr. R. B. Brew for their help in the electron microscopy suite, Mr. D. Hutchinson for assistance with the mechanical properties evaluation and the technicians of the Materials Science Centre whose support has been invaluable.

Isolda for incentive and collaboration.

His past and present colleagues of E-14 for their help and friendship.

Finally to everybody whose effort direct or indirectly contributed to the elaboration of this work.

CONTENTS

	Page
CHAPTER 1: INTRODUCTION	11
CHAPTER 2: LITERATURE REVIEW	13
2.1 Scope	13
2.2 Materials	14
2.2.1 The boron fibre	14
2.2.1.1 Manufacturing process	14
2.2.1.2 Microstructure of boron fibres	15
2.2.1.3 Fibre mechanical properties	15
2.2.2 The silicon carbide coating	16
2.2.3 The aluminium alloy matrix	17
2.2.4 The composite manufacturing	19
2.2.5 The aluminium alloy boron fibre composite	21
2.3 Composite theory	22
2.3.1 Principles of fibre composite strengthening	22
2.3.2 Continuous fibre composites	22
2.3.3 Stress-strain curve	23
2.3.4 The cyclic microstrain behaviour	25
2.3.5 The effect of fibre orientation	25
2.3.6 Stress and strain distribution at fibre ends	27
2.3.7 Interaction between fibre ends and cracks	29
2.4 Interfaces in metal matrix composites	29
2.5 Fabrication defects	33
2.6 Fatigue	34
2.6.1 Fatigue of metals	34

	Page	
2.6.1.1	The initiation of fatigue cracks	35
2.6.1.2	Propagation of fatigue cracks	36
2.6.1.3	The influence of cyclic deformation on microstructure	36
2.6.2	Fatigue of composite materials	37
2.6.2.1	The fatigue of boron aluminium composites	38
2.6.2.2	Fatigue failure	39
2.6.2.3	The fatigue failure criterion	42
2.7	Fatigue damage accumulation	42
2.8	Particle cracking	47
2.9	Concluding remarks	48

CHAPTER 3:	EXPERIMENTAL	50
3.1	Introduction	50
3.2	Composite manufacturing	50
3.3	Bulk chemical analyses	51
3.4	Radiographic examination	51
3.5	Specimen geometry and preparation	51
3.5.1	Fibre specimens	51
3.5.2	Aluminium alloy prior to infiltration specimens	52
3.5.3	Composite specimens	52
3.6	Mechanical testing	53
3.6.1	Tensile testing	53
3.6.1.1	Fibre tensile testing	53
3.6.1.2	Aluminium alloy tensile testing	54
3.6.1.3	Composite tensile testing	54
3.6.2	Fatigue testing	54
3.6.2.1	Aluminium alloy fatigue testing	55

	Page	
3.6.2.2	Composite fatigue testing	55
3.7	Fatigue damage measurements	55
3.8	Microstructural characterization	57
3.8.1	Microstructural characterization of the fibres	57
3.8.2	Optical metallography	57
3.8.2.1	Metallographic specimen preparation	57
3.8.2.2	Metallographic measurements	58
3.8.3	Scanning electron microscopy	58
3.8.4	Transmission electron microscopy	59
3.8.4.1	Thin foils preparation	59
3.8.4.2	Dislocation density measurements	60
3.8.4.3	Energy dispersive spectroscopy	60
CHAPTER 4:	RESULTS AND DISCUSSION	61
4.1	Prior testing microstructural characterization	61
4.1.1	Fibres	61
4.1.2	Aluminium alloy	63
4.1.3	Composite material series 28%	63
4.1.3.1	Bulk chemical analyses	63
4.1.3.2	Fibre volume fraction and distribution	64
4.1.3.3	Microstructural characterization	65
4.1.4	Composite material series 48%	72
4.1.4.1	Bulk chemical analyses	72
4.1.4.2	Fibre volume fraction and distribution	72
4.1.4.3	Microstructural characterization	72
4.1.5	Fabrication defects	75
4.1.5.1	28% series material	75

		Page
4.1.5.2	48% series material	76
4.2	Fibre mechanical properties	77
4.3	Aluminium alloy mechanical properties	78
4.3.1	Aluminium alloy tensile testing	78
4.3.2	Aluminium alloy fatigue testing	79
4.4	Composite material mechanical properties	79
4.4.1	Composite material tensile testing	79
4.4.2	Composite material fatigue properties	81
4.5	Fatigue damage accumulation	83
4.5.1	Fatigue damage at 0° fibre orientation	83
4.5.1.1	Fatigue damage series 28% at 0° fibre orientation	83
4.5.1.2	Fatigue damage series 48% at 0° fibre orientation	87
4.5.2	Fatigue damage at 10° fibre orientation	88
4.5.3	Shake down	90
4.6	Post testing microstructural characterization	92
4.6.1	Aluminium alloy	93
4.6.2	Composite material tensile tested	93
4.6.3	Composite material fatigue tested	95
4.7	Concluding remarks	98
4.8	Summary	100

CHAPTER 5:	CONCLUSIONS AND SUGGESTIONS FOR FURTHER WORK	103
5.1	Conclusions	103
5.2	Suggestions for further work	105

REFERENCES

106

Appendix 1	Statistical characterization of strength	184
Appendix 2	Strain gauge techniques	188
Appendix 3	Second phase volume fraction determination	192
Appendix 4	X-ray microanalysis of second phase particles in thin foils	195
Appendix 5	Foil thickness measurement	197

CHAPTER 1

INTRODUCTION

History books refer to the fabrication of composite materials as one of the ancient materials technologies. In the ancient Mesopotamia, circa 2400 BC, a composite bow made of strips of wood and horn was used during the Akkadian period in the Sumer^[1]. The use of mixtures of straw as a reinforcing fibre and mud matrix was used in ancient times as non fired building bricks. Although these antique materials can be considered as a type of composite material, the modern composite in the form it is thought today owe its origin to the second world war^[2]. Whereas metal matrix composites have been studied over the past four decades motivated by potential structural applications, some serious structural applications only recently have been realised.

New requirements are constantly being placed on materials by advances in engineering technology, and an important one is lightweight structures. The aluminium boron composite system combines the outstanding mechanical properties of the boron fibres with the fabricability and reliability of an aluminium alloy matrix. One of the key properties in structural design is stiffness and the corresponding material property specific modulus (the ratio of elastic modulus to the specific gravity). Many engineering metals have similar specific modulus, and the high specific strength (the ratio of strength to the specific gravity) of some high-strength alloys is a serious limitation on structural projects. Thus, composite materials can circumvent some of these limitations by taking advantage of high specific moduli of certain covalent bonded materials combined with a matrix that allow structure fabrication and application.

The major attributes of interest in aluminium alloy composites are the increase in stiffness and strength coupled with significant improvements in high temperature strength when compared to plain aluminium alloys. The serious drawback is the reduced levels of ductility and toughness but improvements have been made in the last few years by use of

more appropriate matrices instead of conventional alloys. Nevertheless aluminium alloy matrix composites offer a real increase in specific stiffness and hence can be used in designs where stiffness is a dominant consideration.

It has been established that changes in stiffness can be indicative of tensile fatigue damage in composite laminates. In metal matrix composites many studies have been made on the boron aluminium system usually manufactured by diffusion bonding process. Interest in the liquid metal infiltration technique is recent because early developments were restricted by quality of fibre supply and adverse interfacial reactions. Thus, this project was aimed to study the fatigue damage of a SiC coated boron fibre Al-Si-Mg alloy produced by liquid metal infiltration technique, and to relate the fatigue damage to stiffness loss and whenever possible to the microstructural characteristics of the composite material.

The author has presented this work from the materials science point of view and has not emphasized aspects of composite design or application. The composite material was fabricated elsewhere and the author had no influence on the choice of the system neither the fabrication parameters. The supplied material was considered, at the fabrication time, to be the state-of-art in composites fabricated by liquid metal infiltration technique. Due to a high production cost, a limited amount of material was supplied.

In this work it was found to be more appropriate to use the term fibre reinforced alloy instead of fibre reinforced metal. The term metal matrix composite is a current well accepted terminology but rarely a pure metal is used as matrix as opposed to the wide use of metallic alloys.

CHAPTER 2

LITERATURE REVIEW

2.1 Scope

In this study of fatigue damage in a fibre reinforced alloy, it is of relevant importance first to consider the aspects pertaining to the material properties. This includes description of the fibre, fabrication process and the fibre mechanical properties. In this context, a survey of the aluminium alloy microstructure as result of the foundry process is given. This section is followed by a description of the composite manufacturing process and composite utilization prospects.

An insight into the composite theory is contained in the body of this chapter. This section is an attempt to outline the basic concepts behind the idea of a composite material. It is worth mentioning that emphasis has been given to the continuous fibre composite behaviour.

The next section deals with the interface. The properties of continuous fibre reinforced composites are to a large extent dependent on the nature of the fibre/matrix interface and some mechanical and chemical requirements are discussed in this section. A section dedicated to the possible defects that arise during the fabrication process is also included.

Following this, the metal fatigue behaviour is reported and compared to the fatigue of metal matrix composites. This is necessary since some aspects of classical fatigue mechanisms may be extended to metal matrix composites. This section is not intended to be comprehensive literature review of the fatigue of metal matrix composites reinforced with continuous fibres, but concentrates on some relevant aspects of the fatigue behaviour of aluminium-boron fibres composites.

Finally a description of the fatigue damage accumulation process is given. A indication of tensile fatigue damage translated as stiffness loss is discussed and a damage model developed for diffusion bonded material is accounted for.

2.2 Materials

2.2.1 The boron fibre

2.2.1.1 Manufacturing process

Boron, which is the fifth element on the periodic table, does not occur freely in nature. It must be isolated from boron containing compounds to be made into usable fibre form. The most economical and feasible process to produce the fibres is chemical vapour deposition^[3].

The boron fibres are usually continuously produced in two nominal diameters, approximately 100 μm and 140 μm ^[4]. It has a high elastic modulus, approximately 400 GPa, a tensile strength that exceeds 3500 MPa, a compressive strength of about 6900 MPa, and a low specific gravity $2.57 \times 10^3 \text{ Kg m}^{-3}$ ^[3]. It is virtually elastic until fracture and has a strain to failure of about 0.0085 ^[5].

A schematic diagram^[6] of a basic chemical vapour deposition unit is shown in Fig.1. A tungsten substrate wire, typically about 12.5 μm in diameter, is continuously drawn through a vertical reactor. Both reactor ends are sealed by a mercury pool, which acts also as electrical contact to the fibre. A variable DC power supply is applied across the ends of the reactor such that the tungsten becomes incandescent, about 1100 °C ^[7]. Prior to entering the deposition reactor, the tungsten substrate is first passed through a cleaning stage, not shown in Fig.1, in which the substrate is heated to incandescence in a hydrogen atmosphere to remove surface contaminants and residual lubricants.

The deposition process can be described by the equation,



where X represents either Cl, Br, or I ^[8], but usually boron trichloride (BCl_3) is used^[6]. At the working temperature, a mixture of BCl_3 vapours and hydrogen is admitted in the reactor tube, and the hydrogen reduction of the BCl_3 to elemental boron on the hot surface of the substrate takes place.

During the deposition of the boron, in the core of the fibre, a solid state reaction between tungsten and the boron mantle occurs to form a number of tungsten borides. Borides phases that have been identified in boron fibres are δ -WB, W_2B_5 , and WB_4 [8].

2.2.1.2 Microstructure of boron fibres

Fig.2 is a schematic diagram of the major characteristics of a boron fibre. The boron deposit grows in the form of cones that originates at the substrate surface^[8]. The typical surface appearance is that of a corn-cob structure. Boron fibres have been called 'amorphous'^[4,8] because of the characteristic diffraction pattern they produce. The pattern is always four broad halos located at the d-spacings 0.43 nm, 0.25 nm, 0.17 nm and 0.14 nm. Calculation of the crystallite size from the diffraction data, assuming the halos to be individual diffraction maxima, gives a value of approximately 2.0 nm. Therefore, the structure would be better classified as microcrystalline^[8].

During the course of the deposition reaction, the core increases in diameter, from 12.5 μm to about 17.5 μm , as the tungsten reacts with the boron^[4]. As consequence, compressive stresses are developed in the core and dilatational tensile stresses in the mantle. The rapid quenching of the outer layers of the fibre after the fabrication process produces a compressive stress in surface layers of the material when the fibre has cooled to a uniform temperature. Typical stress distribution^[9] for a 100 μm fibre is shown in Fig.3. Since the fibre surface is placed in compression, its strength will be less susceptible to surface damage. However, radial cracks occur within the central region of the fibres and may extend axially over a considerable distance but their radial extension is terminated by the compressive zones near the fibre surface.

2.2.1.3 Fibre mechanical properties

The strength of boron fibres is determined by the statistical distribution of flaws produced during the deposition process^[6]. The fibre strength histogram does not follow a normal distribution but rather is skewed by having a low strength tail. Fig.4 shows a histogram of boron fibre strength with a average ultimate tensile strength (UTS) of about 3600 MPa and a coefficient of variation of about 15% [4].

The major flaws types are voids near the tungsten boride/boron interface, radial cracks, and surface flaws^[6]. The effect of such flaws in reducing the strength of the fibre depends upon the nature and scale of the stress distribution developed in the fibre, on the fibre length and on the loading conditions.

The tensile strength of a boron fibre would not be expected to be influenced significantly by a radial flaw extending only in a plane parallel to the fibre axis^[7]. However, such flaws reduce the transverse strength of the fibre and may control transverse strength in some composites where the matrix/fibre interface is strong.

As mentioned previously, many factors may influence the strength of the fibre and it will be impossible to discuss all of them here. However, fibre length and diameter have a large effect on strength. It has been shown that the average strength of boron fibres decreases with fibre length^[10], Fig.5. It has also been shown^[11,12] that this type of behaviour is consistent with fibres whose strength distribution is of the Weibull type. For more information on the Weibull distribution see Appendix 1. Physically, the results of Fig.5, indicate that flaws are present on the surface and interior of the fibres and the probability of encountering more dangerous flaws increases with fibre length. Sometimes, however, two types of population defects coexist so that a bimodal distribution is obtained. An example of double distribution is given in Fig.6 for boron fibres. In this figure, the A-type flaws, appear to be associated with the surface and are found several centimetres apart, whereas the B-type flaws appear to lie within the fibre^[13].

2.2.2 The silicon carbide coating

Experimental results have indicated that boron fibres can be bonded, by diffusion, to an aluminium alloy such as ASM 6061 at 500 °C for processing times less than one hour in order to form the composite, without significant fibre degradation^[14]. However, any further fabrication step like brazing or heat treatment, or any metal liquid manufacturing technique utilized, would impair the composite properties due to compound formation, oxidation, and melt leaching or liquid metal corrosion.

In order to improve the upper limit of the fabrication temperature, the development of a protective coating for the fibre was successfully achieved by chemical vapour deposition of silicon carbide. The silicon carbide coating may be produced in a silicon methane mixture type reactor similar to the boron deposition reactor already described^[15].

The silicon carbide coating on boron fibres causes the fibre to have an outstanding resistance to oxidation^[16]. In addition, boride formation in aluminium alloy composites is completely inhibited, since boron does not contact the aluminium. Aluminium does not form compounds with silicon, and the aluminium carbide reaction is thermodynamically unfavourable in the presence of silicon carbide^[14] and silicon in the matrix^[17].

The silicon carbide coating produced by chemical vapour deposition consists of columnar subgrains preferentially oriented such that $\{111\}\beta$ planes lie perpendicular to the radial growth direction^[18]. This coating degrades the fibre tensile strength properties by approximately 10% when compared to the uncoated boron fibre^[19]. This decrease in tensile properties is related to the surface morphology of the coating which resembles a sawtooth. These sawtooth notches concentrate stresses at the silicon carbide subgrains boundaries leading to failure at lower stresses^[20].

2.2.3 The aluminium alloy matrix

Aluminium is one of the most used foundry metals. It has a light weight, a low melting point, negligible solubility for gases except hydrogen, most alloys display good fluidity and the composition can be selected with solidification ranges appropriate to a particular application^[21]. Thus, it has been a model material for production of metal matrix composites, either by diffusion bonding or by casting techniques like squeeze casting or liquid metal infiltration .

Aluminium alloys with silicon make up the main bulk of the aluminium casting alloys. The reason is a high fluidity imparted by the presence of somewhat large volumes of the Al-Si eutectic which results in good castability and weldability. Other advantages are a low thermal expansion coefficient controlled by the silicon content and a high corrosion resistance^[22]. In aluminium silicon alloys the fatigue resistance is relatively

low, especially if the silicon is not modified or spheroidized by heat treatment. Values of fatigue resistance of the order of 50-70 MPa are given for straight hypoeutectic alloys^[22].

During normal foundry practice, the typical cast structure of an Al-Si hypoeutectic alloy consists of primary aluminium rich dendrites surrounded by the aluminium-silicon eutectic. The silicon may appear as a flake structure containing many multiple twins formed as result of growth accidents in a continuous aluminium matrix^[23].

Although Al-Si alloys show some response to heat treatment, a much greater strengthening is achieved by making additions of Cu, Mg and Ni ^[21]. In particular, for Al-Si-Mg alloys, small additions of Mg induce significant age hardening through precipitation of Mg₂Si in the matrix. The alloy finds particular use for aircraft and automotive applications^[21].

Besides heat treatment, porosity, second phases, dendrite spacing and grain size affect the mechanical properties of an aluminium cast alloy. The presence of second-phase brittle particles impairs strength and ductility. Such phases are preferred sites for crack initiation and as size and volume fraction increases, tensile strength and ductility decreases^[23].

Iron is the main impurity in most aluminium silicon alloys and appears partially in solid solution but occurs mostly in intermetallic phases. According to the equilibrium Al-Si-Fe diagram^[22,24], different and complex intermetallic phases can be formed. The complexity of the Al-Si-Fe system makes the phase equilibria very difficult to be established. This is due to: 1) the occurrence of several phases over a relatively small range of composition in the Al corner of the phase diagram; 2) many invariant reactions which take place when solidification conditions deviate from equilibrium and 3) the presence of complex crystal structures^[24]. Table 1 compiled by Rivlin and Raynor^[24] from published literature up to 1981 lists some of these phases, together with composition and available crystallographic data.

According to this review^[24], the τ_5 phase is well established as having a hexagonal structure. This phase is sometimes referred as α -AlSiFe^[25,26,27] or α (Fe-Si)^[28] and often precipitates during solidification with a characteristic morphology called 'Chinese script'. As

stated by several authors, this phase may have a range of homogeneity^[22,24]. The τ_5 phase has also been claimed^[29] to be metastable and under non equilibrium conditions it can replace τ_6 phase. The cubic structure, vide Table 1, has been attributed by Munson^[30] to a dissolution of transition elements such as manganese, copper and chromium, which stabilize the cubic symmetry at the expenses of the hexagonal structure.

The τ_6 phase appears to have a monoclinic structure although a tetragonal structure has been reported^[22,24]. This phase is also referred as β (Fe-Si) ^[28], and forms very thin platelets which in section appears as long needles. Another phase, τ_4 , has been identified as tetragonal, vide Table 1, and a τ_2 phase has been reported as cubic or monoclinic.

2.2.4 The composite manufacturing

Many manufacturing methods to incorporate fibres into a metallic matrix have been tried. Early research into boron fibre reinforced aluminium alloys was carried out in the USA^[31]. However, adverse interfacial reactions, between the boron fibre and the aluminium matrix when held at temperatures above 600 °C for any length of time, restricted the fabrication to diffusion bonding process. The development of a SiC coating to prevent fibre degradation made the liquid metal infiltration technique a viable manufacturing process.

The diffusion bonding process, although being a feasible production route, has considerable disadvantages. It is an expensive process, generally limited to simple shapes like tubes and plates, and usually requires secondary fabrication if complicated structures are needed. Because of the high mechanical forces involved, fibre breakage can be a problem and the use of multifilament yarns is precluded^[32].

An alternative approach is the use of a liquid metal infiltration process in which the fibres are infiltrated by molten matrix material. If the metal wets the fibres well, it may readily infiltrate the fibres with little or no external pressure. On the other hand, if the metal and fibres are non wetting, then pressure is required to force the molten metal in, either by a hydraulic ram such as in the squeeze casting process or by gas pressurization infiltration.

The use of liquid metal infiltration technique, has many advantages. It is a one shot process with relatively short cycle time which can produce net shape components in a wide

range of shape and sizes^[32]. Any fibre capable of withstanding contact with the molten metal for relatively short periods may be used. Hybrid components with different fibres are foreseeable. Application of pressure by gas rather than by mechanical process also reduces the extent of fibre breakage and misalignment^[31].

The liquid metal infiltration apparatus includes a die which contains a cavity in the shape of the component to be produced. The reinforcing fibres are stacked or made into a preform whose shape, fibre orientation and volume fraction are dictated by the component needs. The basic fabrication steps, Fig.7, consist of placing the fibre preform in a heated die which is then evacuated. High pressure gas is then injected in the furnace container, forcing the molten metal into the die cavity to infiltrate the fibres. The die is then opened and the component ejected^[33]. The evacuation serves several purposes: removal of volatile binding agents, degassing of the melt, removal of air from the die that may cause porosity, and reduces aluminium oxide formation^[32].

The liquid metal infiltration process is similar in many ways to a conventional casting route and, as such, is likely to produce an as cast structure in the metal matrix. In aluminium silicon alloys, the as cast hypoeutectic structure consists typically of primary aluminium rich dendrites surrounded by the eutectic and second phases. This cast structure is controlled by the interaction between the geometry of fibre distribution and solidification kinetics. During the solidification process, the local solidification time is the most important parameter influencing the final microstructure in terms of dendrite size and morphology, which in turn can be related to the microsegregation (segregation of solute elements over the distance of the order of dendrite arm spacing). All of these effects may affect the mechanical properties^[34].

If the solidification time is sufficiently short that the dendrite arm spacing is less than the fibre spacing, the final microstructure is not expected to be affected by the presence of the fibres. However, for longer solidification times, the presence of fibres might constrain the dendritic growth resulting in a modified morphology^[34]. It has been reported^[35] that during solidification of infiltrated metal matrix composites, a noticeable phenomenon occurs. At a critical solidification time, the dendrite arms are suppressed, and disappear

totally during the solidification process. This is a phenomenon which never occurs in usual casting process, regardless of how slow cooling is.

2.2.5 The aluminium alloy boron fibre composite

Boron reinforced aluminium matrix composites are characterized by their high strength and stiffness, high thermal conductivity, low coefficient of thermal expansion (depending on fibre orientation), light weight and useful mechanical properties up to 510 °C. Typical material produced by diffusion bonding contains approximately 50% fibre volume fraction, although a range from 20% to 60% has been fabricated. Sheet sizes ranging from 1 ply to 100 plies, and from 305 mm x 610 mm to 760 mm x 9200 mm have been produced^[3].

The most celebrated use of boron/aluminium composite material was for the structural tubular struts of the American space shuttle. In this application, several hundred tube assemblies were fabricated with titanium collars and end fittings. The tubes varied from 25 mm to 67 mm in diameter and from 609 mm to 1850 mm length and were produced by diffusion bonding^[3].

For marine applications, a number of components have been developed at ARE Portland, U. K., as a 330 mm diameter hull section made from 60% volume fraction of Borsic®[‡] fibres wound in the hoop direction and liquid metal infiltrated with an aluminium alloy^[31]. Another potential application of this material is for reinforced propeller blades.

In the nuclear industry field, boron/aluminium composites are being examined as a neutron shielding material. Elemental boron has a naturally high neutron absorption cross section. Some possible applications are spent fuel transportation casks, portable shielding, spent fuel storage pools, and control rods^[3].

[‡] *Borsic is a tradename of Avco Specialty Materials Division, Textron Inc., Lowell, MA, USA.*

2.3 Composite Theory

2.3.1 Principles of fibre composite strengthening

The concept of fibre strengthening resides in the fact that materials strength can be increased not by interfering directly with the motion of dislocations but by transference of load to the fibre through the matrix. In order to achieve this^[36] the fibres must be strong, have a higher elasticity modulus than the matrix, and be present in a sufficient number. The matrix should provide a suitable medium into which the fibres can be incorporated and protected from surface damage which in turn can lead to loss of strength. The matrix must separate the fibres in order to increase toughness by avoiding crack propagation through the brittle fibres. It usually achieves this by plastic flow or by crack deflection on a weak fibre/matrix interface. The matrix must also transfer the stress to the strong fibres.

2.3.2 Continuous fibre composites

The best strength and modulus in a uniaxially stressed composite may be obtained if the following assumptions are fulfilled: the fibres should be aligned parallel to the loading axis, isostrain condition should exist in fibres and matrix at all stress levels, and a perfect bond exist between fibre and matrix. Thus, under isostrain condition the composite Young's modulus, E_c is given by the rule of mixtures,

$$E_c = E_f V_f + E_m (1 - V_f), \quad (2)$$

where E_f and E_m are the fibre and matrix modulus of elasticity respectively, and V_f is the fibre volume fraction.

Specific gravity also obey a similar relationship,

$$\rho_c = \rho_f V_f + \rho_m (1 - V_f), \quad (3)$$

and stress,

$$\sigma_c = \sigma_f V_f + \sigma_m (1 - V_f), \quad (4)$$

It should be pointed out that Eq.(4) does not refer to the strength of composite, matrix and fibre^[37], it applies to nominal stresses in the composite, fibre and matrix at a particular composite strain. The stress in the matrix becomes σ_m' , once the fibres have reached their breaking strain, Fig.8. When the fibres break, the stress on the matrix is

raised, and if it then exceeds σ_m^* the matrix will also fracture. The strength of the composite is then,

$$\sigma_c^* = \sigma_f^* V_f + \sigma_m' (1 - V_f). \quad (5)$$

Otherwise, the matrix continues to bear an increasing load until its ultimate tensile strength (*UTS*) is reached, when the composite strength is,

$$\sigma_c^* = \sigma_m^* (1 - V_f). \quad (6)$$

These two relationships are illustrated in Fig.8. It can be seen that small volume fractions of fibre weaken the matrix, and a critical volume fraction V_c of fibres must be added before any strengthening is achieved:

$$V_c = \frac{\sigma_m^* - \sigma_m'}{\sigma_f^* - \sigma_m'}, \quad (7)$$

where $(\sigma_m^* - \sigma_m')$ is a stress due to work hardening of the matrix^[36]. A matrix which work-hardens more requires a higher critical volume fraction of fibres before the strength of the composite begins to increase^[37].

2.3.3 Stress-strain curve

In discussing the stress-strain behaviour of strong metal fibres in a metal matrix, McDanel, Jech and Weeton^[38], have pointed out that the deformation can occur in four stages, Fig.9, namely:

Stage I) elastic deformation of fibres and matrix;

Stage II) plastic deformation of matrix, elastic deformation of fibres;

Stage III) plastic deformation of fibre and matrix;

Stage IV) tensile fracture of composite.

During stage I, the stresses in the composite and its components are related by the rule of mixtures. The elastic limit of the composite occurs at the same strain as the elastic limit of the matrix,

$$E_c(I) = E_f V_f + E_m (1 - V_f), \quad (8)$$

where $E_c(I)$ is the initial modulus of elasticity of the composite during stage I, E_f and E_m are the elastic moduli of the uncombined fibre and matrix, respectively, and V_f is the fibre volume fraction.

For stage II, a change of the modulus occurs and a secondary modulus of elasticity is defined by:

$$E_c(II) = E_f V_f + (\partial\sigma/\partial e)_m (1 - V_f), \quad (9)$$

where $E_c(II)$ is the secondary modulus of elasticity during stage II, and $(\partial\sigma/\partial e)_m$ is the slope of the matrix stress-strain curve at a given strain. Stage III only exists if the reinforcement can undergo plastic deformation.

For the boron aluminium system, Stuhrke^[39] showed typical stress-strain curves, Fig.10. The tensile tests consisted of an initial loading followed by unloading to no load and then, loading to fracture. The pretest showed a small fully elastic stage, implying that the matrix had yielded at very small stresses. It was argued that this is due to the residual strains in the aluminium at room temperature prior to testing. The residual strains are caused by the difference in thermal expansion coefficient and this should account for a considerable portion of the yield strain of the aluminium.

Stuhrke^[39] reported a four stage behaviour. The initial stage 1 is the only portion of the tensile behaviour in which both components behave in a elastic manner. The extent of stage 1 after reloading, depends on the pretest plastic flow. The second region of the stress-strain curve is designated stage 2. In this region, the slope of the curve changes from the uniform modulus of stage 1 to the approximately straight portion of stage 3. This region (stage 2) is characterized by the flowing of the aluminium from elastic to a quasi-plastic type behaviour. Plastic flow of the matrix in this latter stage does not introduce a permanent set in the composite material. Stage 3 is the most extensive and as the boron fibre behaves elastically it contributes to the overall behaviour as an elastic member. The aluminium matrix behaves through stage 3 in a plastic manner. The modulus in this region (stage 3) can be given by the expression:

$$E_c = E_f V_f. \quad (10)$$

A comparison between Eq.(9) and Eq.(10) shows that in the latter, the matrix contribution to the modulus of elasticity has been discarded as the value of $(\partial\sigma/\partial e)_m$ is normally much less than the fibre modulus.

Stages 2 and 3 are of practical importance, and the plastic strain in the matrix is limited by the elastic extension of the fibres. This becomes important in relation to fatigue cycling. In stage 4, the stress-strain behaviour leads to failure.

2.3.4 The cyclic microstrain behaviour

The cyclic microstrain behaviour of metal matrix composites has been described in several papers^[40-43]. Typical microstrain behaviour^[40] for a metal fibre, metal matrix composite is shown schematically in Fig.11. At low stresses the deformation is elastic up to σ_E , when the elastic limit is reached. The first hysteresis loops are observed at stresses greater than σ_E . At increasingly higher stresses, open loops appears and, finally, if the strain amplitude increases further, plastic strain is noticed.

2.3.5 The effect of fibre orientation

Aligned fibre composites are highly anisotropic. Their properties depend on fibre orientation and even in supposed aligned composites, the fibres rarely achieve perfect alignment. The anisotropic strength of composites has been described by Kelly and Davies^[36] based on Stowell and Liu analyses^[44] and by Azzi and Tsai^[45]. Kelly and Davies' analyses is a micromechanical approach in which they consider separately the behaviour of the two components. They postulated three failure mechanisms, each being the controlling over a different range of fibre orientation. When the tensile axis deviates by a small angle, φ , from the fibre alignment, the tensile failure of the fibres is the controlling mechanism, and, since the resolved stress on the fibre decreases with misalignment, an increase in strength is expected, Fig.12. The relationship governing the composite fracture stress for low angle misorientation is given by:

$$\sigma = \frac{\sigma_0}{\cos^2 \varphi} , \quad (11)$$

where σ_0 is the composite strength for perfect alignment, φ is the angle between the load axis and fibre orientation and σ is the tensile stress applied. At larger angles, the strength of the composite becomes limited by the shear strength of the matrix parallel to the fibres. The composite fracture stress is then,

$$\sigma = \frac{\tau}{\sin \varphi \cos \varphi} , \quad (12)$$

where τ is the shear strength of the matrix. At greater angles, the simple tensile strength of the matrix between the fibres becomes limiting and:

$$\sigma = \frac{\sigma_m}{\sin^2 \varphi} , \quad (13)$$

where σ_m is the matrix tensile strength after allowance for matrix constraints. Kelly and Davies^[36] have argued that in continuous fibre reinforced metal, the matrix behaves differently in the composite when constrained between fibres than when tested separately. Thus, the values of τ and σ_m used in Eq.(12) and Eq.(13) should be some unknown factor times the separately determined value.

The maximum stress theory of fracture assumes that the fracture occurs when the stresses in the principal material directions reach a critical value. Thus, for intermediate angles, the angles at which the transition from one fracture mode to another occur will depend on the relative magnitudes of, σ_0 , σ_m and τ , which in turn will be the smallest values of Eqs.(11-13). Clearly, the composite fracture stress increase showed in Fig.12 for angles higher than approximately 53° does not occur.

Petrasek and Signorelli^[46] have modified the Stowell and Liu^[44] and Kelly and Davies^[36] approaches so that the composite fracture stress will not increase for the off-axis loading at small angles of misalignment. In their modification, Eq.(11) becomes,

$$\sigma = \sigma_0 , \quad (14)$$

and the composite fracture stress is constant as φ increases until shear failure occurs.

Azzi and Tsai^[45], considered a phenomenological approach and thus independent on failure mechanism. In their approach they evaluated the mechanical anisotropy as a function of the longitudinal, the transverse and the shear strength of the composite. The equation

given by these authors was based on the maximum work of distortion, and the composite stress-angle profile is described by:

$$\frac{1}{\sigma^2} = \frac{\sin^4 \varphi}{\sigma_{90}^{*2}} + \frac{\cos^4 \varphi}{\sigma_0^{*2}} + \left(\frac{1}{\tau^{*2}} - \frac{1}{\sigma_0^{*2}} \right) \sin^2 \varphi \cos^2 \varphi, \quad (15)$$

where σ is the composite stress, σ_{90}^* is the transverse tensile strength, σ_0^* is the longitudinal tensile strength, and τ^* is the shear strength of the composite. They found good agreement between experimental and theory for a composite of glass filaments in resin.

2.3.6 Stress and strain distribution at fibre ends

For purposes of description, it is convenient to consider composites as composed of either continuous or discontinuous fibres surrounded by a matrix. Many continuous fibre composite materials contain discontinuous fibres prior to final fracture due to the fabrication process or due to fibre fracture during loading. The fabrication process, either of the fibre or of the composite, may break down long fibres into several discrete lengths. During the composite loading, many fibres may fracture at stresses below the fibre average strength due to inherent flaws produced during the fibre fabrication process. As the number of these fibre ends increases, their effect becomes more significant since the stress and strain fields in the fibre and in the matrix are modified by the discontinuity. If the broken fibres become so short that they can no longer be loaded directly through their ends, the stress must be transferred into them from the matrix by shear forces at the fibre/matrix interface. Thus, the fibre efficiency in stiffening and reinforcing the matrix diminishes due to a higher proportion of fibre ends where the stress is still building up to its equilibrium value.

The stress distributions in the matrix and in discontinuous fibres have been treated analytically by Cox^[47] using the so-called shear-lag analysis. In this analysis it is assumed that both fibre and matrix remains elastic and a perfect bond exists between fibre and matrix. Briefly, the shear stress at the fibre matrix interface τ_i is maximum at or close to the end of the fibre and decreases to zero at the centre of the fibre, Fig.13. The tensile stress, σ_z , in the fibre builds up from the end. Fig.13 also shows that the broken fibres can

still carry a high proportion of load on the composite. However, there is a section at the end of the fibre where the fibre tensile stress is building up and in this region the fibre reinforcing efficiency is diminished. It is evident that the reinforcing efficiency is dependent on the interfacial strength since the load transfer requires a strong interface bond.

The simplest theory of stress transfer to a broken fibre in a metallic matrix neglects elastic interactions and assumes that traction forces at the surface of the fibres arise from the shear strength of the matrix^[37], $\sigma_m^* / 2$. To a first approximation, the tensile stress in the fibre σ_z , is allowed to build up linearly from the end of the fibre, Fig.13. For a fibre longer than a critical length, l_c , the fibre stress increases over a length $l_c/2$ at each end until the central stress equals the fibre strength. For a fibre of radius r ,

$$\sigma_z = \frac{2 \tau_i z}{r} , \quad (16)$$

where τ_i is the maximum shear stress that can be supported in either the matrix or the interface, whichever is smaller, and z is the distance measured along the fibre axis from one of its ends^[11].

Continuous brittle fibres, like boron, fracture when a critical tensile stress σ_f is produced in the fibre parallel to the fibre axis. Thus from Eq.(16) this stress level will achieve a distance, z :

$$z = \frac{r \sigma_f}{2 \tau_i} , \quad (17)$$

from the end of the fibre. Consequently the fibre must have a length, l_c :

$$l_c = 2 \left(\frac{r \sigma_f}{2 \tau_i} \right) = \frac{d \sigma_f}{2 \tau_i} \quad (18)$$

before it can be broken. In Eq.(18) d is the fibre diameter, and

$$\frac{l_c}{d} = \frac{\sigma_f}{2 \tau_i} \quad (19)$$

is defined as the critical aspect ratio. Typical values of l_c/d for metal matrix composites lie between 20 and 40 ^[37]. For a SiC boron fibre, $\sigma_f \cong 3200$ MPa, and for an ASM A.356 cast aluminium alloy, $\sigma_m^* \cong 130$ MPa, therefore $l_c / d \cong 25$.

2.3.7 Interaction between fibre ends and cracks

In the previous section it has been shown that for a fibre perfectly bonded to the matrix, the shear stress concentration parallel to the interface is maximum at the end of the fibre. If τ_{max} exceeds the shear strength of the interface, or that of the surrounding matrix material, fracture will occur at or close to the interface. The fracture will start at the end and grow as the stress on the system increases. There are three main processes, illustrated in Fig.14, which can take place at the broken fibre. In (a) the crack in the fibre has propagated into the surrounding matrix as a brittle crack, in (b) the matrix has yielded blunting the sharp crack and the yield zone has spread along the fibre, and in (c) the interface or the matrix immediately adjacent to the fibre has failed in shear allowing the unloaded fibre to shrink back into the matrix^[48].

When a brittle crack meets a fibre, the stress concentration around the crack is proportional to $(c/r)^{1/2}$, where r is the radius of curvature at the crack tip and c is the crack half length. The stress state near a crack tip under uniaxial loading is triaxial. In anisotropic materials, the actual stresses will depend on crack orientation and the degree of anisotropy. From Fig.15, it can be seen that as this crack reaches a fibre, the stress at the crack tip σ_1 will tend to cause fibre fracture, the stress σ_2 will lead to tensile separation at the interface and the stress τ_{12} will cause shear failure at the interface^[49]. Depending on the critical failure stresses, each of the above mechanisms can account for the process which will control fracture toughness and fatigue life^[48].

2.4 Interfaces in metal matrix composites

The properties of continuous fibre reinforced composites are to a large extent dependent on the nature of the fibre/matrix interface which is defined as 'the region of significantly changed chemical composition that constitutes the bond between the matrix and the reinforcement' ^[50]. The primary function of the interface is to transfer load between the fibre and the matrix. This is a mechanical requirement and must be satisfied for all types of loading. Failure at the interface may be expected to occur depending on loading conditions. Longitudinal tensile loading is the least demanding since any transfer of loads takes place

over extended lengths, and as such the interface shear needs not to be high. In the case of off-axis and transverse tensile loading, the interface bears a more severe loading condition^[51]. Alternating load conditions that occurs during fatigue may provide a severe test on the interface.

The mechanical requirements of the interface so far discussed relate to load transfer. Another important condition is a stable interface that lasts throughout the composite life and this constitutes a physical chemical requirement of the interface. The interface stability is best achieved by using suitable fibres which are thermodynamically stable with respect to the matrix. Another possibility, is to coat the fibre thus reducing fibre-matrix interaction. Matrix alloy additions also may diminish fibre-matrix interaction by reducing activity of diffusing species.

A general scheme for the classification of the interfaces based on the type of chemical reaction occurring between the fibre and the matrix was reported by Metcalfe^[50]. Three classes were proposed: in class I, fibre and matrix are mutually non reactive and insoluble; in class II fibre and matrix are mutually non reactive but soluble; and in class III, fibre and matrix react to form compound or compounds at the interface. The term reactive is restricted to the systems where a new chemical compound or compounds are formed. Although being considered somewhat elementary^[52], this type of classification provides a background against which to discuss the interface characteristics.

A requirement stipulated in early theoretical works, such as the rule of mixtures and the shear-lag analysis for load transfer, is that the interface should be strong enough to transfer and equally distribute the load among all fibres. The interface should also permit load redistribution to surrounding fibres after a weaker fibre had failed. Such theories are applied if the interface has enough strength to execute these functions. The theories that take into account this type of interface have been termed theories of strong interfaces^[53].

In general, the theories of strong interfaces were developed for non reactive systems with insoluble fibres in the matrix, i.e., class I. For less ideal systems, where the interface was not always strong enough to satisfy the theories for strong interface, attempt analysis

have been developed to cover the cases where failure initiates at the interface. These theories are called theories of weak interfaces^[53].

The theories of weak interface take interface failure into account directly, but this class is the most complex and least developed^[51]. They cover composites where the fibre-matrix bond may be the weakest link in the system causing the failure path to move from the matrix or fibres to the interface. Early work by Cooper and Kelly^[54], has pointed out that the properties of the composite will be affected by the extent at which the properties of the interface differ from those of the matrix and fibre. They have divided the mechanical properties of the composites into those affected by the tensile strength of the interfaces, e.g., transverse strength, compressive strength and crack arrest by tensile delamination, and those dependent on the shear strength (critical or load transfer length, fibre pull out and matrix deformation in fracture). These concepts of interfacial tensile and shear strength were developed to fit class I, where they were applied to the stress in the matrix immediately adjacent to the fibre.

For systems belonging to class II and class III, a zone of finite width is introduced with distinct properties. An analysis^[55] to predict the effects of interfacial diffusion on the mechanical properties of composite has been attempted for systems of class II. More complexity is introduced when chemical compounds are formed, class III. The resultant chemical compounds, often intermetallic in nature in many systems, may reduce the capability of the interface in carrying out its primary functions of load distribution and resistance to fracture.

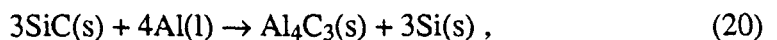
Metcalf^[56] used a model based on elastic stress concentrations generated at the interaction zone for the system Ti-B and Al-B composites. A relationship between the thickness of the interaction zone and strain at fracture for the system Ti-B was possible. Hunt^[57], using a similar approach found that increasing the reaction zone thickness of a continuous fibre FP/Al-Li metal matrix composite, the axial strength was reduced accordingly with theory.

One interesting system group is termed pseudo-class I composites. This term describes an apparent non reactivity when the composite is fabricated under optimum

process in contrast to the true reactivity of the components. The systems aluminium-boron and aluminium-silicon carbide composites fabricated by diffusion bonding are included in this group. The composites of this group appear free of interaction after fabrication under optimum conditions, but thermodynamic data indicate that the constituents should react for instance if the aluminium is melted. In aluminium-boron composites made by diffusion bonding, a layer of aluminium oxide is accounted for the apparent non reactivity^[50]. Breakdown of this layer occurs if the fabrication procedure is continued beyond the point regarded to be optimum, or if any subsequent additional processing is needed. Thus, fabrication of aluminium-boron composites by the liquid metal infiltration technique is only possible if the fibres are coated with a non reactive layer, e.g., silicon carbide.

According to the literature^[50,58], no evidence of chemical interaction is observed in aluminium/boron fibre composites, manufactured by hot pressing plasma arc sprayed fibres, when the boron fibres are coated with silicon carbide. More recent literature^[59] reports that aluminium alloys reinforced with silicon carbide whiskers, which were fabricated by powder metallurgy route at temperatures above the alloy solidus line, have interfaces characterized by the presence of second phase particles including oxide and intermetallic phases. Oxides are incorporated into the composite as a result of the powder metallurgy processing and migrate to the interface during liquid phase hot processing, while intermetallic phases nucleate heterogeneously on the whisker interface during quenching. A continuous oxide layer seems to form an intermediate zone which enhances the bonding between the SiC and the aluminium matrix.

A reaction between particulated silicon carbide and liquid aluminium has been reported^[17]. In regard to the reaction of SiC and aluminium, the following reaction equation is usually quoted,



but, since the free energy change of this reaction is positive in the temperature range of 973 K to 1473 K, the reaction does not spontaneously proceed from the thermodynamic point of view. In the above equation it is assumed that silicon does not form a liquid phase, but referring to the phase diagram of Al-Si system^[22], silicon dissolves into the liquid

phase in the temperature range considered and consequently lowers the free energy allowing the reaction to occur^[17]. Whereas the amount of silicon in liquid aluminium increases as the reaction proceeds, the reaction tends to saturate. It has also been observed^[17] that the reaction (20) decreases by addition of silicon to the aluminium. The presence of aluminium carbide has also been reported to occur in continuous carbon fibre reinforced aluminium-silicon-magnesium alloy composite manufactured by liquid metal infiltration technique^[60].

2.5 Fabrication defects

The composite fabrication process usually involves bringing together two or more constituents carefully prepared in order to achieve the most desirable properties. However many problems are associated with incorporating reinforcing fibrous materials into a metal matrix. Fig.16 outlines some of the problems associated with metal matrix composites^[61].

The main types of defects may be classified in four wide groups as follows: matrix associated flaws, structural factors, fibre strength factors, and interface factors. It will be impossible here to discuss all the problems associated with each particular group, but some aspects will be mentioned.

Composite materials made by molten aluminium alloy infiltration are prone to defects inherent to the process like porosity, slag entrapment, segregation, coring, and metal leaching contaminations. In spite of the process being vacuum and pressure assisted, porosity may also be present due to the presence of atoms of gas phase that are likely to be released when in localized areas a small volume of liquid finds itself enclosed by solid. In this case a localized vacuum may develop and, if it does, gas bubble nucleation will be promoted. Shrinkage porosity may also appear in the last liquid to be solidified. During the melting process slag is formed and it may be ending up entrapped between fibres. Another source of melt contamination is due to liquid metal leaching of parts of the apparatus utilized, leading to the presence of undesirable intermetallics in the composite. Depending on the composite solidification kinetics, segregation and coring may appear in the matrix. The fibres might introduce contaminants occurring in varying amounts such as oil or greases,

chlorides and sulphides (from handling), dust or other foreign matter. Even though some of such contaminants are burnt in the process, others still can leave traces behind.

Incorporation of fibres into a metallic matrix must be carried out in a manner that ensures minimum fibre breakage since it might give rise to aspect ratios which are less than the minimum value for efficient strengthening. Regions with low fibre volume fraction and fibre misalignment should also be avoided in order to allow efficient transfer of stress through the matrix to the reinforcing fibre. If optimized composite preparation routes are used, the composite performance is more dependent on the interface factors. The bond existing between a metal matrix and a ceramic fibre might either be of chemical origin or of a mechanical one. Mechanical bonds require an absence of any chemical source of bonding and involve mechanical interlocking.

2.6 Fatigue

2.6.1 Fatigue of metals

Fatigue of metallic materials under cyclic loading accounts for a high proportion of all ruptures and catastrophic damage of parts or entire structures. In practice fatigue is caused by a gradual accumulation of damage under varying mechanical loading, substantially lower than the ultimate strength or flow stress of the material^[62].

The fatigue process can be divided into a number of stages, each involving different mechanisms or stress criteria^[63]. For multi stage models^[64] it is postulated that failure by fatigue includes the following processes:

1. *Crack initiation.* In smooth specimens of ductile metals this involves the initiation of cracks in slip bands or other regions of strain localization and is controlled by shear stress. This stage is usually followed by changes in mechanical properties, lattice defect concentration and distribution, and may produce other structural changes such as polygonisation, and in age hardened alloys, localized re-solution or precipitate overageing.

2. *Slip band crack growth*. It entails the deepening of the initial crack on a plane, or conjugate planes of high shear stress. It may involve up to 90% of the total cycles to failure in low stress tests.

3. *Crack growth on planes of high tensile stress*. This mode of growth is controlled by the stress intensity at the crack tip. The fracture surfaces associated with this stage often show striation patterns. This process leads to final fracture.

2.6.1.1 *The initiation of fatigue cracks*

The formation of fatigue cracks usually takes place on the surface of cyclically loaded parts, at points of concentration of cyclic plastic deformation, i.e., at points of stress concentration^[62,65]. The surface is important for several reasons: slip is easier at the surface than in the interior of the grains, the environment is in contact with the surface and any load misalignment will give higher stresses at the surface. At these points, notches of different types and origins are found, e.g., inclusions, precipitates and working surface imperfections.

In many cases, fatigue cracks originate in fatigue slip bands and the adjacent material. Under high stress amplitudes, fatigue cracks may originate in grain boundaries. Fatigue cracks also originate at hard inclusions or at inclusion/matrix interface.

Fatigue cracks in slip band are formed due to the incomplete reversible plastic deformation in a surface layer of the material. Cyclic loading activates dislocations sources mainly in the region of the surface grains. A relief pattern appears on the surface at points of stress concentration due to repeated production of dislocations. This relief is characterized in the form of layers of material inserted under the original surface, the so-called intrusions, and in the form of layers of material shifted out above the original surface, the so-called extrusions^[66]. A model to explain the nucleation of cracks assumes that the intrusions are considered as a microcrack and its initial growth is explained as the deepening of the intrusion by repeated slip in one, Fig.17, or two slip systems. The analogy of the relative movement of a stack of cards makes possible an understanding of the development of the deepening of the intrusion leading to the occurrence of a crack^[67]. The intrusion acts as a

stress concentrator^[68], which will manifest itself in the gradual increase of the number of slip lines to slip bands.

2.6.1.2 Propagation of fatigue cracks

The microcracks that emerge in the nucleation stage are located along the active slip systems, in which the highest shear stress is acting. Under continuous cycling, the individual cracks become interconnected spreading in the crystallographic orientation penetrating deeply into the material. With increase of the depth of penetration, the cracks gradually incline towards the direction perpendicular to the principal tensile stress, spreading in a non crystallographic way. At this point a plastic zone appears at the crack tip. This last stage terminates after causing a extensive reduction in the material section that can no longer withstand the load.

Examining the fracture surface, it is possible to discern the region or regions of crack nucleation, the region of crack propagation, usually identifiable by grooving, and the region of final fracture. A realistic explanation for the origin of striations and the gradual crack propagation was presented by Laird^[69]. The concept is based on repeated blunting and sharpening of the crack tip, Fig.18. In (b) the crack under the tensile loading part of the cycle generates shear stresses at the tip. With increasing tensile loading the crack opens up and a new surface is created (c), separation occurs in the slip band and projections are formed at the end of the crack. The plastic deformation causes the crack to be both extended and blunted. On the compressive part of the cycle the crack begins to close (d), the shear stresses are reversed and with increasing load the crack almost closes (e). In this part of the cycle the new surface folds and the projections correspond to the new striations. The presence of striations unambiguously defines that failure was produced by fatigue, but their absence does not precludes the possibility of fatigue fracture.

2.6.1.3 The influence of cyclic deformation on microstructure

The early observation of the influence of cyclic deformation on internal microstructure of single phase materials, like aluminium and stainless steel, revealed that for high stress cycling a dislocation structure was formed similar to that formed in uniaxial

tension, but having a larger cell size. However for low cyclic stresses a cell structure was not created, even though the dislocation density was similar to that of the high stress amplitude case^[63,70,71].

During the first fatigue cycles, rapid dislocation multiplication can take place in the form of debris associated with the directions of the traces of slip planes. This debris includes jogged and tangled dislocations, prismatic loops, and dislocations dipoles and multipoles^[72]. In face centred cubic structures the dipoles are elongated in the $\langle 211 \rangle$ directions, as in unidirectional deformation. The loops were often associated with dislocations and were thought to originate from both dislocation/dislocation interaction and the collapse of vacancy discs^[63]. However, Smallman^[65] pointed out that most of the dislocations loops observed from cold worked metals are not formed by collapse of a sheet of vacancies, rather, they are formed from the motion of a multiple jog in a screw dislocation.

As with uniaxial testing, the major factors influencing the types of dislocation produced in fatigue and their arrangement are strain amplitude, stacking fault energy and temperature^[70]. At low strain amplitudes, a high stacking fault energy favours prismatic loop and dipole formation, whereas dislocation multipoles predominate in low stacking fault materials^[63]. In low-strain cycling or in material with low stacking fault energy, the dislocation debris agglomerates into isolated clumps or bands surrounded by a relatively dislocation free matrix. As the strain increases, the bands enlarge. With a higher incidence of cross-slip, either by greater cyclic strain amplitude or larger stacking fault energies, there is tendency to form a cellular dislocation structure. Further strains may be accommodated by dislocation motion across cells or cell-wall migration. A schematic diagram by Feltner and Laird^[70] provides a good summary of the type of fatigue induced defects under varying experimental conditions.

2.6.2 Fatigue of composite materials

The basic concept of fatigue of composite materials is not so different than that for metals but rather more complicated^[73]. This is because composite materials as a whole are

inhomogeneous (on a gross scale) and anisotropic^[74,75]. They exhibit complex failure mechanisms under static and fatigue loading due to their anisotropic characteristics of strength and stiffness^[75].

There are at least three well accepted basic differences between the fatigue phenomena in continuous fibre composite materials and the fatigue response of more common structural materials such as steel and aluminium. The first difference is that fatigue failure of composite materials is usually accompanied by a general damage accumulation rather than by a dominant single crack, as often observed in common isotropic materials^[74-76]. A second difference derives from the fact that a common consequence of fatigue in composites is a reduction in stiffness which can begin very early in the fatigue life and which reaches significant magnitudes long before the component breaks^[77,78]. The third difference is that in metals fatigue cracks nearly always initiate at free surface whereas in continuous fibre metal matrix composites, fatigue cracks can also initiate inside the material at fractured fibre ends^[18].

2.6.2.1 The fatigue of boron aluminium composites

There have been a number of studies of the fatigue properties of boron aluminium composites produced by the diffusion bonding process^[18,76,79-81]. Although there are many ways to show fatigue test data, the majority of the results from the above studies were presented by plotting the fatigue life against maximum stress. From this data it appears that some features are characteristic of these materials, namely: (a) the scatter in fatigue lives is relatively large^[18], Fig.19, (b) the shape of the S-N curve can be sigmoidal or flat with a very small slope, or alternatively fall between these two extremes^[81]. Although some composite materials may not have an endurance limit, the term fatigue limit is used in this work to indicate the maximum stress which does not cause failure at 10^6 to 10^7 cycles.

The S-N curve for a composite reinforced with SiC coated boron fibre is usually flat and has a very small slope^[18,79], Fig.19. Compared to the uncoated boron fibre composite, the coated fibres material exhibit poor high-stress, low-cycle, fatigue resistance. However, some data on the low-stress, high-cycle region for the longitudinal direction is controversial.

Hancock^[18] claims that the SiC coating appears to reduce preferentially the low cycle fatigue resistance, but the high cycle fatigue resistance is only slightly (6%) below that of the uncoated fibre composites. Nevertheless, Christian^[79] has found that the coated fibre composite fatigue resistance is lower only in the low cycle region, Fig.20. This latter author also pointed out that the uncoated boron-aluminium composite has fatigue strength superior to those of coated boron fibre composites at all stress levels for the transverse direction, Fig.20.

The ratio of axial fatigue limit to ultimate tensile strength is given in Table 2 for several boron-aluminium composites manufactured by diffusion bonding. The results indicate a trend for the uncoated fibre, that is, while the axial reinforcement increases fatigue strength, the fatigue ratio is usually less than that of the unreinforced metal. Thus, strengthening by axial uncoated fibres is more effective under unidirectional tensile loads. For the SiC coated fibres, the axial fatigue to ultimate tensile strength ratio can be higher than that for the matrix. This might be due to the poorer composite tensile strength given by the coated fibres. The interpretation of these results is complicated by the fact that a metallurgical bond existed between the uncoated fibre and the aluminium alloy matrix, but a mechanical bond was present between the SiC and the aluminium matrix. Furthermore, the SiC coating layer has a preferred crystallographic growth direction and an elongated grain structure, both perpendicular to the filament axis which is thought to affect its fracture behaviour^[18].

Published data for the off-axis fatigue behaviour of continuous boron fibre aluminium composite is very scarce. Toth^[82] has reported that the influence of off-axis loading on the fatigue behaviour of boron reinforced 6061 aluminium composites was found to be similar to that observed on their tensile properties, i.e., it was characterized by a rapid reduction of fatigue strength with increasing off-axis orientation, Fig.21.

2.6.2.2 Fatigue failure

In boron-aluminium composites loaded in the fibre direction, the elastic fibres support the greater part of the applied load and they may control the material failure by their

progressive fracture. It is considered that boron fibres are not sensitive to fatigue. The fibre fracture stress values under both cyclic and normal tensile loading condition are similar^[82,85]. Thus, during the fatigue of the composite material, some initial fibre breakage occurs during loading and this is attributed, in part, to the statistical variation of fibre strength and, therefore, unavoidable. Since the boron fibres have a relatively high resistance to fatigue, additional fibre failure after first loading must be due in some way to the cyclic behaviour of the matrix^[5,80]. Boron fibres have a strain to failure of about 0.8% [5] while the strain to failure of a as cast aluminium ASM A 356.0 alloy is around 2% [86]. This latter fails at strains between 0.1% and 0.2%. Therefore, under static loading the fibres could reach their critical fracture strain first and fail before the matrix. Under fatigue loading, however, the matrix would cyclically flow at strain levels far below critical strains for the fibres. This cyclic flow could result in fatigue damage to the matrix but not to the fibre. So, if the matrix requires much less cyclic strain to fatigue than the fibre, then the composite will be matrix dominated^[5].

It is possible to describe the fatigue process in terms of crack propagation mechanisms, and various attempts to report the fatigue process have been published^[18,80,82]. In summary, the fatigue fracture process of boron-aluminium composites can be described in the following manner.

Fibre fracture. Initially, fibres fracture occur during the composite fabrication process. Subsequently, fibres are broken near the surface during machining operations. Finally, fibres break at the points of weakness during actual fatigue loading.

Stress concentration in the matrix. Stresses build up in the matrix due to fibre fracture, growing in magnitude with time under cyclic loading as the result of matrix work hardening and some fatigue damage. In these stress concentration sites, classical metal fatigue events can take place in the matrix.

Initiation of fatigue cracks. Each fibre fracture may be a possible site for the initiation of fatigue cracks in the metal matrix. However, it is not the only cause. Many fatigue cracks may initiate in the matrix at machined edges at the surface, and internally at

defects like porosity, inclusions and second phase particles. Brittle fibre coatings or reaction products may also initiate fibre fracture and subsequent fatigue cracks at these sites.

Growth of fatigue cracks. The nucleated cracks propagate both transversely and longitudinally. Longitudinally, cracks propagate by shear mechanism or by debonding along the matrix fibre interface, to a point where the existing stress level exceeds the fibre tensile fracture stress resulting in fibre fracture. For brittle fibre composites, in which fibre fractures occur immediately upon loading under conditions of low-cycle fatigue, crack initiation can be regarded as having occurred almost immediately and practically all of the life of the specimen is spent growing fatigue cracks.

Composite failure. The growth of fatigue cracks in the matrix reduces the load bearing capacity of the composite and when coupled with fibre fracture, produces final fracture of the composite.

The above sequences occur locally with some areas in the composite in a more advanced stage of fracture than others. Therefore, fatigue failure in aluminium boron composites is the result of the growth of many cracks at random sites producing irregular fracture surfaces^[18].

A simple fatigue model has been proposed by Gouda, Prewo and McEvily^[81], based upon crack growth processes alone, Fig.22. This model accounts for two micromechanical damage modes during the fatigue growth of matrix cracks in the direction perpendicular to the fibre axis (type A) and that of interfacial debonding (type B). Fatigue crack growth of type A is similar to the usual Mode I type of growth observed in alloys in which the rate of crack growth as function of ΔK , (the range of the stress intensity factor), is sigmoidal between the limits of ΔK_{th} and K_c , the threshold level crack growth and the fracture toughness, respectively. For crack growth of type B, however, the slope of the S-N curve may be quite different. If the interfacial debonding (or crack) progresses along a fibre with no weak points (called perfect fibre), then the growth of this interfacial debonding will not contribute to final fracture. If all fibres are of perfect form, then the S-N curve will be flat, i.e., the endurance limit will be equal to the static strength. However, in actual

unidirectional composites some fibres may be perfect, but the majority of fibres usually have weak points. Then the S-N curve will be a mixture of those of types A and B.

2.6.2.3 The fatigue failure criterion

The lack of an adequate definition of a fatigue failure is a major problem when fatigue tests are conducted on composite materials. As pointed out by Smith and Owen^[87], the definition of fatigue failure based on a number of cycles to complete separation of the broken halves is quite meaningless if the sample has lost its integrity. Most fatigue data in the literature are based on cycles to fracture. Nevertheless, it may be that loss of stiffness with cycles would constitute a more useful definition for fatigue failure. For example, fatigue damage in a metal matrix can reduce the composite stiffness by as much as 50% without causing complete fatigue fracture^[5].

2.7 Fatigue damage accumulation

It has been shown in many experimental and theoretical studies that the amplitude of the plastic component of deformation is the controlling factor of the process of fatigue damage accumulation. It has been also shown that an important characteristic of a metallic material is its reaction to cyclic microplastic deformation^[62]. In composite materials, several authors^[76,88-91], have shown that changes in stiffness are indications of tensile fatigue damage. As mentioned earlier, section 2.6.2, fatigue of metal matrix composites can be quite complex, with the matrix playing a very active role due to its relatively high strength and stiffness compared to the fibre.

The understanding of fatigue behaviour of metals may simplify the metal matrix composite fatigue problem. It is known that elastic-plastic bodies or structures subjected to variable repeated loads in the plastic range can experience failure by cyclic plastic deformation or, alternatively, can shake down, i.e., resume an elastic deformation mode after a certain number of plastic strain cycles^[92]. Therefore, it is possible to argue that, if the cyclic stresses in the matrix do not exceed its fatigue limit, then the matrix material may be able to contain cracks nucleated at fibre breaks and prevent them from spreading.

The first shake down theorem or Melan's theorem^[93] states that a body can shake down for an arbitrary loading program within described limits, if any time-independent selfstress (residual stress) state can be found such that the superposition of this residual stress state and the elastic response for all possible combinations of external forces and temperature within described limits, must not lead to stress at or above yield at any point. The shake down limits ensure that the body is safe against plastic failure but not necessarily against other failure modes such as fatigue^[94].

Consequently, if composite fatigue failure in general and low cycle fatigue in particular is to be avoided, it is essential to ensure that the cyclic applied load produces only elastic strains in the constituents. However, some localized plastic deformation is permitted to occur in the first few cycles, provided that a shake down state is achieved, i.e., the residual microstresses reach such magnitudes that only elastic deformation can take place under the loading condition.

A method for determining the applied load amplitudes which will cause the body to shake down have been developed for fibrous composites based on known shapes of the initial yield surfaces of the composite^[94]. The principal application of that method was to prevent fatigue in metal matrix composites. Specifically, it was found that the shake down limits coincided with the fatigue limit for a given number of cycles in as fabricated aluminium boron composites. The reason for this relationship stems from the fact that the flow stress of some aluminium alloys in the as fabricated or annealed condition is very nearly equal to the fatigue strength of the alloy after 10^6 to 10^7 cycles at $R = -1$ (full reverse mode)^[95,96].

A possible relationship between fatigue and shake down in metal matrix composites was first suggested by Dvorak and Tam^[95] and related to experimental data obtained for unidirectional 6061 Al-B material produced by diffusion bonding process. The determination of the shake down stress range for a simple mechanical model of fatigue behaviour is shown in Fig.23. Let S be the uniaxial composite stress, σ^f and σ^m the normal microstresses in the fibre direction, in the fibre and matrix respectively and ε^f and

ε^m , the respective microstrains. As this model is regard as an isostrain model, at any instant of loading the strains must be compatible, and the stresses must be in equilibrium, that is:

$$\begin{aligned}\varepsilon^f &= \varepsilon^m = \varepsilon^c \\ \sigma^f V_f + \sigma^m V_m &= S,\end{aligned}\tag{21}$$

where ε^c is the composite strain and V_f and $V_m = (1-V_f)$ are the volume fraction of the constituents. If E_f and E_m denote the instantaneous Young's moduli of the constituents, the instantaneous modulus of the composite E_0 is then,

$$E_0 = E_f V_f + E_m V_m.\tag{22}$$

Let σ_y^m denote the magnitude of the uniaxial flow stress of the matrix material. Then, the proportional limit of an initially stress free composite is,

$$S_y = \sigma_y^m \frac{E_0}{E_m}.\tag{23}$$

For $0 \leq S \leq S_y$, the composite deforms elastically, the matrix follows the loading path OA , and the fibre the path OA' , Fig.23. For $S_y \leq S \leq S_{max}$, the respective paths are AB and $A'B'$. It is assumed that at B' , the fibre does not exceed either its yield or ultimate strength.

Along the path $A'B'$, the stress in the fibre then is:

$$\sigma^f = \frac{(S - \sigma_y^m V_m)}{V_f} = \frac{(S - S_y)}{V_f} + S_y \frac{E_f}{E_0}.\tag{24}$$

When the composite is unloaded at $S = S_{max}$, the unloading paths are BC and $B'C'$. In the absence of Bauschinger effect, the matrix will remain elastic on path BC , provided that,

$$S_{max} - S_{min} \leq 2S_y.\tag{25}$$

Eq.(25) defines the shake down stress range of the composite. If the shake down stress range is exceeded, upon unloading, the matrix resumes plastic straining along the path CD , and the cyclic loading paths $BCDE$ and $B'C'D'E'$ are followed in the matrix and in the fibre, respectively. Under such circumstances, the matrix does not shake down. In the absence of sufficient cyclic strain hardening, which could restore the shake down state

within several load cycles, the matrix will experience cyclic plastic straining, and consequently low cycle fatigue failure.

Although shake down of the matrix is a necessary condition for prevention of a fatigue failure, it may not be a sufficient one if the matrix flow stress exceeds the fatigue limit of the matrix. Specifically, the fatigue limit of some heat treated aluminium alloys, such as 6061 T6, is much lower than their yield strength, in which case, the elastic straining within the shake down limits will always cause matrix microstresses larger than the fatigue limits^[95].

This fatigue behaviour analysis led to the development of a damage model that predicts stiffness loss due to fatigue^[89]. The model starts with the matrix cycling plastically. As cracks develop due to plastic cycling, the effective modulus is reduced for the portion of the matrix that is in tension. The model presents simple equations to approximate the effective matrix modulus due to cracking at an assumed cyclic strain range.

Fig.24 illustrates this behaviour in terms of applied composite stresses and the corresponding axial stresses in the matrix and the 0° fibres. The dashed lines in Fig.24 represent the initial loading response. Accordingly, the first load cycle causes the matrix and fibre stresses to follow the dashed loops. The composite has an ideal elastic-plastic matrix (for simplicity of illustration) and is subjected to a constant cyclic stress range ΔS . σ_{sh}^m is assumed to be the axial stress in the matrix, in the loading direction, at the shake down stresses limit ΔS_{sh} . σ_{sh}^m is assumed to be equal to the cyclic flow stress for unidirectional composites as opposed to the previous model where σ_y^m was assumed to be equal to the matrix flow stress. Assuming that the matrix flows at the same value in tension and in compression, σ_{sh}^m equals half of the composite strain range $\Delta S_{sh} / E_0$ times the matrix tensile modulus, E^m , so:

$$\sigma_{sh}^m = \Delta S_{sh} \frac{E^m}{2 E_0} . \quad (26)$$

The ΔS_{sh} in this equation is the shake down stress range, E_0 is the undamaged elastic modulus of the composite material in the loading direction, and E^m is the undamaged matrix's modulus. With subsequent cycling, the cyclic plasticity causes the matrix cracks to

initiate and grow, effectively decreasing the matrix tensile modulus until a saturation damage state is reached. The dashed loops in Fig.24 narrow to zero-width loops, shown as solid lines, which represent a saturation damage state (SDS). After the saturation damage state is reached, it is assumed that the composite will neither accumulate more damage nor fail under the present loading condition.

The decrease in matrix modulus in the load direction due to fatigue damage can now be determined using Fig.25. The strain in the matrix and composite is plotted versus the matrix stresses σ^m or the composite stress S . The damage state has an associated cyclic strain range, $\Delta\epsilon$. If this cyclic strain range is assumed, an effective tensile modulus of the matrix material E_{ef}^m can be estimated. The compressive strain range of the matrix $\Delta\epsilon_{comp}^m$ is approximated as,

$$\Delta\epsilon_{comp}^m = \frac{\Delta S_{sh}}{2E_0} . \quad (27)$$

The effective tensile modulus of the matrix material now can be approximated by dividing σ_{sh}^m by the cyclic strain minus the compressive portion,

$$E_{ef}^m = \frac{\sigma_{sh}^m}{(\Delta\epsilon - \Delta\epsilon_{comp}^m)} . \quad (28)$$

E_{ef}^m is used to calculate E_{SDS} , the elastic modulus of the composite in its saturation damage state.

Returning to Fig.25, the modulus for each of the two linear segments and the strain ranges are now known. Therefore, the overall composite stress range ΔS can be calculated as follows,

$$\Delta S = (\Delta\epsilon_{comp}^m) E_0 + (\Delta\epsilon - \epsilon_{comp}^m) E_{SDS} . \quad (29)$$

Eq.(29) is rewritten using Eq.(27),

$$\begin{aligned} \Delta S &= E_{SDS} \Delta\epsilon + \frac{1}{2} \Delta S_{sh} \left(1 - \frac{E_{SDS}}{E_0}\right) && \text{for } \Delta S > \Delta S_{sh} \\ \Delta S &= E_0 \Delta\epsilon && \text{for } \Delta S \leq \Delta S_{sh} \end{aligned} \quad (30)$$

By selecting a number of different strain range values $\Delta\epsilon$, the corresponding composite stress range ΔS can be calculated and plotted versus $\Delta\epsilon$, Fig.26. The composite secant modulus then is:

$$E_s = \frac{\Delta S}{\Delta \epsilon} . \quad (31)$$

This model has predicted the secant modulus loss, under either stress or strain controlled fatigue loading of boron/aluminium composites^[89], and of a silicon carbide fibre in aluminium matrix^[97]. This model has also been applied to composites test specimens containing holes or slits^[5].

2.8 Particle cracking

There has been a considerable number of investigations of the fracture characteristics of two-phase alloys where the second phase is a discrete precipitate, an inclusion or a particle, and the matrix is ductile^[98-101]. In metal matrix composites where the matrix is an aluminium-silicon alloy, it would appear to some extent that, the matrix fracture characteristics, could be analyzed in terms of these models. The aluminium-silicon alloy matrix may consist of the primary aluminum dendrites and second phase particles like silicon flakes and some intermetallics which by their own nature have different characteristics from the aluminum solid solution. These second phase particles differ chemically from the surrounding aluminium, they have negligible ductility and even have an aspect ratio.

It is known that stress concentrations at inclusions occur mainly for two reasons: 1) differential thermal contraction during cooling, and 2) concentration of remote applied stresses due to differences in the elastic constants between matrix and inclusion^[98] For cementite particles in iron and steel, the elastic modulus of cementite is considered to be the same of the ferrite, and no stress concentration due to elastic deformation alone is expected. Nevertheless, the elastic energy stored in a particle under load may be large enough to provide the surface energy of a particle crack when it cracks^[101].

Some observations indicate that the stored elastic energy is not a sufficient criterion for particle cracking, but that plastic flow also must be considered. It has been observed that cracks found in cementite particles in steels appear only after yielding^[101]. It has also been found that the cracking of silicon particles embedded in an aluminium matrix occurs progressively over a range of plastic deformation. Alternatively, the plot of the fraction of broken particles versus strain, extrapolates at zero fracture incidence, implying strain values still in the plastic region^[99].

Gangulee and Gurland^[99], using a large amount of data, developed an expression for the fracture probability of silicon particles in Al-Si alloys. Their results indicate that the fracture probability P increases with increasing stress (strain), increasing particle size, and decreasing volume fraction of silicon particles. This fracture probability can be expressed by the relation:

$$P = \left(\frac{k_p \sigma d^{\bar{t}}}{f^{\bar{t}}} \right) - k_0, \quad (32)$$

where, σ is the applied stress, d is the average particle size, f is the particle volume fraction and k_p and k_0 are constants.

It has been reported that for an aluminium-silicon-magnesium alloy (ASM 356), the fracture path is almost exclusively through dendrite cell boundaries. Furthermore, the silicon particles along the fracture path were usually broken and near the fracture surface. Silicon particles were often found broken, whose direction of fracture was normal to the tensile axis, even when this was the longest path in the particle^[100]. For an aluminium silicon alloy in which the silicon appears as flakes, the cracks propagate through across the plane of flakes. The cleavage plane of silicon is $\{111\}$ and since this is often the plane of faceted flakes in which there are also parallel twins, it is understandable that cracks may spread easily^[102].

2.9 Concluding remarks

One of the objectives of this chapter was to present the updated published literature on the tensile, fatigue and fracture behaviour of continuous composite materials. From the

presented literature, it can be said that there is a general consensus that the axial fatigue limit can be improved by reinforcing alloy matrices with strong and stiff fibres. It is a collective opinion that aluminium alloys reinforced with SiC coated boron fibres are slightly sensitive to repeated fatigue tensile loading. Conversely, differences in absolute mechanical properties values are indicative that additional work is required in terms of improving manufacturing quality.

It is generally accepted that composite materials have unique characteristics under fatigue, that is a general damage accumulation which is reflected in terms of stiffness loss. Thus, the fatigue strength would be better evaluated in terms of stiffness loss rather than on fracture criterion.

There is a relationship between fatigue damage and shake down in metal matrix composites. However, there are some ambiguities in assigning actual matrix flow or cyclic flow stress values which would prevent fatigue in metal matrix composites. This difficult is an indication that additional work is still required regarding fatigue damage in composites.

In the past great emphasis was placed on manufacturing composites via diffusion bonding process and as such, the majority of literature data regard this technique. The advent of suitable fibres which made the liquid metal infiltration technique feasible, implied the necessity of basic assessment of the composite mechanical and microstructural characteristics. These characteristics should in turn be compared to the existing studies and theories in metal matrix composites.

As far as is known, no work on fatigue behaviour has been carried out on continuous fibre composites fabricated by liquid metal infiltration technique. For composite material fabricated by this technique, interface interactions, residual stresses, cast matrix microstructure and brittle second phases can play an important role in their mechanical properties.

CHAPTER 3

EXPERIMENTAL

3.1 Introduction

An aluminium alloy-SiC coated boron fibre composite material, made by a liquid metal infiltration technique, was supplied in two different batches. The received material was microstructurally characterized and mechanically tested in the as cast condition.

Specimens machined from these two composite batches were tensile and fatigue tested as described in the following sections. The initial materials, fibre and aluminium alloy were also mechanically tested. The fibres were tensile tested and the aluminium alloy was tensile and fatigue tested. The aim of the composite fatigue tests was to evaluate fatigue damage in terms of stiffness loss.

Metallographic characterization was carried out in order to assess the material microstructure before and after the mechanical testing. Some techniques used in this work were described in the Appendices' section. Emphasis was particularly given to optical and electron metallographic examination of fatigued specimens, to establish the extent of fatigue damage.

3.2 Composite manufacturing

The composite material used in this work was manufactured elsewhere by a liquid metal infiltration technique as described in section 2.2.4. The fibres consisted of 0.142 mm diameter SiC coated boron fibres commercially known as Sicabo®‡. The fibres were obtained in tapes, which are produced by collimating and interweaving a large array of fibres with a thin titanium strip as shown in Fig.27. The matrix used to infiltrate the fibres was an aluminium alloy of excellent castability designed as BS 2L 99 and had a composition similar^[103] to the ASM A356.2^[104]. The chemical compositions are listed in Table 3.

‡ Sicabo® is a trade name of Composite Inc., Manchester, Connecticut, USA.

The composite material was supplied in two different batches, one with an average volumetric fraction of fibres around 28% and other with around 48%. These two batches will be referred herein as series 28% and series 48%. The composite material series 28% was fabricated into strips, 2.5 mm thick, 30 mm wide and 230 mm long, Fig.28. The material series 48% was fabricated into square sections, 146 mm by 146 mm, and 2.65 mm thick.

3.3 Bulk chemical analyses

Bulk chemical analyses of the matrix alloy prior to infiltration and of the composite were performed using either atomic emission spectroscopy or wet chemical analysis. The aim of the analysis was to detect the level of matrix contamination after infiltration and to examine if any bulk chemical composition difference had occurred between the two series, 28% and 48%.

3.4 Radiographic examination

The composite material was radiographed before any machining operation in an attempt to detect defects such as cracks, porosity, slag inclusions, fibre misalignment and the extent of fibre agglomeration. The fibre agglomeration is caused by the liquid metal front passing through the fibres during infiltration causing fibre misalignment and volumetric fraction changes. Some machined specimens were also radiographed. The boron fibres and the aluminium matrix alloy show similar contrast under X-rays. However, the tungsten boride fibre cores are less transparent to X-rays, appearing as dark lines in a positive print as shown in Fig.29.

3.5 Specimen geometry and preparation

3.5.1 Fibre specimens

For tensile tests, individual fibres were epoxy-bonded to low modulus card tabs as shown in Fig.30, following recommendations by Hughes^[105]. The fibre gauge lengths utilized were 50 mm and 80 mm. The purpose of testing the fibres at different gauge lengths was to evaluate if there is fibre strength length-dependence.

3.5.2 Aluminium alloy prior to infiltration specimens

The aluminium alloy specimen geometry for tension-tension fatigue tests was of a type with a continuous radius between ends^[108]. This specimen geometry was chosen to ensure failure in the test section (reduced area), and to guarantee proper specimen alignments through pin joints. Fig.31 outlines the geometry and the nominal dimensions of the matrix fatigue test specimens. The same type of specimens was used for tensile tests with a slight gauge length modification in order to obtain a constant cross section long enough to fit a 10 mm gauge length extensometer.

3.5.3 Composite specimens

Composite specimens for tensile and fatigue tests were cut with fibre orientations at 0°, 10° and 90° using a diamond wheel to minimize surface damage due to the machining operation. The specimens at 0° and 10° were cut as rectangular coupons 75 mm long and 8 mm wide, at the end of which soft aluminium sheet tapered tabs were epoxy-bonded for gripping purposes, Fig.32. For the 90° specimens the width was 20 mm and the length depended on stock material geometry.

Due to the limited amount of composite material supplied, in the 10° fibre orientation specimens, the fibres could not run across the full width of the specimen in the gauge length. The specimen at 10° fibre orientation was chosen as a best compromise between keeping the amount of material wasted to a minimum and obtaining sensible measurement of off-axis properties. A lower fibre angle degree probably would not produce sensible changes in mechanical off-axis properties, because fibre alignment in the composite material was not always kept constant due to fibres movement during the infiltration process. A fibre angle departure of 5° from the original fibre direction was found in specimens supposedly oriented at 0° to the tensile axis. At higher fibre angle than 10°, a large and undesirable wastage of material would be produced.

3.6 Mechanical testing

3.6.1 Tensile testing

Tensile testing was performed on the as received fibres, matrix material prior infiltration, matrix material in the as cast composite condition and on the composite material at fibre orientations of 0°, 10° and 90°.

3.6.1.1 Fibre tensile testing

The fibre tensile strength distribution and modulus of elasticity were assessed by testing several fibres taken from a fibre tape. The fibre tensile data were analyzed in terms of Weibull statistics, for more detail see Appendix 1.

Great care was taken during specimen preparation and testing to ensure that no bias was introduced by improper specimen handling or testing. The tests were performed in a mechanical testing machine equipped with a load cell, which was calibrated by a dead weight. The testing grips used were of the pin joint type. The fibre load-displacement results were recorded in X-Y plotter.

Precise fibre modulus measurement is a difficult task. The fibre modulus measurement is greatly affected by grip movement, fibre sliding inside the binding resin and also by the card tabs stiffness. To account for all these undesirable effects, an indirect method was employed.

Specimens made of a tungsten wire of similar fibre size and diameter were tested under the same fibre testing condition. The tungsten modulus of elasticity is quite close to the boron fibre. Boron fibre modulus of elasticity is usually quoted to be between 385 GPa and 400 GPa and tungsten modulus to be 411 GPa [103,107]. Therefore, it was possible to calculate for the tungsten wire an average displacement error given by any fibre or grip sliding. Assuming that the displacement error for the tungsten wire was similar to the fibre, it was possible for the actual fibre modulus of elasticity to be evaluated.

3.6.1.2 Aluminium alloy tensile testing

The aluminium alloy material was tensile tested in a mechanical testing machine equipped with wedge grips. The deformation was measured by a 10 mm gauge length extensometer attached to the specimen by rubber bands. The tests results were recorded using an X-Y plotter and the ultimate tensile strength, the flow stress, the modulus of elasticity, and the elongation were measured.

For the 28% series, it was possible to evaluate the matrix properties in the actual composite material casting conditions. In some strips, a movement of the fibre preform had occurred inside the die during the infiltration manufacture, thus leaving a portion of the strip without fibres, which was appropriately sectioned and tensile tested. This fact had allowed a comparison of tensile properties of the matrix in different microstructural conditions.

3.6.1.3 Composite tensile testing

The composite material was tensile tested in a mechanical testing machine equipped with wedge grips. Great care was taken to ensure specimen alignment, since the composite mechanical properties are strongly dependent on the fibre orientation in respect to the tensile axis, see section 2.3.5.

The strain was measured by two strain gauges wired in series (grid size: 6.35 mm by 3 mm) and located on both sides of the specimens. The experimental apparatus was designed to fit two additional dummy strain gauges located next to the specimen. This circuit combination eliminated bending and temperature dependent strains that may affect the effective strain measurement. For more details on the strain gauge techniques refer to Appendix 2.

3.6.2 Fatigue testing

The aluminium alloy material prior to infiltration and the composite material at fibre orientations of 0° and 10° to the tensile stress, were fatigue tested as described below. The composite material at 90° fibre orientation showed very poor tensile properties, *UTS* between 26 MPa and 37 MPa, see Table 7, making fatigue tests impossible to be performed in the available equipments.

3.6.2.1 Aluminium alloy fatigue testing

The aluminium alloy material prior to infiltration was fatigue tested using a closed-loop servo-hydraulic machine. The fatigue tests were performed in tension-tension mode at 20 Hz. All the specimens were cycled at a constant stress level. The stress ratio used was 0.4 ($R = 0.4$). The matrix fatigue data was evaluated by plotting the number of cycles versus maximum stress.

3.6.2.2 Composite fatigue testing

The composite material in the as received condition was fatigue tested using a closed-loop servo-hydraulic machine. The fatigue tests were performed in tension-tension mode at 20 Hz, except when the stress-strain data were taken, since the equipment used to take the stress-strain data only allowed measurements to be performed at very low frequencies, e.g., 0.02 Hz. The strain was measured by two strain gauges wired in series (grid size: 6.35 mm by 3 mm) and located on both sides of the specimens.

All the specimens were cycled at a constant stress level until failure or until 5×10^6 to 7×10^6 cycles were reached, except a number of specimens which were unloaded to zero stress followed by subsequent reloading to the previous stress level. The stress ratio R was kept at 0.4. The stress ratio R employed in fatigue testing metal matrix composite materials usually ranges between 0.1 and 0.5 [5,81]. The composite was tested under two conditions, the first with the fibres aligned parallel to the direction of the tensile stress axis (0°), and the second with the fibres aligned at 10° to the tensile stress. The fatigue characterization was determined by plotting the number of cycles to failure versus the maximum stress.

3.7 Fatigue damage measurements

In this work the fatigue damage was interpreted in terms of moduli variation. The stress-strain data were taken at intervals to record the modulus change as function of elapsed number of cycles. To evaluate the amount of fatigue damage inferred from the changes in elastic modulus, it was necessary to decide how this modulus variation was measured and how it was normalized.

During specimen loading, the stress-strain behaviour follows path OAB in Fig.33 and it is characterized by an initial linear region, path OA , followed by a non linear region path AB . The linear region corresponds to the region of truly elastic behaviour of both matrix and fibre^[39]. This elastic modulus will be referred in this work as the initial loading modulus E_0 . Straining the composite in the non linear region and relaxing the applied stress, the stress-strain behaviour of the composite follows path BCD . This unloading is characterized by a linear portion followed by a non linear segment. From the linear portion is possible to measure the unloading modulus E_{un} . If series of load-unload cycles are repeated, path EF , stress-strain loops are developed and depending on the stress range, they can be open with permanent set, open without any permanent strain, or completely closed. From the open loops it is possible to measure the unloading modulus E_{un} and the secant modulus E_s .

The fatigue damage can be evaluated by plotting the fractional change of elastic modulus versus number of elapsed cycles, either in linear or logarithmic scale. The fractional change of elastic modulus ΔE can be defined in different ways as follows:

$$\Delta E_t = \frac{E_t - E_0}{E_0}, \quad (33)$$

where ΔE_t is the fractional change of initial loading modulus, E_t is the reloading modulus at a certain number of elapsed fatigue cycles, path OA' , Fig.33, and E_0 is the initial loading modulus path OA , Fig.33;

$$\Delta E_{un} = \frac{E_{un} - E_0}{E_0}, \quad (34)$$

where ΔE_{un} is the fractional change of unloading modulus, E_{un} is the unloading modulus at a certain number of elapsed fatigue cycles, path BC , Fig.33, and E_0 is the initial loading modulus path OA , Fig.33. The unloading modulus E_{un} after a certain number of cycles is replaced by the secant modulus, E_s , when the hysteresis loops close;

$$\Delta E_s = \frac{E_s - E_{s2}}{E_{s2}}, \quad (35)$$

where ΔE_S is the fractional change in secant modulus, E_S is the secant modulus at certain number of elapsed fatigue cycles, Fig.33, and E_{S2} is the secant modulus at the second cycle.

3.8 Microstructural characterization

3.8.1 Microstructural characterization of the fibres

The fibres were analyzed by X-ray diffraction technique in a Debye-Scherrer camera. The phases were identified in comparison to 'JCPDS' standards^[108] using the Hanawalt method for manual search/match of powder diffraction^[109].

According to the literature^[8], the structural development of the core influences the tensile properties of the fibre, i.e., the fibre strength increases with core development. The core development can be followed by changes in the X-ray traces of the constituent phases.

3.8.2 Optical metallography

3.8.2.1 Metallographic specimen preparation

Samples for metallographic examination were cut either by a diamond wheel or by spark machining. Samples taken from the various materials, before and after mechanical testing, were mounted in thermoplastic material and subsequently ground using silicon carbide paper down to grit 4000. Then, the samples were mechanically lapped to 1/4 μm diamond finish. Colloidal silica suspension was finally used to polish the surface of the samples. Some samples were etched in a water solution of sodium hydroxide and potassium ferricyanide to delineate the second phases present in the aluminium alloy. The same solution was used to deep etch the composite material.

Some samples were prepared in order to determine the distribution and volume fraction of the fibres. Samples on the transverse and longitudinal directions were prepared for the observation of the cast matrix microstructure and for determination of size and distribution of second phase particles. Some mechanically tested specimens, fractured or not, were sectioned longitudinally in the gauge length region. Before thermoplastic mounting, these samples were nickel plated to retain the original edges during grinding and polishing operations, i.e., to avoid polishing relief. Optical micrographs were then

taken from highly polished surfaces to show the extent of mechanical damage due to the machining operation, due to the tensile testing and above all due to the fatigue testing.

3.8.2.2 Metallographic measurements

The metallographic measurements undertaken were, the determination of fibre and second phases volume fractions, the determination of porosity content and dendrite cell size. The linear intercept method was used to evaluate dendrite cell size of the aluminium alloy. This method considers the mean linear intercept (m.l.i.) of random test lines as a measure of apparent cell size. To obtain the actual cell size from the apparent size, a correlation factor whose value depends on the shape of the cells must be used. To avoid any ambiguity the m.l.i. in this work is quoted as dendrite cell size. For second phase volume fraction measurements, see Appendix 3.

In order to determine fibre volume fraction, samples were prepared by sectioning the material in the transverse direction, i.e., perpendicular to the fibre direction. It was found that mechanically grinding transverse sections of the specimens, down to grit 1200, was enough to produce a suitable surface finish to be observed in a metallurgical microscope equipped with a projection screen. From the projected composite surface image, the number of fibres was counted. As the fibre diameter is known and it varies very little from fibre to fibre, it was possible to calculate the fibre volume fraction since the total composite area, the number of fibres and fibre diameter were known.

3.8.3 Scanning electron microscopy

Scanning electron microscopy (SEM) was carried out on longitudinal and transverse sections of the composite material. These sections were prepared using the technique described in section 3.8.2.1, with a subsequent carbon coating to avoid electron charging in the microscope. Electron micrographs were taken from polished samples to show the matrix microstructure and extent of fatigue damage.

Fracture surfaces of the ruptured tensile and fatigue specimens were also examined using the scanning electron microscope. This was done with the intention of detecting where the cracks occurred and to determine the fracture mode.

Many aluminium matrix second phase particles were analyzed in polished samples using energy dispersive X-ray spectroscopy (EDS). The results were interpreted in terms of solute-solvent plot method as described by Feest^[110], so that the matrix contribution to the chemical analysis results could be taken into account. Quantitative analysis^[111] were obtained using standard less software. For more details on the technique, which was originally developed for bulk microprobe analysis and extended to thin foil specimens^[112], see Appendix 4.

3.8.4 Transmission electron microscopy

3.8.4.1 Thin foils preparation

Thin foils, from the as received composite material, from the tensile and the fatigue specimens, were prepared for observation by transmission electron microscopy (TEM). The foils were prepared by cutting slices approximately 1 mm thick from either transverse or longitudinal composite sections. These slices were then trepanned to 3 mm discs. After these discs were mechanically polished to a thickness of about 300 μm , using the flattening tool from the dimpler and diamond paste 6 μm , to remove any mechanically damaged layer. The foils were finally dimpled to a centre thickness of about 30 μm from one side only. Subsequently the foils were ion-beam thinned till perforation. The ion guns were set at 4 KV and the specimen current was set at 2 mA for two guns. The foils were held by tantalum plates. These values of accelerating ion voltage and specimen current were found to be the most suitable settings for the composite, producing the least observed amount of surface scaling and good thin areas. A best compromise for the elemental sputtering onto the foil from the holder plates, the ion-milling damage, and the production of thin areas was found with the foil kept at 16° ion beam incidence angle.

As an attempt to assess the ion-milling damage, some specimens were thinned in a twin jet polishing machine operating with an electrolyte of nitric acid in methanol. Unfortunately, no areas thin enough to be observed at a transmission electron microscope operating at 300 KV were produced.

It should be mentioned that all the thin foils prepared from the tensile tested specimens and the fractured fatigue specimens were usually taken from the transverse section at approximately 5 mm behind the fracture surface. The thin foil from interrupted fatigue test specimens were taken from the middle of the gauge length section, in the transverse direction.

3.8.4.2 Dislocation density measurements

The measurements of the dislocation density were carried out in thin foils obtained from selected specimens. Each area was imaged in the same multi-beam bright field condition, $\langle 110 \rangle$ zone axis orientation, so that all the dislocations in the illuminated area were in contrast. Foil thicknesses were determined in the vicinity of the investigated region using either the convergent beam diffraction technique or the grain boundary tilting method, see Appendix 5.

For the dislocation density determination, the line intercept method was used^[113]. A grid of reference lines was placed over the TEM negatives on a translucent screen, then, intersections of dislocation with the grid lines were counted.

The dislocation density, ρ , is given by,

$$\rho = \frac{2NM}{Lt} , \quad (36)$$

where, N is the number of dislocations intersections with the grid lines, M is the magnification of the negative, and t is the foil thickness. It should be mentioned that the dislocation density measurements were performed in the aluminum matrix away from any fibre or second phase particle.

3.8.4.3 Energy dispersive spectroscopy

Thin foil chemical analysis were performed using energy dispersive X-ray spectroscopy (EDS), with the electron microscope operating in the nanoprobe mode. Quantitative analysis were obtained using the ratio technique with fluorescence correction and K-factors previously obtained^[114,115].

CHAPTER 4

RESULTS AND DISCUSSION

4.1 Prior testing microstructural characterization

In this work a microstructural characterization of the materials were carried out prior testing and it is presented next.

The fibres microstructure has been characterized by X-ray diffraction, scanning electron microscopy (SEM), and transmission electron microscopy (TEM). Optical metallography (OM), chemical analyses and energy dispersive spectroscopy (EDS) were used for the characterization of the aluminium alloy material prior to infiltration. The composite material, series 28% and 48%, were also characterized by chemical analyses, optical metallography, scanning electron microscopy, transmission electron microscopy and energy dispersive X-ray spectroscopy.

4.1.1 Fibres

Fig.34 shows a SEM micrograph of a typical fibre surface, before infiltration. It can be seen from this figure that the fibre surface consisted of areas of preferred growth of nodules, separated by definite boundaries. The size of the nodules varied from region to region on the same fibre, and occasionally, isolated gross nodules have been observed, Fig.35. The presence of extraneous material at the fibre surface is also shown in this figure.

The fibre was analyzed by X-ray diffraction technique. The numerical values of the X-ray diffraction pattern of the fibre are shown in Table 4 together with identified phases in comparison to 'JCPDS' standards, and to results from TEM diffraction patterns.-The resulting diffraction pattern indicated the presence of β -SiC (the coating), the tungsten borides W_2B_5 , WB_4 , δ -WB and the presence of the boron mantle. Two very weak diffraction peaks could not be assigned to any of the phases (0.340 nm and 0.118 nm diffraction peaks). According to the literature^[8], in commercial fibres only W_2B_5 and WB_4 are present in appreciable amounts. The X-ray diffraction pattern also showed that the

tungsten substrate has been completely transformed into tungsten borides, implying that the fibre can achieve its maximum strength as far as the core development is concerned. When no boride phases are observed, there is little bonding between the boron mantle and the core, and the fracture usually nucleates at the interfacial region impairing the fibre strength. With diffusion and reaction of boron with tungsten a bond is formed which allows the applied fibre stress to be transferred across the interface more easily, improving the tensile strength^[8].

The fibre characterization by TEM was performed in the metal infiltrated condition. Examination of the boron mantle in the TEM revealed that there was neither division boundaries, nor preferential crystallographic orientation, as opposed to the SEM observations. The TEM diffraction pattern of the boron mantle, Fig.36, showed the presence of four broad diffuse halos, and the d-spacings correspondent to these halos are given in Table 4. It has been reported^[4,8], that the boron mantle, often called 'amorphous' boron is due to the type of diffraction pattern given, is not truly amorphous but microcrystalline with a crystallite size of approximately 0.2 nm.

Observation of the fibre nucleus in the SEM revealed the presence of a fine distribution of small tungsten boride grains at the centre and mid region, and an outer layer approximately 2 μm thick with larger grain size, Fig.37. Further examination of the fibre nucleus in the TEM revealed an average grain size of 100 nm in the centre region, Fig.38. Fig.39 shows a micrograph of a selected area diffraction pattern obtained from the fibre tungsten-boride nucleus. It can be seen from this figure that some orientations exhibited more intense reflections indicating a preferred orientation. One of the possible reasons for this preferential orientation is that the substrate where the diffusion reaction takes place, the drawn tungsten wire, has a highly orientated structure along the $\langle 100 \rangle$ direction.

Fig.40 shows the SiC coating, produced by chemical vapour deposition process, 'CVD'. In this figure are easily seen columnar subgrains of β -SiC that grew out radially from the boron substrate. The average columnar subgrains width was 100 nm, and their length was in the range of up to 1 μm . It must be mentioned however that some difficulties were found in distinguishing ending points. The term 'subgrains' is used here to refer to

adjacent grains of small crystallographic misorientation^[116]. Selected area diffraction pattern from the coating, Fig.41, showed intense {111} β -SiC reflections which were arc shaped. The arcs indicated a strongly preferred orientation of the SiC subgrains. It is suggested from circumstantial evidence that the outer layer of the coating might be under a compression stress state. A crack that was originated in the boron substrate is showed in Fig.42. This crack has been deflected around the coating middle section and seemed to be following the SiC subgrains boundaries. A possible explanation for this crack deflection is the existence of a compression stress state in the outer layer of the coating that made the front crack to curve towards less stress compressed subgrains, as schematically shown in Fig.43.

4.1.2 Aluminium alloy

The matrix material prior to infiltration was an Al-7%Si-0.4%Mg alloy. The chemical composition of the material is listed in Table 3. Optical metallographic observations were undertaken on polished and etched surface and showed the presence of Al dendrites, interdendritic phases, and the presence of rod like precipitates, probably Mg₂Si, inside the dendrites. Fig.44 shows the main microstructural characteristics of the aluminium matrix. The estimated dendrite cell size was around 70 μ m.

4.1.3 Composite material series 28%

4.1.3.1 Bulk chemical analyses

Wet chemical analyses were performed on samples taken from two strips of composite material series 28%. The strips were coded Al/B 2 and Al/B 4. In the case of the Al/B 2 strip it was possible to analyse the aluminium matrix material with and without the fibres. During the liquid metal infiltration process a movement of the fibres preform inside the die occurred in some strips, due to a dragging effect caused by the liquid metal front. This fibre preform movement left portions of strips without fibres. These strip portions were appropriately sectioned and analysed chemically.

From the Al/B 4 strip, four samples were taken from different locations. One of the samples was sent to an independent research institution^(‡) to provide this work with a

‡ ARE Holton Heath, Poole, Dorset, U.K.

control chemical analysis. All chemical analyses results are shown in Table 5, together with the analyses of the matrix material prior to infiltration.

It can be deduced from Table 5 that during the infiltration process, the molten aluminium alloy lost Mg and picked up others elements from the apparatus used. Thus, the original alloy composition was modified in the composite material. The number and level of elements impurities like Ni, V, and mainly Cr and Fe increased. Generally, it seems that the matrix chemical composition varied between strips and even from place to place in the strip. The chemical analyses of the matrix material, AL/B 2 strip, without fibres showed that the amount of Fe and Cr clearly decreased in comparison to the analyses of the fibre region. This indicates that these elements were preferentially present in phases which had their formation associated with the fibres, as will be discussed in section 4.1.3.3. Some samples showed a higher amount of silicon than the original matrix and this discrepancy may be due to the extraction of Si from the SiC coating during the chemical dissolution of the aluminium alloy.

4.1.3.2 Fibre volume fraction and distribution

The fibre volume fraction, V_f , was measured at both ends of each tensile or fatigue test specimens, at fibre orientations of 0° and 10° . The results showed an average fibre volume fraction of 28.6% with a coefficient of variation of 14%, but some specimens showed a V_f variation of up to 30% from one end to the other. There are two possible causes for fibre volume fraction variation. One might occur before the composite is actually manufactured, when the fibres are interweaved into tapes. Another source of fibre movement is the liquid metal front passing through the fibres during the infiltration process.

It was observed that the local fibre distribution and packing geometry varied from a relatively uniform spacing between fibres to clustering with significant numbers of interfibre contacts. Fig.45 shows transverse sections of the composite material series 28%. It can be seen that the interweaving strip, a thin continuous strip meandering through the fibres, did not keep the fibres equally spaced, Fig.45 a). Some fibres tended to cluster together leaving

‡ ARE Holton Heath, Poole, Dorset, U.K.

some matrix regions without reinforcement. There was also a tendency for banding, i.e., to have the fibres packed in the form of bands intercalated with matrix regions free of fibres, Fig.45 b).

4.1.3.3 Microstructural characterization

Optical and scanning electron microscopy

The liquid metal infiltration technique used in the fabrication of the composite material produced an as cast microstructure in the matrix material, i.e., primary aluminium rich dendrites, interdendritic areas of rich solute and coarse intermetallic compounds (sometimes called constituents^[21]). The investigation of the microstructure of the hypoeutectic aluminium alloy, after infiltration, showed that the dendritic structure was not clearly defined. It consisted of what seems to be, small dendrites cells of aluminium solid solution as the primary phase, and an eutectic filling the interdendritic spaces, Fig.46 a and b. The average dendrite cell size was estimated to be around 40 μm and it was usually smaller than the interfibre spacing or alternatively of the same size. The interdendritic mixture consisted of the Al-Si eutectic and intermetallics. Deep etching the aluminium alloy matrix into water solution of sodium hydroxide and potassium ferricyanide revealed a complex network consisting of silicon flakes and lath particles, Fig.47.

The observed intermetallics were classified accordingly to their morphology and preferential localization sites. Only two types of intermetallics were observed. The first type had a shape of thin curved platelets which in section appeared as long needles, Fig.48, usually interspersed into the Al-Si eutectic region. The second type was of a globular shape, and was often associated with the fibres or the interweaving Ti strip. The preferential precipitation site for the globular type of intermetallic was readily seen when the composite was examined in the longitudinal direction, i.e., parallel to the fibre direction, Fig.49.

EDS analyses of the platelet type intermetallic with cross sections around 4 μm thick showed generally the presence of Al, Si, and Fe, and in some constituents small amounts of Ni were also detected. A typical energy dispersive spectrum obtained from this type of constituents is shown in Fig 50. An average size of 10 μm was estimated for the globular

constituents and EDS chemical analyses indicated the presence of Al, Si, Fe, and Cr, and in some constituents small amounts of Ni and V. Fig.51 shows a typical EDS spectrum from this globular phase.

The constituents size was large enough to allow reliable in-situ chemical analyses by energy dispersive spectroscopy in the SEM. Usually the material activated by an electron beam (30 KeV and a 100 nm diameter electron probe), which gives rise to characteristic X-rays, reaches a depth in an aluminium matrix of approximately $1.5 \mu\text{m}$ ^[118]. Thus, for constituents with dimensions larger than $1.5 \mu\text{m}$, there is a large probability that some of them would yield chemical data from the constituent only with little information from the surrounding matrix. As for SEM it is not possible to visualize what is the constituent shape beneath the surface, some matrix interaction with the electron beam path is expected and somehow its effects must be taken into account. The matrix effect can be analysed when the EDS results are plotted in a solute-solvent plot as explained in Appendix 4 for thin foils. In this work, EDS data were obtained in atom percent after ZAF (atomic number, absorption and fluorescence) corrections and normalized assuming that the detected elements total 100%. No attempts were made to take into account any ZAF correction errors, or raw data statistics acquisition errors.

Solute-solvent plots were constructed from 80 and 97 analysed constituents of platelets and globular types, respectively. Fig.52 shows a solute-solvent plot for the platelets type particles. The atom percent of Si, Fe and Ni were plotted against the Al atom percent and the fitted lines for Si and Fe extrapolated to zero at a common high Al composition. For this particular alloy as far as EDS chemical analyses is concerned, the metal matrix can not be considered as consisting of only one type of element or phase. Rather it contains the aluminium primary phase and the silicon flakes. As both phases may be interacting with the electron beam during the constituent analyses and at indeterminate quantities, this implies that any information regarding the second phase chemistry can not be inferred from the solute-solvent plot. This fact also explains some of the data scatter. Alternatively, when the amount of Al and Si were plotted against the amount of Fe, Fig.53,

the Al and Si variations seemed to attain a plateau, and then the amount of Si apparently started to decrease.

The occurrence of the plateau (or maximum/minimum) can be interpreted based on the following facts. First, the intermetallic can be larger than the volume of material which interacted with the electron beam. Second, there is a smaller chance to find another intermetallic containing Fe and interacting with the electron beam, than to find a silicon flake or the aluminium solid solution. Third, the intermetallics can exist at a range of homogeneity^[22,24]. It is not yet clear whether at the point where the Al and Si variation against Fe attained the plateau, the analysis was performed with a constant matrix interaction or only in the constituent without any matrix contribution. If the plateau analysis results were due to a constant matrix interaction, one would expect at some point a change in behaviour when the results would be yielded only from the intermetallics. Indeed, the results showed a tendency for the detected amount of Si to decrease after the plateau. The results, Fig.53, also indicated that the amount of Al and Si (after the plateau) in the platelets type intermetallics was around 67% and 18% atom percent respectively. Thus, it is deduced that these intermetallics contain Al, Si and Fe approximately in the ratio 67:18:15.

For the globular constituents, similar solute-solvent plots were constructed. In this case it was found that the data were best represented when they were plotted against Si instead of Al, Fig.54. This is because this phase usually appears next to the fibre and thus, the most likely material to be found underneath it is the SiC coating. It was also found that when the amounts of Al, Si and Cr were plotted against the amount of Fe, the variation of Al and Si attained a plateau at approximately 71% and 12% respectively, Fig.55. Therefore, it can be deduced that the globular constituents have Al, Si, Fe and Cr in the ratio 71:12:15:2. The difference between Fig.53 and Fig.54 with respect to the curves concavity direction is due only to the fact that in Fig.53 the matrix is taken as Al and on Fig.54 it is taken as Si.

The volume fraction of the globular type intermetallics was measured in several longitudinal sections as described in Appendix 3. It was found that the average globular phase volume fraction in the aluminium matrix material is approximately 2.2%. This amount

is consistent with an alloy content of approximately 0.08 wt% of Cr and a constituent density of $3.4 \times 10^3 \text{ Kg m}^{-3}$ [22].

The literature^[22,24,26,28] reports that some ternary phases present in commercial aluminium alloys are not equilibrium phases but require small amounts of transition metal elements such as Mn and Cr, or Cu to stabilize it. These phases are extensions of the Al-Mn-Si or Al-Cr-Si ternary phases in which most of the Mn or Cr is replaced by Fe. Most of these phases form by peritectic reaction and when they crystallize from the liquid they are not easily nucleated^[22]. Similarly, the globular intermetallics appeared in considerable amount at the fibre/matrix interface or at the Ti interweaving strip, and the chemical composition of the phase contained Al-Si-Fe-Cr. Thus, it is possible that this phase nucleated first at the fibre surface at a higher temperature and then, the solidification of primary aluminium dendrites started in the interfibre region.

Transmission electron microscopy

Thin foils from different strips of the composite materials series 28% were observed in the TEM. Around 15 constituents of each type, platelets or globular, were chemically analysed with the transmission electron microscope operating in nanoprobe mode. For chemical analyses results see Table 6 and for typical energy dispersive spectra see Fig.56 and Fig.57. It can be seen that the results obtained from the SEM analyses, following the procedure described above, agree very well with the results from the in-situ TEM analyses.

As far as is known, the above graphical EDS data analysis manipulation has not been previously tried on results obtained in the SEM and to some extent to TEM. Some of the drawbacks of the energy dispersive spectroscopy results obtained from SEM are; first, the particle shape beneath the surface is not known and second, absorption correction factors are very large and prone to errors, at least for silicon. As the SEM results agreed with TEM results, which are calculated in a total different way and since the absorption effects are not significant due to the thinness of the the foil, consequently there is a certain degree of confidence in the results yielded by this technique. The EDS data can be collected in the SEM with relative easy and with little specimen preparation. It is possible to analyse

in the SEM around 15 particles per hour. However, in the TEM the achievement of such performance is improbable. The thin foil preparation is a very laborious process and due to the size of the constituents, very few particles can be found in condition that allow EDS analysis to be performed. The full implications of the solvent solute plot on SEM energy dispersive spectroscopy results are beyond the scope of this theses.

The energy dispersive results obtained in the SEM and the TEM indicates that the probable chemical composition of the platelet type particles is $Al_{67}Fe_{15}Si_{18}$ and with the aid of electron diffraction, the platelets were identified as having a tetragonal structure, $a = 0.608$ nm and $c = 0.940$ nm. Fig.58 shows two selected area diffraction patterns (SADP) from a platelet type constituent with their respective indexed diagrams. The structure results agreed very well with published literature^[22,24]. Mondolfo^[22] reported the presence of a phase $FeSi_2Al_4$, in high-silicon alloys, with a tetragonal structure and lattice parameters: $a = 0.612-0.616$ nm and $c = 0.948-0.949$ nm. Rivlin and Raynor^[24] also reported a similar structure called τ_4 , see Table 1. The published^[22,24] chemical composition for the tetragonal phase however did not match the results obtained in this work. Although this phase is reported as having approximately twice the amount of Si compared to Fe, in this work it was established that the atom amount of Si is slightly higher than Fe, see Table 6. It should be pointed out that the chemical compositions mentioned in above literature were none obtained by in-situ chemical analyses and a large number of equilibrium and metastable Al-Si-Fe phases are commonly found in aluminium commercial alloys.

No precipitation was observed by TEM in the aluminium rich dendrites. The wet chemical composition, Table 5, still revealed a substantial amount of Mg in the matrix alloy after infiltration. As no precipitates were found and the observed second phases were Mg free, the remaining Mg seemed to be contained within the fibre surface amorphous layer or slag inclusions, as will be presented next and in section 4.1.5, or alternatively, in solid solution within the aluminium dendrites.

Dislocation density measurements in the aluminium matrix were carried out away from any second phase or fibre interface and showed a high dislocation density of

approximately $3.5 \times 10^{13} \text{ m}^{-2}$. In Fig.59 is shown a typical dislocation structure for the as received material series 28%. The literature^[119,120] quotes dislocation densities values of the order of 10^7 m^{-2} to 10^{10} m^{-2} for a good annealed crystal, and above 10^{14} m^{-2} for cold worked metal. One of the probable reasons for the high dislocation density found in this work was the matrix deformation associated with thermal stresses caused by the mismatch in the coefficients of thermal expansion, ($\sim 5:1$), between the aluminium matrix and the fibre. This high dislocation density within the matrix material implies that the matrix was in a cold worked condition before testing.

Interfaces

Results obtained by transmission electron microscopy showed that the interfaces between the SiC coating and the aluminium alloy matrix consisted of four main types as follows. The first type can be described as a product of contact between the SiC and the aluminium alloy. This interface is prone to reaction producing aluminum carbide that grows from the SiC to the aluminium. The second type of interface consisted of SiC and the free Si as twinned flakes. The third type of interface occurred between the SiC and second phases other than Si. The fourth type of interface corresponded to a layer of extraneous material at the interface.

According to the literature ^[50,58,117] there is no evidence of any reaction taking place between the aluminium alloy matrix and the silicon carbide coating irrespective of the fabrication process route, inclusive metal liquid infiltration. The interface in this case may be described as a pure mechanical interlocking between the aluminium and the fibre. Fig.60 shows a TEM micrograph of the SiC/aluminium interface and no reaction products were revealed even after careful examination. The serrated interface profile is not a reaction product between the SiC and the aluminium. It is just the SiC coating surface roughness with the aluminium following all the minute SiC surface relief.

In this work the presence of aluminium carbide was observed at the matrix/fibre interface, Fig.61. This interface, a consequence of the reaction between the SiC and the molten aluminium, produced some needle like particles which grew from the SiC coating

into the aluminium. Fig.62 is a magnification of a similar region as the region showed in Fig.61. and it clearly shows that there are some particles growing from the SiC towards the aluminium. An enlargement of one of these particles, properly orientated, showed lattice fringes with d-spacing of 0.83 nm, Fig.63. This is in good agreement with the parameter quoted by 'JCPDS' card number 35-799 for Al_4C_3 carbide at (003) directions. Further chemical analyses of these particles, with the transmission electron microscope operating in nanoprobe mode, revealed no qualitative chemical difference between the particles and its surrounding matrix. The EDS spectrum from the particle is shown as an insert in Fig.63. The spectrum showed the presence of mainly Al but the presence of Ar, Fe and Ta was also noticed. The presence of Ar and Ta was caused by contamination of the foil in the ion thinner and the presence of Fe was probably due to matrix interaction with the electron beam.

The second type of interface consisted of SiC and the free silicon in the form of twinned flakes, Fig.64. The third type of interface occurred between the SiC coating and the platelets and globular intermetallics. Like the aluminium, these phases seem to follow closely the SiC surface relief and was not observed any type of reaction or compound formation. These second phases, in contact with the SiC, consisted essentially of large single crystals as opposed to the fine grained SiC indicating a lack of epitaxy, which might be a evidence that some of these phases are formed at the end of the matrix solidification.

The fourth type of interface can be described as an amorphous layer. Selected area diffraction patterns of these areas always give very diffuse rings. Fig.65 shows this type of interface and the insert is a SADP of the layer. The measured d-spacings from these rings coincided with graphitic carbon with interplanar spacing $a = 2.46$ nm and $c = 6.70$ nm. Energy dispersive spectroscopy at this region revealed the presence of Al, Si, Fe, Na, Mg, P, S, Cl, P and Ca. Fig.66. This layer could consist of slag segregation entrapped between fibres or a fibre surface contaminant.

4.1.4 Composite material series 48%

4.1.4.1 Bulk chemical analyses

Wet chemical analyses was performed on samples originated from the composite material series 48%. Four samples were taken from different locations of the material and coded Al/B 8. One sample was sent to a research institution to provide an independent control chemical analyses, see section 4.1.3.1. The chemical analyses results are shown in Table 5. The results showed similar trend as the material series 28%, regarding an increase in number and level of elements impurities like Ni, V, and mainly Cr and Fe. The major difference found was in the measured amount of Mg. For the material series 28% the average amount in weight percent of Mg was 0.27% while for series 48% it was 0.05%.

4.1.4.2 Fibre volume fraction and distribution

The fibre volume fraction, V_f , was measured at both ends of every tensile or fatigue test specimens, at fibre orientations of 0° and 10° . The results showed an average fibre volume fraction of 45.3% with a coefficient of variation of 6%. The maximum fibre volume fraction variation observed between the ends of a specimen was 5%.

The higher fibre volume fraction might have caused the small variations in the local fibre distribution and packing geometry, with significant numbers of interfibre contacts and some matrix regions without reinforcement. This explains the smaller coefficient of variation, 6%, when compared to 14% for the 28% series material. Fig.67 shows a transverse section of the composite material series 48%. This results does not imply that the fabrication technique has improved but rather that the fibre movement inside the die during the infiltration must have being restrained by a higher fibre volume fraction. Is this fibre movement which causes great fibre volume fraction variations and local fibre packing alterations.

4.1.4.3 Microstructural characterization

Optical and scanning electron microscopy

The microstructure of the composite material in the longitudinal direction showed the presence of the primary aluminium dendrites and the eutectic Al-Si. In this case the dendritic

structure was well defined and clearly the last part to be solidified, occurred at the fibre surface since the eutectic is surrounding and in contact with the fibres, Fig.68. The average dendrite cell size was estimated as 80 μm , that is, approximately equal or smaller than the interfibre spacing, Fig.67. The microstructure also showed the presence of a platelet type second phase, usually interspersed in the Al-Si eutectic region. EDS chemical analyses revealed the presence of Al, Si and Fe and small amounts of Ni.

Solute-solvent plots were constructed from 159 analysed platelet type constituents, Fig.69. The atom percent of Si, Fe and Ni were plotted against the Al atom percent and the fitted lines for Si and Fe did not extrapolate to zero at a common high Al composition. Again, the data is best presented if the amounts of Al and Si are plotted against Fe, Fig.70. It can be deduced from Fig.70 that the amount of Al and Si (after the plateau) in atom percent is around 66% and 18% respectively. Thus, it is concluded that these platelet type constituents contain Al, Si and Fe in a ratio of approximately 66:18:16. These results agreed quite well with the results for the same constituent morphology from the 28% series material. The presence of any globular constituent or second phase particle containing Cr was not detected, and thus no satisfactory explanation has been found other than solid solubility of Cr in the aluminum rich dendrites.

Some structural differences exist between the two composites series material regarding the solidification kinetics. The presence of the fibres seemed to have little effect on the way the alloy started to solidify, as for both series it seemed that the solidification of the primary aluminium dendrites started at the interfibre region. Both composites series presented quite different cast structure and it is likely that the manufacturing parameters were not kept constant during the production of the composites. It can be argued that the different fibre volume fraction might have been one of the causes for the dissimilar cast structures. However, it has been reported^[35] that the variation of the secondary arm spacing with the solidification time is only slightly dependent on fibre volume fraction. These results were obtained for Al-4.5 wt%Cu reinforced with alumina fibres 20 μm in diameter, with a fibre volume fraction variation between 21% to 55%. Therefore, the 28% series material (average dendrite cell size 40 μm , smaller than the interfibre spacing) might have been solidified at a

higher rate than the 48% series material (average dendrite cell size 80 μm , that is smaller or similar size as the interfibre spacing). The average dendrite cell size for some portions of matrix material without fibres, 28% series only, revealed a cell size larger than the material with fibres. The measured dendrite cell size for the matrix without fibres was 60 μm as opposed to 40 μm cell size for the composite material. Thus, it can be inferred that inside the fibre preform the solidification rate was higher than at the region without fibres. Besides, the presence of the fibres might have restrained some dendrite cell growth as well.

Transmission electron microscopy

TEM dislocation density measurement for series 48% showed a slightly inferior value, $\sim 3.0 \times 10^{13} \text{ m}^{-2}$, than for the 28% series material. It should be mentioned that the standard TEM dislocation density measurement usually involves many uncertainties like actual foil thickness, mechanical or ion thinning damage, which could nullify attempts to determine the effect of different volume fraction on the dislocation density. According to the literature, the average dislocation density for different composite materials in the as manufactured or annealed condition is high and around 10^{14} m^{-2} . For example, Arsenault and Fisher^[121] working with an aluminium alloy reinforced with 20% β -SiC fibre in the annealed condition reported a dislocation density of $2 \times 10^{14} \text{ m}^{-2}$. The investigation of Hancock and Grosskreutz^[122] on an aluminium alloy reinforced with 25% stainless steel wires in the as quenched condition also produced a dislocation density around 10^{14} m^{-2} . It is worth mentioning that the TEM specimens used in their work were prepared by jet polishing, while in this work they were prepared by ion thinning. It has also been reported^[123] that annealed aluminium/silicon carbide whiskers composites exhibit a relatively high density of dislocations of at least 10^{13} m^{-2} . In this latter work it was also quoted^[124] that ion milling does not introduce or remove dislocations in the TEM foils, although some point defects are introduced by ion bombardment.

Interfaces

The analysed interfaces for 48% series were basically of the same type as for the material series 28% with the exception of the globular phase / SiC coating interface, which

was not found in the series 48%. Due to the limited number of examined foils, the reaction between the aluminium alloy and the SiC coating producing aluminium carbide has not been observed. The amorphous layer interface was found in a greater extent for the 48% series material than for the 28% series.

4.1.5 Fabrication defects

4.1.5.1 28% series material

The fabrication defects were classified into four broad groups in section 2.5 and among these groups several types of defects were observed. In the structural factors group, low fibre volume fraction and poor fibre distribution were observed in some regions. Both types of defects are caused by the liquid metal infiltration process, i.e., the fibres are not kept equally spaced in the interweaved tape and fibre movement occurs inside the die due to the liquid metal front passing through them. For this series, many misaligned fibres were also observed, and in some specimens small pieces of fibres were observed to be lying in the transverse direction. These pieces of fibre might have become loose inside the fibre preform due to cutting and handling operations of the fibre tape. The Ti interweaving strip is a foreign material added deliberately to the composite material to keep the fibres together but it has mechanical properties completely different from the aluminium alloy and it does not seem to chemically react with it. The bonding between the Ti strip and the aluminium is very weak and this interface has proved to initiate fatigue cracks as will be presented later.

Among the matrix flaws, many slag inclusions were found containing Na, P, S, K, Ca, Fe, Al, Si and Mg, Fig.71. The slag volume fraction was estimated to be around 1%. Slag inclusions were found everywhere in the composite, i.e., within the matrix, at fibre surface and some entrapped between fibres acting as bridge phase, Fig.72. In this case, the slag might have reached some fibre regions before the molten alloy and ended up by being entrapped and solidified between the fibres. Then, peritectic and eutectic solidification took place on the already solidified slag. Porosity, gas-or-shrinkage-caused, was also found either adjacent to fibres or in the interfibre region, Fig.73. As previous evidence showed that the molten alloy started to solidify in the interfibre region, see section 4.1.3.3, porosity

is not expected to be found in the interfibre region since it should have occurred in the last region to be solidified, i.e., near the fibres. Thus, it is suggested that the solidification sequence was inhomogeneous. In some areas it started at the interfibre region and the last part to be solidified was at the fibre interface, see Fig.46 b). In other regions, the solidification started at the fibres leaving porosity in the interfibre region. The volume fraction of porosity was evaluated by area analyses and it was found to be around 0.2%.

Some fibre strength factors that may affect its performance as load carriers were observed. The reaction between the SiC coating and the molten aluminium alloy gives Al_4C_3 which might adversely affect mechanical properties and make the material susceptible to environmental attack. Aluminium carbide is a water soluble compound and its dissolution might lead to pitting attack at the interface. It exhibits a platelet morphology with the largest facets on the basal plane of the hexagonal structure, which under stress may initiate cracks. Some fibre ends were also observed in longitudinal sections of the composite and this might have been originated during the composite fabrication. Fibre ends have a deleterious effect on the composite mechanical properties because they reduce the reinforcing efficiency at their ends. As the stress-strain fields are modified in the fibre and in the matrix by the discontinuity, under fatigue, this may generate cracks.

Between the interface factors, the most striking is probably the poor or weak bond between the matrix alloy and the fibre. This is indicated by the absence of reaction between the SiC coating and the aluminium alloy matrix, and the presence of the amorphous layer. A weak interface can improve toughness properties by deflecting or branching the cracks, but on the other hand, weak interfaces lead to very poor off-axis and transverse mechanical properties.

4.1.5.2 48% series material

The 48% series material showed basically the same type of defects as the 28% series with the exception of an apparently better fibre distribution and a smaller fibre volume fraction variation. The presence of coring was only found in the 48% series material and this is a marked difference, Fig.68. The presence of microsegregation, (segregation of solute

ements over distances of the order of the dendrite arm spacing), can affect the mechanical and the corrosion properties of the alloy.

This section about fabrication defects emphasize the fact that, if the control of the fabrication process is not well exercised, the composite produced by liquid metal infiltration technique may present a catalogue of defects that have a detrimental effect in the mechanical properties.

4.2 Fibre mechanical properties

The mechanical properties of the composite material depends on characteristic properties of the fibres used to produce the composite. Thus, appropriate fibre mechanical properties data must be gathered in order to evaluate the composite properties. In this study the fibre properties had to be evaluated mainly for two reasons. First, there is a large number of published data on boron fibres^[3,4,6] and these data usually give a good indication of the fibre properties. However, the literature can also be misleading since the full details of the employed techniques are usually not known, and batch to batch variations may occur during the fibre fabrication process. Second, the process of fabrication of the fibres used in this study involved the work of two different manufacturers. One produced the boron fibre and the other applied the SiC coating and weaved the fibres into a tape. The fibre mechanical data after the coating process and tape manufacturing were not available.

The fibre strength obtained in this work is presented in a histogram form, Fig.74, showing that the strength distribution has a low-strength tail. The low strength tail is related to various circumstances that can lead to premature fibre failure during the tensile test.

The strength of these fibres is determined by the distribution of flaws produced during the deposition processes and any subsequent operation like weaving or handling. The fibre strength distribution is better described by Weibull statistics and for more details, see Appendix 1. Fig.75 shows a plot of the probability of failure against fibre strength. This plot indicates a departure from linearity which may be due to a bimodal fibre flaw distribution. Physically this means that there are two types of fibre flaws, each with a different failure probability distribution. It should be pointed out that 30 fibre tests were

performed, 10 tests at fibre gauge length of 80 mm and 20 tests at fibre gauge length of 50 mm.

The SiC coated boron fibres showed an average ultimate tensile strength dependence on the gauge length. For the 50 mm gauge length, the average fibre UTS was 3400 MPa and the coefficient of variation was 12%. For the 80 mm gauge length, the average fibre UTS was 3000 MPa and the coefficient of variation was 22%. This means that the probability of finding a more dangerous fibre flaw increases with fibre length. The reported^[3] average UTS for boron fibres is about 3600 MPa with a coefficient of variation of about 15%, but no reference is made to the fibre diameter and to the gauge length used. Thus, it has been found very imprecise to use literature data on calculations of composite properties.

Fibre modulus of elasticity, on the other hand showed very little variation. The average modulus measured was 383 GPa and the coefficient of variation was 2%. The average fibre strain to fracture can be calculated assuming that all fibres fail at the same elastic strain, by using the average fibre UTS value for a gauge length of 80 mm and the average modulus of elasticity value. Therefore, the estimated average fibre strain at fracture was 0.85%.

4.3 Aluminium alloy mechanical properties

The matrix material prior to infiltration was tensile and fatigue tested. The material was tested in the as received condition.

4.3.1 Aluminium alloy tensile testing

The aluminium alloy matrix prior to infiltration was tensile tested and the results are presented in Table 7. The results are within the range for Al-Si: 5-10% Si, 0.2-0.3% Mg alloys, not modified and sand cast, i.e., UTS range of 100-150 MPa, flow stress between 60-80 MPa and 1-3% of elongation^[22].

4.3.2 Aluminium alloy fatigue testing

The fatigue characterization of the aluminum alloy was determined by plotting the number of cycles to failure versus the maximum stress. This is shown in Fig.76. The material showed very little fatigue scatter and an S-N curve which sloped gradually downwards with increasing number of cycles. As nonferrous metals like aluminium do not have an endurance limit, the fatigue strength is given at 5×10^6 cycles. The fatigue results indicate that fatigue strength, σ_{FS}^m , is approximately equal to the flow stress and nearly half the value of the ultimate tensile strength, see Table 7 for results comparison. The measured fatigue strength, $\sigma_{FS}^m = 64$ MPa is in the same range as published data^[22] for straight hypoeutectic alloys, 50-70 MPa.

4.4 Composite material mechanical properties

4.4.1 Composite material tensile testing

The tensile properties of the composite material were measured for the series 28% and 48% at fibre orientations of 0° , 10° and 90° , Table 7. For the series 28%, it was possible to evaluate the matrix properties without the fibres. This fact allowed a comparison of tensile properties of the matrix in different microstructural conditions. It has been reported^[100] that the flow strength for similar Al-Si-Mg alloy is not a function of the dendrite cell size while the ultimate strength is controlled by the dendritic cell limitation on elongation. It can be seen from the results presented in Table 7 that the average UTS and flow stress for the aluminium alloy prior to infiltration are slightly superior to the value of the aluminium alloy in the as cast condition, although the indicated errors encompass the difference.

The tensile results indicated an increase in the ultimate tensile stress at 0° fibre orientation, with an increase in the fibre volume fraction. This however was not observed when the composite material was tested at others fibre orientations, i.e., 10° and 90° . It was established that the type of interface present in the composite material was of the weak type. Therefore, an increase in fibre content achieves its reinforcing purpose in the composite material when under longitudinal tensile loading, but not on other types of loading where interface failure or matrix rupture play an important role. The ultimate tensile properties for

28% series material at 0° fibre orientation showed a larger scatter variation than for the 48% series. The main reason was probably the smaller fibre volume fraction variation of the 48% series material.

Both material series presented very low strength properties at 90° fibre orientation. The transverse composite strength may lie between upper and lower limits depending on the interface strength. The upper limit is for strong interfaces, and it can be taken as the strength of the matrix constrained by the fibres. The lower limit is due the matrix strength in the case of holes replacing fibres. Thus, for the weak interfaces, the transverse strength depends on the fibre volume fraction and packing geometry which are related to the reduced cross section. Similarly, in this work the interface was taken as a weak type and a higher volume fraction meant a lower tensile strength. Indeed the 48% series material showed a lower tensile strength than the 28% series. Comparison of the transverse tensile results obtained in this study with published work^[79] on aluminium alloy (ASM 6061) 50% B-SiC fibre composite, produced by the diffusion bonding process, revealed that the material produced by liquid metal infiltration technique had a inferior tensile strength. For series 48% at 90° fibre orientation a value of 37 MPa was obtained whereas the ASM 6061-50% B-SiC material produced a value of 100 MPa. These results can be partially explained by the fact that the wrought aluminum alloy 6061 has higher mechanical properties than the cast alloy used in this work.

The axial tensile stress-strain behaviour of the composite material manufactured by the liquid metal infiltration technique was also analysed. It was characterized by an initial linear region, followed by a non linear region of transition prior to another linear region that finally led to fracture. The stress-strain curve for the composite material used in this work had similar shape as the curve presented in Fig.10, however the stage 4 was not observed. The modulus in the initial stage can be related to the elastic moduli of the matrix and fibre using the rule of mixtures, as is presented next.

The modulus of elasticity results at 0° fibre orientation for both 28% and 48% series agreed satisfactorily with the predicted results from the rule of mixtures. The composite modulus of elasticity in the fibre direction predicted by the rule of mixtures resulted in

values of 161 GPa and 211 GPa for the 28% and 48% series respectively. These results were arrived at by using average fibre volume fraction of 29% and 45%, and average fibre and matrix modulus of elasticity of 383 GPa and 70 GPa respectively. These values are well situated inside the measured range of modulus variation, see Table 7. No attempts have been made to predict the off-axis modulus.

The total strain at failure (ϵ_f) and the plastic strain (ϵ_p) of the composite materials are also listed in Table 7. The total strain in all cases were considerably less than the average fibre strain at fracture, 0.85%. This emphasizes the fact that fibres have a significant range of strengths and their random breakage throughout the composite, together with other types of defects, causes local stress concentrations which in turn control the composite failure.

4.4.2 Composite material fatigue properties

The fatigue behaviour of the composite material was expressed in the form of a relation between the maximum applied fatigue stress and fatigue life (number of elapsed cycles to failure). The large scatter in lifetime data was due to the complexity of damage development under cyclic loading and to large fabrication defects like slag inclusions, porosity, lack of infiltration, and transverse pieces of fibres. The fatigue testing results suggested that the composite 28% series was only slightly sensitive to repeated tensile loading in the fibre direction, Fig.77. The slope of the S-N curve was relatively flat mainly because of the fatigue insensitivity of the boron fibres. The scatter in fatigue lifetime decreases considerably if the results generated by specimens with identifiable major defects such as, slag, lack of infiltration and transverse pieces of fibres are sorted out from the fatigue data. The specimens with major defects are indicated by the symbol (o) on Fig.77. The stresses required to cause fatigue failure after 10^2 to 5×10^6 cycles were higher than 0.70 times the ultimate tensile strength when the data was corrected for specimens without major defects.

For the 48% series at 0° fibre orientation to the tensile axis, the fatigue tests showed that the material had a slightly higher sensitivity to cyclic tensile loading, Fig.78. Bearing in mind the limited number of samples used, the slope of the S-N curve was slightly steeper

than for the 28% series. The stresses required to cause fatigue failure after 10^2 to 5×10^6 cycles were higher than 0.70 times the ultimate tensile strength

Fig.19 shows some fatigue data from the literature^[18] on boron/aluminium composites produced by diffusion bonding process. Compared to the uncoated boron fibre composites, the 40% fibre volume fraction SiC coated material exhibit poor low cycle fatigue resistance. In the low strain region (high cycle), the fatigue strength is only slightly inferior to that of the uncoated fibre composites. A comparison of fatigue data from this work with the above published results, shaded areas in Figs.77 and 78, indicated for instance that the 48% series material, with an average volume fraction of 45% had a low cycle fatigue strength slightly inferior than the 40% material. At high cycle fatigue, the composite material used in this work showed a lower fatigue strength (about 25% decrease in fatigue strength). If the trend for the 40% fibre volume fraction (published results) is followed at 30% fibre volume fraction uncoated fibre composite, the results obtained in this work for series 28% (average fibre volume fraction of 29%) correlates again at the same fatigue strength levels similarly to the 48% series material.

The fibre orientation to the tensile axis affects the fatigue behaviour in the same manner as it does to the tensile properties. It was observed that both materials at 10° fibre orientation showed a significant decrease in fatigue strength, but the 48% series material revealed a higher decrease in fatigue strength. At this point it could be reasoned that the fatigue strengths of both materials are strongly dependent on microstructure and on the aluminium/fibre interface. Compared with the 0° fibre orientation, the fatigue ratio (fatigue strength divided by the tensile strength) was lower for the 10° material. A value of 50% fatigue ratio was produced by this material as opposed to a value of 70% fatigue ratio for the 0° material. This indicated a higher fatigue sensitivity when the fatigue behaviour was influenced by the matrix and interface properties.

The composite material at 90° fibre orientation showed very poor tensile properties, *UTS* between 26 MPa and 37 MPa, see Table 7, making fatigue tests impossible to be performed in the available equipment.

4.5 Fatigue damage accumulation

4.5.1 Fatigue damage at 0° fibre orientation

Fatigue damage measurements were carried out at 0° fibre orientation for 28% and 48% series material in order to examine the fatigue stiffness loss in the longitudinal direction. At 0° fibre orientation the composite mechanical properties were less dependent on the matrix and interface strengths than other fibre orientations, since the fibres carry the load from the damaged matrix and interface.

4.5.1.1 Fatigue damage series 28% at 0° fibre orientation

The fatigue damage was evaluated by plotting the fractional change in elastic modulus versus number of elapsed cycles in either logarithmic or linear scale. The fractional change in elastic modulus was calculated using Eqs.(33-35). Specifically, for unidirectional composite specimens, the influence of the mean stress on the magnitude of the fatigue limit is considered to be negligible^[81,95]. Therefore, the fatigue damage results are basically discussed in terms of stress range values.

It was found in this work, that the average fractional modulus change experimental error due to chart reading was around 0.3%. This value did not take into account the strain gauge error in strain indication (gauge factor $2.030 \pm 0.5\%$).

The fatigue damage behaviour for series 28%-0° and at stress ranges ΔS , ($\Delta S = S_{max} - S_{min}$) less than or equal to 172 MPa, are typically shown in Fig.80 (log scale) and Fig.81 (linear scale). The composite material showed a very small decreasing variation in initial loading (ΔE_i) and secant modulus (ΔE_s) fractional change. If fatigue damage is translated into moduli variations, it can be implied that under such conditions the material was almost fatigue proof since, very little damage is either produced or detected. The stress-strain data under such particular circumstances showed that only closed hysteresis loops were generated and the secant, E_s , modulus was approximately equal to the initial loading modulus, E_0 .

For stress range equal and above 186 MPa, the fatigue stress-strain behaviour changes. The first few cycles are characterized by open hysteresis loops which gradually

close and this usually represents a measure of work done in the matrix material. Some of this work is stored as plastic deformation of the matrix, some is associated with configuration changes, such as fibre realignment, and some is emitted as heat. As the hysteresis loops close, the unloading modulus, E_{un} , gradually approximates the secant modulus, E_s , until it becomes the same. It can be seen from Fig.82, that the fractional change in secant modulus (ΔE_s) increases after few cycles, while the matrix work hardens or the fibres realign. At this stress range the material seems not to be losing stiffness, at least in the range of 6×10^6 elapsed fatigue cycles.

Testing the material at higher stress range, equal or above 214 MPa, the fractional change in secant modulus (ΔE_s) increased after few cycles till a plateau was attained, then it started decreasing due to fatigue damage, Fig.83. When the modulus fractional change was calculated using Eq.(34), for (ΔE_{un}), the results showed a decrease of this fractional modulus as a function of elapsed fatigue cycles till a plateau was attained. It is suggested that at the stress ranges where the unloading modulus was measured, there was a matrix plasticity effect that lowered its value causing a decrease in the fractional unloading modulus change. Then, due to fatigue damage the fractional unloading modulus started decreasing again, and finally the specimen fractured.

The criterion for evaluation of fractional change in elastic modulus depends on whether the fatigue loops are open or closed. When the fatigue loops are open, it is possible to measure both secant and unloading fractional modulus change. In some cases it is preferred to evaluate fractional modulus change in terms of the fractional change in unloading modulus (ΔE_{un}), because it is a more reliable measure of fatigue damage, which depends only on the constituents moduli. Conversely, the fractional change in secant modulus (ΔE_s) is a function of the matrix flow strength in the composite material. This increases as the matrix cyclically strain hardens during fatigue, then decreases due to fatigue damage. The measurement of the fractional change in unloading modulus was difficult in the present case, since it corresponds to a very small portion of the stress-strain loop and therefore its limit is strongly affected by the sensitivity of the strain measurement device. Thus, in this work it was found useful to represent the fatigue damage results using both

criteria whenever the experimental results allowed reliable measurements. Further discussion of Figs.81 and 83 is deferred until after the discussion of Figs.84 and 85.

In summary, at stress range ΔS , below 172 MPa, it can be seen that the material shows a very small variation in the fractional change of secant modulus ΔE_s . At stress range ΔS , equal to 186 MPa, the matrix material strain hardens but does not lose stiffness and at a higher stress range (above 214 MPa) the material starts undergoing fatigue damage. Fig.84 shows the fractional change in secant modulus for the 28%-0° series material, at different stress ranges. The initial increase in fractional modulus change depends on the stress range and will reach a maximum when it is equal to the ultimate tensile strength of the material. In this study, a test was made at $\sigma_{max} = 480$ MPa, which is about the maximum of the UTS range variation of the material, see Table 7. It was then found that for the 28%-0° series the maximum increase in fractional secant modulus was around 1.7% for a stress ratio $R = 0.4$.

Fig.85 shows the fractional change of unloading modulus, (ΔE_{un}), versus log number of cycles for different stress ranges. Apparently, each specimen at a stress range higher than 214 MPa reached a stabilized value after a decrease in the fractional modulus. After this region, the material resumed a decreasing fractional modulus behaviour leading to failure.

As mentioned in section 3.6.2.2, some specimens have been unloaded to zero stress, at some intervals, in order to evaluate the loading modulus variation as a function of the elapsed fatigue cycle number. It was noticed that the measured residual strain in the material after unloading was lower than the plastic deformation measured at the highest loading stress point. This residual strain was only observed for stress ranges over 186 MPa, when the composite showed signs that the matrix was strain hardening. The extent of this residual strain was too large (40% less than the plastic deformation for specimen at stress range of 274 MPa) to be explained by anelastic behaviour. This could only have been caused by a contraction of the fibres, enough to put the matrix under a compression stress state. It is believed that the composite residual stress state is determined by the thermal and mechanical history of the composite. Residual stresses originate when the composite is heated or cooled because of the difference in matrix and fibre coefficients of thermal expansion. On cooling

from the fabrication temperature, the matrix is left in tension and the fibres in compression. During the fatigue test, the matrix undergoes some plastic relaxation while the fibres remain elastic. Over subsequent unloading, the fibres recover their elastic strains, and the matrix contracts plastically and elastically beyond its previously fabrication level, i.e., into a compression stress state.

The composite fatigue behaviour, during subsequent specimen reloading from zero stress to maximum stress, changes for the particular stress range that causes the matrix to strain harden. The specimen stress-strain curve exhibits a linear portion from where the reloading modulus, E_r , is obtained. This linear portion is followed by a non linear region, path $OA'B'$, Fig.33. The subsequent fatigue loops start with open loops which gradually close again. It should be emphasized that the fatigue cycles prior to unloading were usually closed, but after the reloading, they started as open cycles till the condition of closed cycles was again established. It is supposed that under such condition, the matrix upon unloading was subjected to a Bauschinger effect, i.e., the matrix went through a compression stress state that consequently has lowered the fatigue flow stress previously attained, allowing more plastic deformation to take place under the new condition. This is a further indication that upon unloading after fatigue, the fibres put the matrix under compression.

Figs.82 and 83 also show the variation of the fractional change of initial loading modulus (ΔE_t) for different stress ranges. Careful examination of the results shows that there is a very small decrease in the loading modulus. This is an important observation because it opposes the results produced by other ways of measuring the modulus fractional change. The reason for this effect is not yet very clear. It is necessary to suggest that the main reason for stiffness loss is fibre breakage and matrix cracking as will be discussed in section 4.6. A possible reason for this phenomenon is that the fibres, when unloaded, caused matrix compression, closing completely the matrix cracks. Upon reloading the specimen, in the stress level where the fractional change of initial loading modulus is measured, the fibres seems to be dominating the composite elasticity behaviour by carrying the load in a strain controlled manner not affecting the net elastic modulus.

The fractional change in secant and unloading modulus versus the linear number of cycles is shown in Fig.86. It can be seen from this figure that the material attained a plateau state after a few cycles, and upon unloading and reloading, a new state was achieved at different fractional modulus change. The unloading-reloading cycle showed a marked change in the fatigue induced stiffness loss, indicating a sharp damage increase in the material. For subsequently continuous cycling, the material showed a progressive damage state that culminated in the specimen fracture.

The literature^[89,97] mentions that aluminum boron composite material under fatigue appears to reach a stabilized value of fractional change in elastic modulus, referred as a saturation damage state (SDS), see Fig.25. After the saturation damage state is reached, the material will neither accumulate more damage nor fail under the present loading condition. When the saturation damage state is reached, the matrix cracking causes the load to transfer to the fibres relieving the matrix from additional damage. This effect does not seem to be occurring with the material used in this work. In fact, the material attained a plateau state similar to the reported saturation damage state, but after this plateau, a progressive damage state appeared leading the specimen to fracture.

4.5.1.2 Fatigue damage series 48% at 0° fibre orientation

The overall fatigue damage behaviour for the 48% series material at 0° fibre orientation was similar to the 28%-0° series material. Fig 87 shows the fractional change in the secant modulus versus the log number of elapsed fatigue cycles. The tests showed that the material at stress range $\Delta S = 238$ MPa did not produced significant fractional change in secant modulus. At stress range $\Delta S = 272$ MPa, there was a clear increase in the fractional secant modulus due to matrix strain hardening. The indication of stiffness loss was not measured in this specific test due to experimental problems. At higher stress range, $\Delta S = 324$ MPa the material underwent fatigue damage and consequently stiffness loss. The highest increase in fractional secant modulus for the 48%-0° series, was around 1%. This value was obtained in a test made at $\sigma_{max} = 542$ MPa, which is below the maximum *UTS* range variation of the material, see Table 7. Therefore, at higher stress range and

consequently higher maximum stress, a higher change in the fractional secant modulus due to matrix strain hardening is expected .

The fractional change in secant, unloading and initial loading modulus versus log number of elapsed fatigue cycles at stress range of 324 MPa is shown in Fig 88. The specimen reached a plateau state after an initial increase in the secant or decrease in the unloading fractional modulus. Subsequently, the material resumed a decreasing fractional modulus behaviour leading to failure. The results also showed that there was no change in the fractional loading modulus.

The fractional change in the secant, the unloading and the initial modulus plotted against the linear number of cycles is shown in Fig.89. It can be noticed from this figure that the material attained a plateau state after a few cycles and after, a progressive damage state finally led the specimen to fracture.

The results presented above for the 28% and 48% series materials indicates that the way the fractional modulus change is measured implies different interpretations and different magnitudes of the fatigue stiffness loss phenomenon in composites materials with metallic matrices. The results interpretation of the fractional change in elastic modulus, for log or linear scale of the number of fatigue cycles are not contradictory but rather complementary. The log scale was found useful in studying the low fatigue cycles effect, whereas the linear scale was found to be more advantageous in high cycles.

4.5.2 Fatigue damage at 10° fibre orientation

The fatigue damage behaviour for the 28% series material, at 10° fibre orientation with the tensile axis, showed essentially the same trend as for the 0° fibre orientation, regarding the fractional secant and unloading modulus change. Figs.90-92 show the fatigue damage behaviour for the 28% series material at different stress ranges in the case of non fractured specimens. It is noted in Fig.90 that the composite material depends on the stress range to develop fatigue damage. A striking difference was however found between the 10° fibre orientation and the 0° fibre orientation, for the fractional change in initial loading modulus (ΔE_i). It follows from Figs.91 and 92 that the fractional change in initial loading

modulus, showed by filled squares, changed considerably following the same trend as the secant and unloading cases. The reason for this lies in the fact that at 10° fibre orientation to the tensile axis, the matrix plays a more important role in the fatigue characteristics of the material. For off-axis tests, once the fatigue damage is established it directly affects the stiffness of the material, since there are no 0° fibres to carry the load in strain controlled manner.

Another important observation of this work is the magnitude of stiffness loss that the material at 10° fibre orientation can undergo before failure. Figs.93-94 show the fractional change of elastic modulus for the 10° fibre orientation which was found to be approximately 30%, whereas small variations of less than 7%, were obtained for the 0° material. These observations confirms results reported elsewhere^[5] for diffusion bonded aluminium-boron composite material. The results of Figs.93-94 indicated that the specimen was fatigue damaged at stresses below that used for the generation of Fig.90. This is a clear indication that the fatigue process at off-axis orientation is strongly dependent on the intralaminar shear strength of the matrix and on the interface strength to fibre debonding.

Some results of the fractional change in secant modulus for the 48% series material at 10° fibre orientation is shown in Fig.95. This series, similarly to the 28% series, showed large stiffness losses (more than 40%) but at a stress range lower than that for the 28% material.

A correlation between stress range magnitude and extent fatigue damage was not found for the 10° fibre orientation for both series materials. At 10° fibre orientation the fatigue characteristic seems to be strongly affected by the matrix microstructure, fibre volume fraction and the presence of defects. Another possibility is an artifact due to the way the moduli were measured. The use of strain gauges did not cover the total specimen width and for off-axis composite testing a development of a main crack in the fibre direction is possible. If this single or multiple cracks does not run through the active strain gauge measurement area, no substantial fractional modulus change will occur. It worth mention that this effect can occur to any fibre orientation, including testing in the fibre direction, but it was found to be more critical during off-axis testing.

4.5.3 Shake down

A comparison was made between the shake down model and some experimental data obtained for the 0° fibre orientation specimens. The composite proportional limit was estimated in this work by Eq.(23), where E_0 was substituted by the average initial loading modulus, σ_{y^m} was substituted by the average matrix flow stress at a strain of 0.001, see Table 7, and E_m is the matrix modulus of elasticity. Then, the average shake down stress range was calculated using Eq.(25) and it was found to be equal to 280 MPa for the 28% series material and equal to 373 MPa for the 48% series. These average shake down stress ranges are higher than some values obtained experimentally. For instance one experiment for series 28% showed that at $\Delta S = 214$ MPa damage was occurring in the material. The same was true for series 48% at $\Delta S = 324$ MPa, see Fig.84 and Fig.87.

The shake down model has been applied to some aluminium composites reinforced with continuous fibres, produced by diffusion bonding [5,88,89,95,97]. There are some ambiguities, however, in which values of σ_{y^m} should be used in Eq.(23). Dvorak and Tam^[95] used the flow stress of the alloy. They chose flow stress values from the reported range of flow stresses, which gave the best agreement between their shake down theory and experimental observations. They also reported that composite fatigue limits coincided with the composite shake down limits and that the matrix flow stress seemed to coincide with the alloy fatigue limit. Johnson^[89] alternatively, used the cyclic flow strength of the matrix and reported that the shake down stress range was lower than the composite's fatigue limits. This latter author also reported that the cyclic flow strength and the alloy high cycle fatigue limit seemed to coincide. The reason for these observations was supported by the fact that the flow stress of some aluminium alloys in the as fabricated or annealed condition is very nearly equal to the fatigue strength of the alloy after 10^6 to 10^7 cycles^[96].

The relationship between shake down and fatigue stiffness loss is not held for the cases where the alloy high cycle fatigue limit is lower than the flow stress or the cyclic flow strength. In this case, the matrix stresses should be restricted to the level of its fatigue strength in the composite material.

An attempt was made to evaluate the fatigue strength of the aluminium alloy prior to infiltration under the same fatigue test conditions applied to the composite, Fig.76. The fatigue limit at 5×10^6 cycles was 64 MPa. The ratio of the aluminium alloy fatigue limit to tensile strength and the ratio of fatigue limit to the flow strength were also determined and found to be 0.5 and 1, respectively. As the experimental results for the aluminum alloy prior to infiltration showed an excellent correlation between fatigue limit, flow stress and UTS, a fatigue limit of 59 MPa is expected for the matrix aluminum alloy under the infiltration condition without fibres, i.e., the same flow stress value, vide Table 7. If this hypothetical fatigue limit is applied to the shake down model it will overestimate the shake down stress range.

In this work it was found that the maximum stress, S_{max} , at the shake down stress range, Eq.(25), was much higher than the fatigue limit of the composite material. S_{max} for $R = 0.4$, was estimate to be 467 MPa and 621 MPa, respectively for the 28% and 48% series materials. For 28% series material, if the fatigue results from the specimens with large fabrication defects are not considered, the fatigue limit was estimated to be 350 MPa. For the 48% series material the fatigue limit was around 460 MPa.

If shake down takes place in these composites during cycling loading at the composite fatigue limit, it is possible to speculate by reverse calculation what is the flow stress level under which the matrix starts undergoing fatigue damage. A crude calculation of this stress level can be done using Eq (25) and a shake down stress range of 214 MPa, which is the stress level where stiffness loss was observed. This calculation gives a value of $\sigma_y^m = 45$ MPa, which is well below the aluminium alloy infiltration condition flow stress, 59 MPa.

Going back a little in the discussion, it was observed that the stress-strain behaviour at the onset of fatigue damage was characterized by open hysteresis loops which gradually closed and for stress ranges where no open hysteresis loops were observed, the material did not show any stiffness loss. The open hysteresis loops are associated with matrix strain hardening and this means plastic flow. As the aluminium alloy matrix contained many second phase particles, often brittle intermetallics and silicon flakes, these constituents can

start fracturing when the matrix is deformed, inducing matrix cracks and consequently stiffness loss. Therefore, the calculated value for the matrix flow stress where fatigue damage starts (45 MPa) might be a value between the proportional limit of the matrix and the flow strength at a strain offset of 0.1%. Unfortunately, it is a difficult task to calculate flow stress values that initiate the cracks of second phase constituents in the composite material (and consequently lead to fatigue damage) when the flow stress results are measured separately in the matrix.

The shake down theory is based on the assumption that the fatigue resistance of the composite material is determined by the fatigue strength of the constituents^[89,95]. For composite materials produced by diffusion bonding, some control over the matrix microstructure is possible if wrought alloys are used to produce the matrix. Thus, it is possible to correlate the fatigue strength of the matrix alone with its fatigue strength in the composite material. Even so, the use of the shake down model is precluded when wrought heat treated aluminium alloys are used to produce the composite material, once the fatigue limit of the alloys are much lower than their flow stresses.

When the composite is made by a liquid metal infiltration technique, the matrix microstructure is controlled by the solidification kinetics, the presence of the fibres, and contamination pick up which increases the amount of intermetallics present. These facts can affect the rate of fatigue microcrack nucleation and propagation, and consequently fatigue life. Thus, if it is difficult to produce equivalent microstructures in the composite matrix and cast alloy alone, it will also be difficult to correlate the composite matrix properties with the separated alloy.

4.6 Post testing microstructural characterization

The aluminium alloy material, prior to infiltration and in the infiltration condition was characterized by optical metallography, and the composite material, series 28% and 48%, after tensile and fatigue testing was characterized by, optical metallography, scanning electron microscopy and transmission electron microscopy. These examinations were

carried out with the purpose of characterizing the microstructure after the tensile testing and emphasis was given to the fatigue damage effect in the composite material.

4.6.1 Aluminium alloy

Metallographic micrographs of polished longitudinal sections of the aluminium alloy prior to infiltration, after tensile testing, are shown in Fig.96. The longitudinal sections revealed a preferential fracture path through the interdendritic region, Fig.96 *a*), and the presence of incipient cracks developing in silicon flakes and intermetallics close to the fractured surface, Fig.96 *b*). These cracks were usually found normal to the direction of the maximum tensile strain in the constituent. Under fatigue conditions, the damage was contained in the interdendritic region where most of the cracks were observed. Similarly to the tensile testing condition, the fracture fatigue path followed the dendrite cells.

The fracture tensile behaviour of the aluminium alloy in the infiltration condition followed similar trend. Fig.97 *a*) show that the fracture path followed the small dendrites cells of aluminium solid solution contours. It follows from Fig.97 *b*) that the fracture initiation stage is attributed to either silicon flakes or intermetallics cracking, or to interfacial failure between the constituents and the surrounding matrix.

4.6.2 Composite material tensile tested

It is often possible to determine mechanisms of deformation and fracture through the study of fractured surfaces of a material which have been loaded to fracture. A survey of the fracture surfaces of the 28% series material at 0° fibre orientation showed debonding and fibre pull out, Fig.98 *a*), which are implication of a weak fibre-matrix interface. This low magnification view of the fracture surface also showed that the fracture path was not planar, but left a very irregular fracture surface. Higher magnification of the matrix fracture, Fig.98 *b*), showed that the matrix failed in a ductile manner with some areas of brittle cleavage fracture corresponding to fractured intermetallics or silicon flakes.

In Fig.99 a micrograph of a polished longitudinal section resulted from a 10° off-axis tensile testing of the 28% series material is shown. It can be seen in this figure that the

fracture path ran parallel to the fibres direction through the matrix-fibre interface causing some intralaminar matrix shearing.

The fracture behaviour of the composite in the transverse direction showed that most of the fibres separated from the matrix at the fibre-matrix interface, Fig.100. The fracture surface showed very few split fibres, indicating that the matrix-fibre interface was the weakest link in the composite. The fracture seemed to run through the most dense fibre packed region of the composite. A debonded fibre surface is shown in Fig.101, and some interaction is observed to be occurring between the matrix and the fibres, as the matrix failing in a ductile mode left some material adhered to the fibre surface.

The fracture surface of the 48% series material at 0° fibre orientation showed some fibre pull out and in some areas shear failure, Fig.102. The raggedness of the fracture surface indicates a multiple crack nucleation at different locations that joined together in the final fracture. Contrary to what is suggested in Fig.98 a) and Fig.102, it was not possible to establish whether the load transfer length (fibre pull out length) differed between series, or if it was a characteristic of the fabrication process. The load transfer length varied considerably from specimen to specimen regardless the series. Similarly, the fracture mode at 0° fibre orientation containing some areas of shear failure was a common feature for both series in some specimens.

It follows from Fig.103 that the preferential path in the the composite matrix material was through the interdendritic region. It indicates that the matrix fracture mode is independent on the presence of the fibres, since the aluminum alloy prior to infiltration and in the composite material showed the same trend in fracture mode. This is suggested by comparison of Figs.96 and 97 with Fig.103.

The 48% series tensile transverse fracture showed that the preferential fracture path was through the matrix-fibre interface with very little fibre splitting, Fig.104. A valley left by a debonded fibre is shown in Fig.105. It can be seen from this figure that the aluminium matrix fracture surface showed a mixture of debonding areas from the fibres and some ductile failure.

The most likely sites for crack nucleation are at defects, at brittle second phase constituents or weak spot in the fibres. Porosity, slag and transverse pieces of fibres can act as stress concentrators for the initiation of fracture cracks. In Fig.106 a fracture surface of a tensile specimen which has exhibited a very low tensile strength is shown. Brittle particles can nucleate cracks once the matrix has undergone some plastic deformation, see previous section. Many individually tested fibres exhibited low fracture strength, and many are probably broken during the composite fabrication process. A fibre break is shown in Fig.107, and in this particular case the fracture surface can be traced back to a initiation site at the fibre surface. Although the aluminum alloy matrix have strain to failure higher than the fibres, local triaxial constraint can substantially reduce its ductility. Any of these effects could have initiated the cracking of the composite.

4.6.3 Composite material fatigue tested

Two approaches were used in this work to describe the fatigue damage process. The first was based on fractography, crack initiation and growth, and the second on dislocation density change and on dislocation structure change concepts.

In order to correlate the fractography, crack initiation and growth with the fatigue damage process, a variety of micrographs of the fracture surface and polished longitudinal sections are presented. A discussion of common the features and their bearing on fatigue behaviour is based on these micrographs.

Metallographic observations after fatigue testing showed that cracking occurred in the matrix of both series material at 0° and 10° fibre orientation. The fibres were usually kept intact and bridged matrix fatigue cracks which run perpendicular to the tensile stress direction. Fig.108 shows a micrograph taken from a longitudinal section of a 0° fibre orientation specimen series 28%. The cracks in this micrograph presented a departure from perpendicularity due to a slight fibre misalignment in one side of the specimen. The fibre misalignment occurred during the liquid metal infiltration process. Usually the fatigue cracks were deflected along the matrix-fibre interface by branching in a shear or debonding mode.

It has generally been observed that fatigue cracks initiate at free surfaces, but they also initiate inside the composite at fractured fibres, fibre ends and at fabrication defects. Internally the material may contain cracked fibres that during the fatigue tests develop cracks. Cracks can also evolve from fractured intermetallics or silicon flakes. Another internal source of cracks is shrinkage porosity and a Ti strip used to weave the fibres.

Figs.109 and 110 show a variety of fatigue cracks whose origin was associated to some extent with fabrication or specimen preparation defects. Fig.109 *a)* shows fatigue cracks caused by a fibre end. The discontinuity at the fibre end caused a modification in the material stress-strain field which acted as a local stress raiser producing cracks. In Fig.109 *b)* a crack originated at a broken fibre near the specimen surface is shown. This micrograph also shows clearly that the main crack has left its plane by a succession of second phases particles breakage. The origin of the cracks at the free surface can be associated either with the stresses involved in the machining operation which can break fibres, or with cracked silicon flakes and intermetallics embedded in the matrix. The machining operation may not be the sole reason for surface particle cracking. Matrix plastic deformation during the fatigue test may also induce cracks in the intermetallics or the silicon flakes

It follows from Fig.110 *a)* that the presence of gas-or-shrinkage origin porosity had a deleterious effect in the fatigue properties of the material by acting as a stress concentrator. The above defects are a direct result of the technique used to produce the composite material. However, the presence of the Ti strip is a defect deliberately introduced. Fig.110 *b)* shows a double feature, that is, a crack associated to the Ti strip and another originating in porosity. The observation of so many deleterious defects highlights the necessity of further optimization of fabrication parameters and a improvement of the process in order to enhance the mechanical properties of the current state of art composites, produced by the liquid metal infiltration technique.

Circumstantial evidence suggested that fatigue cracks may be initiated at intermetallic or silicon flakes. Such constituents have negligible ductility and small microcracks were frequently observed to be associated with these particles, Fig.111. Depending on test stress range, these microcracks may have appeared early in life and if this was the case, their

microscopic growth then took place over the most portion of the fatigue lifetime. Because of the many possible sites for crack initiation, and a nonuniform matrix/fibre interface, irregular fatigue fracture surfaces were encountered.

Crack growth, which occurred both transversely and longitudinally, was a possible consequence of different interfacial characteristics and fibre strength variation. For cyclic loading, when a crack front met a weak fibre-matrix interface, crack branching occurred and the crack propagated along the matrix-fibre interface, Fig.112. Fig.112 *a*) shows a transverse fatigue crack that branched over a fibre (not shown in the micrograph) into a cylindrical / debonding crack and then grew away in opposite directions. This micrograph also shows a secondary crack but it is not clear if this crack is the consequence or cause of the cylindrical crack. In Fig.112 *b*) a surface crack branching at a fibre surface in a cylindrical mode is shown. It is possible that the extent of the cylindrical cracks may affect the amount of fibre pull out. For example, the fibre pull out is only observed when the fibre failure occurs associated with the tip of a cylindrical crack. This effect has a detrimental effect in the composite when the debonding or shear crack meets a weak fibre spot causing its rupture. Otherwise, this effect contributes to the composite toughness by blunting and deflecting the cracks. The composite material eventually failed when the growth of fatigue cracks in the matrix impaired the load-bearing capacity of the material.

The fractographic results revealed that the the fatigue fracture surfaces, consisted of regions containing fatigue striations marks that propagated through the matrix, regions with cleavage facets due to presence in the fracture path of silicon flakes, and intermetallics and regions whose appearance is characteristic of fast fracture of a ductile material. Some fractography micrographs of selected fatigued regions are shown in Fig.113.

Dislocation density measurements by TEM, on either tensile or fatigue tested specimens for the 28% series material, revealed no general change when compared to the as received material, Fig.114. In the previous sections it was mentioned that the aluminium matrix has work hardened to some extent. In the considered stress-strain region, dislocation motion must have occurred in lower density dislocation regions within the matrix and on localized high stress regions of the matrix. This means that the plastic deformation of the

matrix material was inhomogeneous and should be highly concentrated around the fractured regions. The dislocation structure were observed in regions around 5 mm away from the fracture surface and away from the matrix/fibre interface.

The observed dislocation structure of the tensile tested 28% series composite, showed the presence of planar arrays or tangled planar arrays, and in some areas, dislocation debris, Fig.115. In fatigued specimens, the cyclic strain induced dislocation debris and dislocation loops, Fig.116, and some incipient dislocation walls, Fig.117. It is proposed that the matrix strain amplitude is not large enough to induce the formation of subgrains. No evidence of persistent slip bands was found.

4.7 Concluding remarks

The fatigue behaviour of the two series at 0° fibre orientation, showed a slight sensitivity of the material to repeated tensile loading in the fibre direction. It is suggested that this lack of stress sensitivity during fatigue testing is mainly controlled by fibre failure. It was demonstrated that the fibres used to reinforce the composite material had a strength distribution, and that they were weakly bonded to the aluminium alloy matrix. It has been reported^[85] that fibres are not themselves susceptible to fatigue damage. Hence, during fatigue loading, some fibres were expected to break in tension at lower stresses due to weakness spots, initiating matrix cracks. Several other sources for cracks were also present in the composite material such as, porosity, slag, pieces of fibres, the interweaving Ti strip and brittle second phases like silicon flakes and intermetallics. Once the cracks had nucleated, classical fatigue events then occurred in the ductile matrix at these sites, as a result of local stress concentration. These events depended on the fatigue stress range. Many striations on fatigue fracture surfaces were observed whose presence unambiguously defines that the failure was produced by fatigue.

After the crack nucleation stage, the subsequent crack growth was controlled by the elastic properties, flow strength, work hardening and microstructure characteristics of the matrix, and by the fibre-matrix interfacial bond strength. It was observed that when transverse fatigue cracks met intact fibres the cracks passed around them, either by branching

at the weak interface or alternatively, the stress concentration at the matrix crack tip was not sufficient to break the strong and thick fibres. The transverse cracks branching into cylindrical cracks might have had a detrimental effect when the cylindrical cracks met a weak spot in an intact fibre consequently leading to its fracture. It seems that the fatigue failure of the composite was due to an increase in the probability of fibre failure which in turn was related to crack propagation mode. When enough fibres had broken, the composite could no longer bear the load and a tensile fracture was entailed. This might have been the reason why the fatigue strength of the composite was closer to its tensile strength.

Conversely, the stiffness loss due to fatigue damage has been observed to be dependent on the properties of the matrix and on the interface strength. A four stage mechanism for the fatigue damage is proposed for the 0° fibre orientation material, based on experimental observation as follows:

Fibre breakage. Initially fibre fractures occurred during from the composite fabrication and specimen machining, subsequently occurring at random sites during the fatigue loading. The initial fibre breakage did not account for the stiffness loss once it was considered to be occurring during the first loading cycle. Any subsequent fibre failure implied in stiffness loss by damaging the matrix.

Fatigue crack initiation. Many fatigue cracks initiated at fibre ends, defects and second phase particles due to stress concentrations in the matrix that resulted from fibre breakage and matrix plastic flow. The overall matrix plastic flow occurred after a few fatigue cycles, and subsequently cyclic strain hardening might have restored the elastic behaviour. This stage might be associated with the plateau observed in the fractional change in elastic modulus.

Fatigue crack growth. The cracks propagated through the matrix, transversely and longitudinally, by shear or debonding along the fibre-matrix interface. These cracks might have appeared early in life and their microscopic growth then occurred over the most portion of the fatigue lifetime. This stage might have occurred during some part of the observed plateau stage in the fractional change in elastic modulus, and in which stiffness loss was not

detected, but it certainly corresponded to the stage where stiffness loss was observed. The occurrence of stiffness loss was dependent on the fatigue stress range.

Composite failure. The presence of matrix cracks and broken fibres finally create irregular planes of weakness which linked up to produce composite failure.

4.8 Summary

In this chapter results concerning the microstructural characterization prior to and after the mechanical properties evaluation of two series of composite material, which contained different fibre volume fractions, have been presented. The fatigue damage behaviour has been examined by uniaxial and off-axis tension-tension fatigue tests and the main findings have been presented.

The as received composite material showed a cast microstructure in which the presence of intermetallics Al-Fe-Si and Al-Fe-Si-Cr were found. The presence of such types of intermetallics were associated with molten aluminium alloy contamination during the composite manufacture. The absence of Mg in the aluminum alloy composite matrix was also attributed to the fabrication process. SEM was extensively used in the evaluation of the composite material microstructure, for energy dispersive chemical analyses, which helped to identify the macro constituents and to evaluate differences between the two series.

Results obtained by TEM showed that the interfaces between the SiC coating and the aluminium alloy matrix consisted of four main types. The first type was described as a product of contact between the SiC and the aluminium alloy. The second type of interface consisted of SiC and the free Si as twinned flakes. The third type of interface occurred between the SiC and the intermetallics. The fourth type of interface was observed to be an amorphous layer, probably graphitic carbon. It was observed that little reaction occurred between the SiC coating and the molten aluminium alloy. Basically, the interface consisted of a mechanical bond between the fibres and the matrix. The absence of general interface reactions, or alternatively the presence of weak interface led to very poor off-axis mechanical properties.

The fatigue testing characterization suggested that the composite 28% series, at 0° fibre orientation to the tensile axis was slightly sensitive to repeated tensile loading in the fibre direction. The large scatter in lifetime data was due to the complexity of damage development under cyclic loading and to large fabrication defects. For the 48% series, the fatigue tests showed that the material had a stronger sensitivity to cyclic tensile loading. It was also observed that both materials at 10° fibre orientation showed a significant decrease in fatigue strength, but the 48% series material revealed a higher decrease in fatigue strength.

The fatigue damage evaluation revealed that the observed stiffness loss was dependent on the stress range. For the 28% series material at stress range ΔS below 172 MPa the material is almost fatigue proof because very little damage was detected. For a stress range around 214 MPa, the fatigue stress-strain behaviour changed and stiffness loss due to fatigue damage was observed. For the 48% series, the material at stress range equals to 238 MPa did not show signs of stiffness loss but at stress range equal to 324 MPa there was a clear change in the fractional secant modulus.

A comparison between the shake down model and some experimental data showed that the calculated average shake down stress ranges were higher than the allowed stresses which did not cause stiffness loss in the type of composite used in this work.

Metallographic observations after fatigue testing showed that cracking occurred in the matrix of both 0° and 10° materials. Many fibre remained intact for much of the specimen fatigue life, bridging matrix fatigue cracks which were perpendicular to the tensile stress direction. It was observed that fatigue cracks usually initiate at free surfaces, but they also initiate inside the composite. Depending on the test stress range, the microcracks appeared early in life and their microscopic growth then took place over most of the fatigue lifetime. Because of the many possible sites for crack initiation, and a nonuniform matrix/fibre interface, irregular fatigue fracture surfaces have been encountered. Crack growth occurred both transversely and longitudinally as a consequence of different interfacial characteristics and fibre strength variation.

Dislocation density measurements by TEM on either tensile or fatigue tested specimens, revealed no general change when compared to the as received material. This means that the plastic deformation of the matrix material was inhomogeneous and highly concentrated around the fractured regions. It is worth remembering that the as received material had a high dislocation density and was considered to be in state similar to a cold worked material. The fatigued matrix showed the presence of prismatic loops and dislocation debris.

CHAPTER 5

CONCLUSIONS AND SUGGESTIONS FOR FURTHER WORK

5.1 Conclusions

From the experimental results described in the previous chapter, the following conclusions can be drawn regarding the fatigue damage of a liquid metal infiltrated composite material.

1. The liquid metal infiltration process used for the fabrication of the composite material utilized in this work poses certain restrictions on the use of cast alloys containing Mg, if it is desired to take advantage of the good castability of the Al-Si-Mg alloy and further strengthen the matrix by heat treatment through the precipitation of magnesium silicides

2. Contamination of the aluminium alloy matrix occurred during composite fabrication, increasing the number and type of intermetallics which were believed to have a detrimental effect upon the mechanical properties. The fabrication process also induced some reaction at the aluminium alloy SiC interface since the presence of aluminium carbide was observed.

3. The composite manufacturing process was basically the same for both series of material. Since different dies were used, microstructural evidences showed that the fabrication parameters were probably not kept constant, because different solidification rates seemed to have occurred during the fabrication of the two batches of composite material.

4. The observation of many deleterious defects highlighted the necessity of further optimization of fabrication parameters and a improvement of the process in order to enhance the mechanical properties of the current state-of-art composites, produced by liquid metal infiltration technique.

5. The fatigue behaviour of the composite material series 28% and 48% at 0° fibre orientation showed a little sensitivity to repeated tensile loading. This lack of stress sensitivity during fatigue is thought to be a consequence of fracture being controlled mainly by the fibre failure.

6. The fatigue damage evaluation showed that the stiffness loss due to fatigue damage was dependent on the stress range. It was demonstrated that when the strains at the matrix were kept below a certain level no stiffness loss due to cycling straining of the material occurred.

7. The fractional change in elastic modulus showed that if during a fatigue test the specimen is unloaded at zero stress and then reloaded to the previous stress level, the process leads to fatigue damage acceleration.

8. The calculated shake down limit was higher than the composite fatigue limit for both series. The allowed fatigue limit of the matrix material in the composite was lower than the measured aluminium alloy fatigue limit prior to infiltration.

9. The results showed that the allowable composite stress range in the shake down regime cannot be evaluated from the sole properties of the matrix. Thus, the shake down model did not safely predict fatigue damage stress ranges for the type of composite material produced by liquid metal infiltration technique.

10. The results suggested that the stiffness loss due to fatigue damage of the composite, is dependent on the characteristics of the matrix and on the interface strength.

11. Metallographic observations revealed that fatigue cracks initiated at the specimen surface due to broken fibres. Internally the fatigue cracks might have initiated at fibre ends, defects and brittle second phases.

12. Classical fatigue phenomena occurred after fatigue crack nucleation, and can be used for data interpretation since the presence of the fibres seemed not to have improved the fatigue properties of the matrix but just limited the plastic strain to which it was subjected.

13. The results led to the proposition of a four stage mechanism for the fatigue damage of an aluminium silicon matrix reinforced with silicon carbide coated boron fibres, at 0° fibre orientation to the tensile axis.

5.2 Suggestions for further work

The present research raised some aspects on the effect of the fatigue damage on the composite materials which might require further work. The following interrelated problems should be addressed in future work on composite materials produced by liquid metal infiltration technique.

1. The study of the fatigue damage and consequently stiffness loss in cross-plyed composites. More realistic composite materials would have reinforcements in the direction of the principal stresses. As such, the change in the stiffness loss due to fatigue damage would be a critical assessment parameter on cross-plyed composites, since it was observed that off-axis fatigue damage could imply in stiffness losses higher than 40%.

2. A study of SiC coated boron fibres composites made by liquid metal infiltration technique using different matrix alloys could also provide valuable information, since the influence of different matrix / different interfaces can lead to different fatigue damage behaviour.

3. A study of the effect of volume fraction on the fatigue stiffness loss for composites with equivalent matrix microstructures, through strict control of the fabrication parameters.

4. A study of heat treated composite materials should be entailed considering that sometimes matrix strengthening is desired, particularly in off-axis composites where the matrix properties plays a more important role in the composites mechanical properties.

References

- [1] ROBERTS, J. M. *The Pelican History of the World*. Revised Edition, Penguin, London, 1988. p. 74.
- [2] SAVAGE, G. Composite materials in Formula 1 racing. *Met. Mat.*, The Institute of Metals, Oct 1991, 7(10): p. 617.
- [3] BUCK, M. E. & SUPLINSKAS, R.J. Continuous boron fiber MMCs. In: *Engineered Material Handbook*. Vol. 1, Composites, ASM International, USA, 1987. 851-7.
- [4] SCHOENBERG, T. Boron and silicon carbide fibers. In: *Engineered Material Handbook*. Vol. 1 Composites, ASM International, USA, 1987. p. 58.
- [5] JOHNSON, W. S. Fatigue damage accumulation in various metal matrix composites. NASA Technical Memorandum 89116. Mar 1987. 1-66.
- [6] SUPLINSKAS, R. J. & MARZIK, J. v. Boron and silicon carbide filaments. In: MILEWSKI, J. V. & KATZ, H. S., eds. *Handbook of Reinforcements for Plastics*. Van Nostrand, New York, 1987. 340-63.
- [7] MORLEY, J. G. *High-Performance Fibre Composites*. Academic, 1987. 39-45.
- [8] WAWNER Jr., F. E. Boron filaments. In: BROUTMAN, L. J. & KROCK, R. H., eds. *Modern Composite Materials*. Addison-Wesley, 1967. 244-69.
- [9] VEGA-BOGIO, J. & VINGSBO, O. Radial cracks in boron fibres. *J. Mat. Sci.* 1977, 12: 2519-24.
- [10] HERRING, H. W. Selected mechanical and physical properties of boron filaments. NASA TN D-3202. Quoted by: ZWEBEN, C. Tensile strength of fiber-reinforced composites: basic concepts and recent developments. In: *Composite Materials: Testing and Design*. ASTM STP 460, 1969. p. 569.
- [11] TETELMAN, A. S. Fracture process in fiber composite materials. In: *Composite Materials: Testing and Design*. ASTM STP 460, 1969. p. 482.
- [12] LANZA, F. Statistical evaluation of the strength of composite materials. In: PIATTI, G., ed. *Advances in Composite Materials*. Applied Science, London, 1978. p. 234.
- [13] METCALFE, A. G. Influence of interactions on fracture of metal matrix-filament composites. In: Monsanto Symp. on . . . , Oct 1967. Quoted by: TETELMAN, A. S. Fracture process in fiber composite materials. In: *Composite Materials: Testing and Design*. ASTM STP 460, 1969. p. 482.
- [14] KREIDER, K. G. & PREWO, K M. Boron reinforced aluminum. In: KREIDER, K. G., ed. *Metallic Matrix Composites*. Vol. 4, Academic, New York, London, 1974. 399-471.
- [15] LEIS, H. O. & PETERS, P. Comparison between B₄C/Boron and SiC/boron reinforced aluminium. In: BUNSEL, A. R., BATHIAS, C., MARTRENCAR, A., MENKES, D., VERCHERY, G., eds. *Advances in Composite Materials*. Vol. 2, Pergamon, 1980. p. 1101.
- [16] BASHE, M.; FANTI, R.; GALASSO, F. Preparation and properties of silicon carbide coated boron filaments. *Int. Fiber Sci. and Tech.*, 1968. 1:1. Quoted by: KREIDER, K. G. & PREWO, K M. Boron reinforced aluminum. In: KREIDER, K. G., ed. *Metallic Matrix Composites*. Vol. 4, Academic, New York and London, 1974. 399-471.
- [17] ISEKI, T.; KAMEDA, T.; MARUYAMA, T. Interfacial reactions between SiC and aluminium during joining. *J. Mat. Sci.*, 1984, 19:1692-8.
- [18] HANCOCK, J. R. Fatigue of metal-matrix composites. In: BROUTMAN, L. J., ed. *Fracture and Fatigue*. Vol. 5, Academic, New York and London, 1974. 371-414.
- [19] KREIDER, K. G.; DARDI, L. E.; PREWO, K. M. Metal Matrix Composite Technology. Technical Report AFML-TR 71-204, Dec 1971. p. 4.

- [20] MAH, T.; HECHT, N. L.; McCULLUM, D. E.; HOENIGMAM, J. R.; KIM, H. M.; KATZ, A. P.; LIPSITT, H. A. Thermal stability of SiC fibres (Nicalon®). J. Mat. Sci., 1984, 19: 1191-201.
- [21] POLMEAR, I. J. *Light Alloys, Metallurgy of the Light Metals*. 2nd Ed., Edward Arnold, 1989. p. 39, 144-59.
- [22] MONDOLFO, L. F. *Aluminum Alloys: Structure and Properties*. Butterworths, 1976. 759-87.
- [23] ELLIOT, R. *Eutectic Solidification Processing Crystalline and Glassy Alloys*. Butterworths, 1983. 157-88.
- [24] RIVLIN, V. G. & RAYNOR, G. V. Critical evaluation of constitution of aluminium-iron-silicon system. Int. Met. Rev., 1981, No 3, 133-52.
- [25] BENDERSKI, L. A.; McALISTER, A. J.; BIANCANELLO, F. S. Phase transformation during annealing of rapidly solidified Al-rich Al-Fe-Si alloys. Metall. Trans. A, 1988, 19A: 2893-900.
- [26] PING LIU & DUNLOP G. L. Long-range ordering of vacancies in bcc α -AlFeSi. J. Mat. Sci., 1988, 23: 1419-24.
- [27] JENSEN, C. L. & WYSS, R. K. Electron diffraction study of α - and α_T -AlFeSi. Metall. Trans. A, 1988, 19A: 893-8.
- [28] DIX Jr., E. H. & HEATH Jr., A. C. Equilibrium relations in aluminum-silicon and aluminum-iron-silicon alloys of high purity. Proc. Inst. Metals Div., AIME, 1928, 78: 164-97.
- [29] IGLESSIS, J.; FRANTZ, C.; GANTOIS, M. Mém. Sci. Rev. Métall., 1977, 73 [4]: 237-42. Quoted by: RIVLIN, V. G. & RAYNOR, G. V. Critical evaluation of constitution of aluminium-iron-silicon system. Int. Met. Rev., 1981, No 3, 133-52.
- [30] MUNSON, D. A clarification of the phases occurring in aluminium-rich aluminium-iron-silicon alloys, with particular reference to the ternary phase α -AlFeSi. J. Inst. Met., 1967, 95: 217-9.
- [31] TRUMPER, R. L.; SHERWOOD, P. J.; CLIFFORD, A. W. Metal matrix composites. In: THE ROYAL AERONAUTICAL SOCIETY, Material in Aerospace. Proc. conf. on...., London 2-4 Apr. vol. 2, 1986. 249-78.
- [32] MIKURA, N. Metal matrix composites - present applications and future potential. In: THE INSTITUTE OF METALS, Abstracts conf. on.. London, 23-24 Nov. 1987. 7/1-3.
- [33] Information leaflet: CRAY ADVANCED MATERIALS Ltd., Yeovil, Somerset, England.
- [34] GUNCOR, M. N.; CORNIE, J. A.; FLEMINGS, M. C. The response of microstructures of metal matrix composites to solidification time. In: DHINGRA, A. K. & FISHMAN, S. G., eds. *Interfaces in Metal Matrix Composites*. AIME, 1986. 121-35.
- [35] FLEMINGS, M. C.; MORTENSEN, A.; CORNIE, J. A. Solidification of infiltrated metal matrix composites. Metall. Sci. and Tech., 1987, 5(1): 3-10.
- [36] KELLY, A. & DAVIES, G. J. The principle of the fibre reinforcement of metals. Metall. Rev., 1965, 10: 1-77.
- [37] PRIESTNER, R. Metal matrix Composites. Institution of Chemical Engineers, North Western Branch Papers, Mar 1988, 3.1-20.
- [38] McDANIELS., D. L.; JECK, R. W.; WEETON, J. W. Analysis of stress-strain behavior of tungsten-fiber-reinforced copper composites. Trans. AIME, 1965, 233: p. 636.
- [39] STUHRKE, W. F. The mechanical behavior of aluminum-boron composite material. In: HERZOG, J. A., ch. *Metal Matrix Composites*. ASTM STP 438, 1968. 108-33.

- [40] HUGHES, E. J. & RUTHERFORD, J. L. Microstrain in continuously reinforced tungsten copper composites. In: *Composite Materials: Testing and Design*. ASTM STP 460, 1969. 562-72.
- [41] LAWLEY, A. & KOCZAK, M. J. Role of the interface on elastic-plastic composite behavior. In: METCALFE, A. G. ed. *Interfaces in Metal Matrix Composites*. Academic, 1974. 211-43.
- [42] CRATCHLEY, D.; BAKER, A. A.; JACKSON, P. W. Mechanical behavior of a fiber reinforced metal and its effect upon engineering applications. In: HERZOG, J. A., ch. *Metal Matrix Composites*. ASTM STP 438, 1968. 169-82.
- [43] PINEL, M. R.; HAY, D. R.; LAWLEY, A. Microstrain behavior of metal-matrix composites. In: HERZOG, J. A., ch. *Metal Matrix Composites*. ASTM STP 438, 1968. 95-107.
- [44] STOWELL, E. Z. & LIU, T. S. On the mechanical behaviour of fibre-reinforced crystalline materials. *J. Mech. Phys. Sol.* 1961, 9: 242-260.
- [45] AZZI, V. D. & TSAI, S. W. Anisotropic strength of composites. *Exper. Mech.* Sept 1965, 283-8.
- [46] PETRASEK, D. W. & SIGNORELLI, R. A. Factors affecting tensile properties of discontinuous fiber composites. NASA TN D 3886, 1967. Quoted by: METCALFE, A. G. Introduction and review. In: METCALFE, A. G. ed. *Interfaces in Metal Matrix Composites*. Vol. 1, Academic, 1974. 1-30.
- [47] COX, H. L. The elasticity and strength of paper and other fibrous materials. *Brit. J. Appl. Phys.*, 1952, 3: 72-9.
- [48] HULL, D. *An Introduction to Composite Materials*. Cambridge University Press, 1981. 135-42.
- [49] COOK, J. & GORDON, J. E. A mechanism for the control of crack propagation in all-brittle systems. *Proc. Royal Soc. London*, 1964, 282(A): 508-20.
- [50] METCALFE, A. G. Introduction and review. In: METCALFE, A. G. ed. *Interfaces in Metal Matrix Composites*. Vol. 1, Academic, 1974. 1-30.
- [51] KLEIN, M. J. Effect of the filament - matrix interface on off-axis tensile strength. In: METCALFE, A. G. ed. *Interfaces in Metal Matrix Composites*. Vol. 1, Academic, 1974. 169-209.
- [52] MILEIKO, S. T. Fabrication of metal-matrix composites. In: KELLY, A. & MILEIKO, S. T. eds. *Fabrication of Composites*. Vol. 4, 1983. 221-94.
- [53] METCALFE, A. G. & KLEIN, M. J. Effect of the interface on longitudinal tensile properties. In: METCALFE, A. G. ed. *Interfaces in Metal Matrix Composites*. Vol. 1, Academic, 1974. 125-67.
- [54] COOPER, G. A. & KELLY, A. Role of the interface in the fracture of fiber composite materials. In: *Interfaces in Composites*. ASTM STP 452, 1968. 90-106.
- [55] EBERT, L. J. & WRIGHT, P. K. Mechanical aspects of the interface. In: METCALFE, A. G. ed. *Interfaces in Metal Matrix Composites*. Vol. 1, Academic, 1974. 31-123.
- [56] METCALFE, A. G. Interaction and fracture of titanium-boron composites. *J. Comp. Mater.*, 1967, 1: 356-65.
- [57] HUNT Jr., W. H. Interfacial zones and mechanical properties in continuous fiber FP/Al-Li metal matrix composite. In: DHINGRA, A. K. & FISHMAN, S. G. eds. *Interfaces in Metal Matrix Composites*. AIME, 1986. 3-25.
- [58] PREWO, K. M. & MCCARTHY, G. Interfacial characteristics of silicon carbide-coated boron-reinforced aluminium matrix composites. *J. Mat. Sci.*, 1972, 7: 919-28.
- [59] NUTT, S. R. Interfaces and failure in Al-SiC composites. In: DHINGRA, A. K. & FISHMAN, S. G. eds. *Interfaces in Metal Matrix Composites*. AIME, 1986. 157-67.

- [60] YANG, M.; SCOTT, V. D.; TRUMPER, R. L. The role of interface on the mechanical behaviour of carbon fibre reinforced aluminium alloy composite. In: THE INSTITUTE OF METALS, Abstracts conf. on... London, 8-9 Nov, 1989. J.1-4.
- [61] CALOW, C. A. & MOORE, A. Are metal matrix composites viable? In: INSTITUTION OF METALLURGISTS, Practical Metallic Composites, Spring Meeting 22-25 Mar, Palma, Majorca, 1974. B17-25.
- [62] PUSKÁR, A. & GOLOVIN, S. A. *Fatigue in Materials: Cumulative Damage Process*. Materials Science Monographs, No 24, Elsevier, 1985. p. 13, 197, 281.
- [63] PLUMBRIDGE, W. J. & RYDER, D. A. The metallography of fatigue. Metall. Rev. 1969, 119-42.
- [64] FORSYTH, P. J. E. Fatigue damage and crack growth in aluminium alloys. Acta Met. 1963, II: 703-15.
- [65] SMALLMAN, R. E. *Modern Physical Metallurgy*. 4th Ed., Butterworths, 1985. 465, 316.
- [66] WOOD, W. A. *Treatise in Materials Science and Technology*. HERMAN, H. ed., vol. 5, Academic, New York, 1974. p. 129.
- [67] MAY, A. N. A model of metal fatigue. Nature, Jan 30, 1960, 185: 303-4.
- [68] WOOD, W. A. Formation of fatigue cracks. Phil. Mag., 1958, 3: 692-9.
- [69] LAIRD, C. Influence of metallurgical structure on the mechanism of fatigue crack propagation. In: *Fatigue Crack Propagation*. ASTM STP 415, 1967. p. 139.
- [70] FELTNER, C. E. & LAIRD, C. Factors influencing the dislocation structures in fatigued metals. Trans. AIME, July, 1968, 242: 1253-7.
- [71] SEGALL, R. L. & PARTRIDGE, P. G. Dislocation arrangements in aluminium deformed in tension or by fatigue. Phil. Mag., 1959, 4: 912-9.
- [72] HANCOCK, J. R. & GROSSKREUTZ, J. C. Mechanisms of fatigue hardening in copper single crystals. Acta Met., Febr 1969, 17: 77-97.
- [73] BOLLER, K. H. Fatigue fundamentals for composite materials. In: *Composite Materials: Testing and Design* ASTM STP 460, 1969. 217-35.
- [74] HARRIS, B. *Engineering Composite Materials*. The Institute of Metals, 1986. p. 81.
- [75] KIM, R. Y. Fatigue strength. In: *Engineered Material Handbook.. Vol. 1, Composites*, ASM International, USA, 1987. 436-44.
- [76] STINCHCOMB, W. W.; REIFSNIDER, K. L.; MARCUS, L. A.; WILLIAMS, R. S. Effects of frequency on the mechanical response of two composite materials to fatigue loads. In: HANCOCK, J. R., ch. *Fatigue of Composite Materials*. ASTM STP 569, 1975. 115-29.
- [77] SALKIND, M. J. Fatigue of composites. In: *Composite Materials: Testing and Design*. ASTM STP 497, 1972. 143-69.
- [78] SIMS, D. F. & BROGDON, V. H. Fatigue behavior of composites under different loading modes. In: REIFSNIDER, K. L. & LAURAITIS, K. N., eds. *Fatigue of Filamentary Composite Materials*. ASTM STP 636, 1977. 185-205.
- [79] CHRISTIAN, J. L. Axial fatigue properties of metal matrix composites. In: HANCOCK, J. R., ch. *Fatigue of Composite Materials*. ASTM STP 569, 1975. 280-94.
- [80] LEDDET, I. & BUNSELL, A. R. Fatigue damage in boron-aluminium. In: TSAI, S. W., ed. *Composite Materials: Testing and Design*. ASTM STP 674, 1979. 581-96.

- [81] GOUDA, M. ; PREWO, K. M.; McEVILY, A. J. Mechanisms of fatigue in boron-aluminium composites. In: LAURAITIS, K. N., ch. *Fatigue of Fibrous Composite Materials*. ASTM STP 723, 1981. 101-15.
- [82] TOTH, I. J. Creep and fatigue behavior of unidirectional and cross-plyed composites. In: *Composite Materials: Testing and Design*. ASTM STP 460, 1969. 236-53.
- [83] MENKE, G. D. & TOTH, I. J. Tech. Rep. AFML-TR 70-174, 1970. Quoted by: HANCOCK, J. R. Fatigue of metal-matrix composites. In: BROUTMAN, L. J., ed. *Fracture and Fatigue*. Vol. 5, Academic, New York and London, 1974. 371-414.
- [84] SHIMIZU, H. & DOLOWY Jr., J. F. Fatigue testing and thermal-mechanical treatment effects on aluminium-boron composites. In: *Composite Materials: Testing and Design*. ASTM STP 460, 1969. 192-202.
- [85] SALKIND, M. & PATARINI, V. Fatigue of boron filament. Communications, Trans. AIME, Aug 1967, 239: p. 1268.
- [86] AMERICAN SOCIETY FOR METALS. Properties and selection of nonferrous alloys and pure metals. In: *Metals Handbook*, Ninth Ed., vol. 2, 1989. p. 166.
- [87] SMITH, T. R. & OWEN, M. J. Proc. 6th Intern. Reinforced Plastic Congress, London, 1968, paper 27. Quoted by: HARRIS, B. *Engineering Composite Materials*. The Institute of Metals, 1986. p. 82.
- [88] DVORAK, G. J. & JOHNSON, W. S. Fatigue of metal matrix composites. Int. J. of Fracture. 1980, 16: 585-607.
- [89] JOHNSON, W. S. Modelling stiffness loss in boron/aluminum laminates below the fatigue limit. In: O'BRIEN, T. K., ed. *Long Term Behavior of Composites*. ASTM STP 813, 1983. 160-76.
- [90] CHAREWICZ, A. & DANIEL, I. M. Damage mechanisms and accumulation in graphite/epoxy laminates. In: HAHN, H. T., ed. *Composite Materials: Fatigue and Fracture*. ASTM STP 907, 1986. 274-96.
- [91] KASEN, M. B.; SCHRAMM, R. E.; READ, D. T. Fatigue of composites at cryogenic temperatures. In: REIFSNIDER, K. L. & LAURAITIS, K. N., eds. *Fatigue of Filamentary Composite Materials*. ASTM STP 636, 1977. 141-51.
- [92] SYMONDS, P. S. Shakedown in continuous media. J Appl. Mech., Mar 1951, 85-9.
- [93] MELAN, E. Der Spannungszustand eines "Hencky-Mises'schen" Kontinuums bei veraenderlicher Belastung. Sitz. Ak. Wiss. Wien, 1938, 147:73-87. Quoted by: SYMONDS, P. S. Shakedown in continuous media. J Appl. Mech., Mar 1951, 85-9.
- [94] TARN, J. Q.; DVORAK, G. J.; RAO, S. M. Shakedown of unidirectional composites. Int. J. Solids Struc., 1975, 11: 751-64.
- [95] DVORAK, G. J. & TARN, J. Q. Fatigue and shakedown in metal matrix composites. In: *Fatigue of Composite Materials*. ASTM STP 569, 1975. 145-68.
- [96] VAN HORN, K. R. *Aluminum*. Vol. 1, ASM 1967. p. 183.
- [97] JOHNSON, W. S. & WALLIS, R. R. Fatigue behavior of continuous-fiber silicon carbide/aluminum composites. In: HAHN, H. T., ed. *Composite Materials: Fatigue and Fracture*. ASTM STP 907, 1986. 161-75.
- [98] LANKFORD, J. Effect of oxide inclusions on fatigue failure. Int. Met. Rev. Sep 1977, 221-8.
- [99] GANGULEE, A. & GURLAND, J. On the fracture of silicon particles in aluminum-silicon alloys. Trans. AIME, Feb 1967, 239: 269-72.

- [100] FREDERICK, S. F. & BAILEY, W.A. The relation of ductility to dendrite cell size in a cast Al-Si-Mg alloy. Trans. AIME, Oct 1968, 242: 2063-7.
- [101] GURLAND, J. Fracture of metal-matrix particulate composites. In: BROUTMAN, L. J., ed. *Fracture and Fatigue*. Vol. 5, Composite Materials, Academic, 1974. 45-91.
- [102] STEEN, A. H. & HELLAWELL, A. Structure and properties of aluminium-silicon eutectic alloys. Acta Met., 1972, 20:363-70.
- [103] BRANDES, E. A., ed. *Smithells Metals Reference Book*. 6th Ed., Butterworth, 1983. 22.2, 15.3.
- [104] AMERICAN SOCIETY FOR TESTING MATERIALS. Standard Specification for Aluminum Alloys in Ingot Form for Sand Castings, Permanent Mold Castings, and Die Castings, Apr 25 1986. (ASTM B 179-86). In: 1989 Annual Book of ASTM Standards, section 2: Nonferrous Metal Products, vol. 02.02: Die Cast Metals: Aluminum and Magnesium Alloys. 117-121.
- [105] HUGHES, J. D. H. A review of techniques for evaluating stiff fibres. Br. Ceram. Trans. J., 1988, 87: 181-88.
- [106] AMERICAN SOCIETY FOR TESTING MATERIALS. Standard Practice for Conducting Constant Amplitude Axial Fatigue Tests of Metallic Materials. Jun 25, 1982. (ASTM E 466-82). In: 1989 Annual Book of ASTM Standards, section 3: Metals Test Methods and Analytical Procedures, vol. 03.01: Metals-Mechanical Testing: Elevated and Low-Temperature Tests; Metallography. p. 540.
- [107] TAYA, M. & ARSENAULT, R. J. *Metal Matrix Composites*. Pergamon, 1989. 245-246.
- [108] JOINT COMMITTEE ON POWDER DIFFRACTION STANDARDS. 'JCPDS' Set 39. International Centre for Diffraction Data, 1990.
- [109] HANAWALT, J. D. Manual search/match methods for powder diffraction in 1986. In: JENKINS, R., ed. *Methods & Practices in X-ray Powder Diffraction*. JCPDS, 1986. 10.1.1-8.
- [110] FEEST, E. A. Automated EPMA techniques applied to microstructures. In: THE METALS SOCIETY Solidification Technology in the Foundry and Cast House. Proc. conf., 15-17 Sept 1980, Coventry, UK. 188-194.
- [111] EDAX 91100 System
- [112] CLIFF, G.; POWELL, D. J.; PILKINGTON, R.; CHAMPNESS, P. E.; LORIMER, G. W. X-ray microanalysis of second phase particles in thin foils. Inst. Phys. Conf. Ser. No 68: Chapter 3, paper presented at EMAG, Guilford, 30 Aug-2 Sep, 1983, UK. 63-6.
- [113] HAM, K. R. The determination of dislocations densities in thin films. Phil. Mag., 1961, 6: 1183-4.
- [114] CLIFF, G. & LORIMER, G. W. The quantitative analysis of thin specimens. J. Microscopy, Mar 1975, 103:203-7.
- [115] MEHTA, S.; GOLDSTEIN, J. I.; WILLIAMS, D. B.; ROMIG Jr., A.D. Determination of Cliff-Lorimer k calibration factors for thin-foil X-ray microanalysis of Na, Mg, and Al in the STEM. In: NEWBURY, D. E., ed. *Microbeam Analysis*. San Francisco Press, San Francisco, 1979. 119-23.
- [116] NUTT, S. R. & WAWNER, F. E. Silicon carbide filaments: microstructure. J. Mat. Sci., 1985, 20:1953-60.
- [117] SAGEESE, M. E; SCOTT, V. D.; TRUMPER, R. L. Characterization of interfaces in Al-Zn-Mg alloy reinforced with Sicabo fibres. Mat. Sci. and Tech., Oct 1988, 4:871-5.
- [118] FLEWITT, P. E. J. & WILD, R. K. *Microstructural Characterization of Metals and Alloys*. The Institute of Metals, London, 1986. p. 12.
- [119] HERTZBERG, R. W. *Deformation and Fracture Mechanics of Engineering Materials*. Third Ed., John Wiley, 1989. p. 111.

- [120] DIETER, G. E. *Mechanical Metallurgy*. Third Ed., McGraw-Hill 1986. p. 139.
- [121] ARSENAULT, R. J. & FISHER, R. M. Microstructure of fiber and particulate SiC in 6061 Al composites. *Scrp. Metall.*, 1983, 17:67-71.
- [122] HANCOCK, J. R. & GROSSKREUTZ, J. C. Plastic yielding and strain distribution in filament-reinforced metals. In: HERZOG, J. A., ch. *Metal Matrix Composites*. ASTM STP 438, 1968. 134-49.
- [123] VOGELGANG, M.; ARSENAULT, R. J.; FISHER, R. M. An in situ HVEM study of dislocation generation at Al/SiC interfaces in metal matrix composites. *Metall. Trans. A*, 1986, 17A: 379-89.
- [124] DUPUOY, G. Megavolt electron microscopy. In: SWANN, P. R.; HUMPHREYS, C. J.; GORINGE, M. J., eds. Proc. 3rd Int. Conf on HVEM. Academic, London, 1974. p. 447. Quoted by: VOGELGANG, M.; ARSENAULT, R. J.; FISHER, R. M. An in situ HVEM study of dislocation generation at Al/SiC interfaces in metal matrix composites. *Metal. Trans. A*, 1986, 17A: 379-89.
- [125] CORTEN, H. T. Micromechanics and fracture behavior of composites. In: BROUTMAN, L. J. & KNOCK, R. H., eds. *Modern Composite Materials*. Addison-Wesley, 1967. 27-105.
- [126] ANDERSSON, C. H. & WARREN, R. The strength and elastic modulus of multifilament SiC fibres. In: BUNSEL, A. R., BATHIAS, C., MARTRENCAR, A., MENKES, D., VERCHERY, G., eds. *Advances in Composite Materials*. Vol. 2, Pergamon, 1980. 1129-39.
- [127] SIEMERS, P. A.; MEHAN, R. L.; MORAN, H. A comparison of the uniaxial tensile and pure bending strength of SiC filaments. *J. Mat. Sci.*, 1988, 23: 1329-33.

TABLE 1

PHASES, COMPOSITIONS [wt%] AND CRYSTALLOGRAPHIC DATA FOR TERNARY SOLID PHASES IN Al-Fe-Si SYSTEM^[24]

phase	formula	Al	Fe	Si	symmetry and lattice spacing, nm
τ_2	35.3	12.8	cubic a = 1.603
	33-38	13-18.5	monoclinic a = 1.78 ± 0.01 b = 1.025 ± 0.005 c = 0.890 ± 0.005 $\beta = 132^\circ$
τ_4	Al ₄ FeSi ₂	47.08	27.04	25.01	tetragonal a c 0.616 0.949
	0.612 0.948
	Al ₃ FeSi ₂	0.607 0.950
	Al ₅₇ Fe ₁₅ Si ₂	0.630 0.941
	Al ₄₇ Fe ₁₅ Si ₃	0.612 0.953
τ_5	Al ₂₀ Fe ₅ Si ₂	62.4	31.9	5.6	cubic a = 1.2548
	a = 1.256 (138 atoms/cell)
	~ 32.5	8.4-10.3	hexagonal a = 1.23 ± 0.01 c = 2.62 ± 0.02
τ_6	Al ₉ Fe ₂ Si ₂	58.2 59.3	27.4 27.2	13.6 13.5	monoclinic a b c β 0.612 0.612 4.15 91°
	26.9	15.2	0.611 0.611 4.14 91°
	Al ₉ Fe ₂ Si ₂	...	27.2	13.7	tetragonal a = 0.618 ± 0.006 c = 4.25 ± 0.05

(...) not determined.

TABLE 2

AXIAL FATIGUE RATIOS [FL/UTS] FOR BORON FIBRES ALUMINIUM ALLOYS COMPOSITES.

Material ^(a)	Ultimate tensile strength UTS MPa	Stress ratio R	Ratio of fatigue limit to UTS (FL/UTS) ^(c)	Ref.
6061-O ^(b) Al	152	0.2	0.73	[82]
60% V _f B ^(d)	1952	0.4	0.71	[83]
50% V _f B	1159	0.1	0.69	[79]
48.7% V _f B (0.142 mm diam.)	1372	0.1	0.66	[79]
40% V _f B	1138	0.1	0.50	[84]
40% V _f B (0.142 mm diam.)	1186	0.2	0.52	[18]
40% V _f B	1248	0.4	0.75	[83]
25% V _f B	724	0.2	0.63	[82]
22% V _f B	579	0.2	0.56	[84]
47.3% V _f B-SiC ^(e) (0.107 mm diam.)	1159	0.1	0.85	[79]
40% V _f B-SiC (0.145 mm diam.)	1014	0.2	0.57	[18]
20% V _f B 2024-O Al	...	0.2	0.42	[82]
25% V _f B 1100 Al	...	0.2	0.76	[82]

a) The matrix is aluminum alloy 6061-O except where otherwise noted.

b) The alloy and composite are as fabricated.(furnace cooled).

c) fatigue limit for number of cycles $\geq 10^6$ - 10^7 .

d) fibre diameter 0.102 mm except where otherwise noted.

e) SiC coated boron fibre.

(...) not determined.

TABLE 3

CHEMICAL COMPOSITION OF ALUMINIUM ALLOYS (wt%).

	Si	Mg	Fe	Cu	Mn	Zn	Ti	
ASM A356.2	6.5 7.5	0.30 0.45	0.13 0.25	0.10	0.05	0.05	0.20	<i>b</i>
BS 2L 99 (nominal)	7.0	0.4						
present alloy prior to infiltration	7.83	0.33	0.14	-	0.01	0.01	0.07	

b) 0.05 max others (each); 0.15 others(total); rem. Al.
(-) nil

TABLE 4

X-RAY DIFFRACTION DATA OF SiC COATED BORON FIBRE AND IDENTIFIED PHASES.

d-spacing ^a	I ^b	β-SiC 29.1129 ^c	W ₂ B ₅ 30.1385	WB ₄ 19.1375	δ-WB 35.738	boron (TEM)	β-SiC (TEM)
0.44	s					0.435	
0.37	m			0.367			
0.345	m		0.347				
0.340	vw						
0.319	m			0.317	0.3063		
0.275	vw				0.2727		
0.260	s		0.2584			0.256	
0.253	vs	0.252	0.2541				0.253
0.228	vw		0.2256		0.2292		
0.212	w	0.218	0.2073	0.212	0.2133	0.212	0.219
0.200	s			0.201			
0.190	m		0.1891	0.1911	0.1909		
0.175	vw				0.1736		
0.165	w				0.1644		
0.154	m	0.15411		0.1540	0.1558		0.154
0.150	s		0.1492	0.1501		0.150	
0.137	m		0.1370	0.1356			
0.136	m			0.1353	0.1353		
0.132	m	0.13140	0.1324	0.1325	0.1341		0.131
0.129	m				0.1288		
0.125	vw	0.12583	0.1225	0.1254			0.126
0.121	w			0.1202			
0.118	vw						
0.114	m					0.114	
0.108	w	0.10893		0.1090		0.109	0.109
		0.09748				0.091	0.099
		0.08895				0.089	0.089
		0.08387					0.084

- a) All d-spacing are in nm.
 b) Intensity visual estimation.
 c) 'JCPDS' card number.

TABLE 5

CHEMICAL COMPOSITION OF ALUMINIUM MATRIX ALLOY
AND COMPOSITE MATERIAL (wt%).

sample	analyses	Si	Fe	Cr	Mg	Zn	Cu	Ni	Ti	Pb	Mn	Sn
matrix	prior to infiltration	7.83	0.35	0.01	-	0.01	0.06	0.01	-	-
Al/B2	composite	9.94	0.91	0.08	0.20
Al/B2	portion without fibres	6.64	0.25	0.05	0.23
Al/B4	A	9.46	1.02	...	0.28
Al/B4	B	...	0.72	0.08	0.29	...	0.05	0.01
Al/B4	C	5.75	0.30	0.08	0.32
Al/B4	control sample	8.88	0.54	0.06	0.29	0.04
Al/B8	A	9.97	1.15	0.09	0.06
Al/B8	B	10.41	0.92	0.04	0.04	...	0.07	0.06
Al/B8	C	7.40	0.49	0.09	-
Al/B8	control sample	8.35	1.02	0.03	0.04	0.05

(-) nil

(...) not measured.

TABLE 6

EDS CHEMICAL COMPOSITION OF SECOND PHASES SERIES 28% (at%).

	Al	Si	Fe	Cr	Ni	V
platelet type (SEM)	67	18	15	-	...	-
globular type (SEM)	71	12	15	2
platelet type (TEM)	67.1±1.4 ^a	17.2±0.4	15.4±0.8	-	0.3	-
globular type (TEM)	71.5±1.2	12.8±1.8	13.7±1.6	1.3±0.9	0.5	0.2

a) indicated errors are standard deviation from the results.

(-) nil

(...) not determined.

TABLE 7

MECHANICAL PROPERTIES OF MATRIX PRIOR TO INFILTRATION, MATRIX INFILTRATION CONDITION AND COMPOSITE MATERIALS AT DIFFERENT FIBRE ORIENTATIONS.

material properties	V _f (%)	Y _{0.1} (MPa)	UTS (MPa)	E (GPa)	ε _t (%) ^a	ε _p (%) ^b
aluminium alloy		64±1 ^c	127±12	70		3.1±2.4
matrix 28%		59±7	123±4	69		1.1±0.5
28 - 0°	29±4		379±91	164±9	0.37±0.07	0.11±0.07
28 - 10°	29±4		281±7	158±11	0.43±0.10	0.23±0.09
28 - 90°			37	101	0.04	0.01
48 - 0°	45±3		661±37	218±6	0.32±0.05	0.05±0.02
48 - 10°	45±3		171	205±11	0.9	0.5
48 - 90°			26	134	0.03	0.01

a) total deformation at fracture (plastic plus elastic).

b) plastic deformation only.

c) indicated errors are standard deviation from the results.

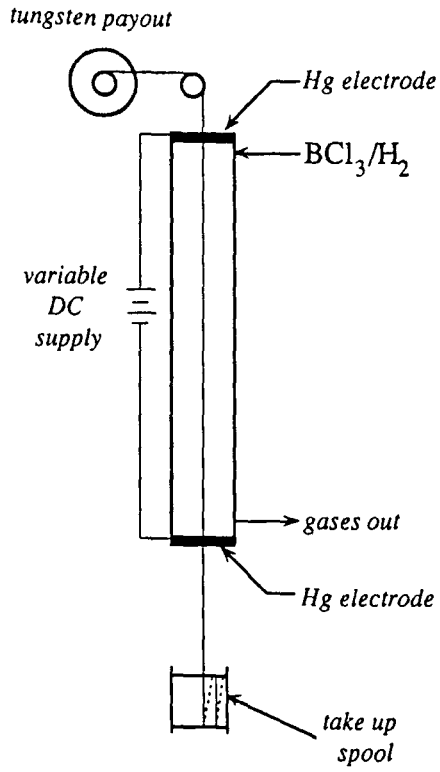


Fig.1 Schematic diagram of a boron fibre deposition reactor [6].

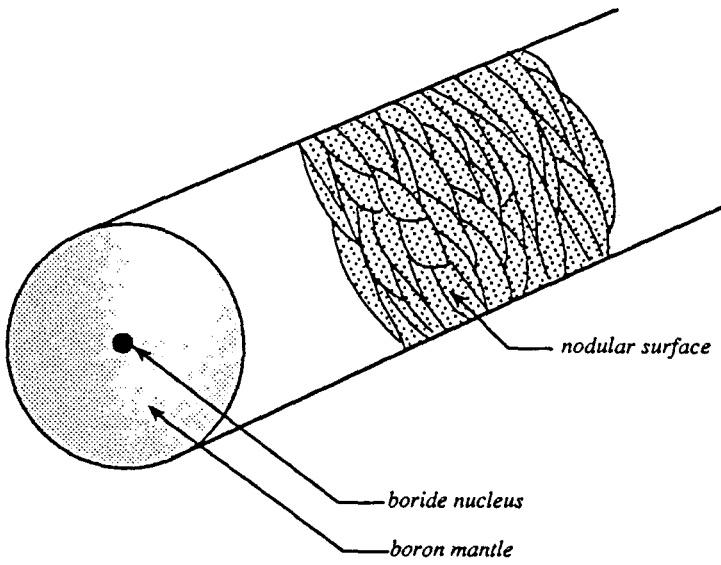


Fig.2 Schematic diagram of a boron fibre [8].

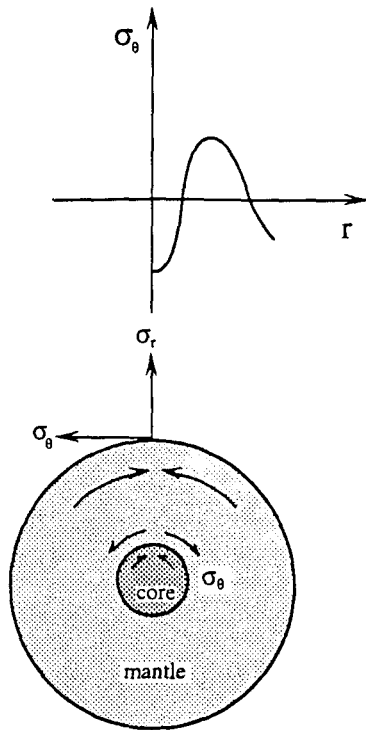


Fig.3 Schematic residual stress pattern in the cross section of a boron fibre [9].

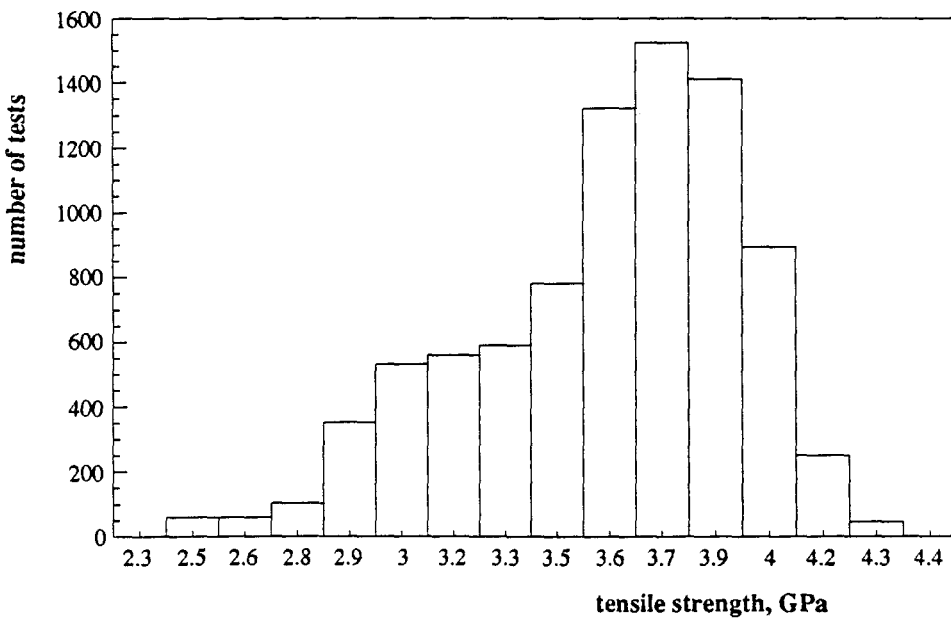


Fig.4 Typical histogram of boron fibre tensile strengths [4].

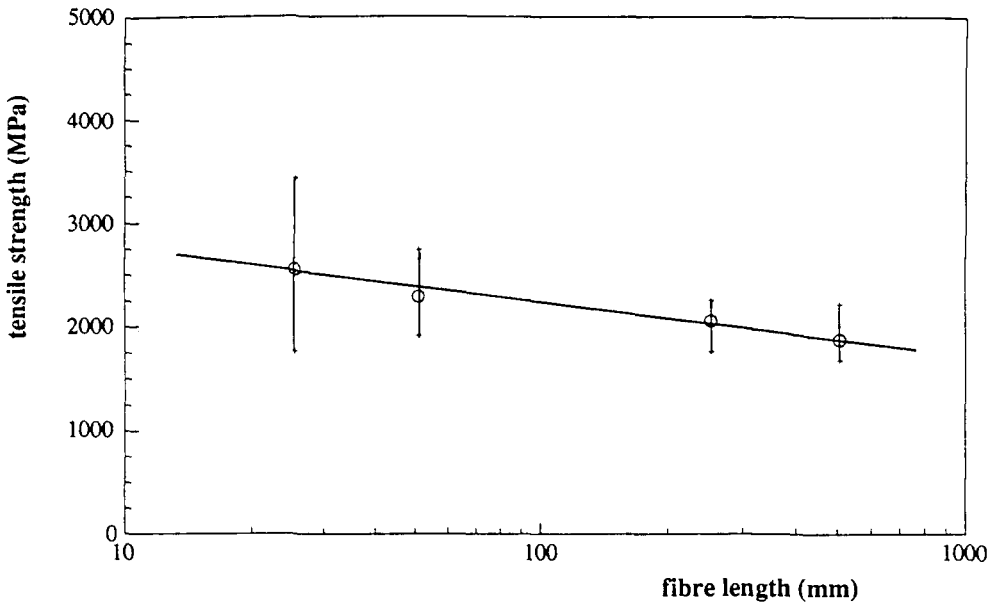


Fig.5 Variation of the mean tensile strength of boron fibres as function of their length [10].

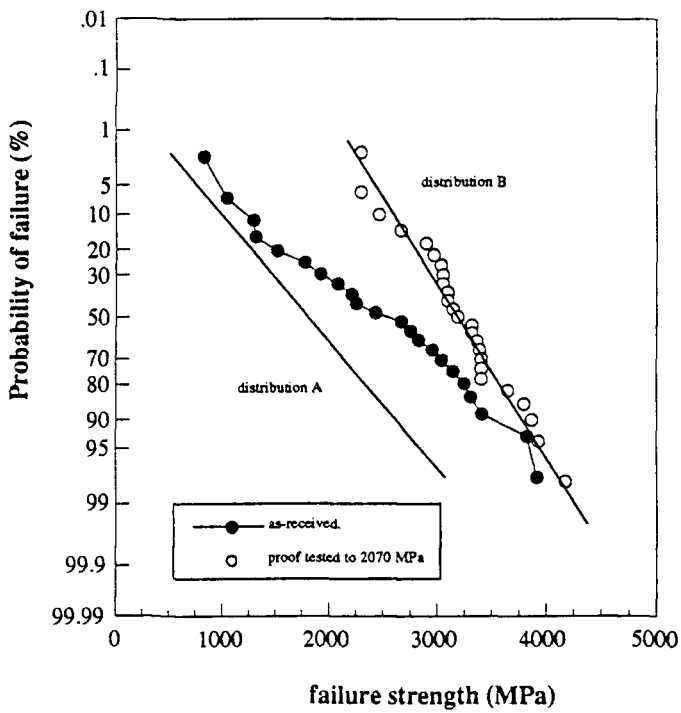
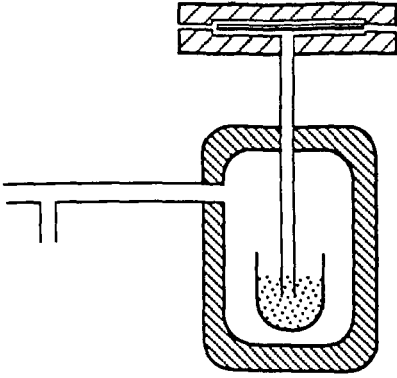
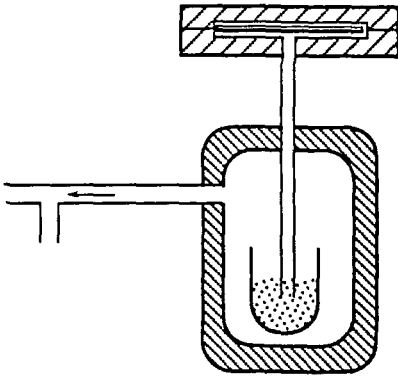


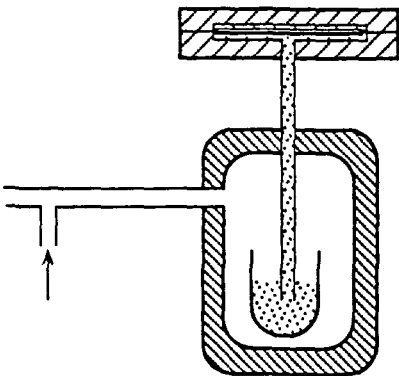
Fig.6 Failure strength distributions of as-received and proof tested boron fibres, 25.4 mm long [13].



1) Insert fibres and close die.



2) Evacuate air.



3) Apply pressure to infiltrate and maintain during solidification, then remove composite.

Fig.7 Liquid metal infiltration process [31].

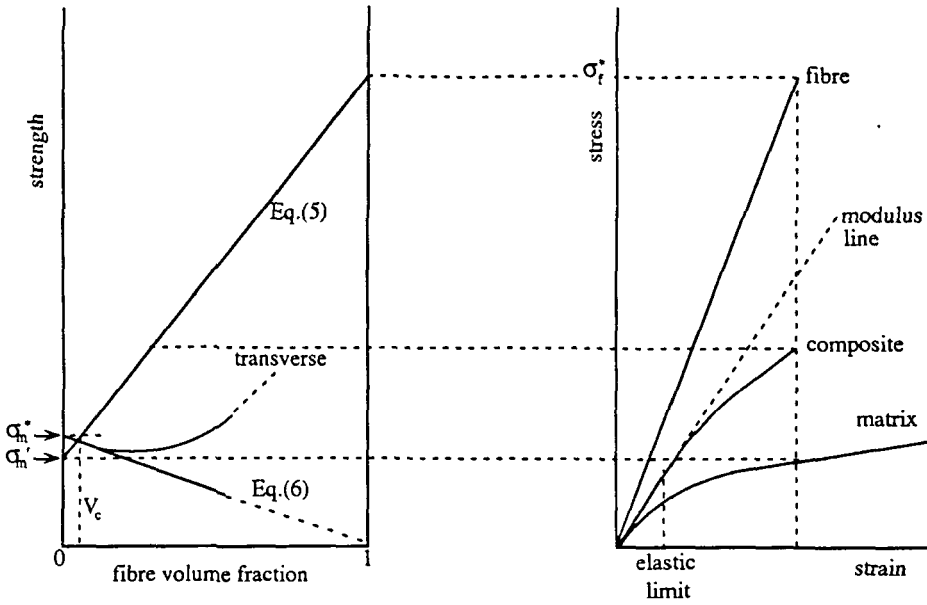


Fig.8 Theoretical variation of composite strength with fibre volume fraction and fibre, matrix and composite in isostrain [37].

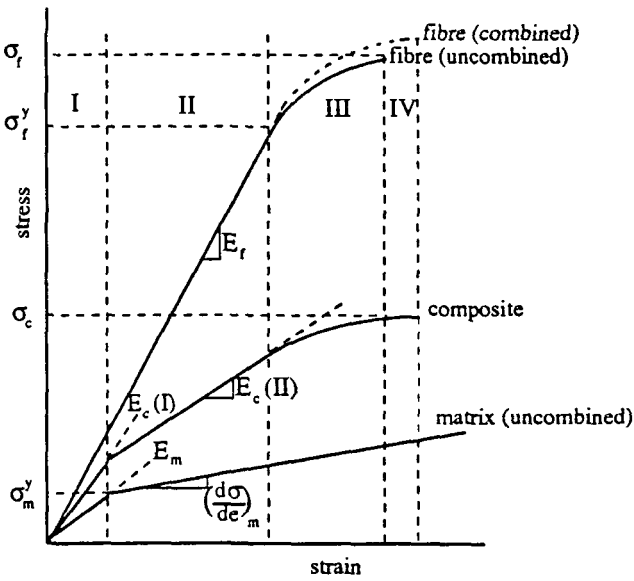


Fig.9 Schematic representation of the stress-strain behaviour of a continuous metal fibre-metal matrix composite [38]

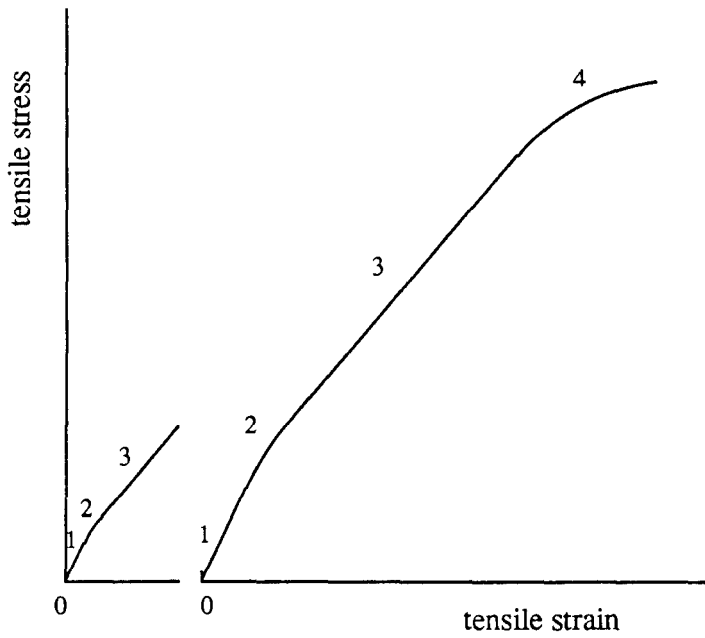


Fig.10 Schematic diagram of typical experimental stress-strain curve for a boron aluminium composite [39].

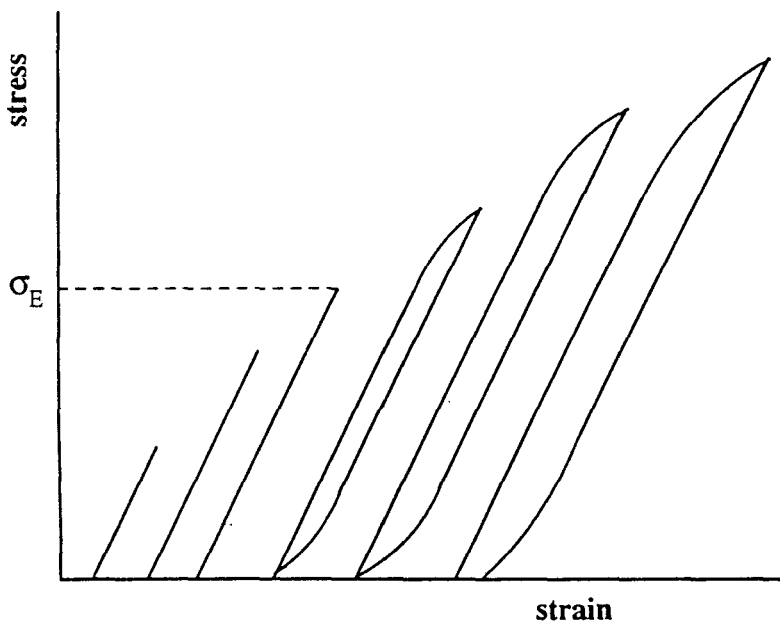


Fig.11 Schematic representation of microstrain behaviour in cyclic load-unload tests for a metal fibre-metal matrix composite [38].

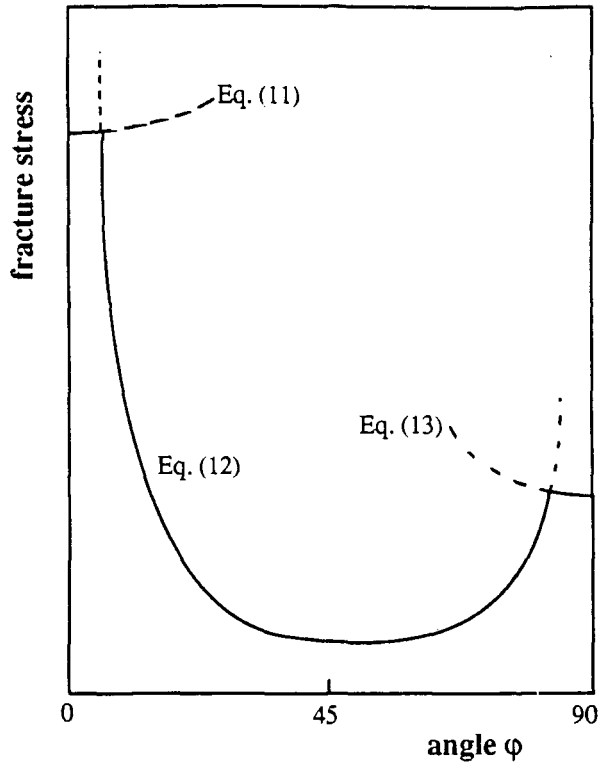


Fig.12 Schematic variation of the composite fracture stress with fibre orientation [36].

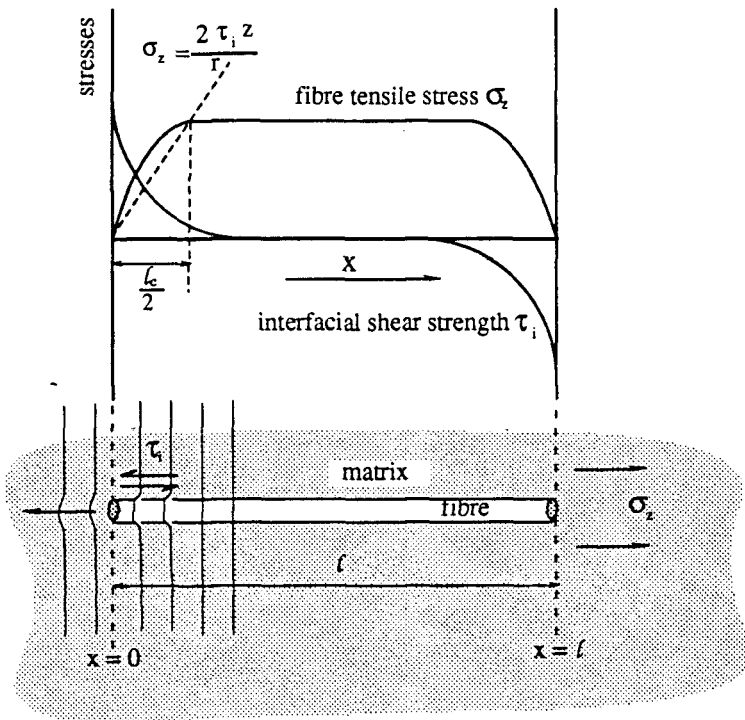


Fig.13 Variation of fibre tensile stress, σ_z , and the interface shear stress, τ_i , along a short fibre length, and diagrammatic tensile-stress distribution in a matrix, when discontinuous fibres are subjected to tensile load [47,48].

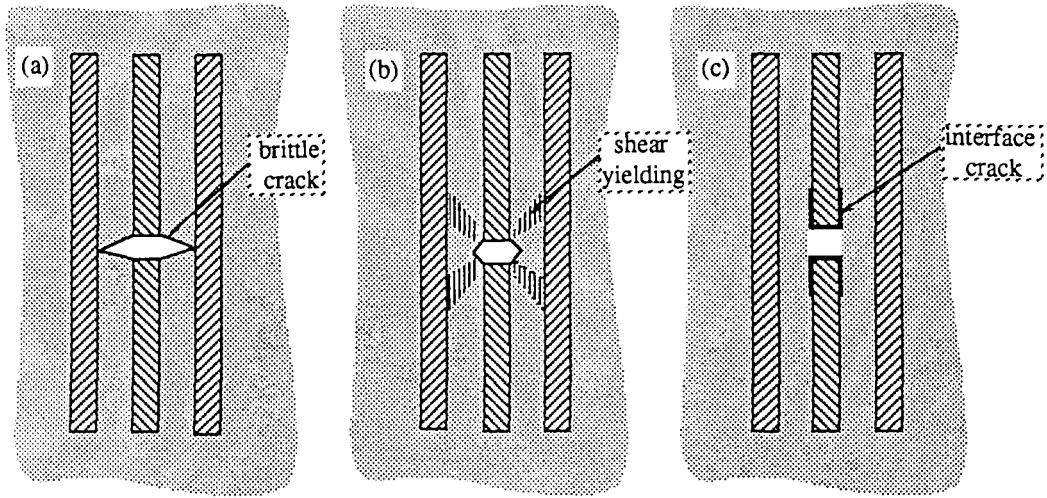
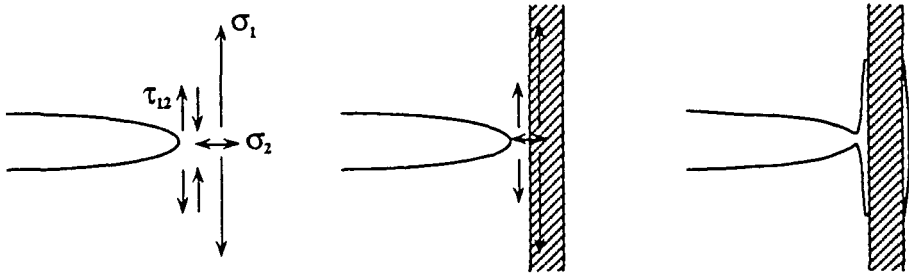


Fig.14 Interaction between fibres and cracks, (a) brittle cracking of matrix, (b) shear yielding of matrix, (c) interface cracking [48].



a) Triaxial stress state at matrix crack tip under uniaxial loading conditions.

b) Crack tip interacting with an adjacent fibre.

c) Interface splitting and crack tip blunting.

Fig.15 Interaction of a matrix crack with an adjacent fibre [49].

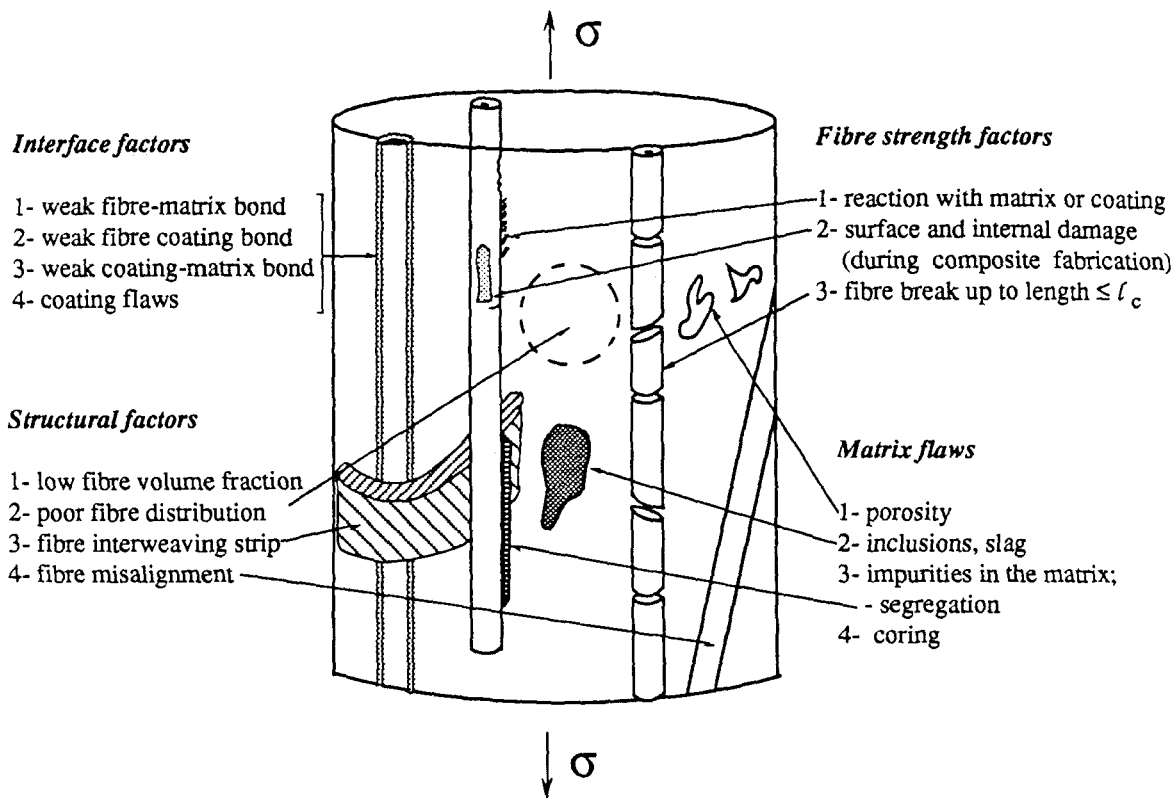


Fig.16 Factors that might affect composite strength (adapted [61]).

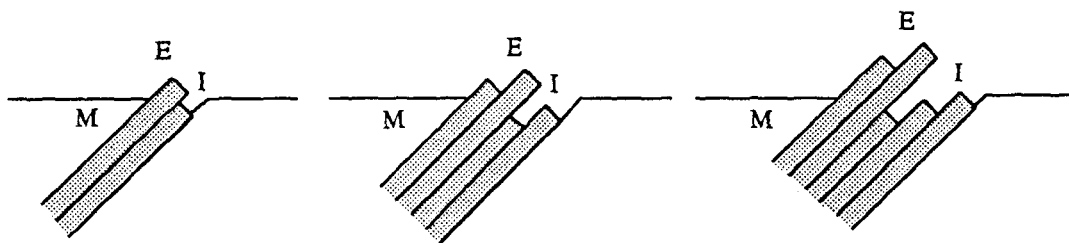


Fig.17 Scheme of formation and development of fatigue slip bands in matrix (M) and of extrusions growth (E) and intrusions (I) [67].

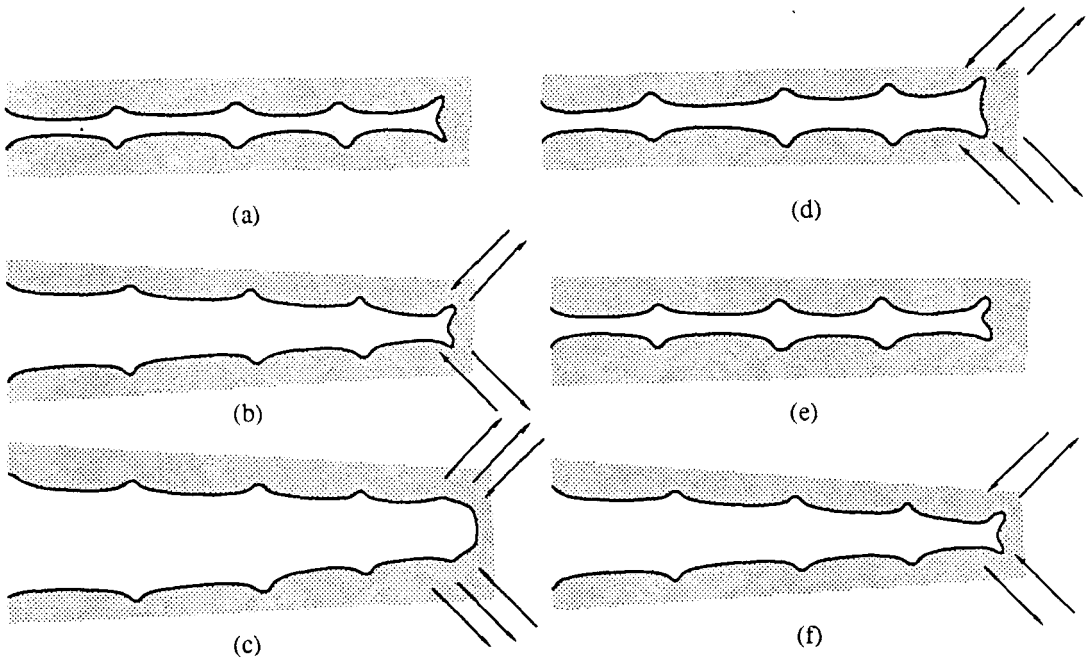


Fig.18 Diagrammatic representation of the mechanism of striation formation [69].

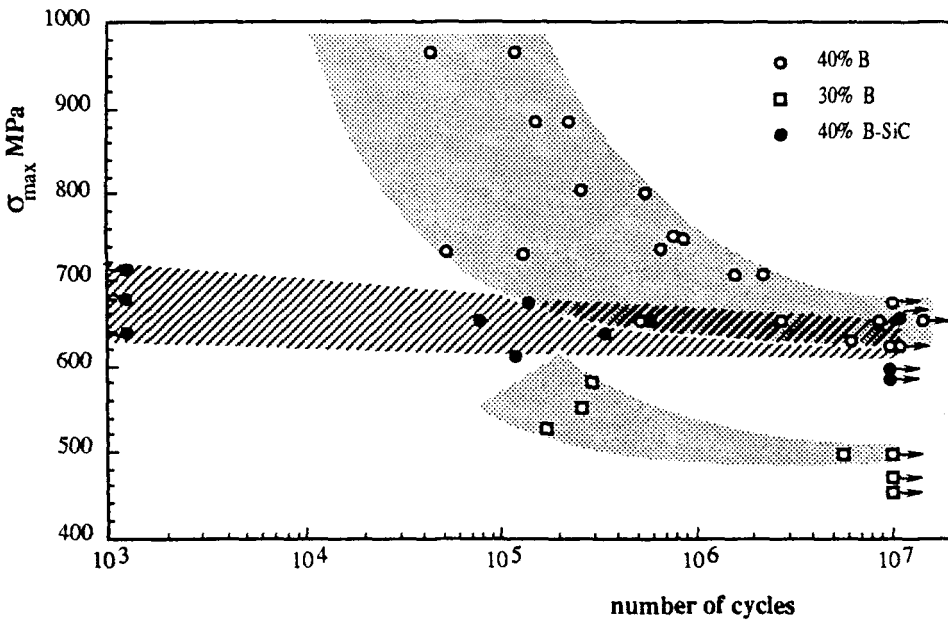


Fig.19 Fatigue resistance of some aluminium-boron fibre composites [18].

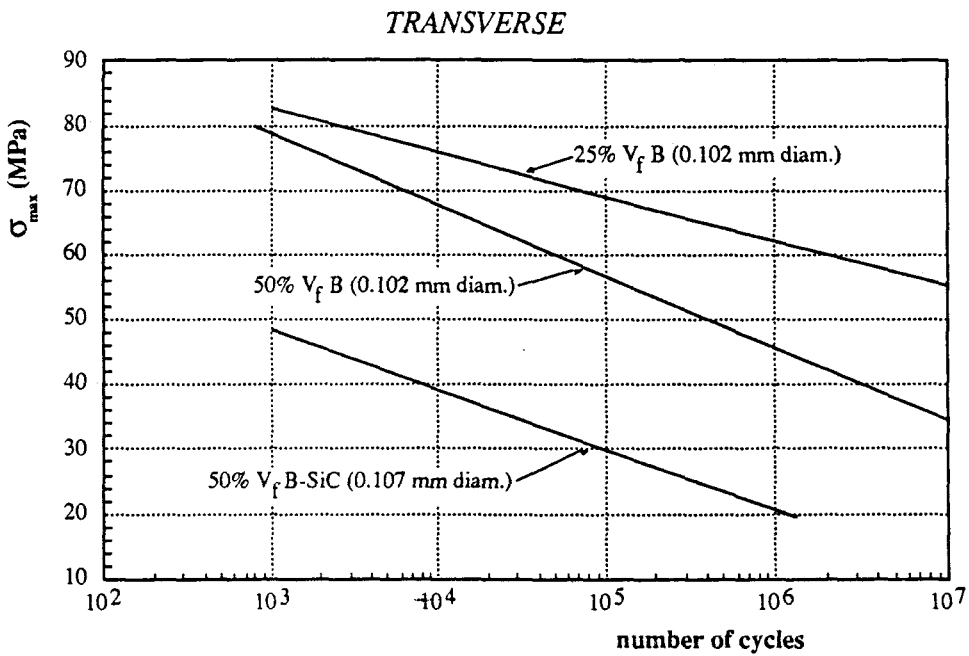
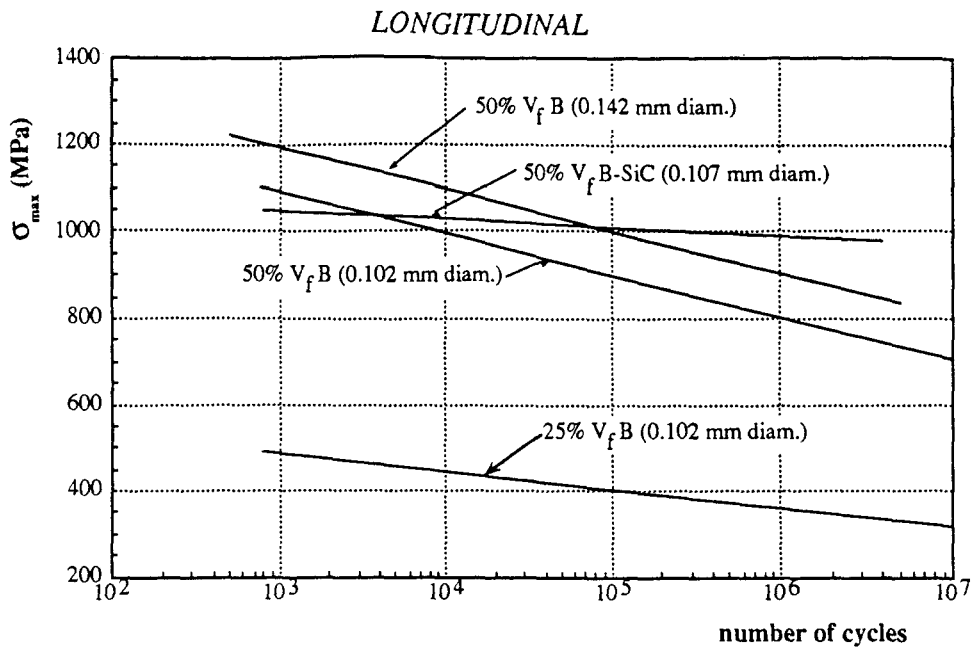


Fig.20 Effect of fibre type, size, and volume fraction on longitudinal and transverse fatigue properties [79].

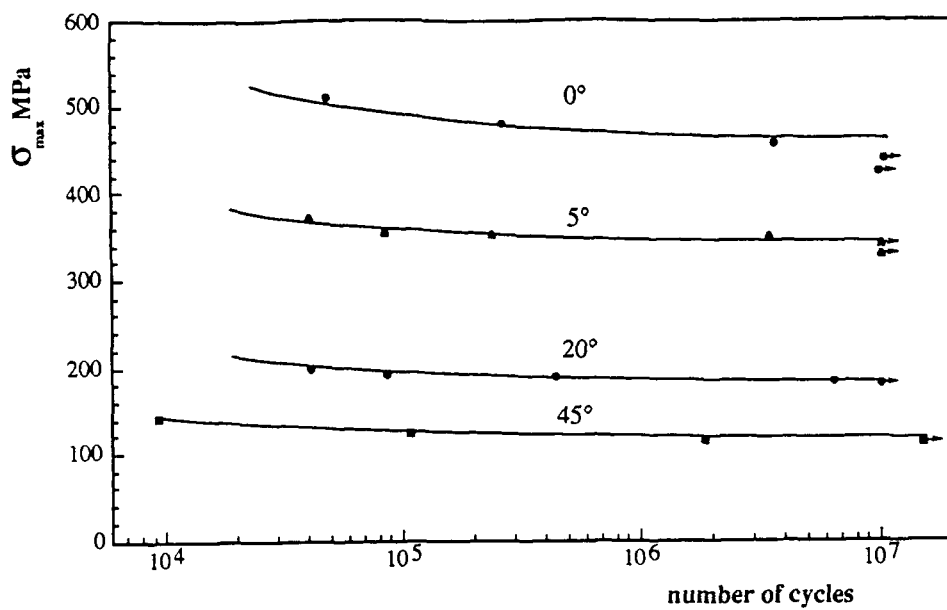


Fig.21 Results of off-axis fatigue tests on 6061-O Al / boron fibres [82].

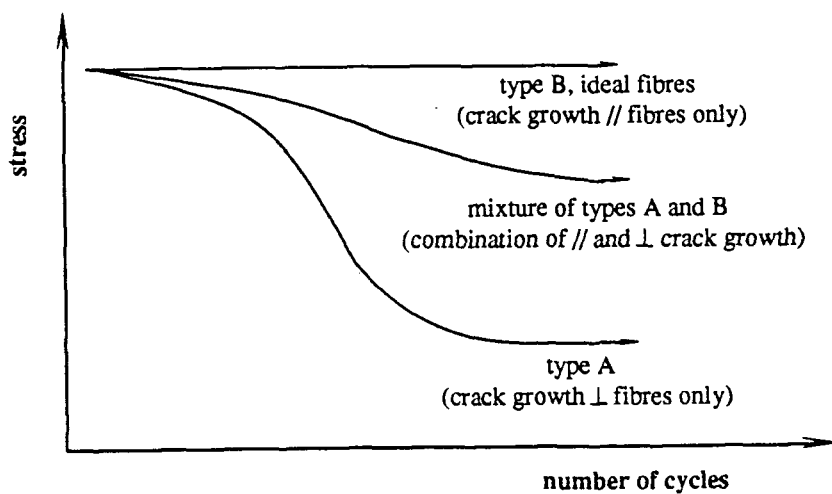


Fig.22 Three shapes of S-N curves in unidirectional composites as influenced by crack path [81].

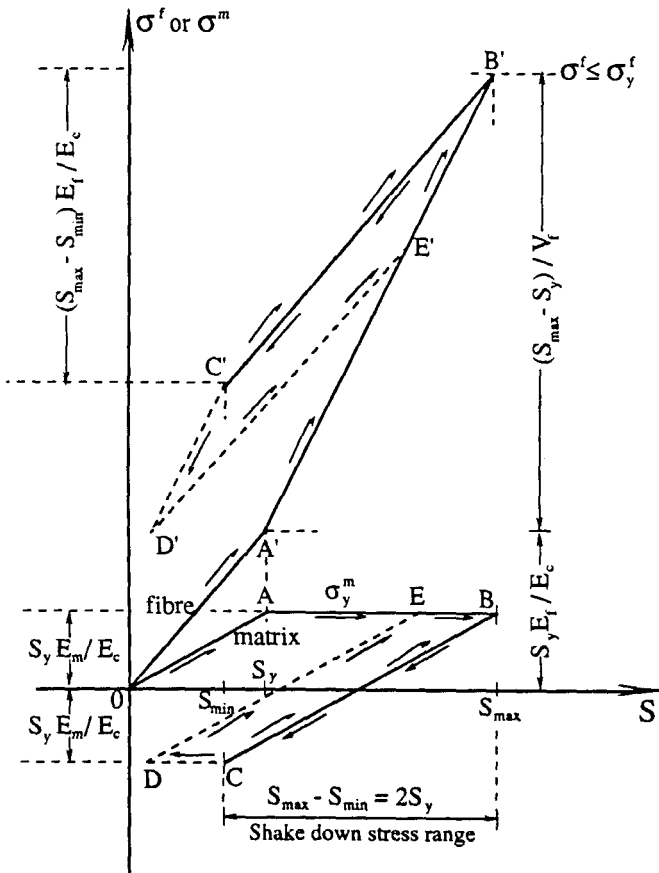


Fig.23 Deformation and shake down of a composite model in a stress controlled uniaxial test [95].

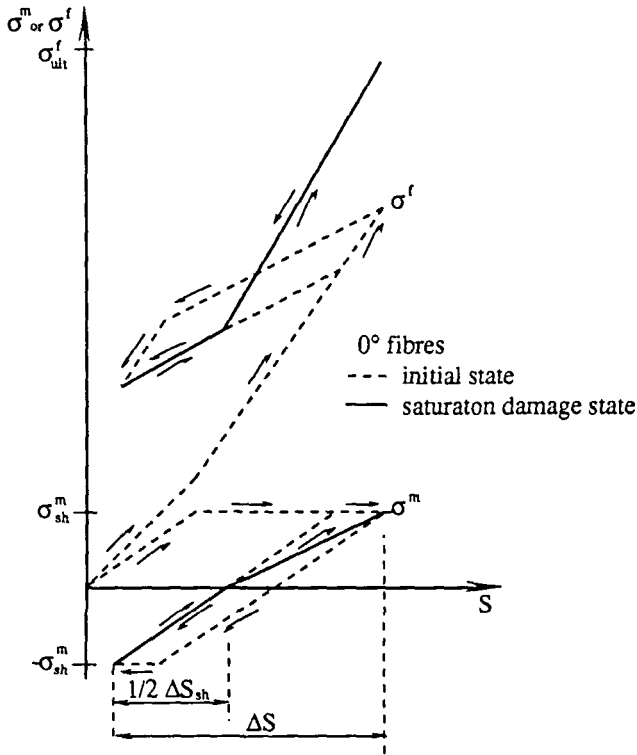


Fig.24 Matrix and fibre stress response to applied stress as the composite attains a saturation damage state [89].

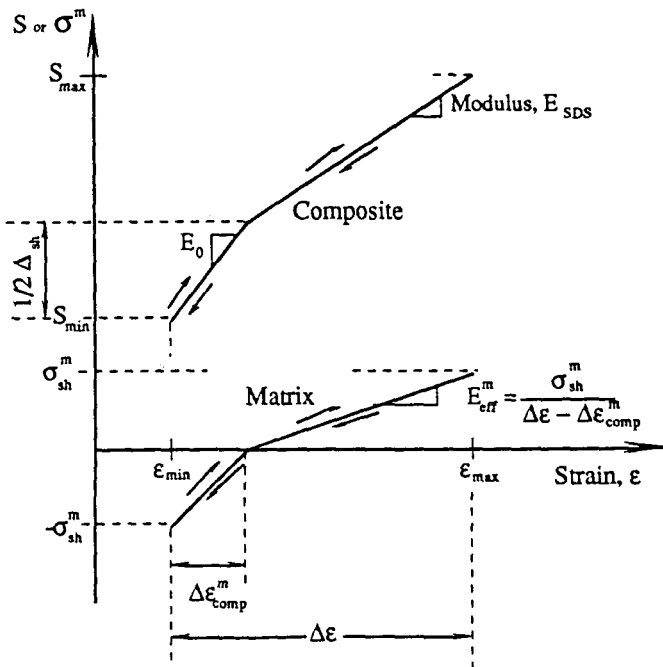


Fig.25 Composite and matrix stress-strain response for a saturation damage state [89].

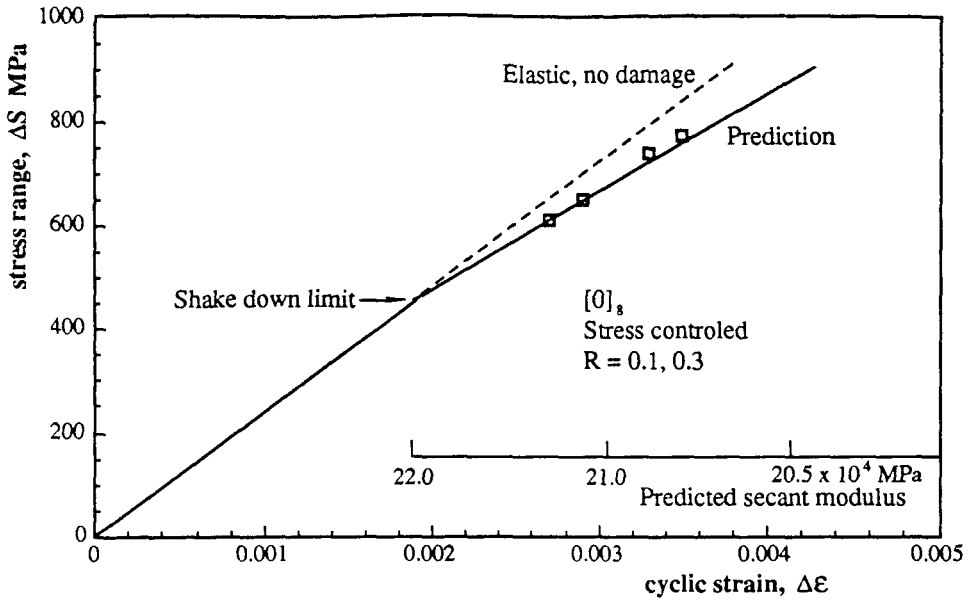


Fig.26 Correlation of experimental data and model prediction for $[0]_8$ laminates after 500 000 fatigue cycles [89].

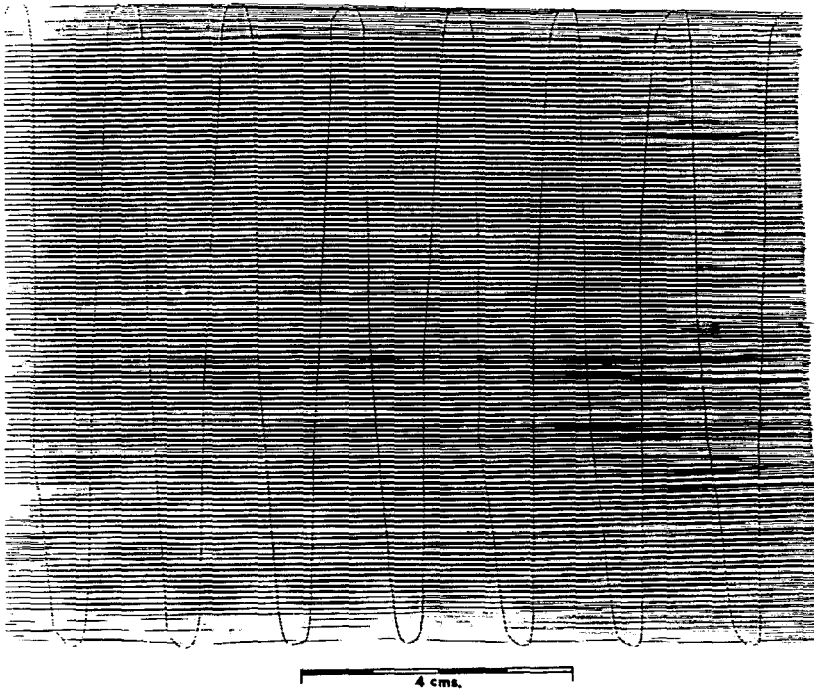
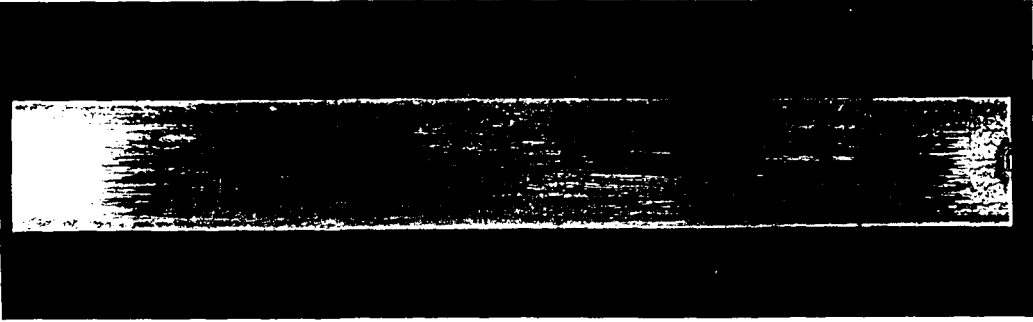


Fig.27 Unidirectional monolayer tape of SiC coated boron fibres interwoven with a titanium strip.



4 cms.

Fig.28 *Aluminium/SiC coated boron fibre composite strip.*



1 cm

Fig.29 *Radiograph of the composite aluminium/SiC coated boron fibres.
Dark lines correspond to tungsten boride fibre cores.*

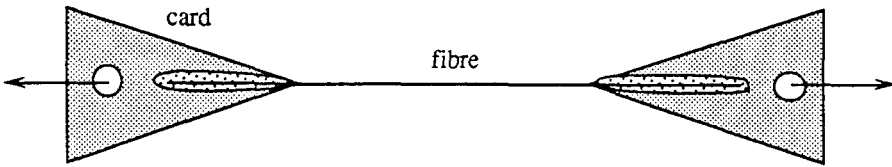


Fig.30 Tapered low-modulus mount for single fibres [105].

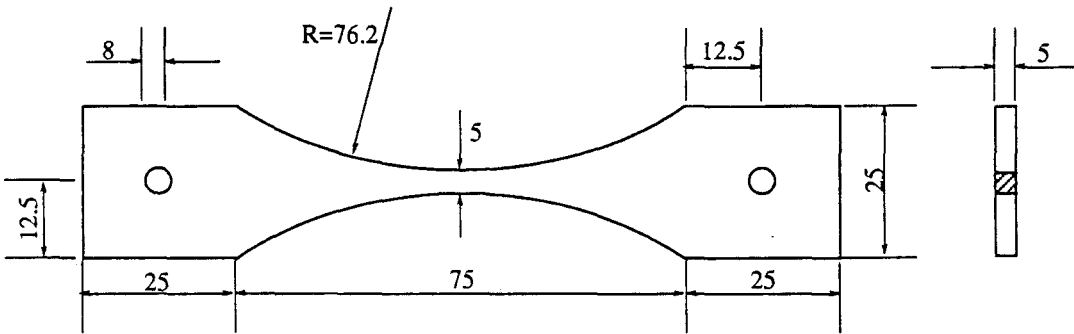


Fig.31 Tension-tension fatigue test specimen geometry.

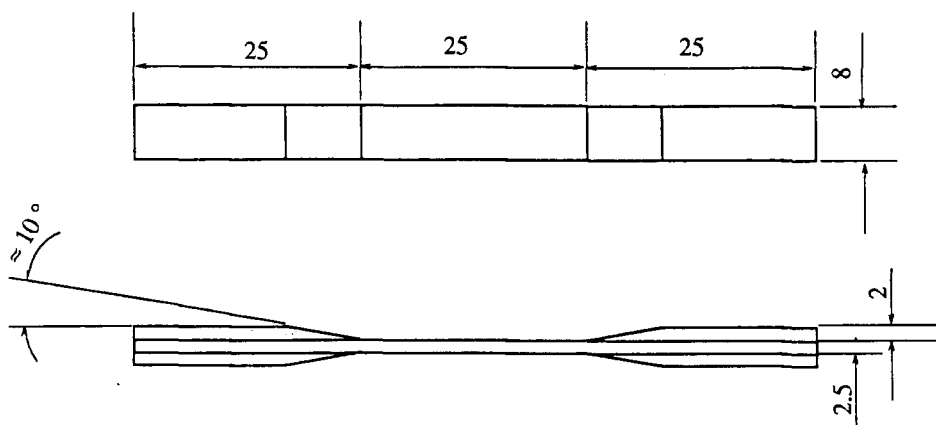


Fig.32 Nominal composite specimen dimensions.

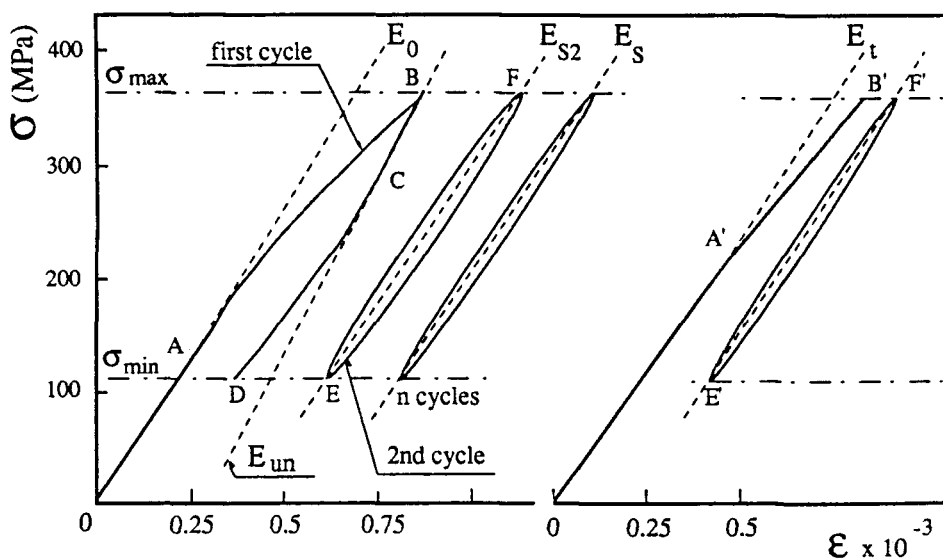


Fig.33 Typical experimental stress-strain curves as function on number of cycles for the 28% series material at 0° orientation.

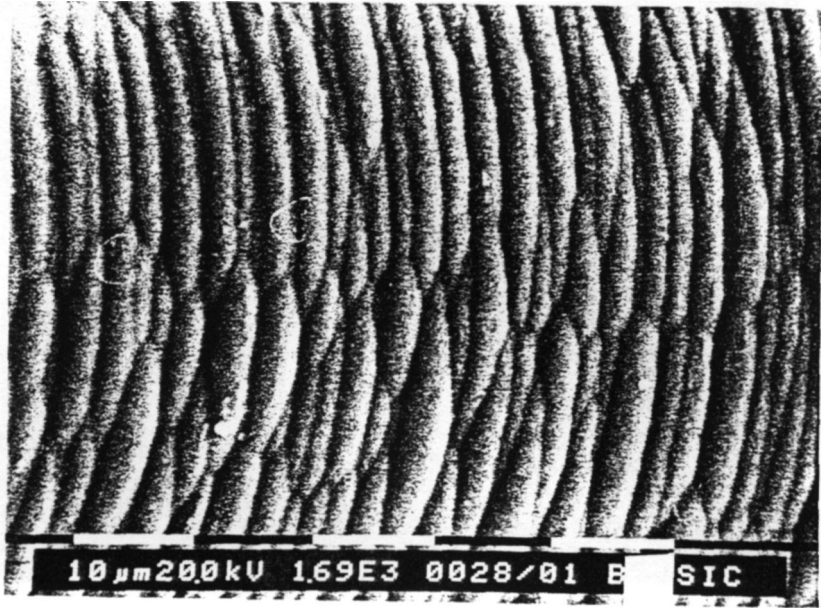


Fig.34 SEM micrograph of a typical fibre surface.

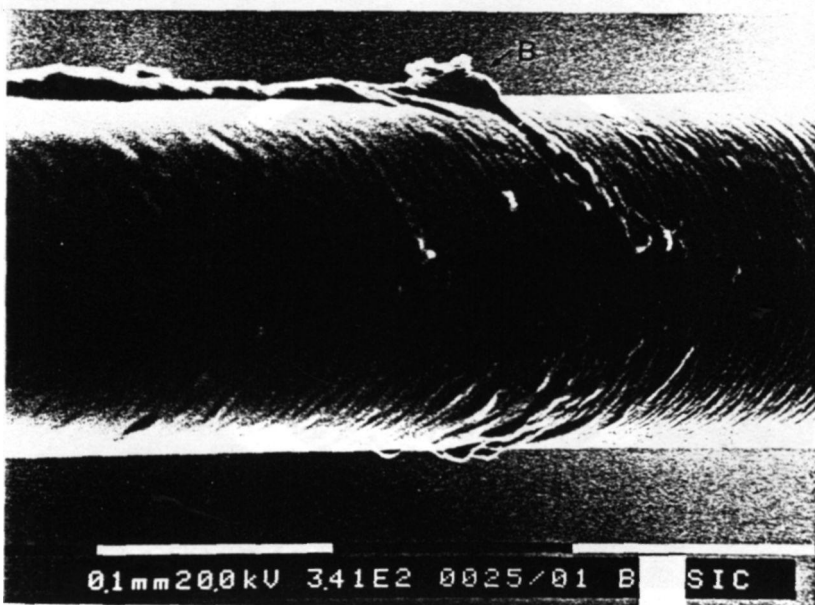


Fig.35 SEM micrograph of the fibre surface showing gross nodules (arrow A) and extraneous material (arrow B).

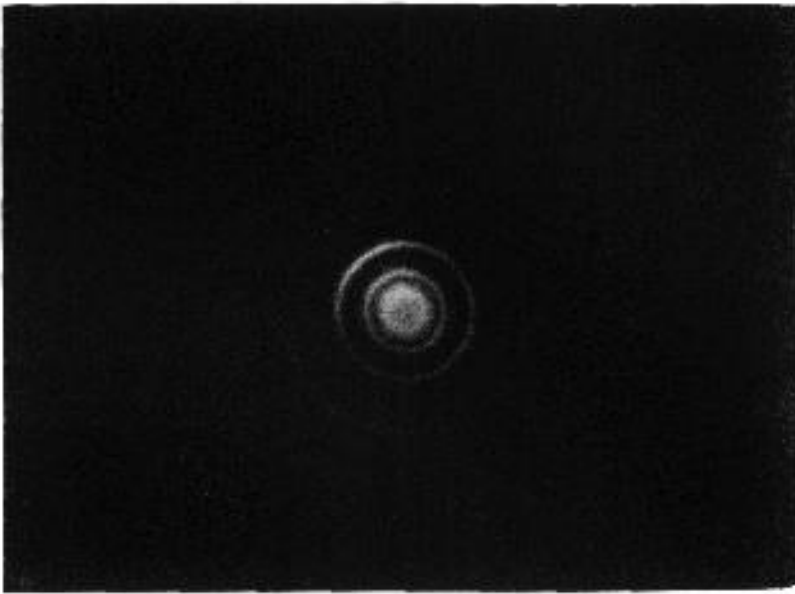


Fig.36 Electron diffraction pattern of the boron mantle showing very diffuse halos.

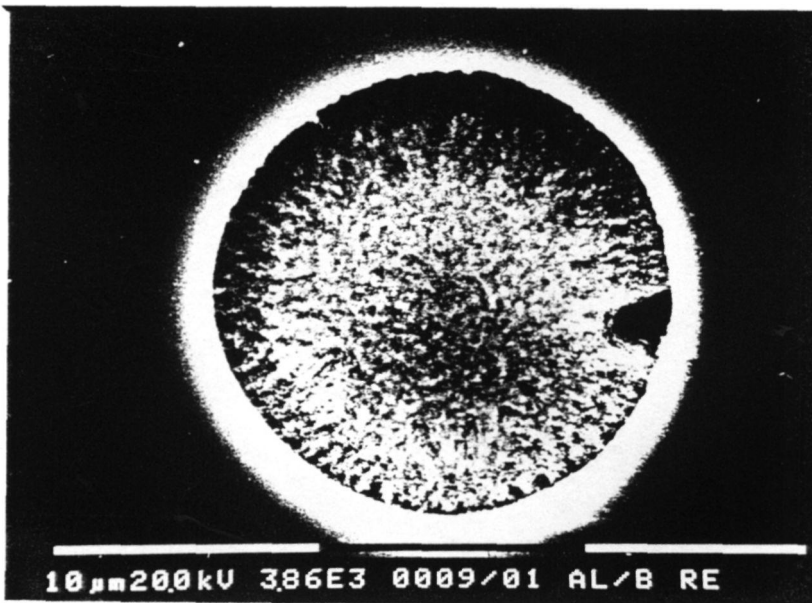


Fig.37 SEM micrograph of the tungsten boride fibre nucleus. The centre region shows smaller grain size particles.



Fig.38 TEM micrograph of the tungsten boride nucleus centre showing the presence of fine grains.

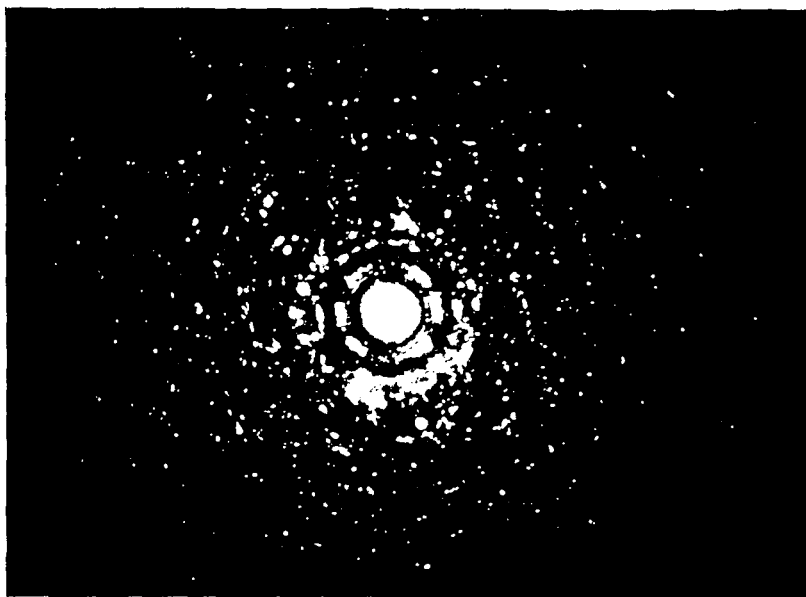


Fig.39 Electron diffraction pattern of the fibre tungsten boride nucleus showing some preferential crystallographic orientations.

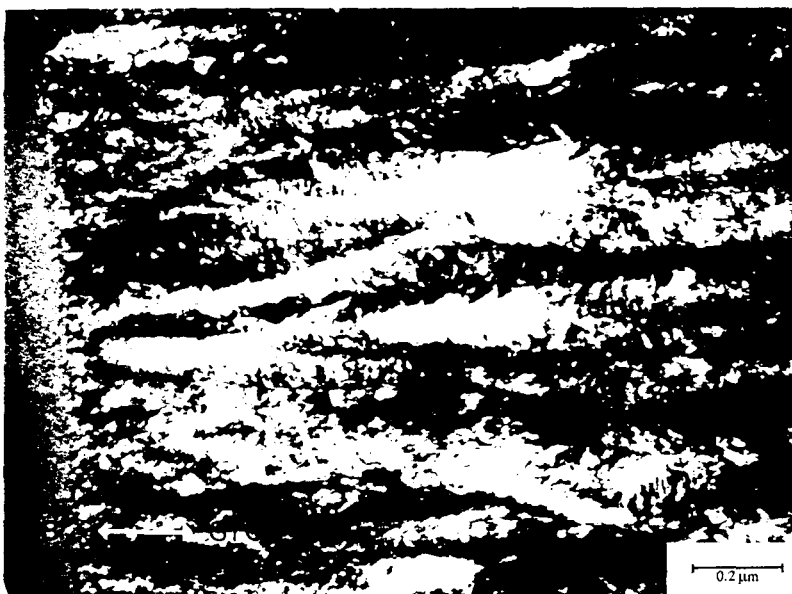


Fig.40 Dark field image of the SiC coating using $\{111\}$ β -SiC reflections showing columnar subgrains. The arrow indicates the growth direction. B is the boron mantle.

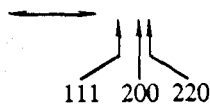
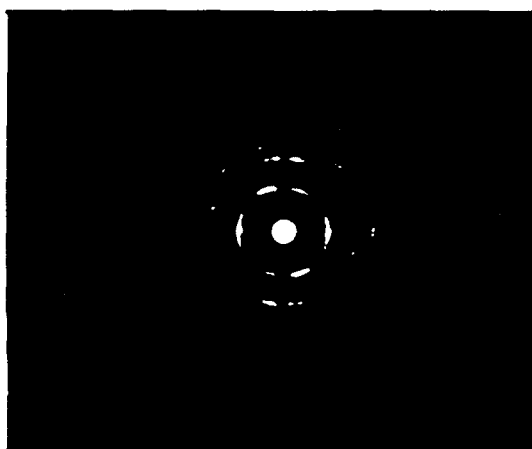


Fig.41 Selected area diffraction pattern of the SiC coating. Arcs indicate preferred orientation. The growth direction is parallel to the arrow.

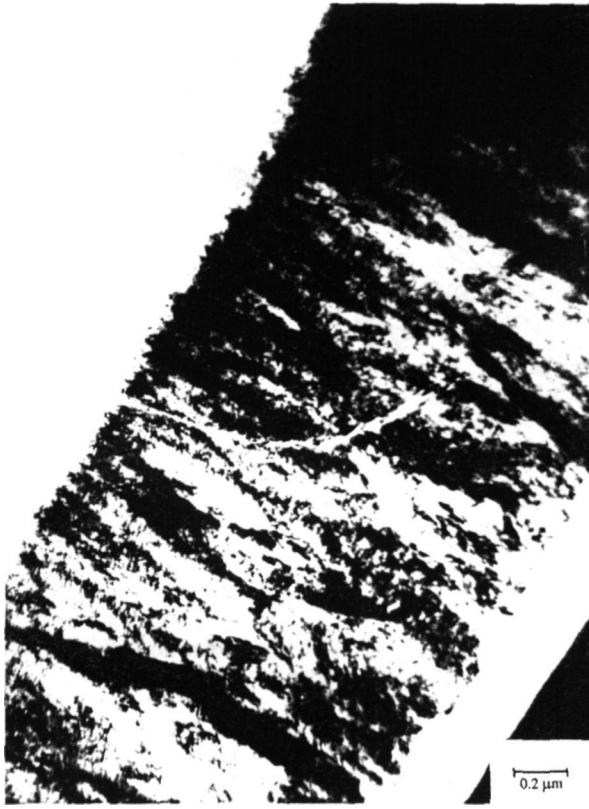


Fig.42 TEM micrograph of the SiC coating showing a crack growing from the boron mantle outwards.

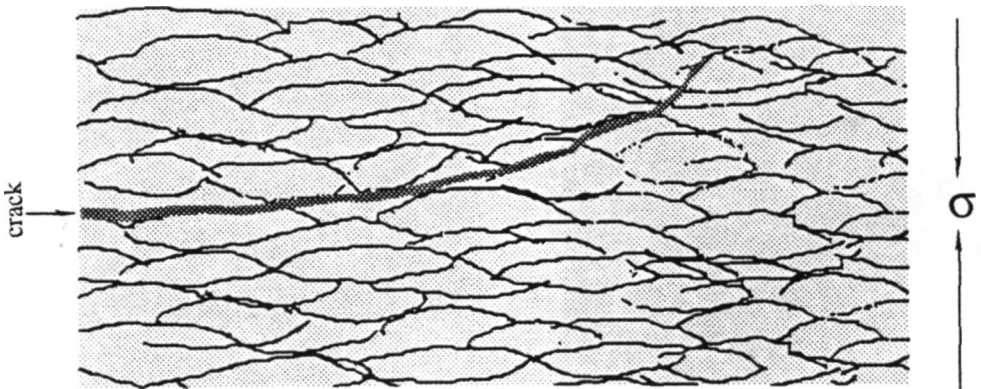


Fig.43 Schematic crack growth path inside the SiC coating.

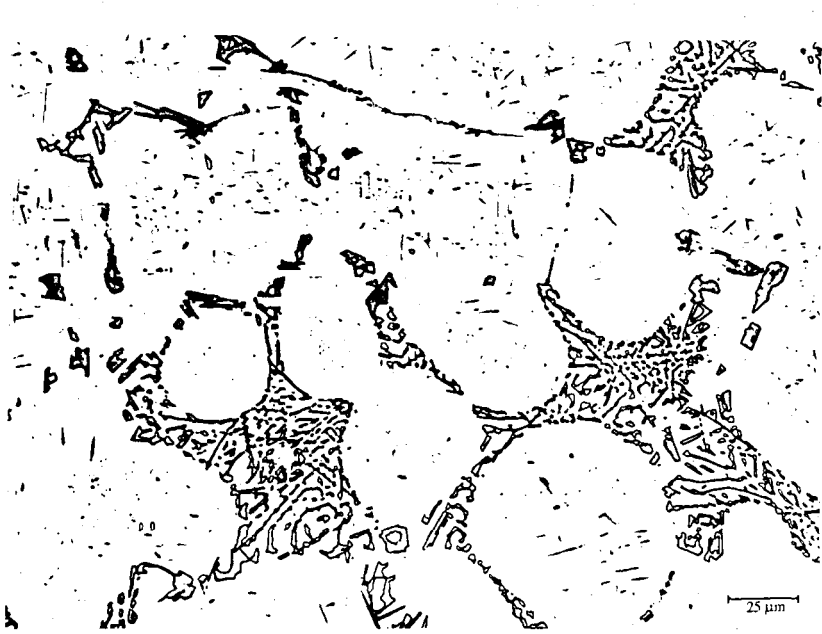
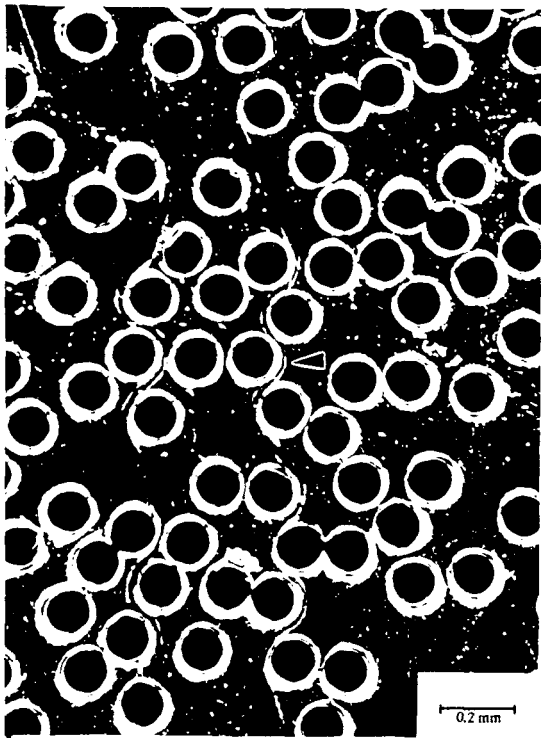
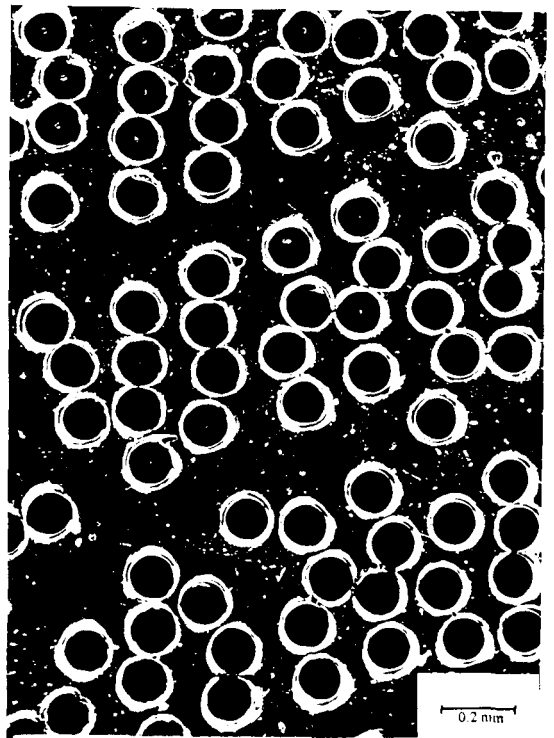


Fig.44 Optical micrograph of the matrix material prior to infiltration showing the presence of the Al dendrites, the interdendritic phases and precipitates inside the dendrites. Keller's etch.

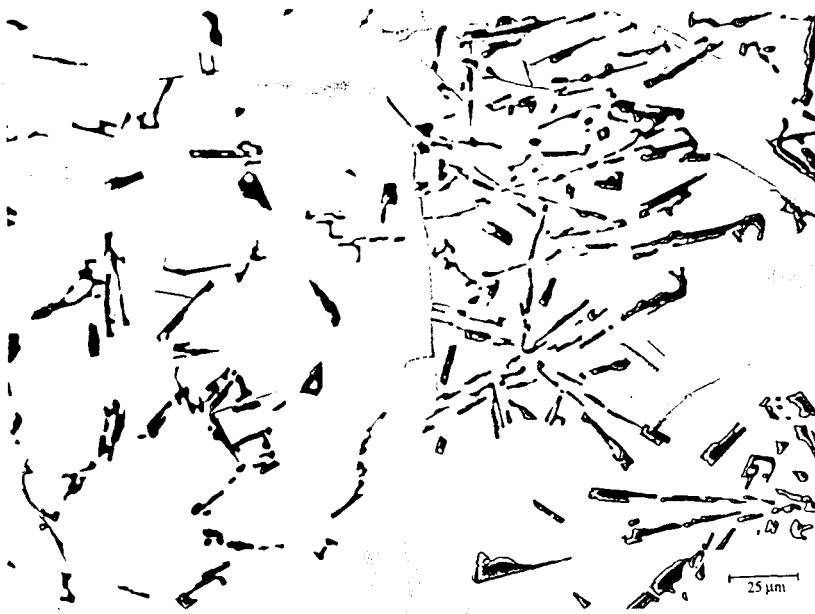


a)

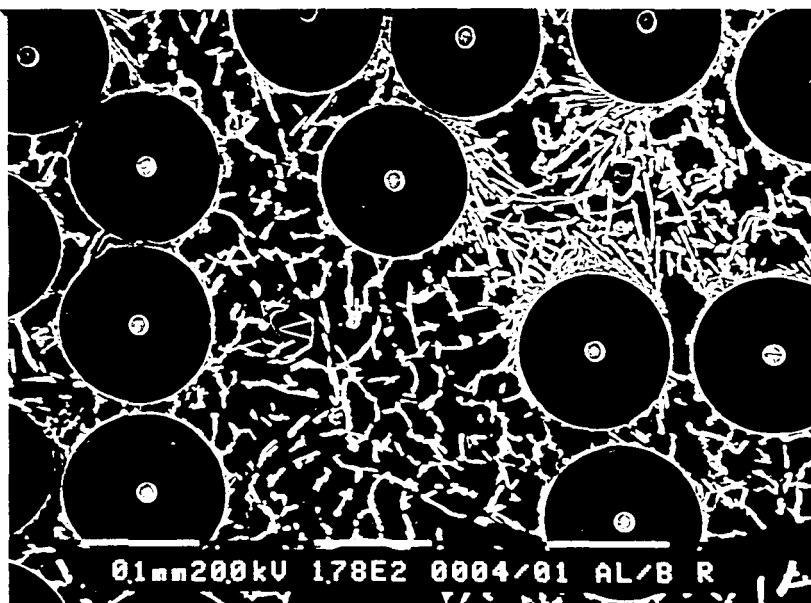


b)

Fig.45 Optical dark field micrographs of the cross section of the composite material series 28%. a) Micrograph showing the matrix, the fibres surrounded by white halos and the interweaving Ti strip (arrow). b) Micrograph showing fibre banding. The white halos are due to polish relief around the fibres.



a)



b)

Fig.46 Micrographs of the transverse section of the composite material series 28%. a) OM micrograph of the aluminium alloy matrix showing a silicon network (grey particles) and intermetallic platelets (light gray particles). Keller's etch. b) SEM micrograph showing the fibres, the dendritic structure and porosity (arrow).



Fig.47 SEM micrograph of deep etched composite material series 28% showing a fibre and a complex particle network.

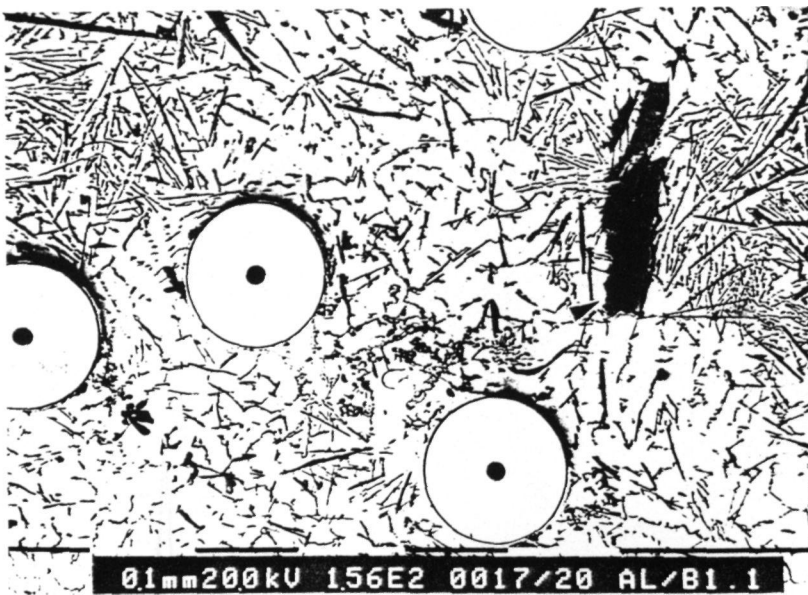


Fig.48 SEM micrograph (inverted signal) of a cross section of the composite material series 28% showing fibres, the aluminum matrix, some intermetallic cross sections (dark contrast) and longitudinal section (arrow).

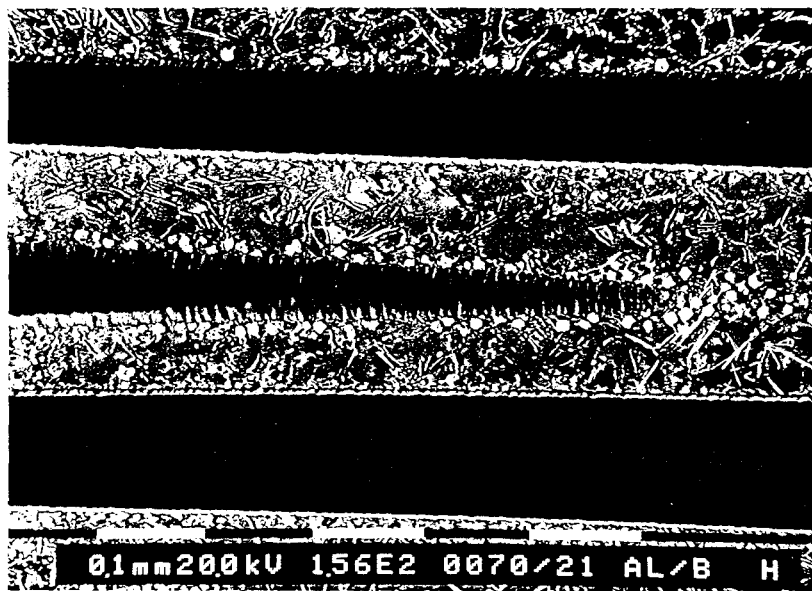


Fig.49 SEM micrograph of the longitudinal direction of the 28% series material showing fibres, a tapered fibre, matrix and second phases.

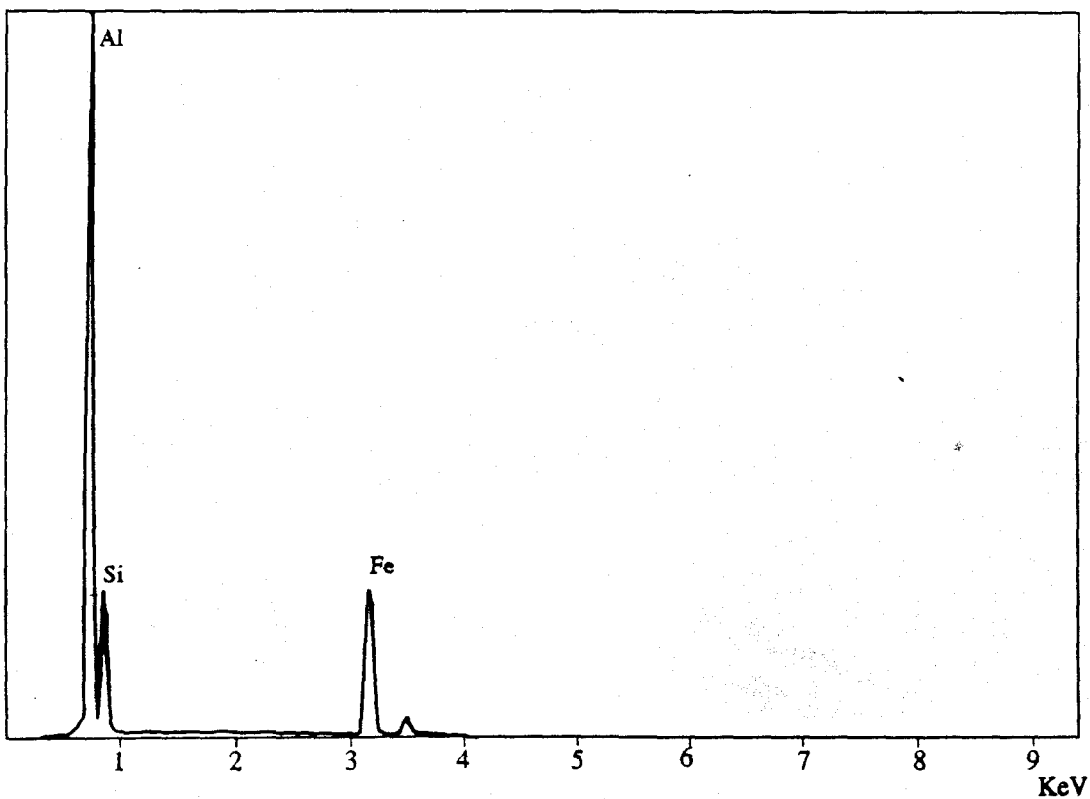


Fig.50 Typical SEM energy dispersive spectrum obtained from the platelet type constituents, 28% series material.

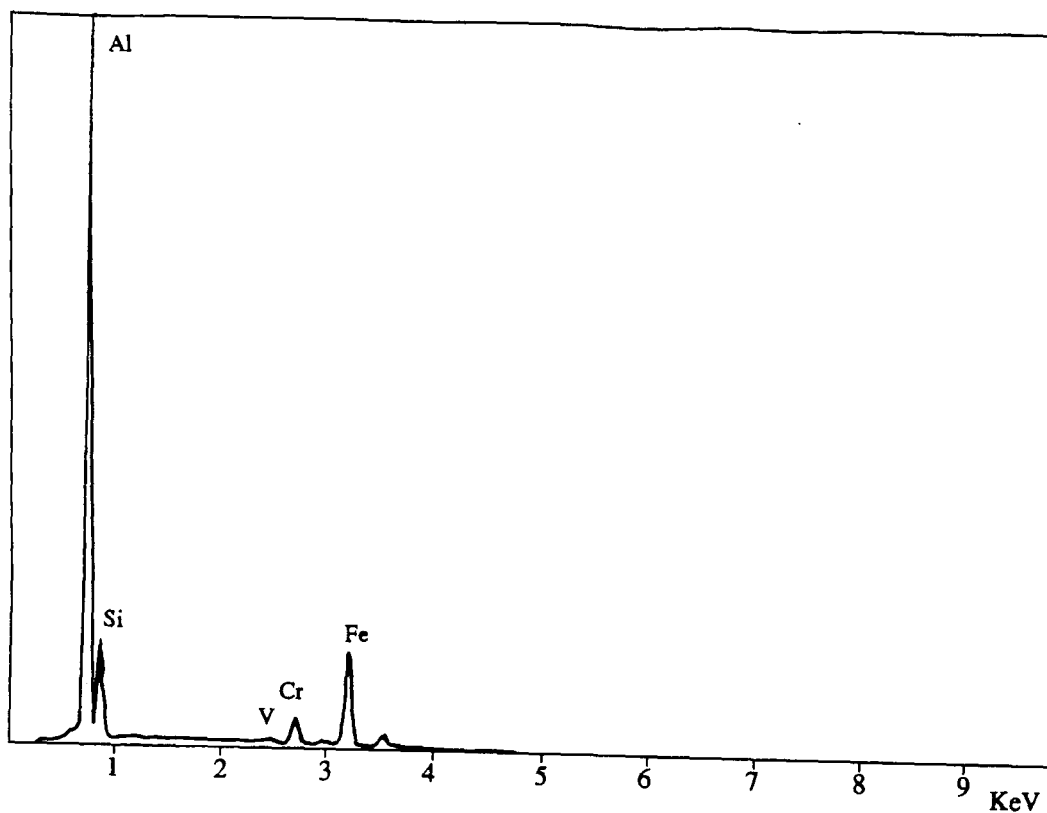


Fig.51 Typical SEM energy dispersive spectrum from the globular type constituents, 28% series material.

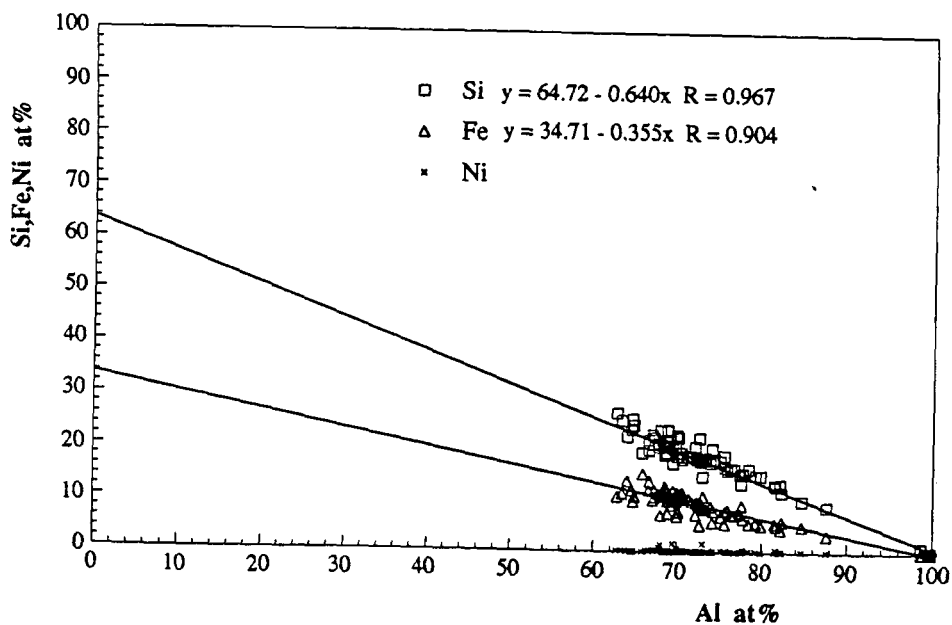


Fig.52 Variation in atom percent of Si, Fe and Ni versus Al for in-situ SEM analyses of 80 similar second phase platelet type.

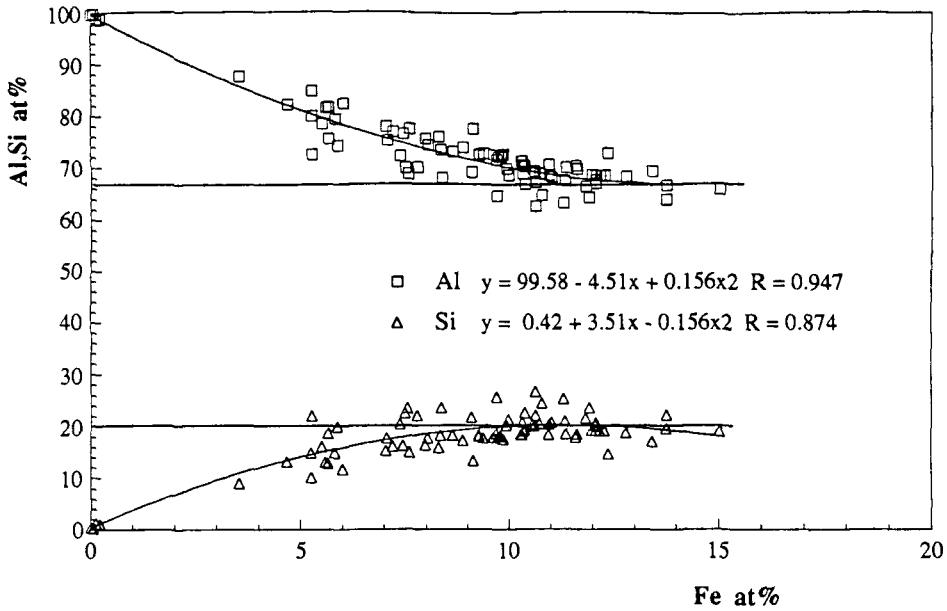


Fig.53 Variation in atom percent of Al and Si versus Fe for in-situ SEM analyses of second phase platelet type.

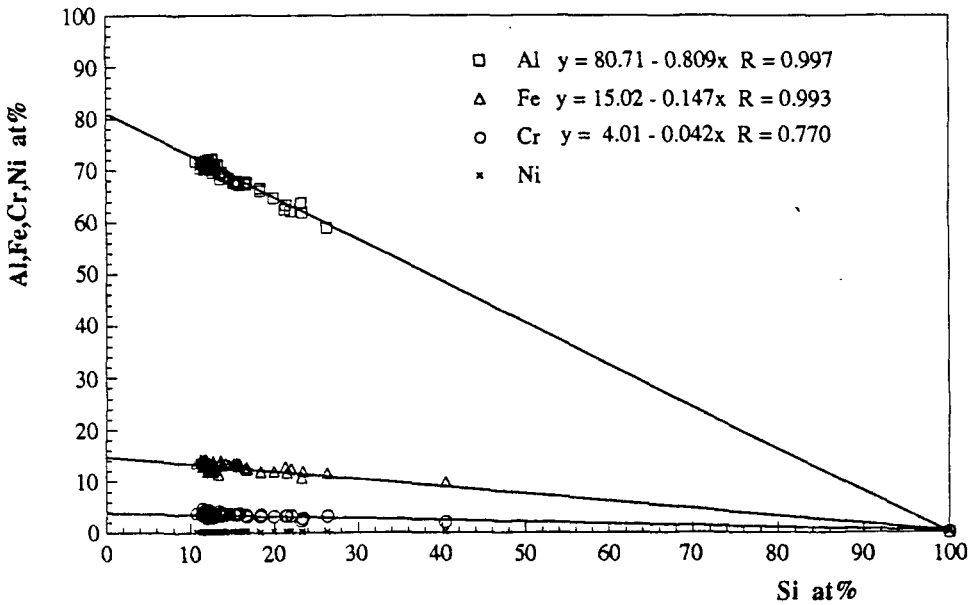


Fig.54 Variation in atom percent of Al, Cr and Fe versus Si for in-situ SEM analyses of 97 similar second phase globular type, 28% series material.

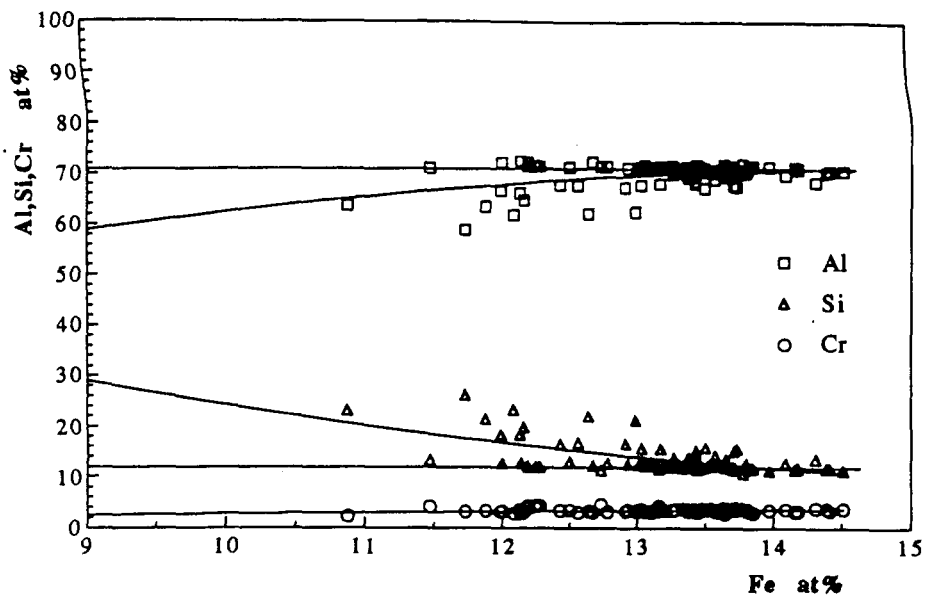


Fig.55 Variation in atom percent of Al, Si and Cr versus Fe for in-situ SEM analyses of second phase globular type.

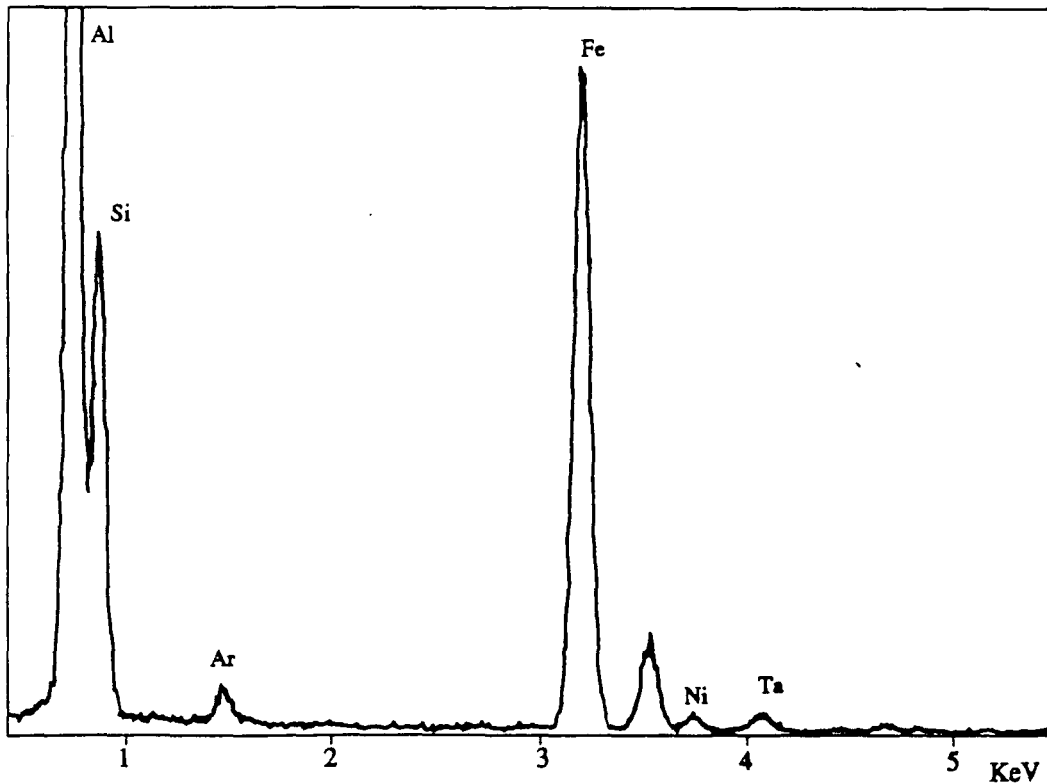


Fig.56 Typical TEM energy dispersive spectrum obtained from the platelet type constituents from the composite material series 28%. The presence of Ar and Ta is due to contamination in the ion thinner.

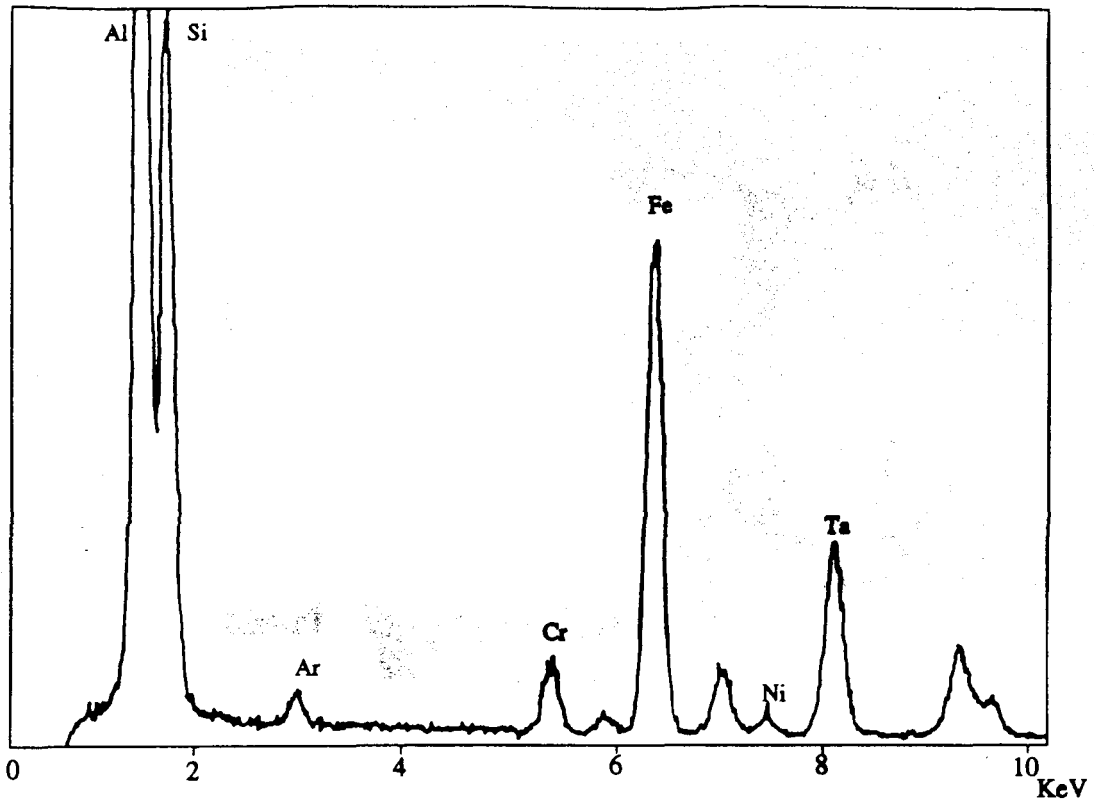
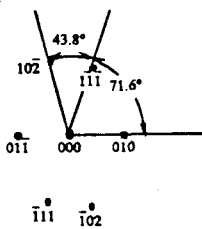
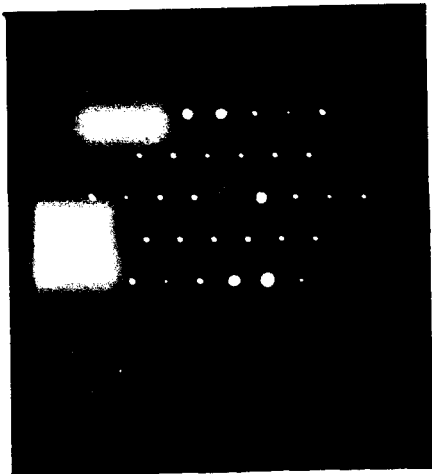
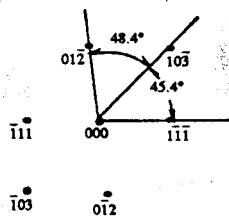
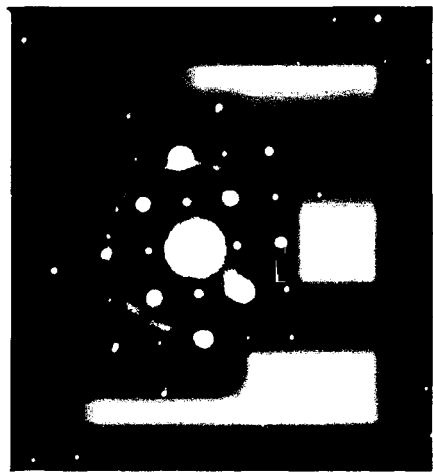


Fig.57 Typical TEM energy dispersive spectrum from the globular type constituents from the composite material series 28%. The presence of Ar and Ta is due to contamination in the ion thinner.



a)



b)

Fig.58 SADP from the [211] and [321] zones of the platelet type tetragonal phase and respective indexed diagrams: a) [211] zone, b) [321] zone.

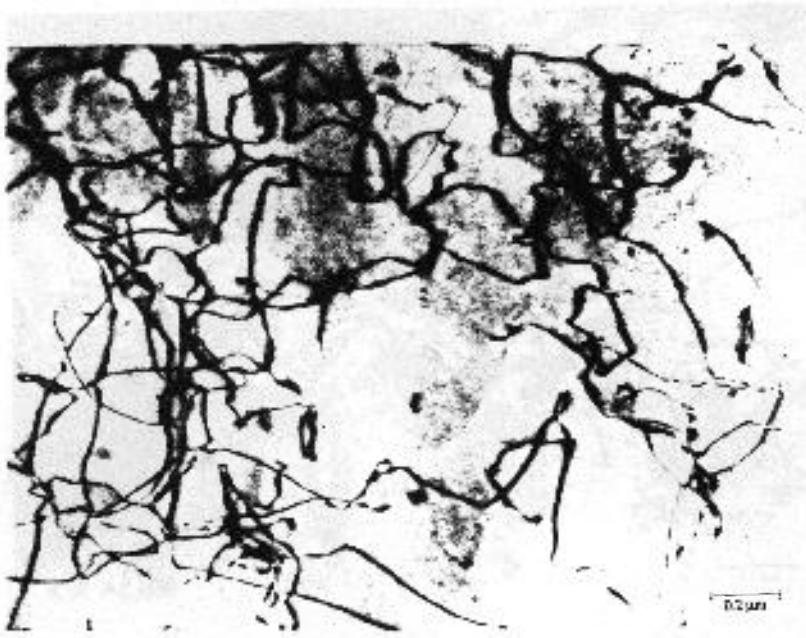


Fig.59 Dislocation structure for the as received material 28% series. B [112]



Fig.60 TEM micrograph of interface aluminium/SiC for series 28% material. The micrograph shows the SiC coating (SiC) and the aluminium matrix with dislocations in contrast (Al). B_{Al} [011].

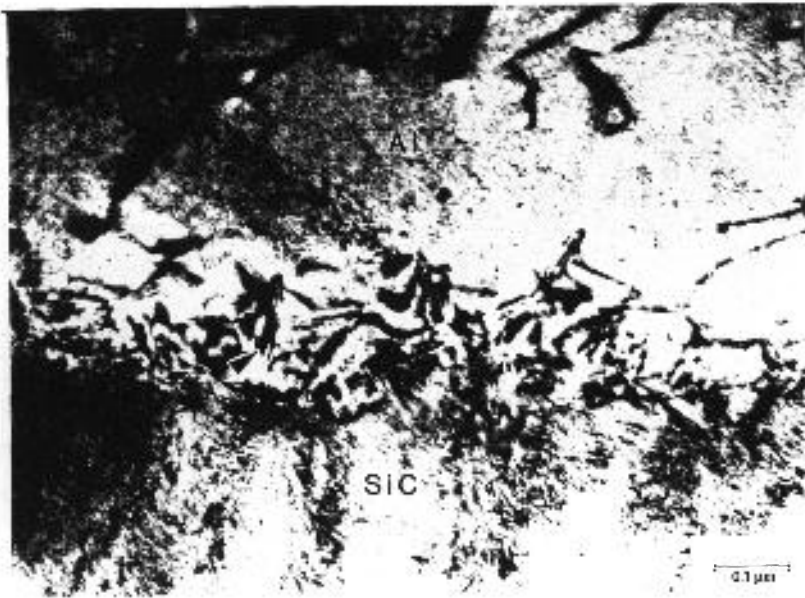


Fig.61 TEM micrograph of the interface Al/SiC showing some product reaction (arrow) growing randomly from the SiC towards the Al.

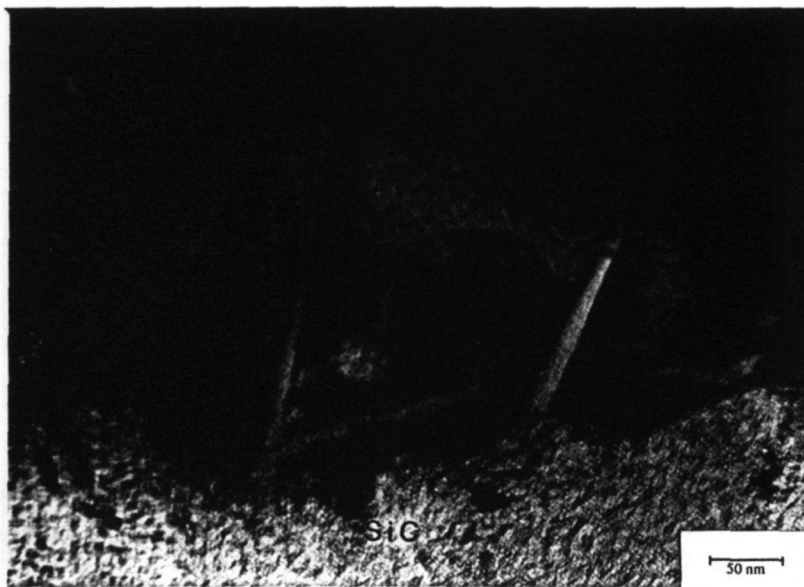


Fig.62 TEM micrograph of a region close to Fig.61, clearly showing needles of a product reaction between SiC and Al.

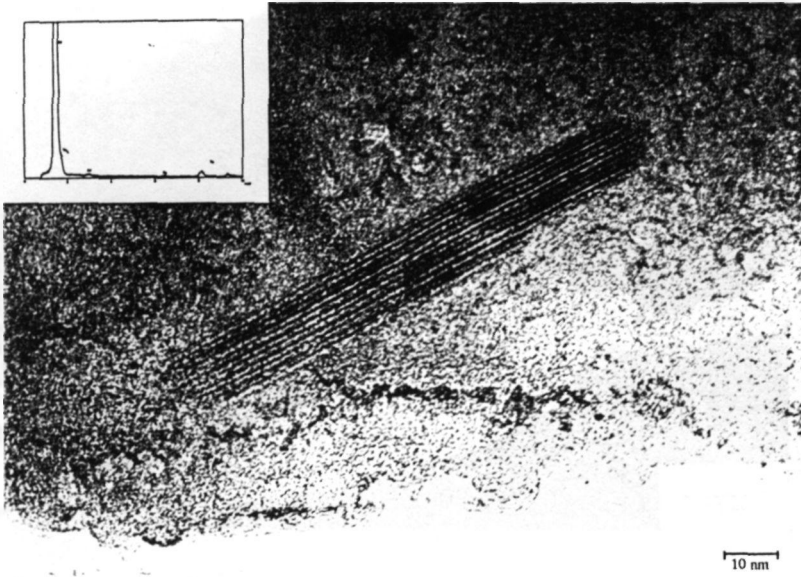


Fig.63 TEM micrograph of (003) lattice fringe of Al_4C_3 carbide with a d -spacing of 0.83 nm. Insert shows the EDS spectrum from this particle. The presence of Ar and Ta is due to contamination in the ion thinner.

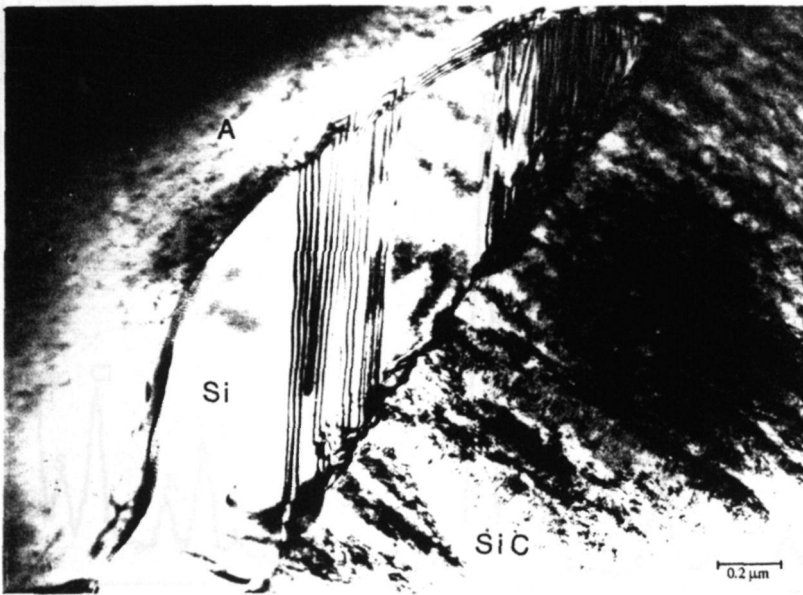


Fig.64 TEM micrograph showing the interface between SiC coating and free silicon as a twinned flake.

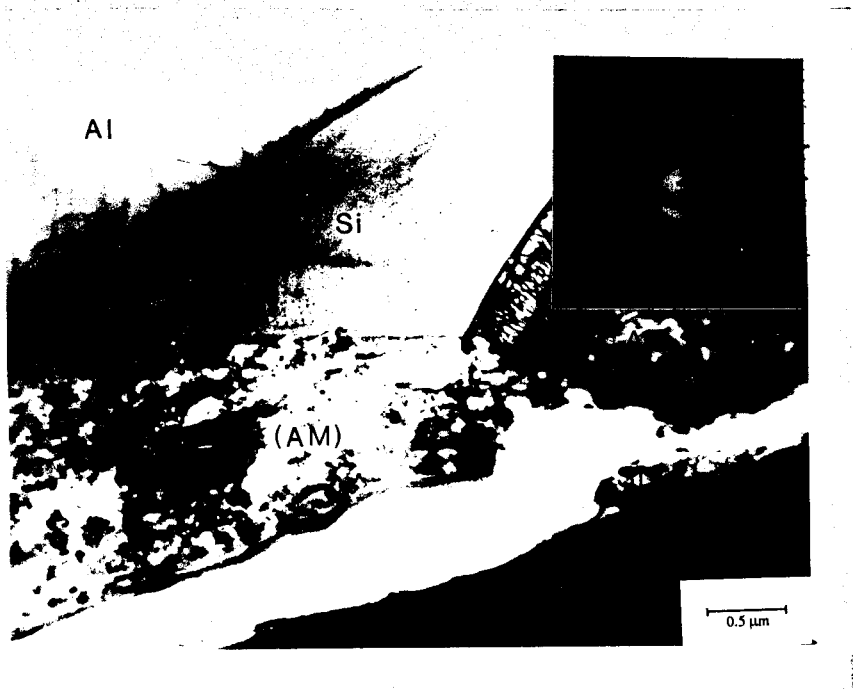


Fig.65 TEM micrograph of amorphous layer (AM) between the SiC coating and aluminium alloy (Al, Si). The gap between the layer and the SiC is probably due to differential ion thinning rates. Insert shows SADP from the layer.

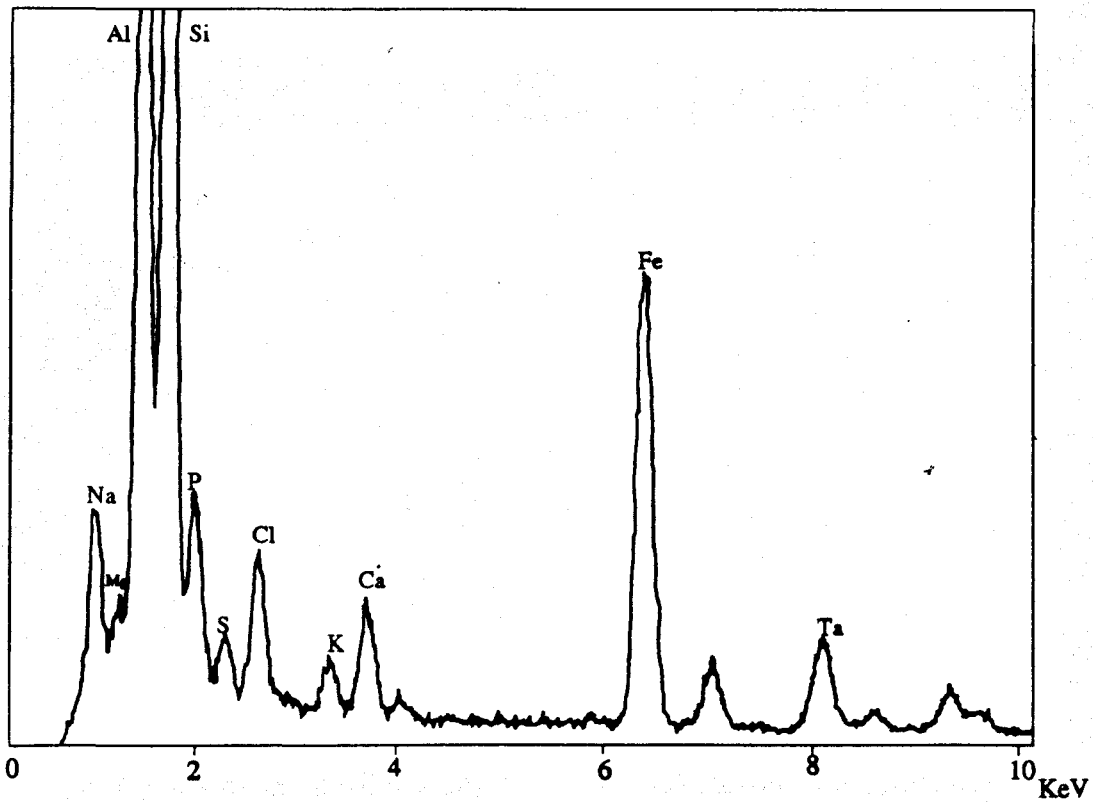


Fig.66 Typical TEM energy dispersive spectrum from the amorphous layer, composite material series 28%.

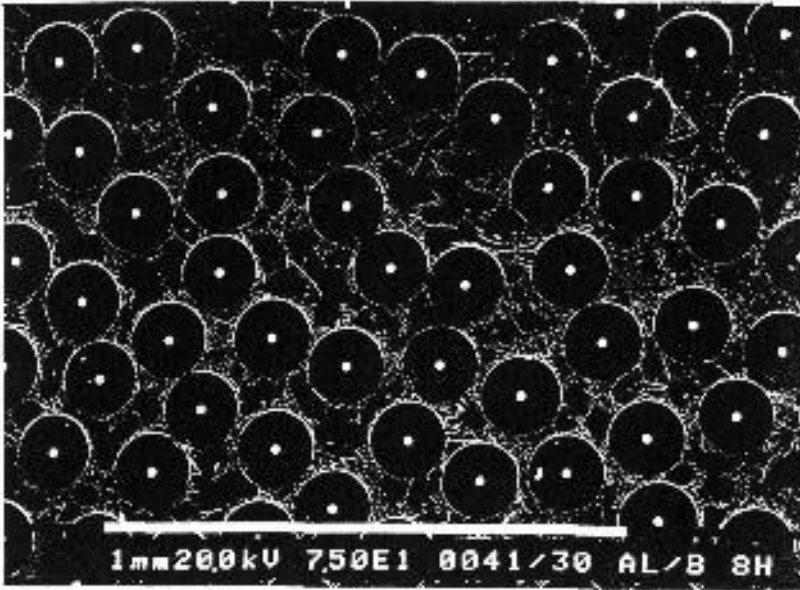


Fig.67 SEM micrograph of the cross section of the composite material series 48%. This picture shows the fibres, the matrix and dendrites cells smaller or similar size as the interfibre spacing.

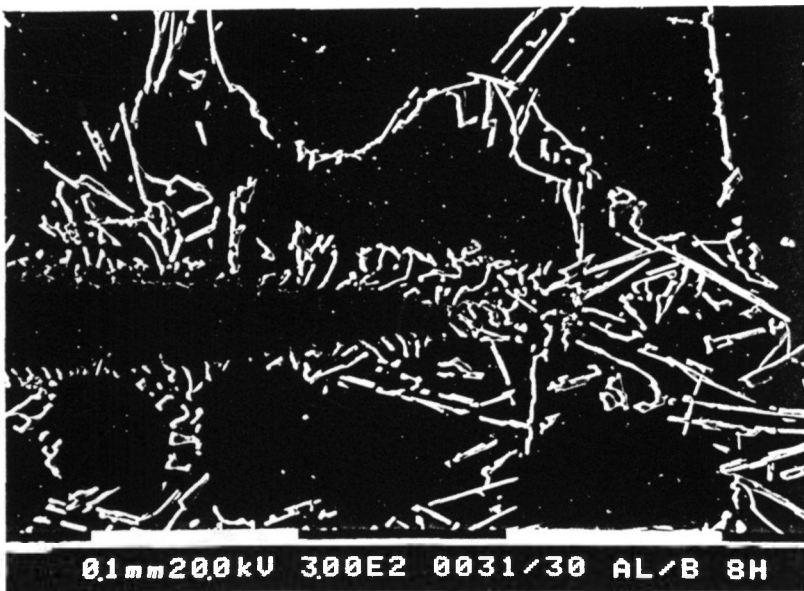


Fig.68 SEM micrograph of the longitudinal section of the 48% series material showing a tapered fibre and the aluminium alloy matrix. It is also possible to visualize a very thin layer on the borders of the SiC fibre coating.

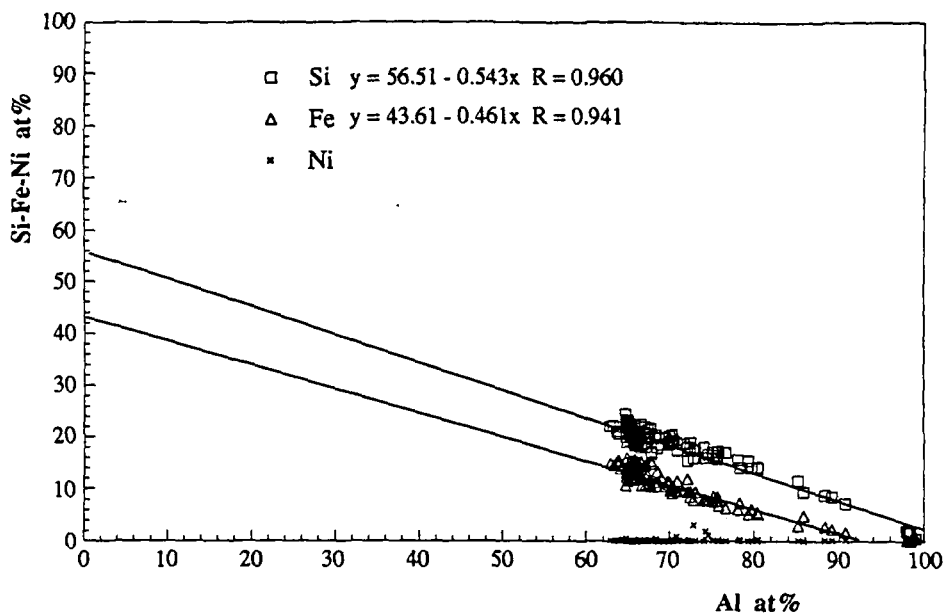


Fig.69 Variation in atom percent of Si, Fe and Ni versus Al for in-situ SEM analyses of 159 similar second phase platelet type, 48% series material.

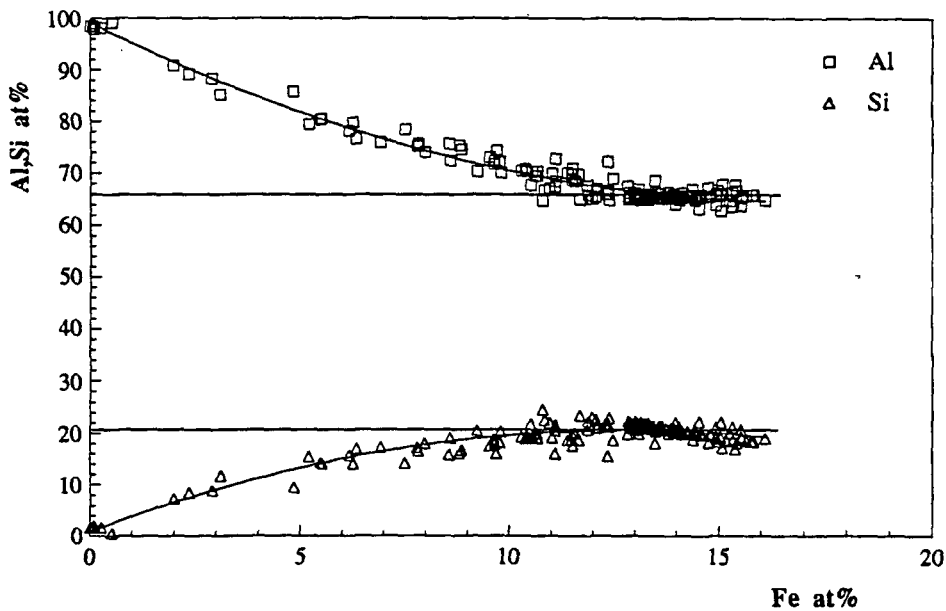
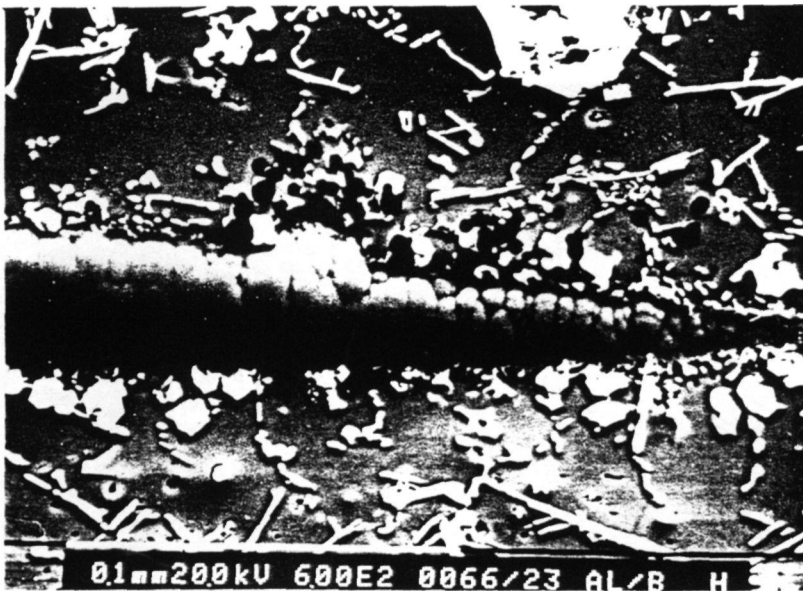


Fig.70 Variation in atom percent of Al and Si versus Fe for in-situ SEM analyses of platelet type constituents for 48% series material.



a)



b)

Fig.71 SEM micrograph of the matrix and slag inclusions in the material series 28%. a) Slag inclusion within the matrix, black contrast phase. b) Slag inclusions at fibre surface (black contrast phase)

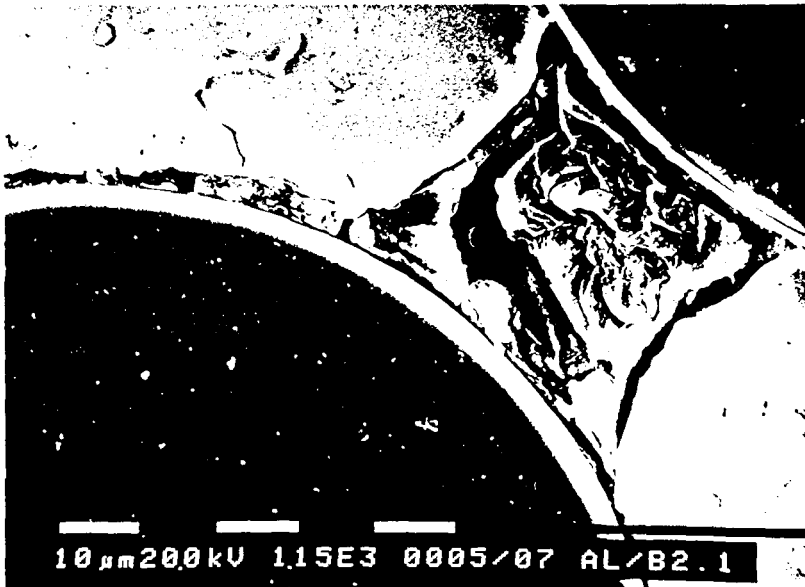


Fig.72 SEM micrograph from the 28% series material showing of a bridge phase between two fibres. This is probably slag entrapped between the fibres.

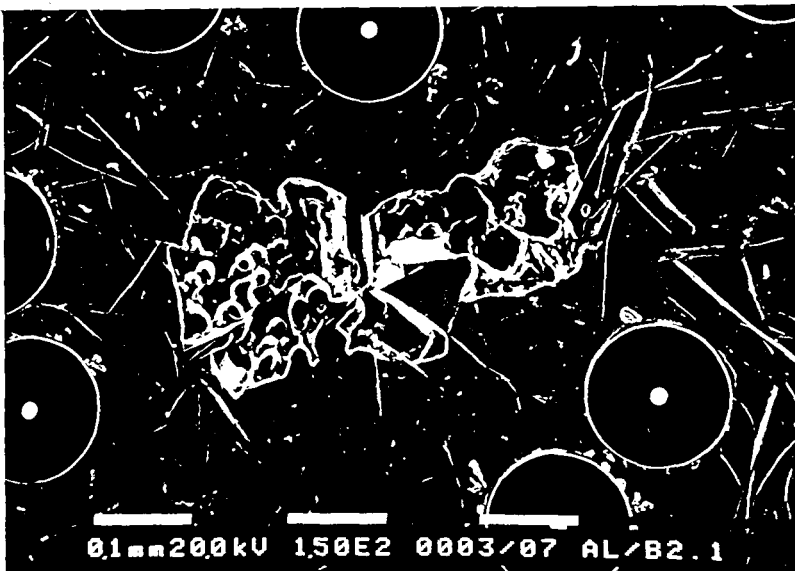


Fig.73 SEM micrograph from the 28% series material in the transverse direction showing a interfibre porosity.

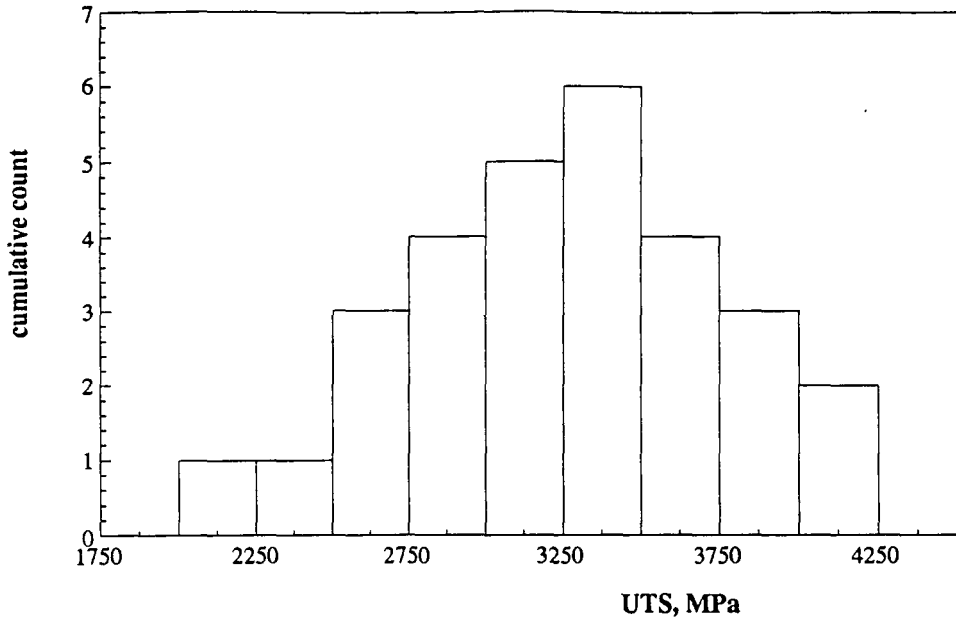


Fig.74 Histogram of SiC coated boron fibre strengths.

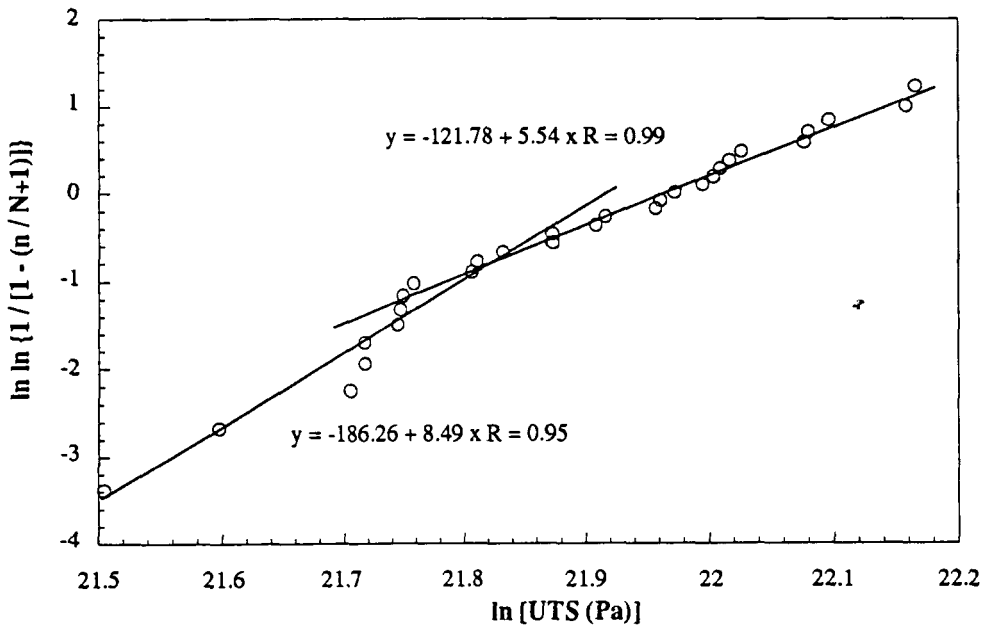


Fig.75 Weibull plot of probability of failure against fibre strength showing two types of flaw distribution.

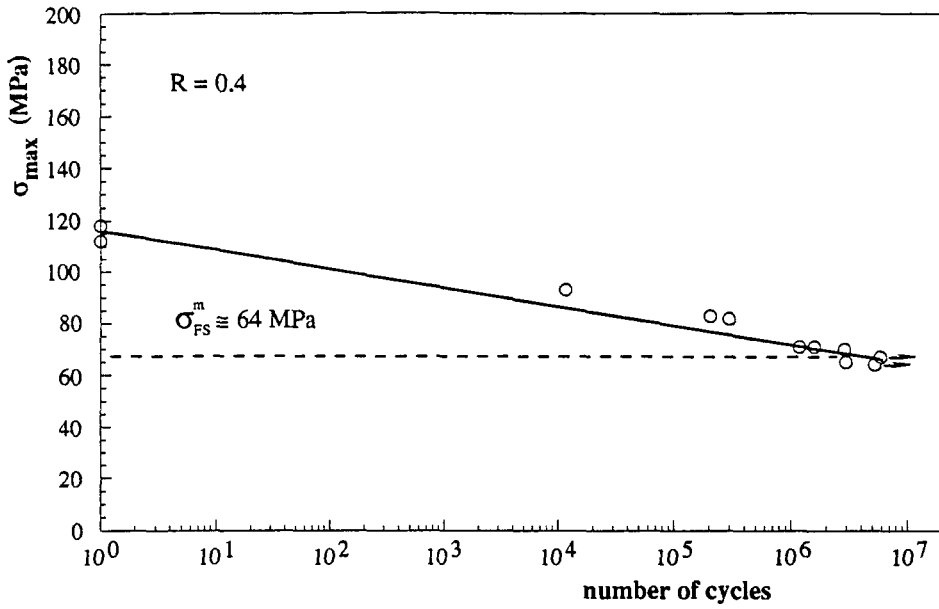


Fig.76 Fatigue tests results for the as received aluminium alloy prior to infiltration.

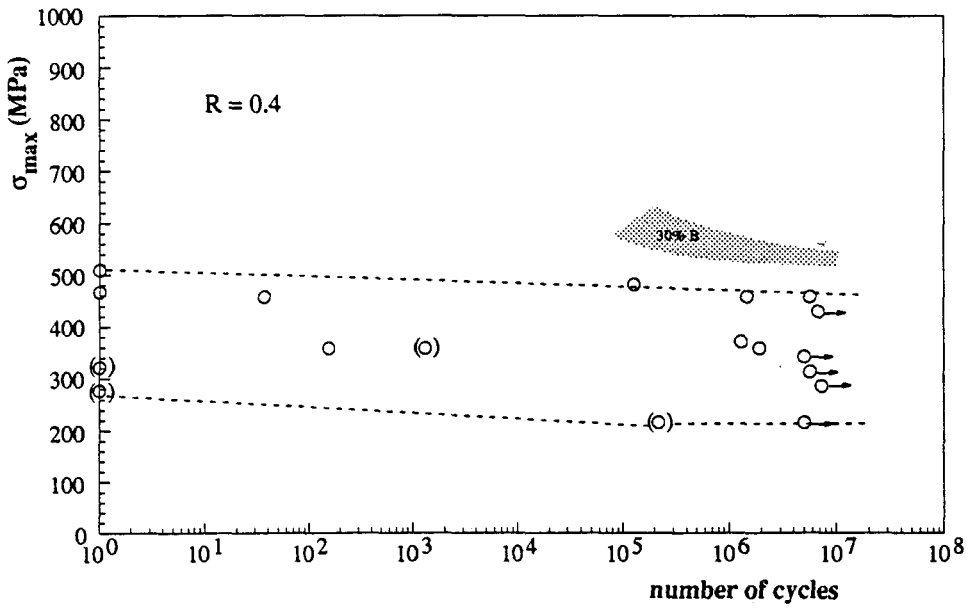


Fig.77 S-N plot for the 28% series material tested at 0° fibre orientation. (\odot) indicates major flaws. Shaded area represents data from literature [18].

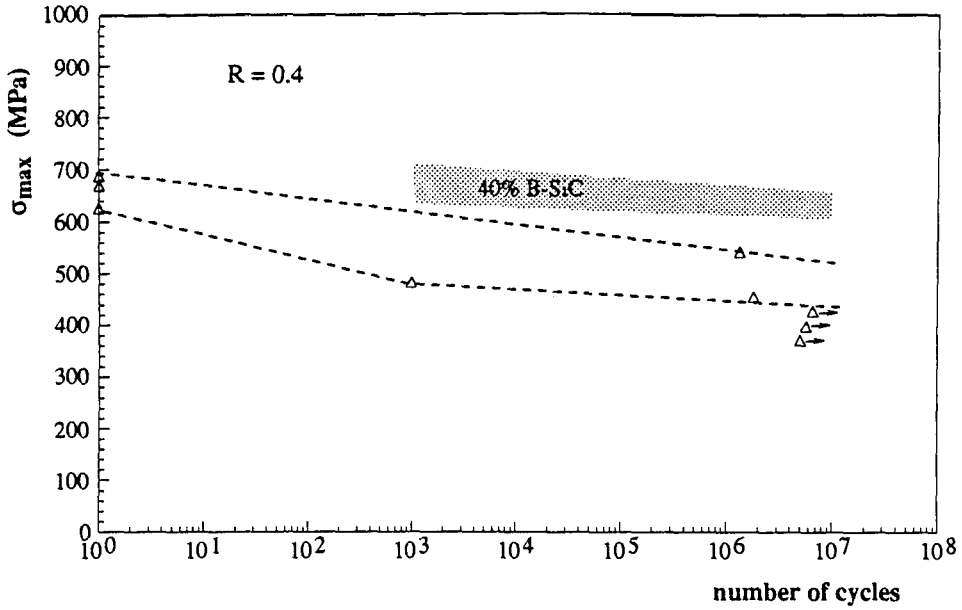


Fig.78 S-N plot for the 48% series material tested at 0° fibre orientation. Shaded area represents data from literature [18].

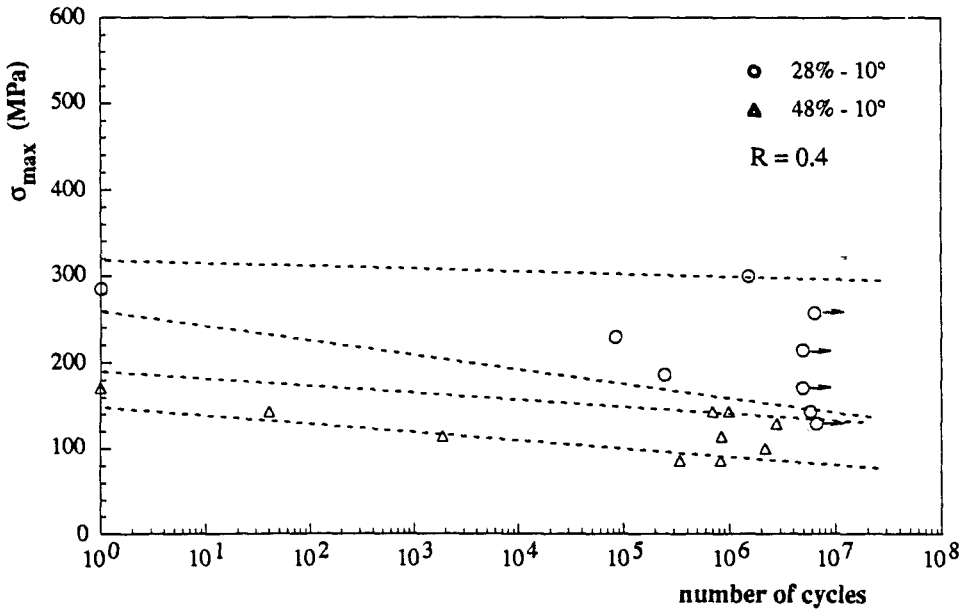


Fig.79 S-N plot for the 28% and 48% series materials tested at 10° fibre orientation.

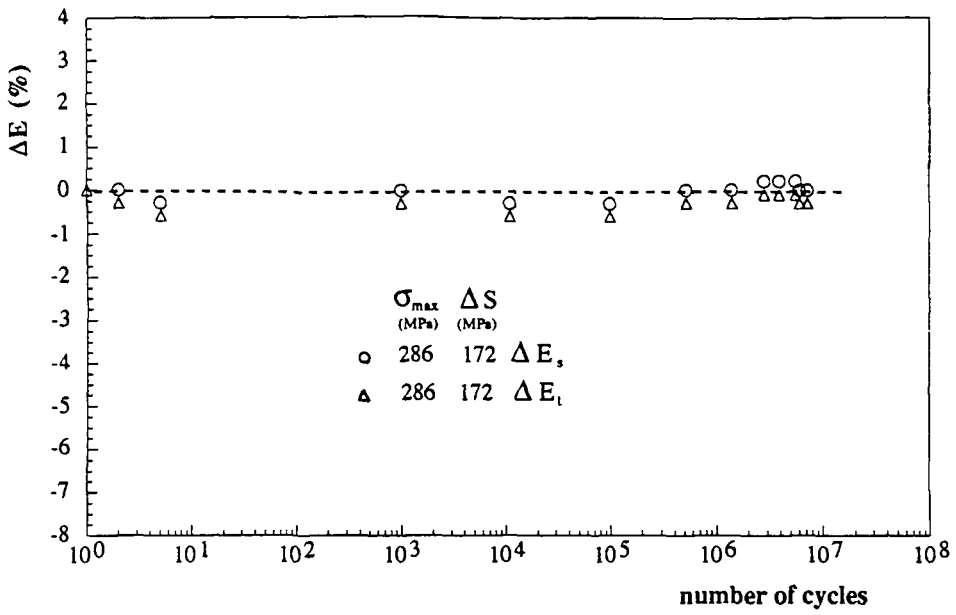


Fig.80 Variation of the fractional change of elastic modulus versus log number of cycles for 28%-0° series material at stress range less or equal to 172 MPa.

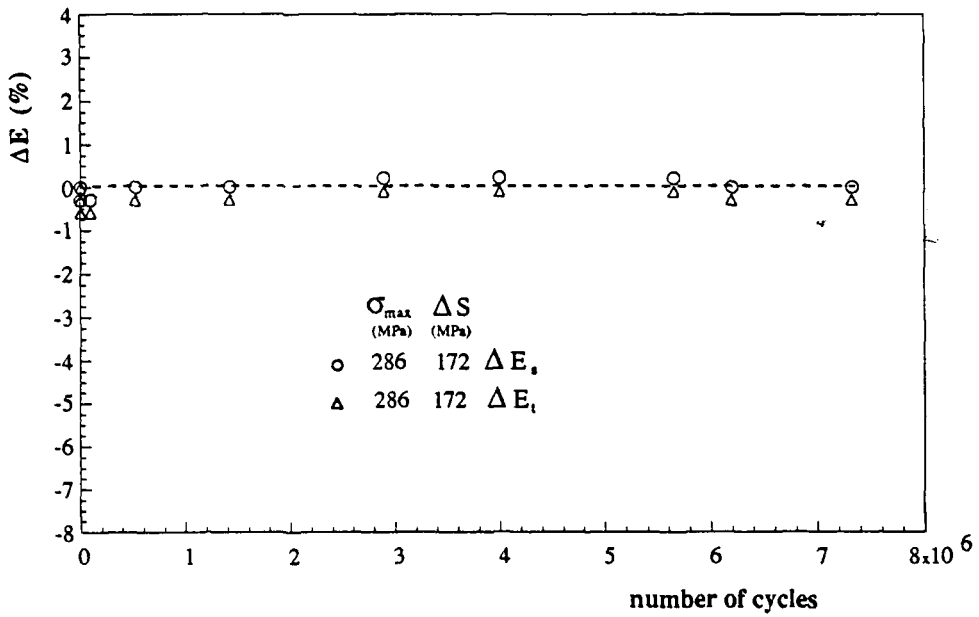


Fig.81 Variation of the fractional change of elastic modulus versus number of cycles (linear scale) for 28%-0° series material at stress range less or equal to 172 MPa.

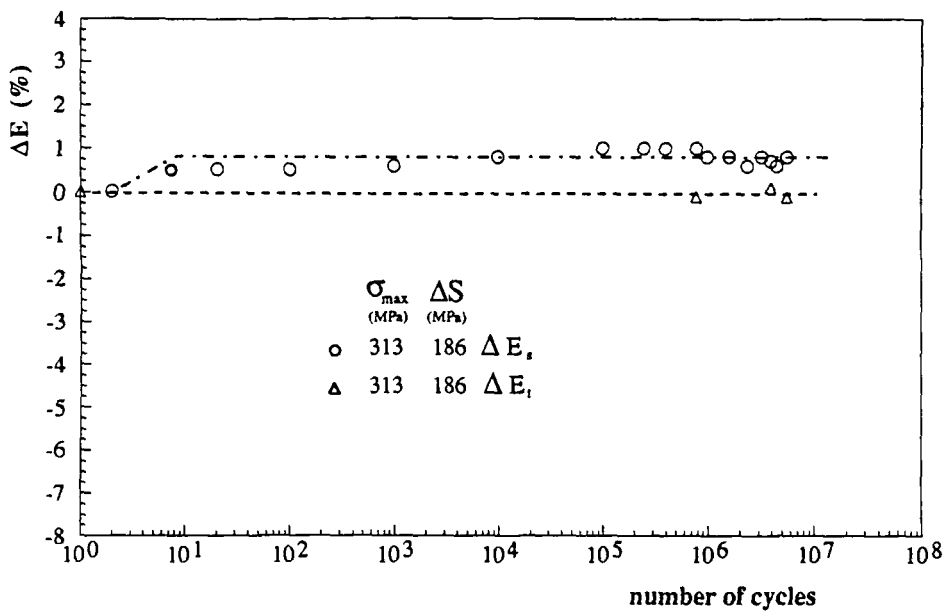


Fig.82 Variation of the fractional change of elastic modulus versus log number of cycles for 28%-0°series material at stress range 186 MPa.

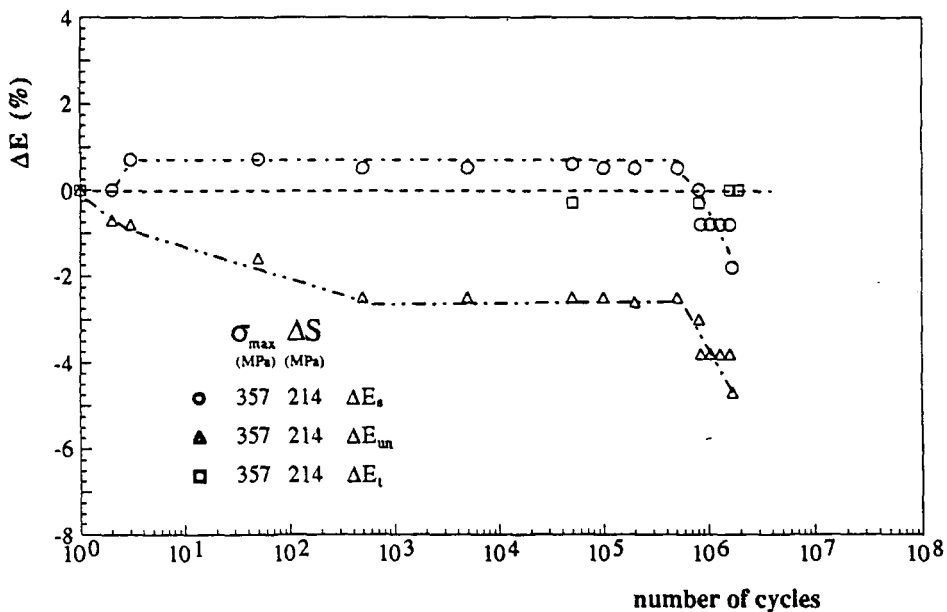


Fig.83 Variation of the fractional change of elastic modulus versus log number of cycles for 28%-0°series material at stress range 214 MPa.

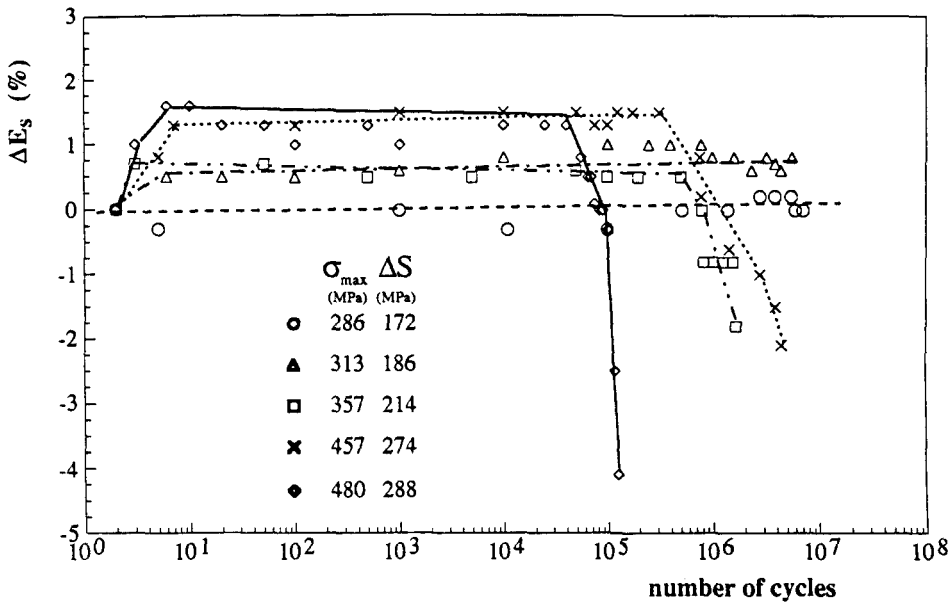


Fig.84 Variation of the fractional change of secant modulus versus log number of cycles for 28%-0° series material at different stress ranges.

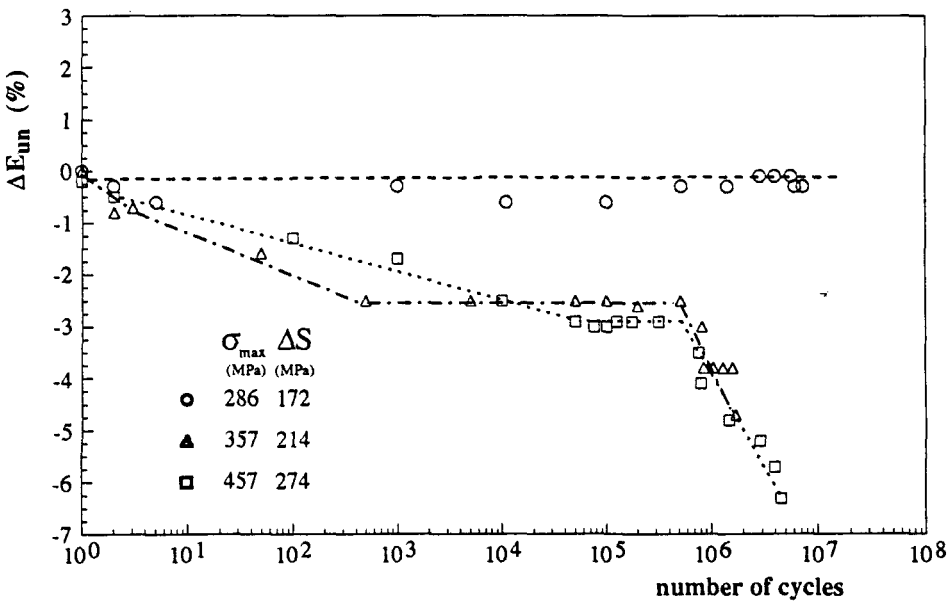


Fig.85 Variation of the fractional change of unloading modulus versus log number of cycles for 28%-0° series material at different stress ranges.

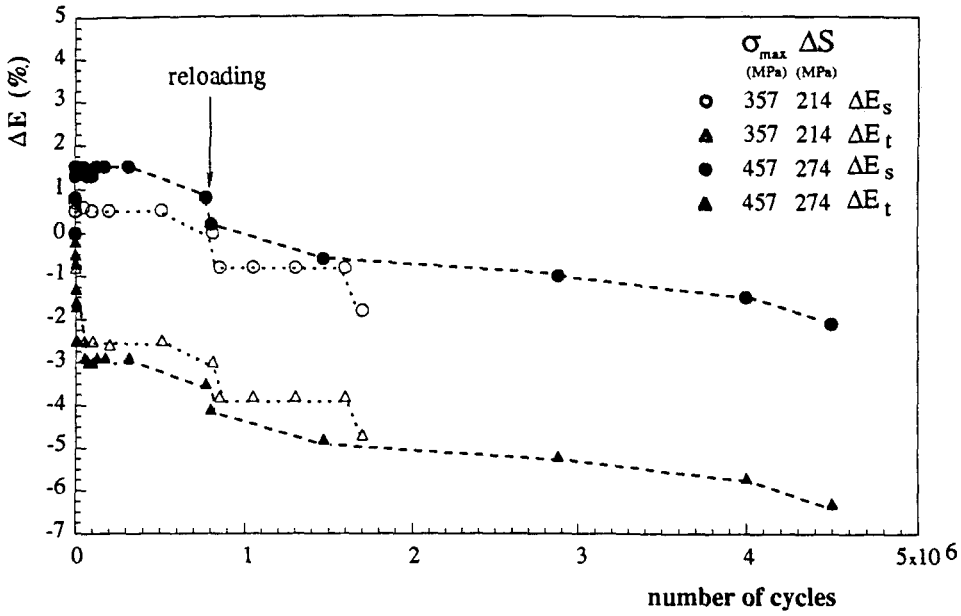


Fig.86 Variation of the fractional change of elastic modulus versus number of cycles (linear scale) for 28%-0° series material at different stress ranges.

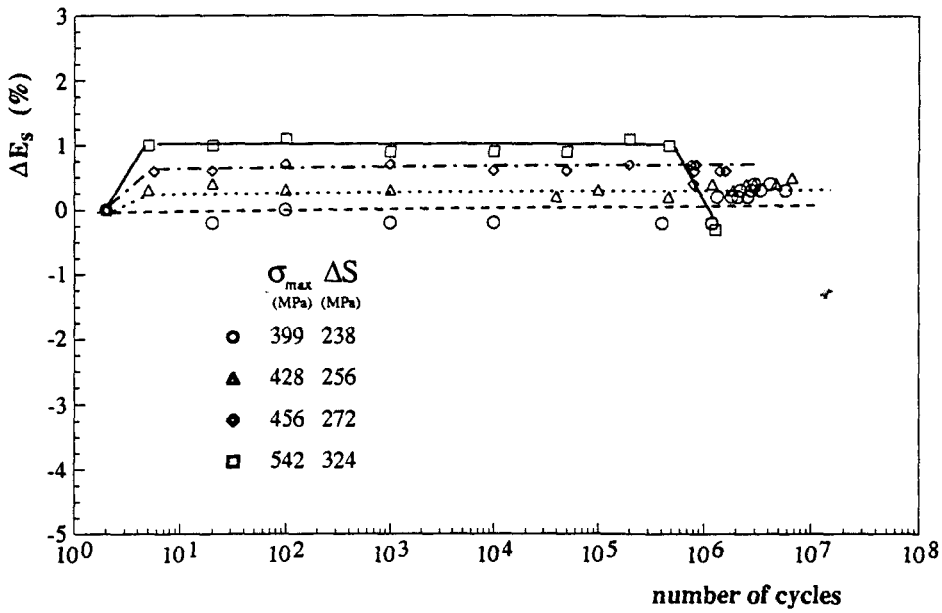


Fig.87 Variation of the fractional change of secant modulus versus log number of cycles for 48%-0° series material at different stress ranges.

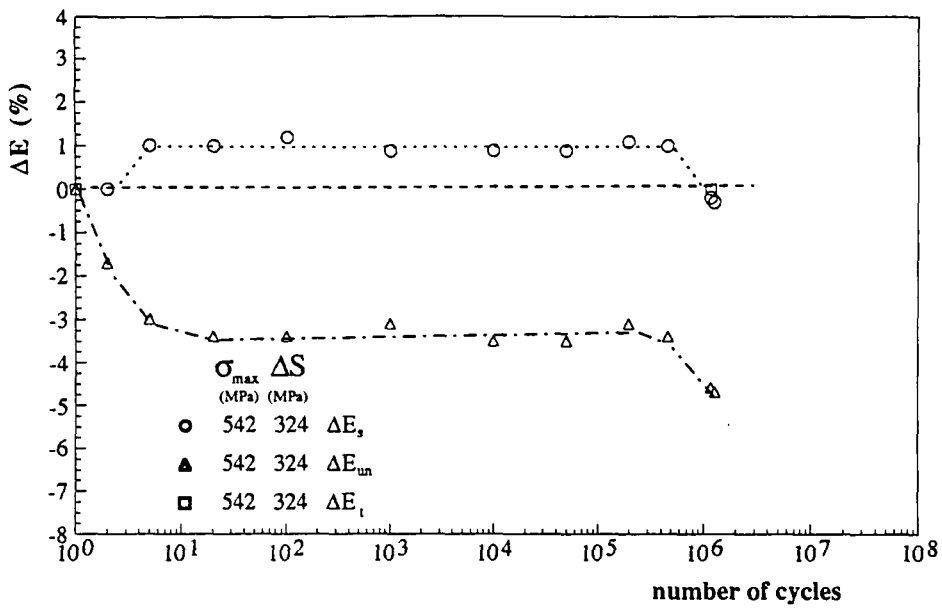


Fig.88 Variation of the fractional change of elastic modulus versus log number of cycles for 48%-0° series material at stress range 324 MPa.

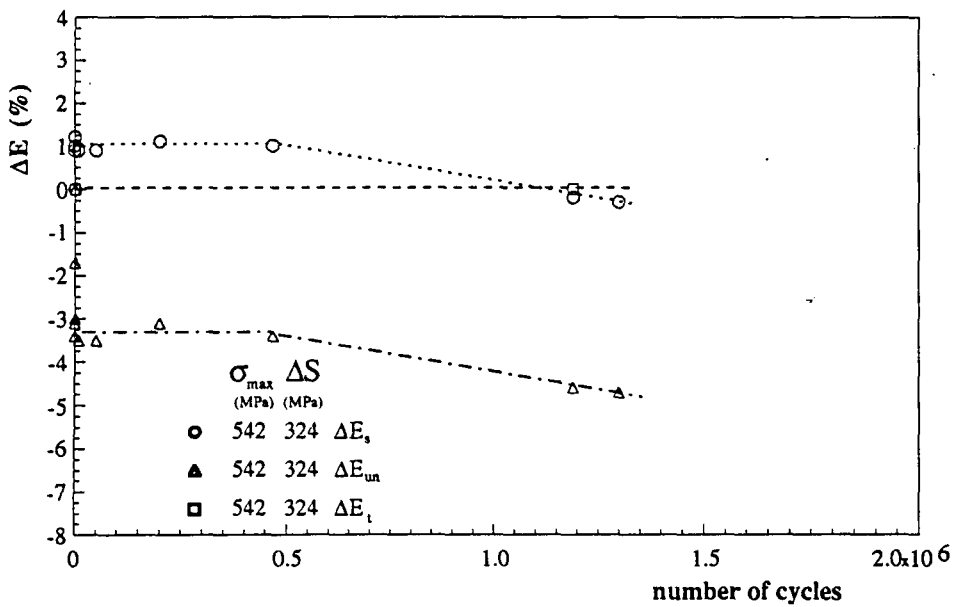


Fig.89 Variation of the fractional change of elastic modulus versus number of cycles (linear scale) for 48%-0° series material at stress range 324 MPa.

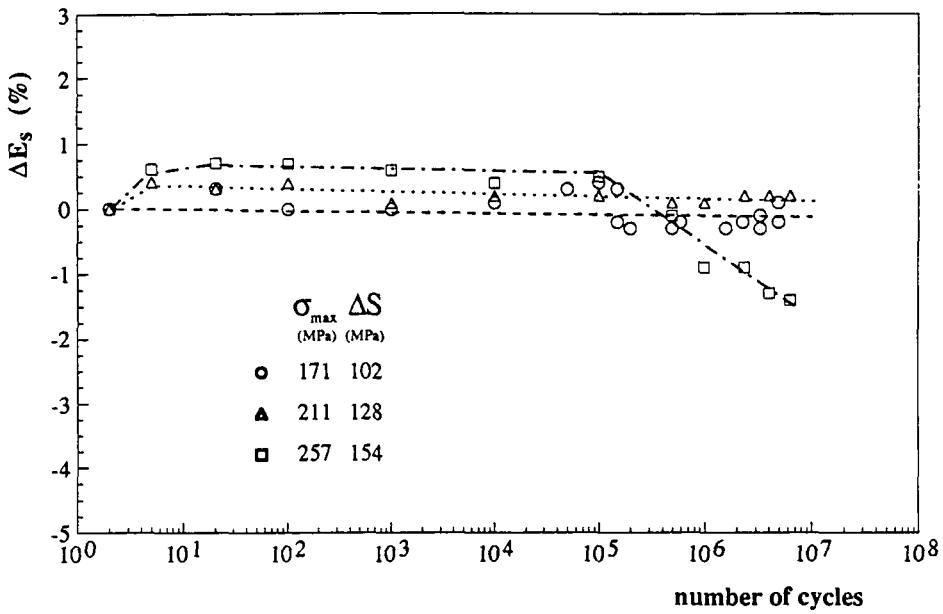


Fig.90 Variation of the fractional change of secant modulus versus log number of cycles for 28% series material, at 10° fibre orientation and at different stress ranges.

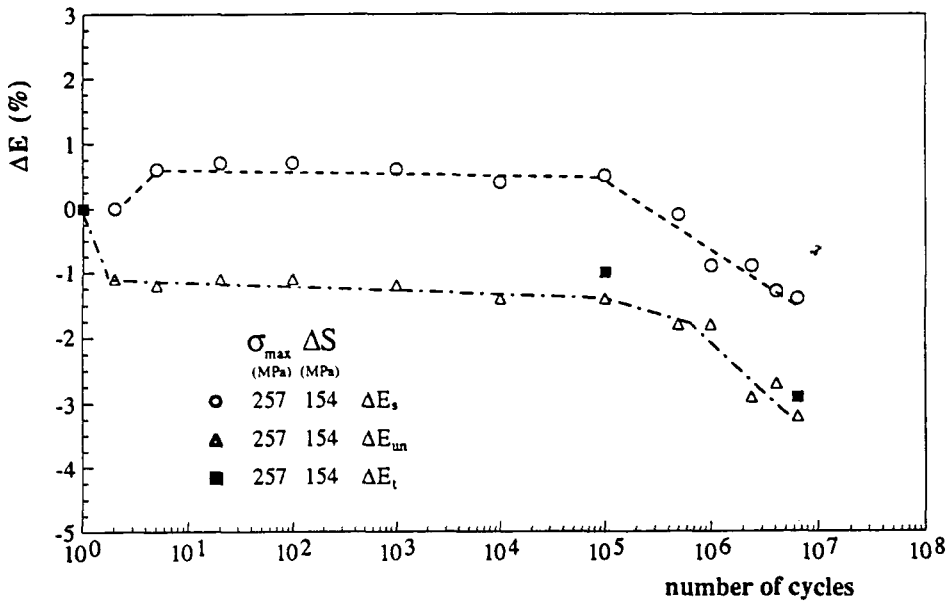


Fig.91 Variation of the fractional change of elastic modulus versus log number of cycles for 28% series material, at 10° fibre orientation and at stress range 154 MPa.

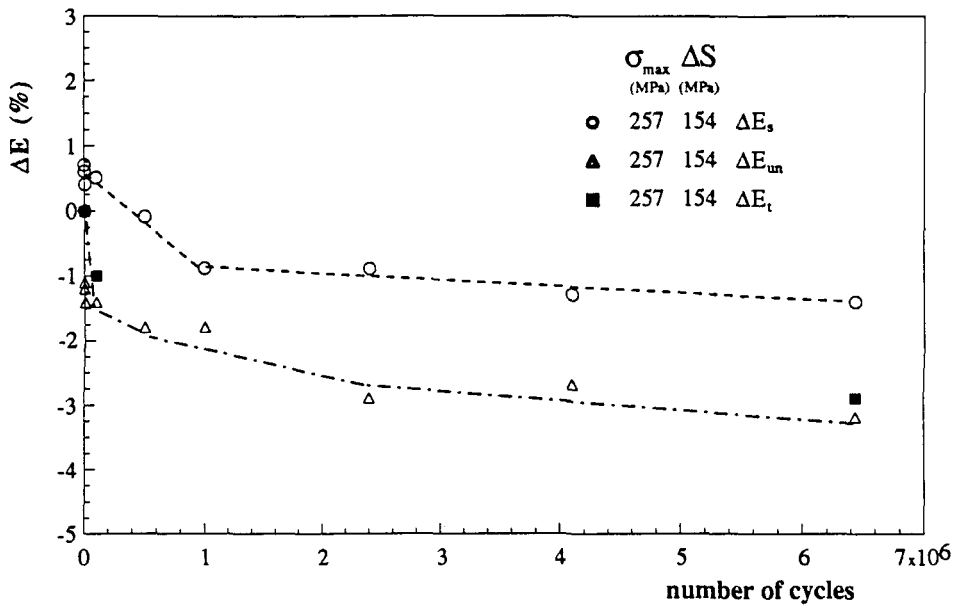


Fig.92 Variation of the fractional change of elastic modulus versus number of cycles (linear scale) for 28% series material, at 10° fibre orientation and at stress range 154 MPa.

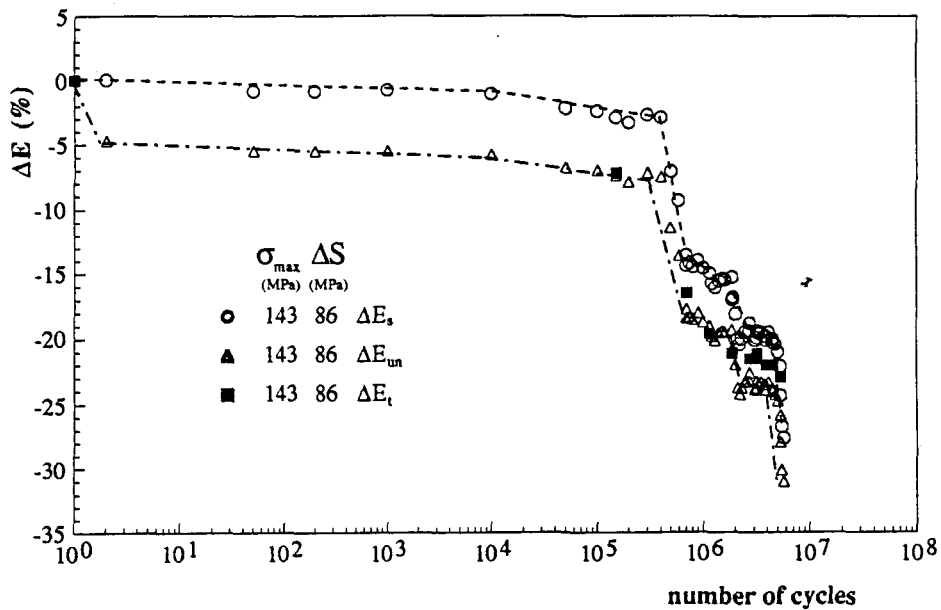


Fig.93 Variation of the fractional change of elastic modulus versus log number of cycles for 28% series material, at 10° fibre orientation.

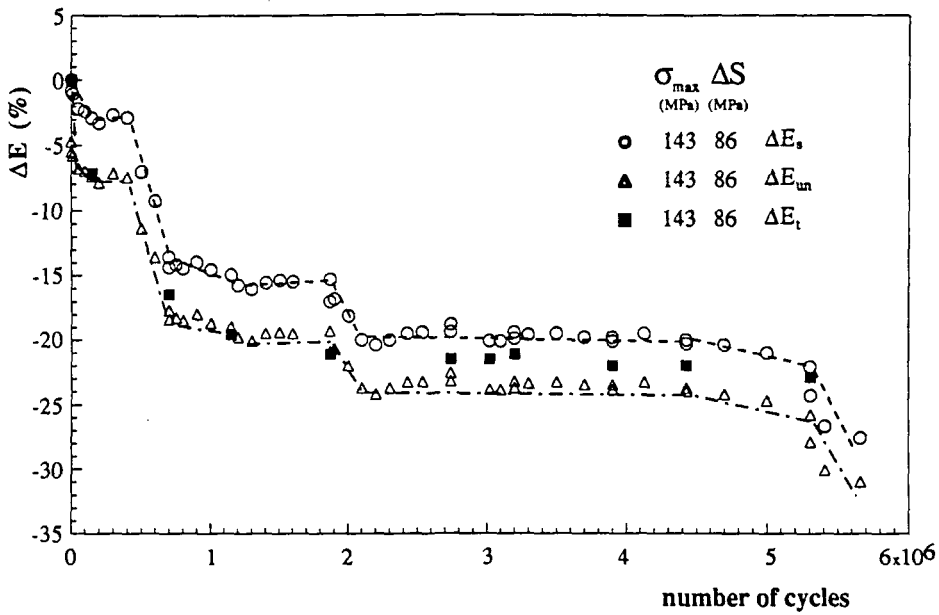


Fig.94 Variation of the fractional change of elastic modulus versus number of cycles (linear scale) for 28% series material, at 10° fibre orientation.

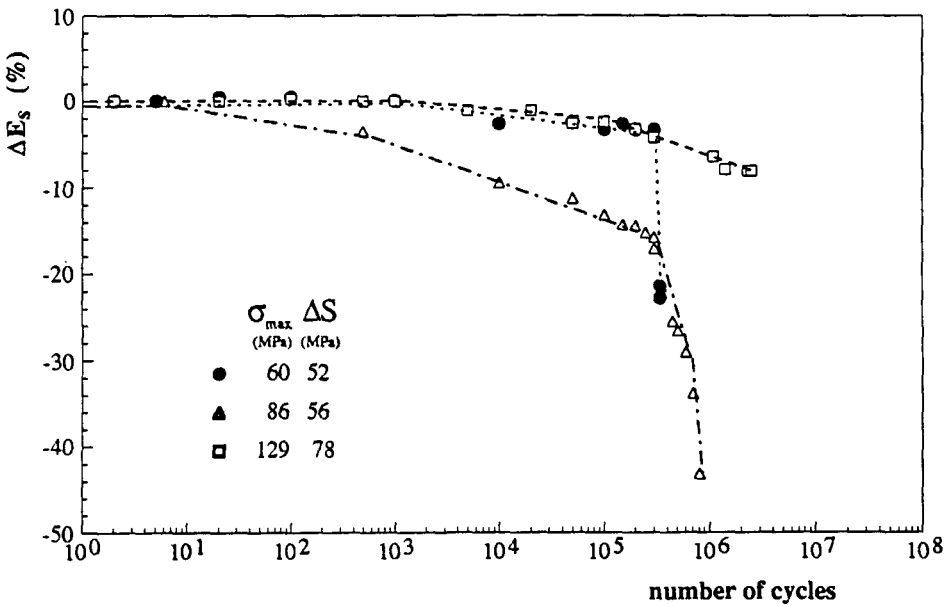


Fig.95 Variation of the fractional change of secant modulus versus log number of cycles for 48% series material, at 10° fibre orientation and at different stress ranges.

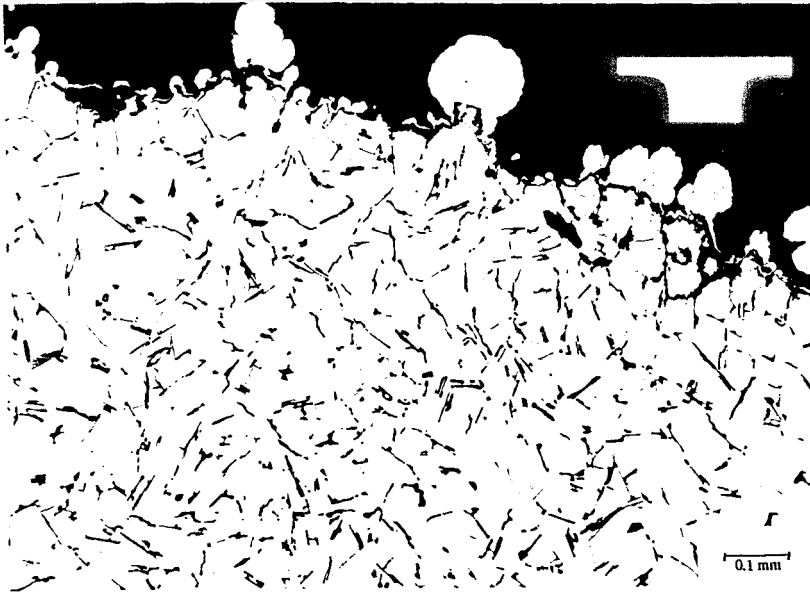


a)

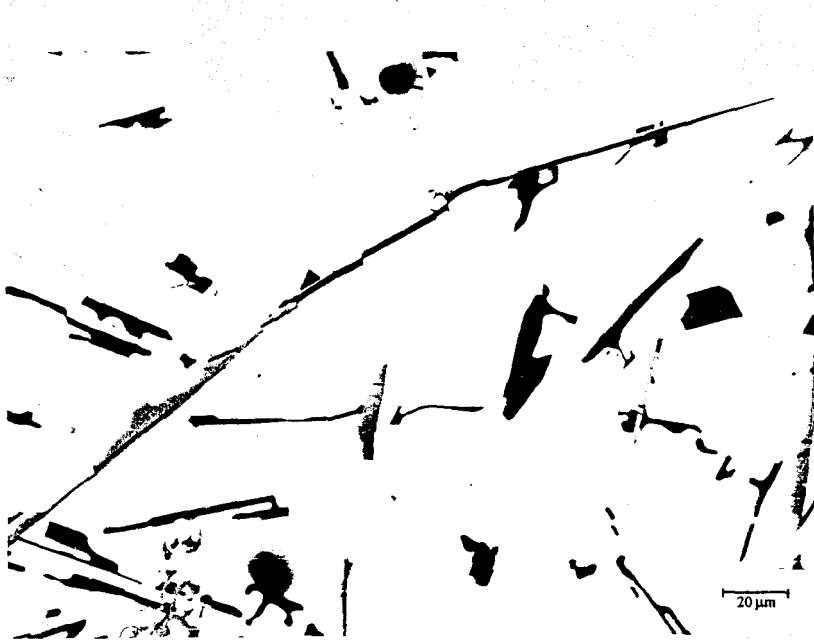


b)

Fig.96 Optical micrographs in the longitudinal section of the aluminium alloy after tensile testing. *a) Surface near fracture edge, showing a preferential fracture path through the interdendritic region. Nickel plated edge. b) Crack perpendicular to the tensile axis following the eutectic phase and cracked silicon flakes and intermetallics.*

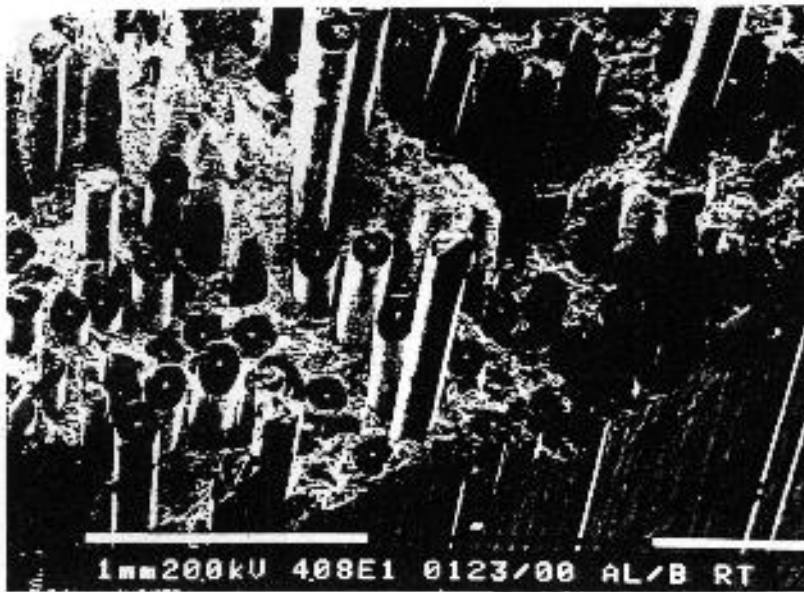


a)



b)

Fig.97 Optical micrographs of the longitudinal section of the aluminium alloy infiltration condition, after tensile testing. a) Surface near fracture edge showing that the preferential fracture path follows the dendrite cells contours. Nickel plated edge. b) A crack behind the fracture surface splitting a intermetallic phase.



a)



b)

Fig.98 SEM micrographs of the fracture surface of a tension test specimen, 28% series material. a) Overall fracture surface showing a irregular surface fracture and fibre pull out. b) High magnification of the fractured matrix between two fibres showing a ductile failure.

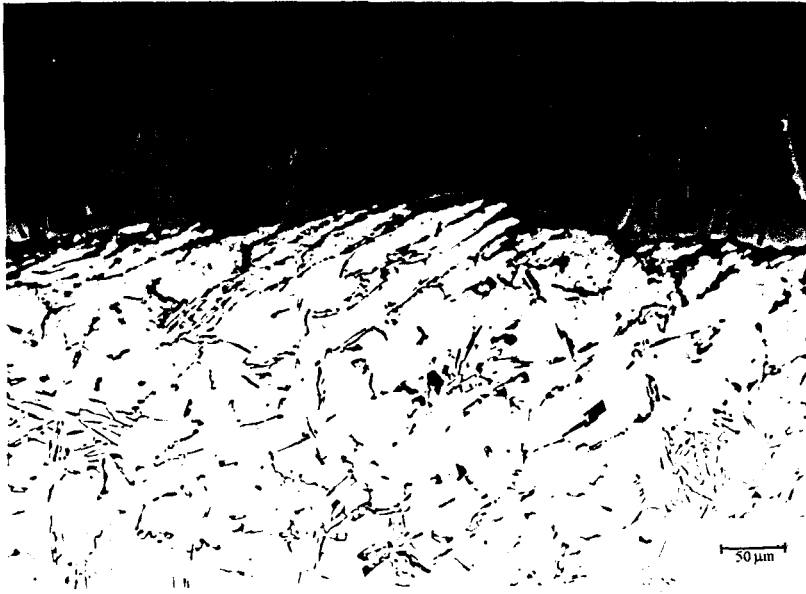


Fig.99 Optical micrograph of a polished longitudinal section of a 28% series specimen, tensile tested at 10° fibre orientation, showing matrix failure by shearing. Nickel plated edge.

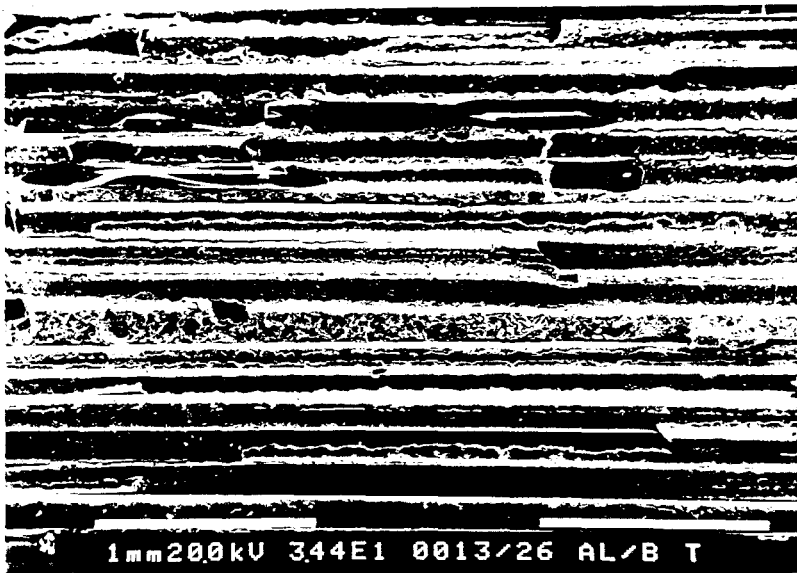


Fig.100 SEM micrograph of a tensile fracture surface of the 28% series in the transverse direction, showing preferential fracture path through the interface matrix-fibre and very little fibre splitting.

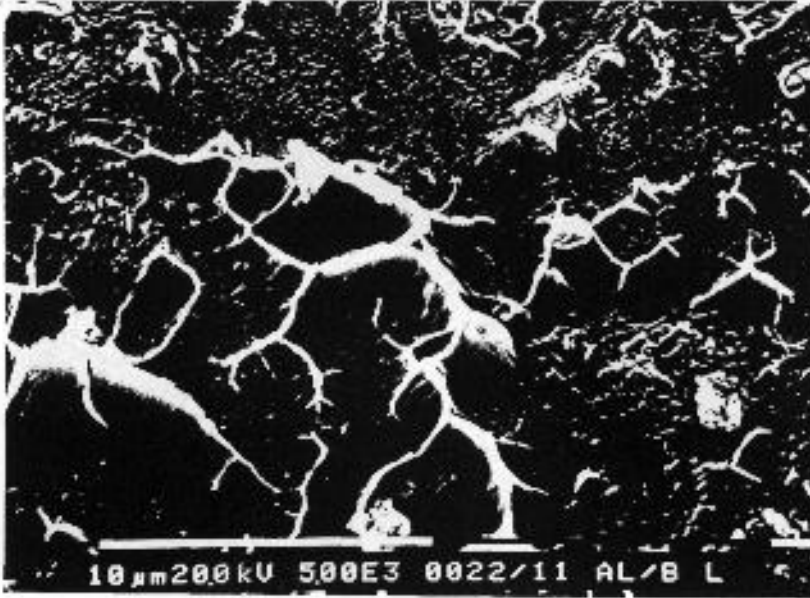


Fig.101 SEM micrograph of a transverse fracture of 28% series material showing in detail a fibre surface with some aluminium matrix adhered. This micrograph also shows that the matrix has fractured in a ductile mode.

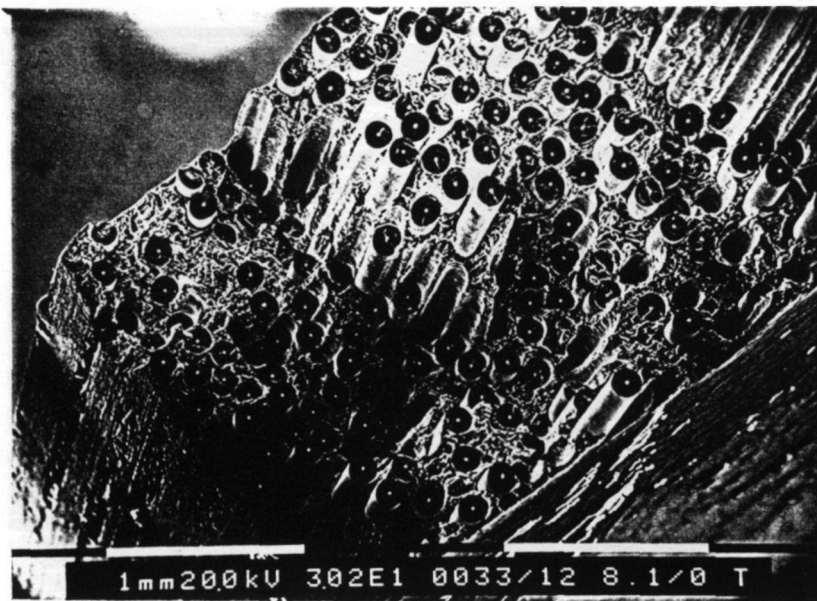


Fig.102 SEM micrograph of the tensile surface fracture of a 48% series specimen showing, fibre pullout and some shear fracture.



Fig.103 *Optical micrograph of a polished longitudinal section of a 48% series specimen, tensile tested, showing that the fracture path followed the interdendritic region. Nickel plated edge.*

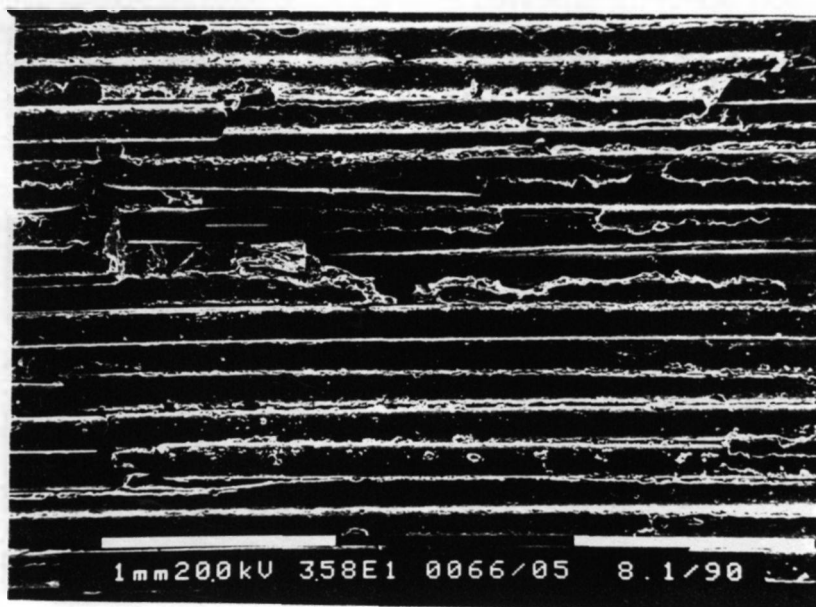


Fig.104 *SEM micrograph of a tensile fracture surface of the 48% series in the transverse direction showing, a preferential fracture path through the weak matrix-fibre interface and very little fibre splitting.*

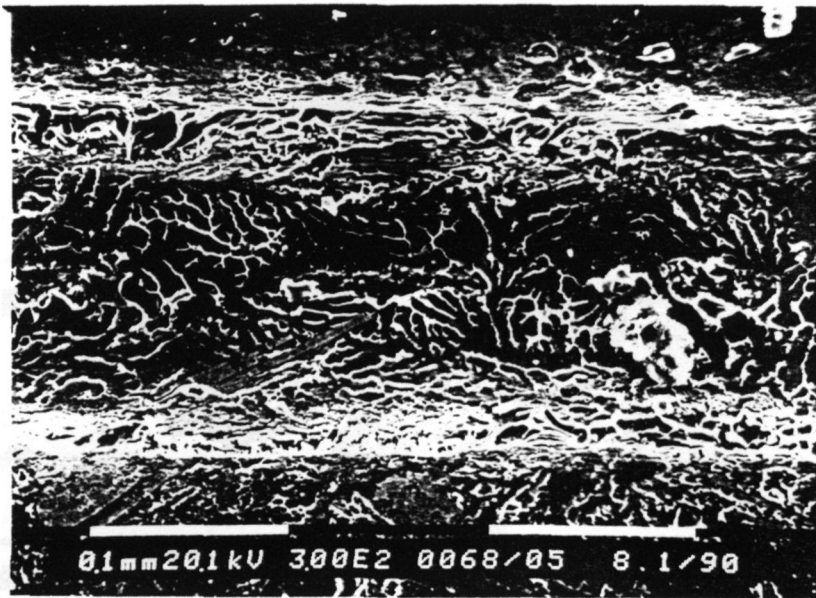


Fig.105 SEM micrograph of a transverse fracture, 48% series material, showing a valley left by a debonded fibre and the ductile fracture surface of the aluminium matrix.

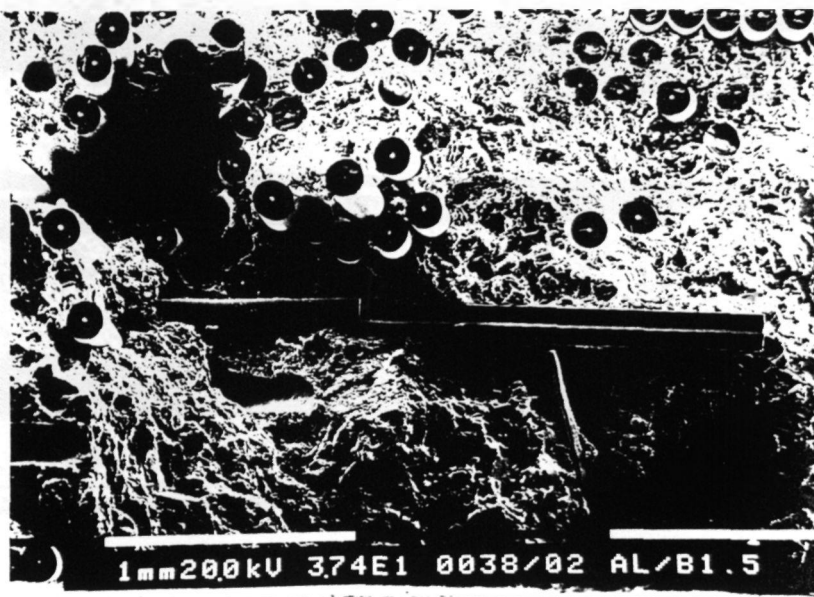


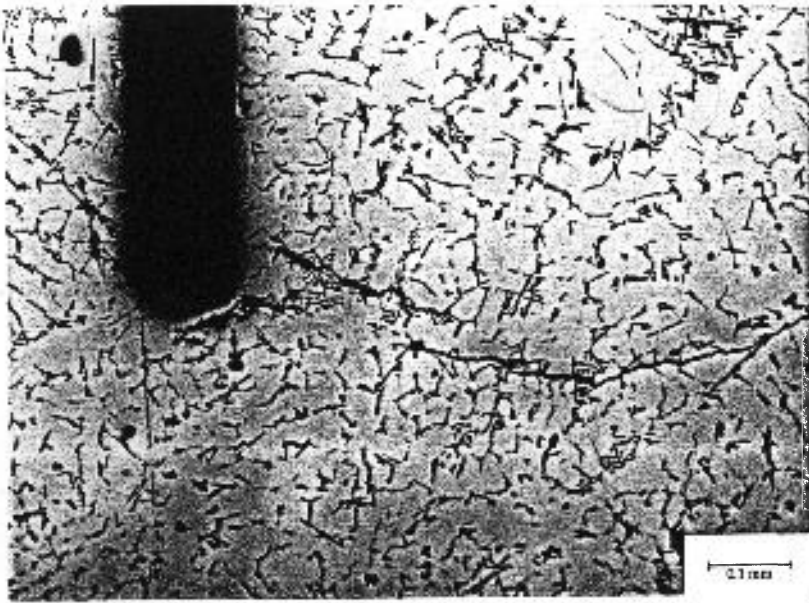
Fig.106 SEM micrograph of a longitudinal surface fracture, 28% series material, showing a transverse piece of fibre and a very low fibre fraction that caused the material to exhibit a poor tensile strength.



Fig.107 SEM micrograph of a fractured fibre showing that the fracture started at the fibre surface.



Fig.108 Optical micrograph of a longitudinal section of a 28% series specimen fatigue tested, showing several matrix cracks. The fibres were usually kept intact. Some pieces of fibres were plucked out during the specimen preparation.



a)



b)

Fig.109 Optical micrographs of longitudinal sections of the composite material, after fatigue testing. a) Fatigue fracture associated to a fibre end, 28% series material. b) Fatigue crack originated at specimen surface due to a broken fibre.



a)



b)

Fig.110 Micrographs of fatigue cracks, 28% series material. a) Optical micrograph of a fatigue crack associated to a porosity. b) SEM micrograph of a crack associated with the Ti interweaving strip, and a crack initiating in a porosity.

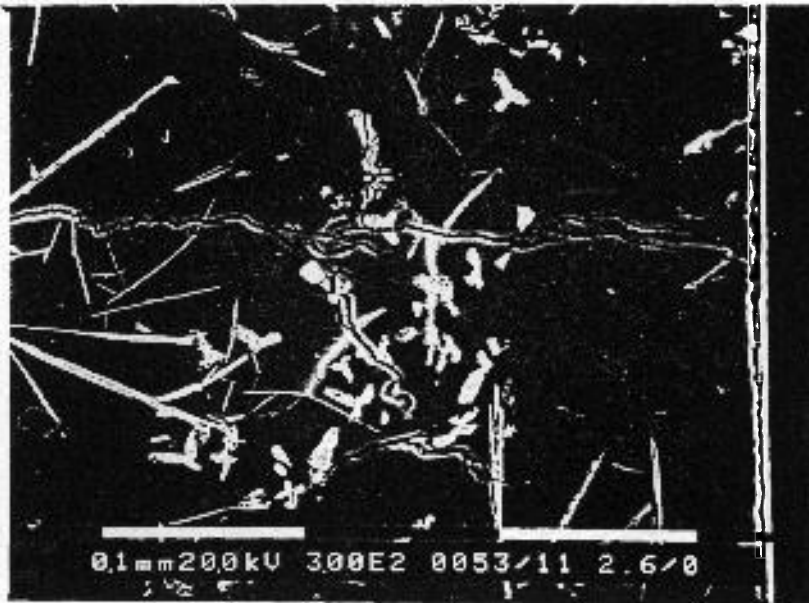


a)



b)

Fig.111 Optical micrographs of longitudinal sections of the 48% series material, after fatigue testing. a) Incipient crack associated with the fracture of two intermetallic constituents. b) Crack associated with a intermetallic constituent growing towards the matrix.

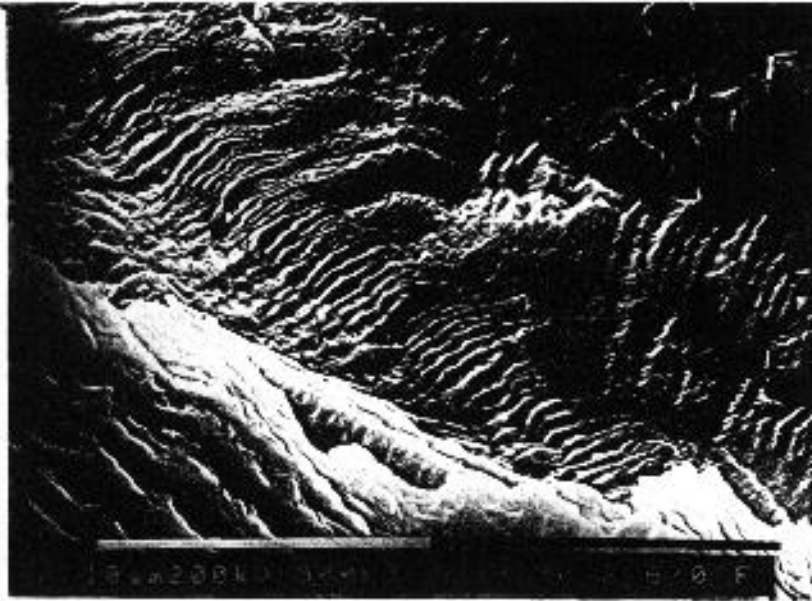


a)

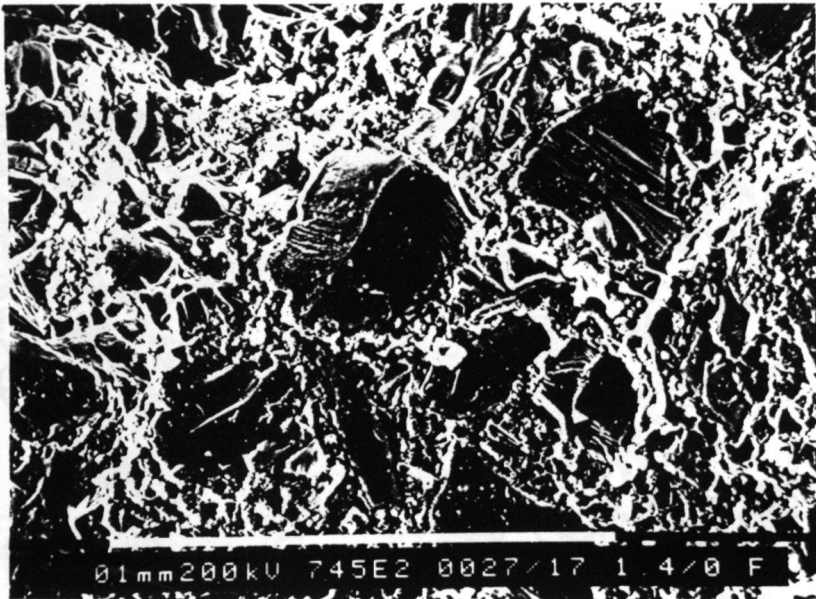


b)

Fig.112 SEM micrographs of longitudinal sections of the 28% series material, after fatigue testing. **a)** Secondary electron image of a fatigue branched crack over a fibre (this fibre is not shown in the micrograph). **b)** Backscattered electron image of a surface origin crack branching.



a)



b)

Fig.113 SEM micrographs of fracture surface, 28% series material. a) Fatigue striations on the aluminium matrix. b) Presence of cleaved particles in the fracture path.

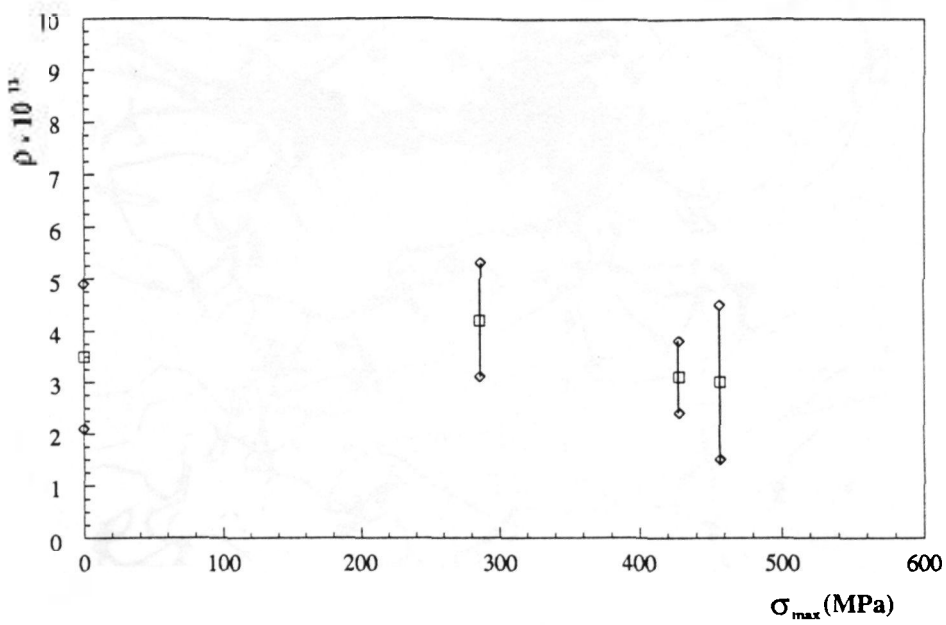
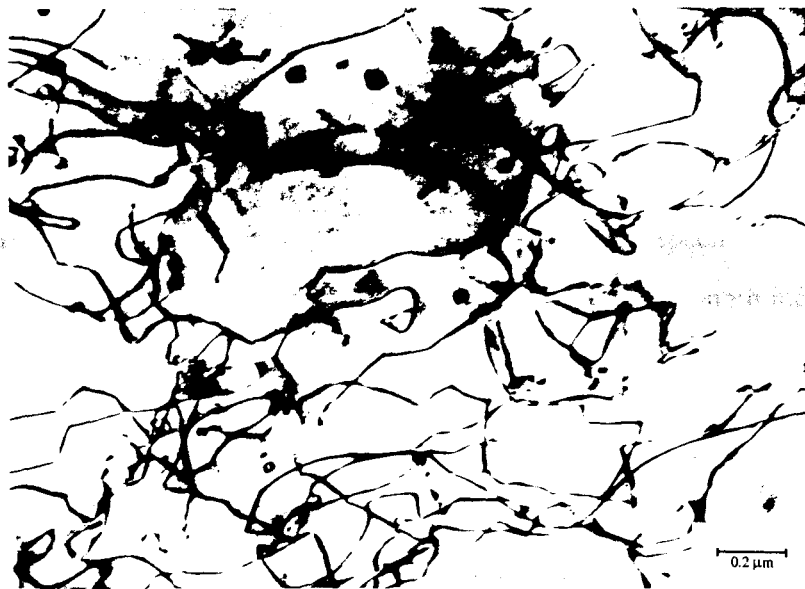


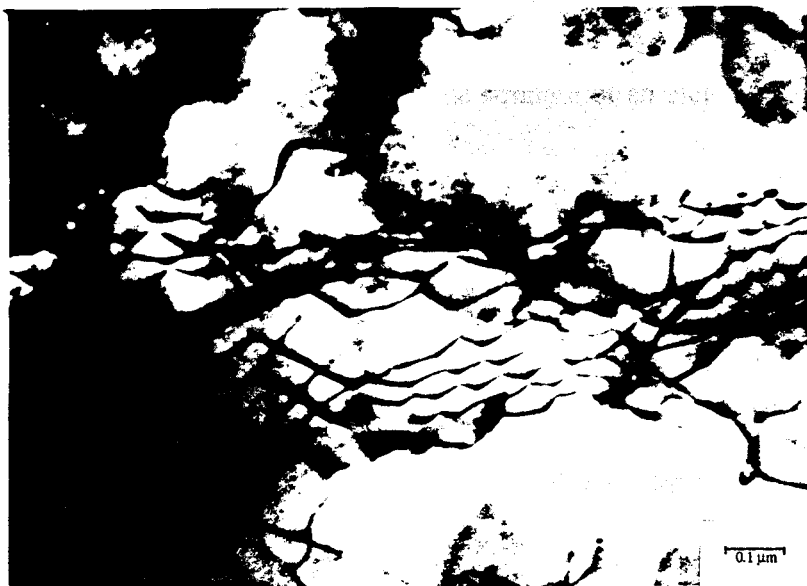
Fig.114 Variation on dislocation densities in the aluminium alloy matrix with maximum stress for the 28% series material tested at 0° fibre orientation.



Fig.115 Dislocation structure of a tensile tested specimen, 28% series, showing some dislocation debris. **B** [001].



a)



b)

Fig.116 Dislocation structure of a fatigue tested specimen, $\Delta S = 274$ MPa, 28% series material. a) Planar array of dislocations and prismatic dislocation loops. b) Incipient dislocation cell wall. B [112].

Appendix 1

Statistical characterization of strength

Scatter in strength values, verified with testing of similar specimens, occurs with all materials. The degree of scatter, however, frequently rises as the strength increases and the plastic deformation decreases. It is possible that cracks or flaws are responsible for the scatter, many of which are undetectable. Thus, a statistical approach can be used to predict and describe strength.

The statistical approach^[1] in this research is limited to the uniaxial tensile testing of fibres. First, it is assumed that fibre cracks either exist or are formed under load. The fibre volume, V , can be ideally divided into ω equal small elements of volume v such that $\omega = V/v$.

The severity of the flaw contained in each of the ω volumes determines the strength of the elemental volumes. The combined strengths of the elemental volumes constitute a population of strengths which can be represented by a probability distribution function, $f(\sigma)$,

where $f(\sigma)d\sigma$ is the probability of finding the strength of an elemental volume in the range σ to $\sigma + d\sigma$.

The cumulative probability distribution function, $F(\sigma)$, of finding the strength of an elemental volume, v , in the range from 0 to σ is defined as

$$F(\sigma) = \int_0^{\sigma} f(\sigma) d\sigma . \quad (1)$$

If σ_f is the theoretical strength, then

$$F(\sigma) = \int_0^{\sigma_f} f(\sigma) d\sigma = 1 . \quad (2)$$

Thus, by definition, $[1 - F(\sigma)]$ is the probability that an element of volume v will not fracture at stress equal or less than σ .

With cylindrical fibres, the volume v is suitably taken as equal to the entire cross section and a length equal to the diameter. Hence, a cylindrical fibre of length l and diameter d_f has $\omega = l/d_f$ elemental volumes.

The probability that a fibre containing ω elemental volumes fractures in the range $\sigma + d\sigma$, is called the probability density function, and is denoted by $g(\sigma)$,

$$g(\sigma)d\sigma = f(\sigma)[1 - F(\sigma)]^{\omega-1} \omega d\sigma, \quad (3)$$

where $f(\sigma)$ is the probability that one of the ω elements will fracture in the range σ to $\sigma + d\sigma$, and $[1 - F(\sigma)]^{\omega-1}$ is the probability that the remaining $(\omega - 1)$ elements will not fracture until the stress exceeds σ . The remaining term, ω , accounts for the sum of these probabilities over the total of ω elements.

The probability that a fibre will fail in the range from 0 to σ is called the cumulative probability distribution function and is denoted by $G(\sigma)$,

$$G(\sigma) = \int_0^\sigma g(\sigma)d\sigma = \int_0^\sigma \omega f(\sigma)[1 - F(\sigma)]^{\omega-1} d\sigma. \quad (4)$$

Integration of Eq.(4) gives

$$G(\sigma) = \{- [1 - F(\sigma)]^\omega\}_0^\sigma \quad (5)$$

and

$$G(\sigma) = 1 - [1 - F(\sigma)]^\omega. \quad (6)$$

Weibull^[2] suggested that the function $F(\sigma)$ is

$$F(\sigma) = \left(\frac{\sigma - \sigma_u}{\sigma_0} \right)^m \quad (7)$$

within appropriate physical limits, i.e., strength range from $+\sigma_u$ to $+(\sigma_0 + \sigma_u)$, a good empirical fit to data and a mathematically simple form.

Then, $G(\sigma)$ becomes

$$G(\sigma) = 1 - \left[1 - \left(\frac{\sigma - \sigma_u}{\sigma_0} \right)^m \right]^\omega. \quad (8)$$

Eq.(8) is not convenient for purposes of calculation. For small values of $x = [(\sigma - \sigma_u)/\sigma_0]$, the Poisson's approximation is;

$$1 - [1 - x^m]^\omega \approx 1 - e^{-\omega x^m} . \quad (9)$$

Thus $G(\sigma)$ is

$$G(\sigma) = 1 - \exp \left[- \omega \left(\frac{\sigma - \sigma_u}{\sigma_0} \right)^m \right], \quad (10)$$

where σ_u is a lower limiting strength below which fracture never occurs, σ_0 is a scale parameter, and m is a parameter that describes the data scatter. In the special case, $\sigma_u = 0$, σ_0 becomes equal to the theoretical strength in Eq.(7).

The Weibull function, Eq.(7), was introduced empirically based on comparison with extensive experimental data. This function, in many cases, was found to fit the observations better than other known distribution functions. Therefore, physical interpretation can be assigned to σ_0 and to σ_u , but no theoretical foundation can be provided for these interpretation.

In Eq.(10) the measurable quantities are the strength σ and ω (l/d for a cylindrical fibre). The quantity $G(\sigma)$ is estimated from a group of N samples by noting the number of samples, n , that have fractured at a stress of σ or less. Thus,

$$G(\sigma) = n / N. \quad (11)$$

As most experiments involve only few samples, N , of a possible large population, it is better to define $G(\sigma)$ as:

$$G(\sigma) = n / (N + 1). \quad (12)$$

Equation (10) can be rearranged by taking twice natural logarithms

$$\ln \ln \left[\frac{1}{1 - G(\sigma)} \right] = \left[\ln \frac{l}{d_f} - m \ln \sigma_0 \right] + m \ln (\sigma - \sigma_u). \quad (13)$$

Equation (13) suggests a useful form for plotting experimental data and for the determination of the parameters σ_u , σ_0 and m . For instance, σ_u is determined to produce the best-fit straight line to the data, on a graph with $\ln \ln \{ 1 / (1 - G(\sigma)) \}$ as ordinate and

$\ln(\sigma - \sigma_u)$ as abscissa. The parameter m is the slope of this line and 1 is often called the Weibull modulus. Knowing ω and m , it is possible to estimate the value of σ_0 from the intercept when $(\sigma - \sigma_u) = 0$.

The mean strength, $\bar{\sigma}$, of a group of fibres is given^[3] by;

$$\bar{\sigma} = \sigma_0 \omega^{-\frac{1}{m}} \Gamma\left(\frac{m+1}{m}\right) + \sigma_u, \quad (14)$$

and the variance of σ , which is equal to the square of the standard deviation, S , is;

$$S^2 = \sigma_0^2 \omega^{\frac{-2}{m}} \left[\Gamma\left(\frac{m+2}{m}\right) - \Gamma^2\left(\frac{m+1}{m}\right) \right], \quad (15)$$

where $\Gamma[(m+2)/m]$ and $\Gamma[(m+1)/m]$ are tabulated gamma functions.

It is usually assumed that the Weibull distribution provides a good fit to the data with $\sigma_u = 0$. σ_u is the stress below which fracture never occurs^[1,4].

Thus,

$$\ln \ln \left[\frac{1}{1 - \left(\frac{n}{N+1}\right)} \right] = m \ln \sigma + \text{constant} . \quad (16)$$

References

- [1] CORTEN, H. T. Micromechanics and fracture behavior of composites. In: BROUTMAN, L. J. & KNOCK, R. H., eds. *Modern Composite Materials*. Addison-Wesley, 1967. 27-105.
- [2] WEIBULL, W. A statistical distribution function of wide applicability. *J. Appl. Mech.*, Sep 1951. 293-7.
- [3] WALHAUS, R. A. A statistical study of factors influencing the strength of glass fibers. Univ. of Illinois, TAM Report no.217, May 1962. Quoted by: CORTEN, H. T. Micromechanics and fracture behavior of composites. In: BROUTMAN, L. J. & KNOCK, R. H., eds. *Modern Composite Materials*. Addison-Wesley, 1967. 27-105.
- [4] ANDERSON, C. H. & WARREN, R. The strength and elastic modulus of multifilament SiC fibres. In: BUNSEL, A. R.; BATHIAS, C.; MARTRECHAR, A.; MENKES, D.; VERCHERY, G., eds. *Advances in Composite Materials*. Vol. 2, Pergamon, 1980. 1129-39.

Appendix 2

Strain gauge techniques

The term strain is used in engineering to refer to a change in any linear dimension of a body usually subjected to the application of an external force. The strain gauge principle was based on the fact that the electrical resistance of certain metal wires varied with the tension to which the wire was subjected^[1]. Commercial resistance strain gauges may consist of a foil grid manufactured from a copper nickel alloy. The grid form is accurately produced by photo-etching techniques. A polyester film is used to encapsulate the grid, which helps to protect the gauge from mechanical and environment damage and also acts as a medium to transmit the strain from the test object to the gauge material.

In using electric strain gauges, two physical quantities are of particular interest, the change in gauge resistance and the change in length or strain^[2]. The dimensionless relationship between these two variables is called the gauge factor of the strain gauge and is expressed as:

$$K = \frac{\Delta R/R}{\Delta L/L} , \quad (1)$$

where ΔR is the change in resistance and ΔL is the change in length. As $\Delta L/L$ is strain, ϵ , then,

$$\epsilon = \frac{\Delta R/R}{K} . \quad (2)$$

Since the bonded resistance strain gauge operates on the principle that the electrical resistance of the gauge varies with strain, it must be connected in some circuit for measuring the small change in resistance, i.e., a Wheatstone bridge, Fig.A.2.1.

Fig.A.2.1 is a schematic diagram of a type of bridge circuit widely used for precision measurement of resistance^[2]. The bridge is composed of four resistors connected in a definite pattern, a current source, and a sensitive galvanometer. In Fig.A.2.1 it is assumed that R_1 is an unknown resistance, R_2 and R_3 are "ratio arms", and R_4 is a

resistance whose value is precisely known. It has been shown^[2] that, when resistance values in this circuit are such that no current flows through the galvanometer, then R_1 is to R_4 as R_2 is to R_3 , that is,

$$\frac{R_1}{R_4} = \frac{R_2}{R_3} . \quad (3)$$

From this,

$$R_1 = \frac{R_2}{R_3} R_4 . \quad (4)$$

In practice R_1 will be the resistance of a strain gauge. There are special Wheatstone bridges designed specifically for use with strain gauges. They allow the reading of the unit strain to be done directly from the instrument.

When using strain gauges, great care must be taken in order to avoid bending strain. The most basic measurement that can be made with a strain gauge is that of a direct strain resulting from tension or compression of a body. The investigation of tensile strains in a tensile or fatigue specimen is show in Fig.A.2.2. A single grid gauge is enough to measure the strain if the strains are parallel to the axis of the specimen but, it is almost impossible to obtain a pure axial loading in any body. Thus, the apparatus will be improved considerably if a second strain gauge of the same type is bonded on the specimen, at a point opposite to the first one. This latter gauge must be connected in the same leg of the bridge circuit, in series with the first gauge as shown in Fig.A.2.2, and it performs the function of eliminating any stray bending strain which may be present due to eccentric loading. How this gauge arrangement operates can be seen in Fig.A.2.2. If the strain at one side of the specimen is higher than the opposite side, the specimen is bent slightly by the loading. Gauge R_{1A} measures a strain somewhat greater than the strain representative of the pure tension but, the gauge R_{1B} will measure a lower strain. R_{1B} should measure the same net amount as gauge R_{1A} . If these gauges are placed in series electrically, the circuit effectively adds the results and divides by 2, which give the true tensile strain and eliminates all the strain indication due to bending.

Another fact that may effect the strain measurement is temperature. The need for temperature compensation of strain gauges arises from two factors. First there is the fact that the resistance of most conductors change with temperature. A second effect occurs if the thermal coefficient of expansion of the strain gauge is different from that of the structure in which it is bonded. Temperature compensation can be easily accomplished by installing a second strain gauge, often known as a "dummy" gauge, on an unstrained piece of the same material to which the active gauge is bonded. If the two pieces of material are subjected to the same temperatures during testing, both gauges will experience identical thermal resistance changes. The dummy gauges (D_1 and D_2) can be connected in series in the Wheatstone bridge as R_2 or R_4 , as shown in Fig.A.2.2.

References

- [1] THONSON, W. (Lord Kelvin). On the electrodynamic qualities of metals. Phil. Trans. Roy. Soc., 1856, 146: 649-75.
- [2] PERRY, C. C. & LISSNER, H. R. *The Strain Gage Primer*. Sec. Ed., MacGraw-Hill, 1962. 17-74.

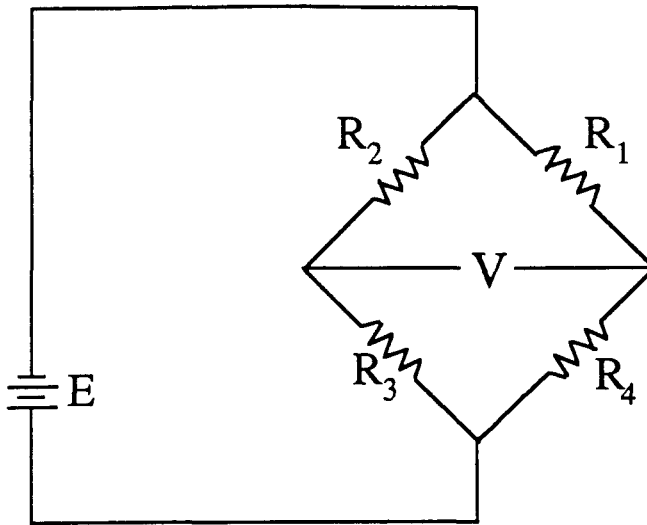


Fig.A.2.1 Wheatstone bridge circuit for measurement of resistance.

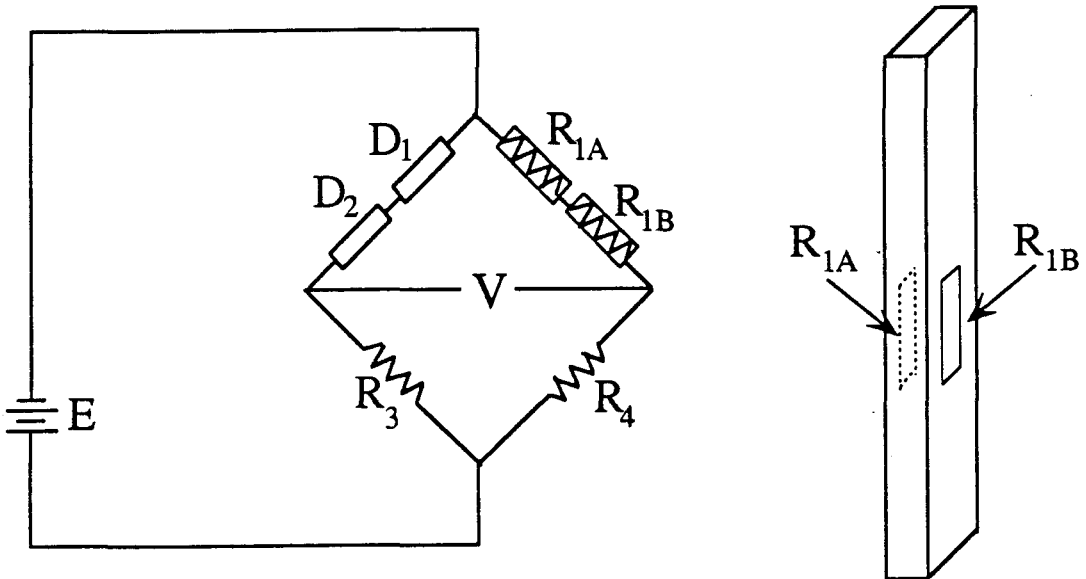


Fig.A.2.2 Electrical and physical arrangement of strain gauges for cancelling the effects of bending strains and for temperature compensation.

Appendix 3

Second phase volume fraction determination

The composite material series 28% showed the presence of globular second phase particles clustered next to the fibres, as shown schematically in Fig.A.3.1. The volume fraction of this globular phase was evaluated by the point count technique for determining volume fraction^[1] and some simple geometric relationships.

As the globular phase appears mainly around the fibres, the amount is assumed to be proportional to the fibre volume fraction. It is also assumed that the globular phase lies inside an imaginary walled tube with an average wall thickness d , Fig.A.3.2 a). If this imaginary tube is opened up, Fig.A.3.2 b), the globular volume fraction can be estimated by the lineal analysis technique^[1], Fig.A.3.2 c), on a longitudinal section of the composite. Hence, the volume fraction of the globular phase, V_p , can be calculated for the volume of material occupied by the imaginary walled tube.

Thus, by lineal analysis, V_p can be estimated as:

$$V_p = \frac{L_i}{L}, \quad (1)$$

where L is the total line length, and L_i is the total length of a random line intercepted by the globular phase, Fig.A.3.2 c).

As the fibres run across the full composite length, their volume fraction can be evaluated from area measurements on the transverse section, one can find the following relationships:

$$V_f = \frac{A_f}{A_T} \quad \text{and} \quad V_d = \frac{A_d}{A_T}, \quad (2)$$

where, V_d is the volume fraction of the layer with thickness d , and V_f is the fibre volume fraction.

From Equation (2),

$$V_d = \frac{A_d V_f}{A_f} . \quad (4)$$

It can be easily demonstrated that,

$$A_d = \pi d (D + d) n \quad (5)$$

and

$$A_f = \pi \left(\frac{D}{2}\right)^2 n , \quad (6)$$

where, n is the number of fibres and D is the fibre diameter.

Thus,

$$V_d = \frac{4d (D + d)}{D^2} V_f . \quad (7)$$

Using Eq.(7) and Eq.(1), the volume fraction of the globular phase particles in the composite material, V_{PC} , can be estimated,

$$V_{PC} = V_d V_P . \quad (8)$$

The volume fraction of the globular phase in the matrix material, V_{PM} , is given by:

$$V_{PM} = \frac{V_{PC}}{(1 - V_f)} . \quad (9)$$

Reference

- [1] PICKERING, F. B. The basis of quantitative metallography. Institute of Metallurgical Technicians. Monograph No. 1. Institute of Metals, 1975. 1-38.

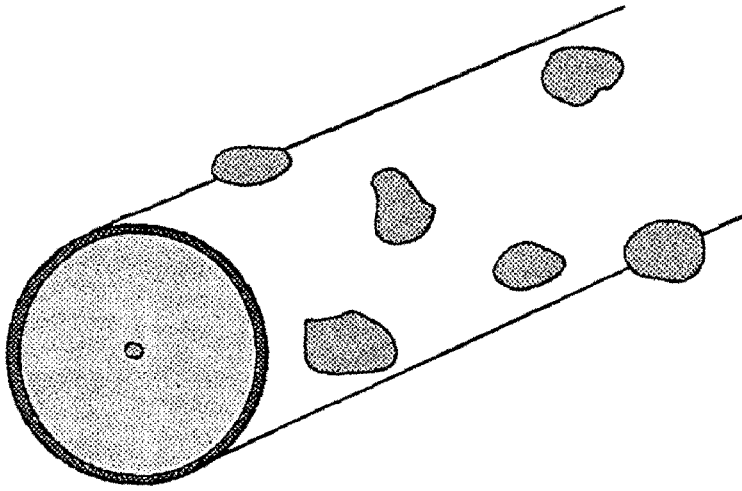


Fig.A.3.1 Schematic draw showing a fibre surrounded by globular phase particles.

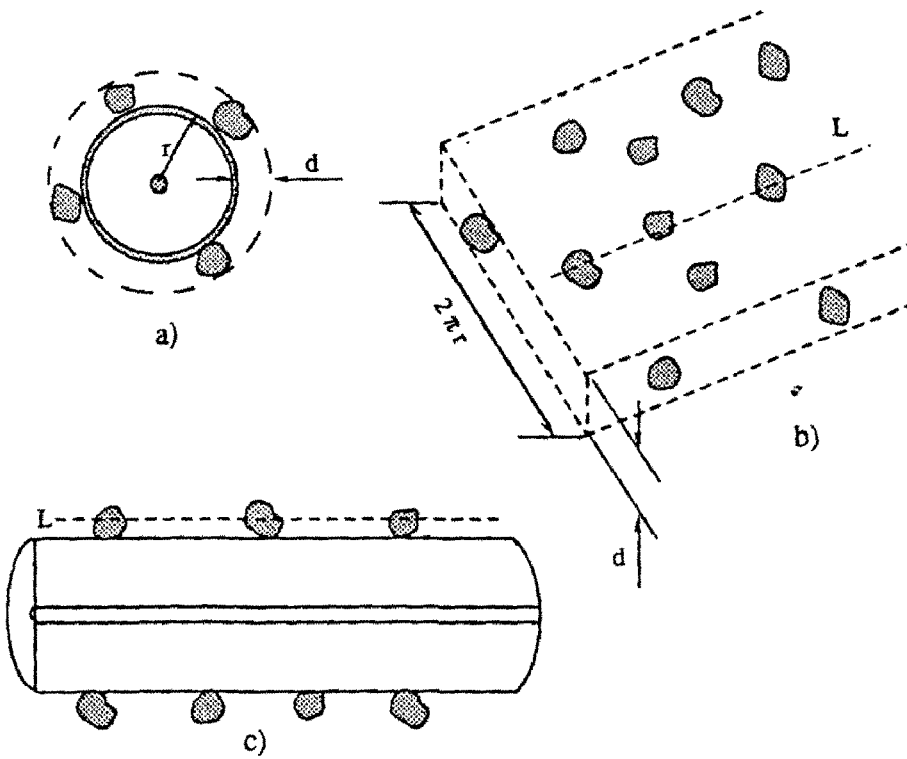


Fig.A.3.2 Schematic representation of an imaginary layer containing the globular phase.

Appendix 4

X-ray microanalysis of second phase particles in thin foils

A simple technique was described^[1] which can be used to carry out the in-situ identification by X-ray microanalysis of second particles in thin foil specimens. The X-ray intensity, I^A , from a particular element A , is proportional to the weight fraction of that element, C^A , and the total X-ray intensity I_T^A from a thin sample which contains second phase particles is given by:

$$I_T^A \propto C_M^A L_M + C_P^A L_P, \quad (1)$$

where C_M^A and C_P^A are the weight fractions of element A in the matrix and particle, respectively, and L_M and L_P the respective electron path lengths. The electron path length may be totally in the matrix, Fig.A.4.1 (a), totally in the particle, Fig.A.4.1 (c), or partially in both, Fig.A.4.1 (b). If element A , a solvent, is concentrated in the matrix, and B , a solute, is concentrated in the precipitate, then the analysis of A from the regions shown in Fig.A.4.1 can be expressed against B , graphically, as in Fig.A.4.2, where C_M^A and C_P^A are the weight fraction of element B in the matrix and particle, respectively. If both, the particle and the matrix, have fixed compositions the data will plot on a straight line.

Reference

[1] CLIFF, G.; POWELL, D. J.; PILKINGTON, R.; CHAMPNESS, P. E.; LORIMER, G. W. X-ray microanalysis of second phase particles in thin foils. Inst. Phys. Conf. Ser. No 68: Chapter 3, paper presented at EMAG, 30 Aug-2 Sep, 1983, Guilford UK. 63-6.

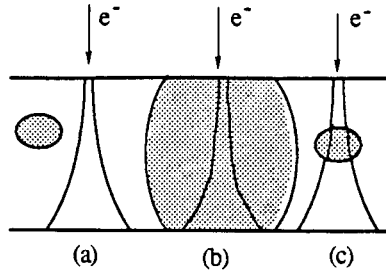


Fig.A.4.1 Schematic diagram of possible electron paths in a thin sample containing second phase particles [1].

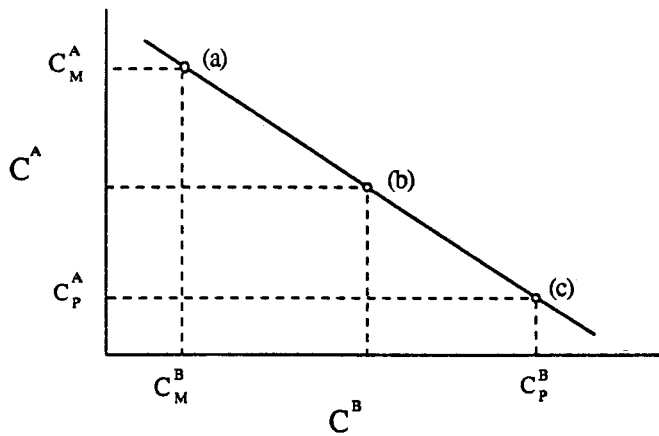


Fig.A.4.2 Schematic diagram of the analytical data obtained from the sample shown in Fig.A.4.1 [1].

Appendix 5

Foil thickness measurement

A number of techniques have been developed to determine the thickness of thin foil samples. These techniques include the use of convergent beam diffraction, parallax measurements, and trace analysis.

5.A Thickness measurement by convergent beam diffraction

The most accurate technique for measurement of the thickness of crystalline specimens is the convergent beam diffraction^[1]. This technique was first described by Kelly, Jostsons, Blake and Napier^[2]. The application and limitations of the technique have been discussed by Allen^[3]. The technique can produce results with an accuracy of $\pm 2\%$ to $\pm 5\%$ if care is taken during the measurements.

Under two-beam diffraction conditions, Kossel-Möllenstedt fringes are observed in the transmitted and diffracted disks, Fig A.5.1, the spacing of which can be used to measure the foil thickness, Fig.A.5.2. Under two-beam kinematical diffraction conditions a complementary series of fringes would be present in the central $\langle 000 \rangle$ disc. In order to determine the foil thickness, the $\langle hkl \rangle$ reflection is identified and the values of $2\theta_B$ and $\Delta\theta_i$ are measured from Fig.A.5.1. Then, the deviation from the exact Bragg condition, s_g , for each fringe is calculated from:

$$s_g^i = \frac{\lambda}{d_{hkl}^2} \frac{\Delta\theta_i}{2\theta_B}, \quad (1)$$

and the thickness of the foil can be determined by plotting a graph of,

$$\left[\frac{s_g^i}{n_i} \right]^2 \times \left[\frac{1}{n_i^2} \right], \quad (2)$$

where ξ_g is the extinction distance, t is the foil thickness, n an integer and $i = 1, 2, 3, \dots$, see Fig.A.5.3.

In practice there is some ambiguity in assigning the correct value of n to the first fringe. When the correct value is chosen, the data plots on a straight line, with a negative slope equal to $1/\xi_g^2$.

5.B Thickness measurement by contamination spots

When a probe of few nanometers in diameter is focussed on the specimen, a contamination spot will be formed on the top and bottom surfaces of the foil, Fig.A.5.4. If the foil is then tilted by an angle θ the separation of the contamination spots (x) can be used to calculate the thickness through the relationship,

$$t = \frac{x}{M} \sin \theta , \quad (3)$$

where M is the magnification. This technique is rapid and can be easily performed, but it can overestimate sample thickness^[1].

5.C Thickness measurement by parallax measurements

The foil thickness can be measured from the projected width of a grain boundary. To achieve this, the specimen must be in the eucentric position in the TEM and rotated horizontally until the grain boundary under analysis becomes parallel to the tilt axis. The specimen must then be tilted until a grain boundary becomes parallel to the electron beam, and be represented by a single line of contrast with no evident thickness fringes. The angle of tilting to achieve this condition is recorded, vide Fig.A.5.5 a). The specimen is then tilted again until the condition shown in Fig.A.5.5 b) is achieved and the new angle of tilting is noted. The projected width of the grain boundary (x) is measured from a micrograph. Using the diagrams shown in Fig.A.5.5 a) and Fig.A.5.5 b), an equation for the foil thickness can be derived,

$$t = \frac{x \cos \theta_1}{\sin (\theta_1 + \theta_2)} , \quad (4)$$

where θ_1 and θ_2 are the tilt angles and (x) is the projected width of the grain boundary.

References

- [1] LORIMER, G. W. & CLIFF, G. Quantitative X-ray microanalyses of thin foils. In: CHAPMAN, J. N. & CRAVEN, A. J. eds. *Quantitative Electron Microscopy*. Proc. of the 25th Scottish Summer School in Physics, Edinburgh, 1984. p 305.
- [2] KELLY, P. M.; JOSTSONS, A.; BLAKE, R. G.; NAPIER, J. G. The determination of foil thickness by scanning transmission electron microscopy. *Phys. Stat. Sol.*, 1975, 31(a): p. 771.
- [3] ALLEN, S. L. Foil thickness measurements from convergent-beam diffraction patterns. *Phil. Mag. A*, 1981, 43 (2): 325-35.

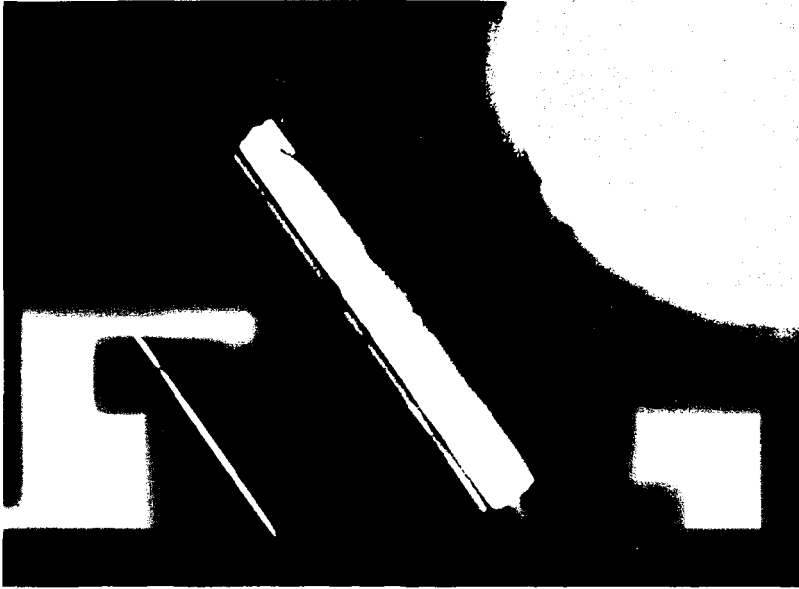


Fig.A.5.1 Convergent beam diffraction pattern showing parallel fringes in the discs with a 220Al reflection strongly excited. The diffraction pattern was obtained from the composite aluminium alloy matrix.

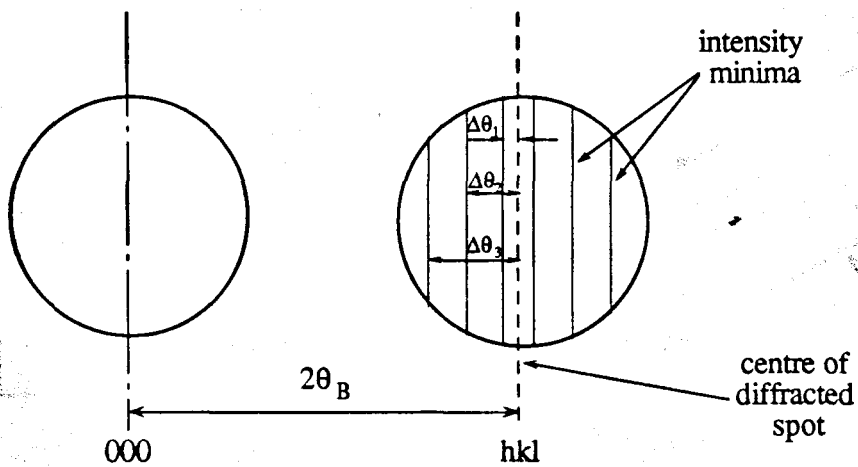


Fig.A.5.2 Schematic representation of a convergent beam diffraction showing the spacing to be measured for thickness determination.

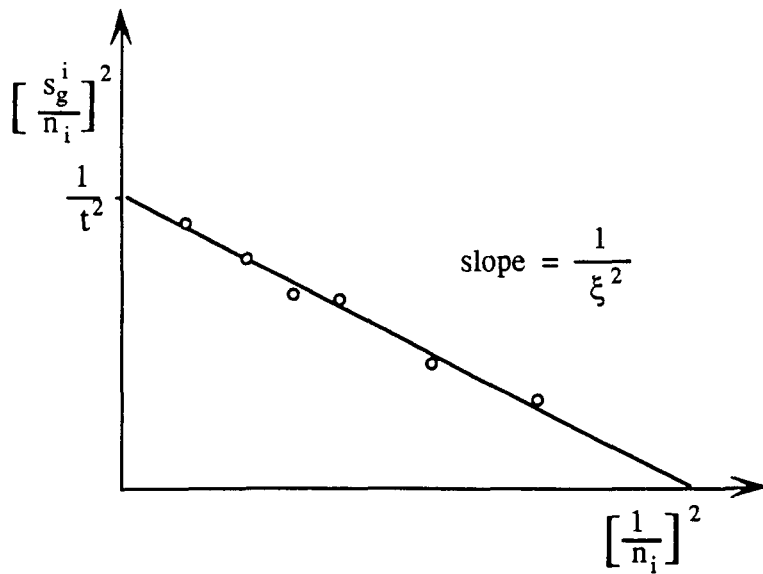


Fig.A.5.3 Graphical determination of thickness from fringe spacing measurements.

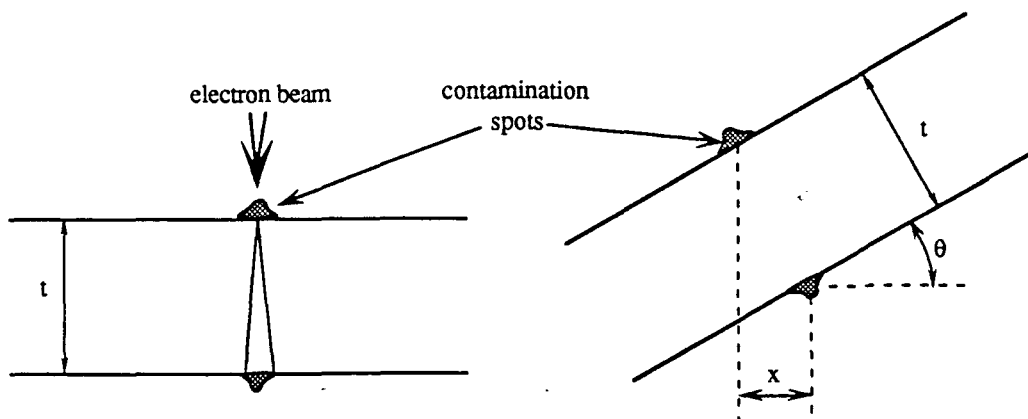


Fig.A.5.4 The measurement of foil thickness from contamination spots formed on an untilted foil and the same foil tilted through an angle, θ .